NASA Contractor Report 4584

p. 194

A Combined Experimental/Computational Study of Flow in Turbine Blade Cooling Passage

D.G.N. Tse, J.P. Kreskovsky, S.J. Shamroth, and D.B. McGrath

(NASA-CR-4584) A COMBINED EXPERIMENT/COMPUTATIONAL STUDY OF FLOW IN TURBINE BLADE COOLING PASSAGE (Scientific Research Associates) 137 p

N94-36957

Unclas

H1/34 0015731

429126

CONTRA
MAY 199

National Ae
Space Adm

NASA Contractor Report 4584

ORIGINAL CONTAINS
COLOR ILLUSTRATIONS

A Combined Experimental/Computational Study of Flow in Turbine Blade Cooling Passage

D.G.N. Tse, J.P Kreskovsky, and S.J. Shamroth
Scientific Research Associates, Inc.
Glastonbury, Connecticut

and

D.B. McGrath
Pratt & Whitney
East Hartford, Connecticut

Prepared for
Lewis Research Center
under Contract NAS3–26251

National Aeronautics and
Space Administration

Office of Management

Scientific and Technical
Information Program

1994

A COMBINED EXPERIMENTAL/COMPUTATIONAL STUDY OF FLOW IN TURBINE BLADE COOLING PASSAGE

D.G.N. Tse, J.P. Kreskovsky, and S.J. Shamroth
Scientific Research Associates, Inc.
Glastonbury, Connecticut

and

D.B. McGrath
Pratt & Whitney
East Hartford, Connecticut

ABSTRACT

Laser velocimetry was utilized to map the velocity field in a serpentine turbine blade cooling passage at Reynolds and Rotation numbers of up to 25,000 and 0.48. These results were used to assess the combined influence of passage curvature and Coriolis force on the secondary velocity field generated. A Navier-Stokes code (NASTAR) was validated against incompressible test data and then used to simulate the effect of buoyancy.

The measurements show a net convection from the low pressure surface to high pressure surface. The interaction of the secondary flows induced by the turns and rotation produces swirl at the turns, which persisted beyond 2 hydraulic diameters downstream of the turns. The incompressible flow field predictions agree well with the measured velocities. With radially outward flow, the buoyancy force causes a further increase in velocity on the high pressure surface and a reduction on the low pressure surface.

The results were analyzed in relation to the heat transfer measurements of Wagner et al. (1991). Predicted heat transfer is enhanced on the high pressure surfaces and in turns. The incompressible flow simulation underpredicts heat transfer in these locations. Improvements observed in compressible flow simulation indicate that the buoyance force may be important.

NOMENCLATURE

Roman character

B.P.	Buoyancy parameter
C_μ	Turbulent model constant
D	Hydraulic diameter
H	Half passage height
k	Turbulent kinetic energy
l	turbulent length scale
Nu	Nusselt number
Nu_∞	Fully developed smooth tube Nusselt number
Pr	Prandtl number
R	Radius
Re	Reynolds number
Ro	Rotation number
U	Streamwise (radial) velocity
U_b	Bulk mean velocity
u'	Rms streamwise velocity
V	Cross-stream velcoity
W	Tangential velocity
x	Streamwise coordinate
y	Vertical or cross-stream coordinate
y^+	Dimensionless distance to solid surface
z	Tangential coordinate
Z	Half passage width

Greek Character

ε	Turbulent energy dissipation
Ω	Rotational speed
ρ	Coolant density
$\Delta\rho$	Difference between bulk fluid density and fluid density at heated surface
μ	Absolute viscosity

1. INTRODUCTION

In advanced gas turbine engines, increased temperatures, stage pressure ratios and rotor speeds are used to increase thrust/weight ratios and reduce the specific fuel consumption. Under these circumstances, the turbine blades are subjected to increased external gas path heat loads in addition to increased levels of stress. Efficient internal convection cooling is essential to achieving good fuel consumption through minimization of secondary gas path losses and acceptable blade life. Knowledge of the local heat transfer in the cooling passages is extremely important in the prediction of blade metal temperatures, which impacts directly upon blade life. The rotation of turbine blade cooling passages gives rise to Coriolis and buoyancy forces which can significantly alter the local heat transfer in the internal coolant passages due to the development of tangential (Coriolis), as well as, radial (buoyant) secondary flows. A better understanding of Coriolis and buoyancy effects and the capability to predict the heat transfer response to these effects is necessary to allow the turbine blade designer to develop cooling configurations which utilize less coolant flow and reduce the thermal stresses on the turbine blade while maintaining structural integrity.

This Phase II program was formulated to determine the influence of Coriolis effects on the flow field and heat transfer. The present program consists of both an experimental and computational component. The main objective of the experimental program was to acquire high quality velocity data in the coolant passage of a rotating turbine blade. The data obtained was then used (i) to explain the heat transfer phenomena obtained at United Technology Research Center under NASA contract NAS3-23691 and (ii) to provide a comprehensive data set which would be used to assess Navier-Stokes codes for this flow configuration. The main objective of the computational program was to predict the flow field and heat transfer of an incompressible coolant within a rotating passage which is representative of a turbine blade cooling passage. With confirmation that the Navier-Stokes code yields accurate predictions under the influence of the Coriolis force alone, the combined effects of buoyancy and Coriolis forces can be assessed.

Under the current effort, streamwise (radial) and tangential velocities were obtained in the straight section of a rotating serpentine passage which is representative of the internal cooling passage of modern gas turbine engines. In addition, tangential and cross-stream velocities were obtained in the vicinity of the first turn. Mean and rms quantities of these velocity components were obtained by laser-Doppler velocimetry (LDV). The measurements were acquired to quantify the influence of Coriolis effects on the flow field in the internal cooling passage and were obtained with the aid of the refractive-index-matching (RIM) technique specially developed for these internal passage detailed flow measurements under the Phase I effort, Thompson et al (1990). Since the current program is isothermal and incompressible, the effect of the Coriolis force has been isolated.

Although previous investigators Wagner et al (1991), and Johnson et al (1992) have shown that both Coriolis and buoyancy forces influence the heat transfer in rotating passages, many of the previous heat transfer measurements can be explained by the flow field measurements obtained under the current effort. The numerical simulations performed under the current effort complement the velocity measurements providing insight to the flow field and heat transfer which is predicted with rotation. In addition to the incompressible flow simulation, which provided a means to assess the ability of the code to predict the impact of Coriolis forces, a compressible flow simulation was conducted in which the impact of the combined effects of Coriolis and buoyancy induced secondary flows on heat transfer could be assessed. As a result, the predicted flow field could be compared with velocity measurements acquired under the current effort and the predicted heat transfer could be compared with previous heat transfer measurement of Wagner et al (1991)

Flow configuration, instrumentation and its associated uncertainties are described in the next section, Section 2. The theoretical analysis procedures are described in Section 3. Stationary reference measurements and a preliminary inlet flow study are described in Section 4. Results are presented and discussed in Section 5. New cooling strategies are assessed in Section 6. Conclusions are stated in the final section.

2. FLOW CONFIGURATION AND INSTRUMENTATION

Figure 1 shows the flow circuit for the rotating turbine blade rig. Fluid was delivered to the serpentine cooling passage by a centrifugal pump. The experiments were conducted with flow rates of 4.4 or 8.8 gpm. The flow rate was regulated by two valves and was monitored by a turbine meter to a precision of ±3 %. The temperature was monitored downstream of the pump and was maintained at 26°C ± 0.2°C by a controller with efficient heating filaments and cooling coils. The working fluid was a mixture of 70 % turpentine and 30 % Tetralin which had a refractive index of 1.49 at 26°C for green light at 514.5nm. This refractive index was identical to that of the acrylic model. The matched index of refraction between the model and the working fluid allows the beam to pass from one medium to the other without being bent. As discussed in Thompson et al (1990), this considerably eases the task of taking measurements when the beam passes through multiple acrylic internal obstructions before reaching the measurement volume. In addition, it allows higher quality measurements in the near wall region.

A shaft encoder was fitted at one end of the shaft to monitor the angular position of the model to a precision of ± 0.018°. The rig was operated at rotational speeds in the range between 308 to 617 rpm. The speed was monitored by means of the index and pulse train from the encoder to a precision of ± 1%. The fluid has a density of 894 kg/m^3 and a kinematic viscosity of 1.74×10^{-6} m^2/s. The flow rates and rotational speed gave rise to Reynolds numbers of 12,500 and 25,000, with the corresponding Rotation numbers in the range of 0.12 to 0.48. The properties of the RIM fluid and the experimental conditions are summarized in Tables 1 and 2. Experiments with Re = 25,000 were conducted with Ro = 0.12 and 0.24 and those with Re = 12,500, with Ro = 0.12, 0.24, 0.36 and 0.48. Two stationary experiments with Re = 25,000 and 12,500 were also conducted to provide reference conditions to quantify the effect of rotation. The experimental conditions in this program are of direct practical relevance, as can be seen in the operating range of Re & Ro presented in Figure 2.

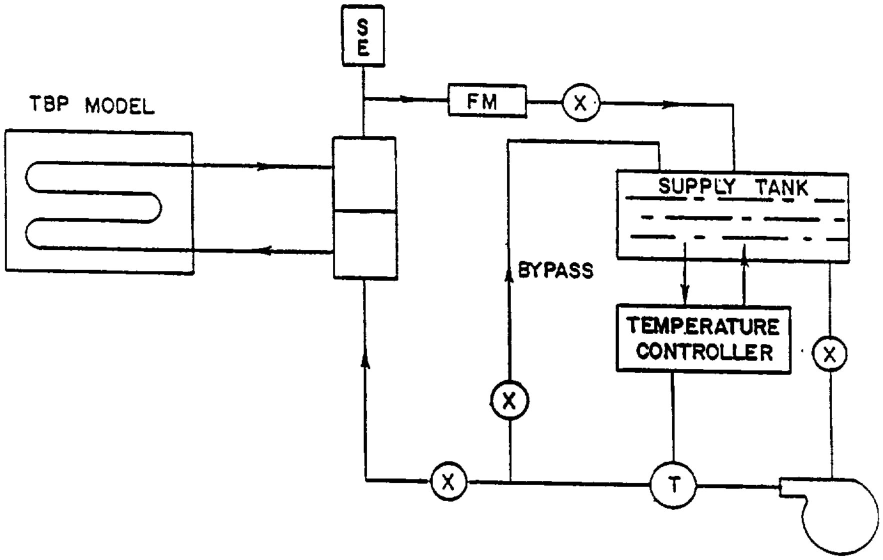
S
E
TBP MODEL
FM
X
SUPPLY TANK
BYPASS
TEMPERATURE
CONTROLLER
X
X
X
T

Figure 1 Flow circuit of the turbine-blade cooling passage rig

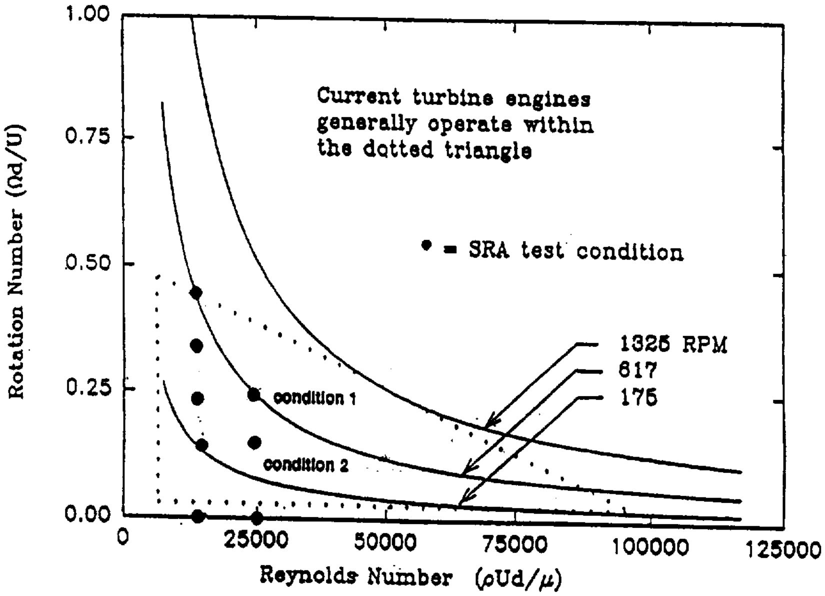

Figure 2 Operating Reynolds and Rotation numbers of current turbine-blade cooling passages.

Table 1
Properties of the refractive-index-matching fluid

Turpentine (% by volume)	70
Tetralin (% by volume)	30
Density (kg/m^3)	893
Viscosity (m^2/s)	1.74 x 10^{-6}
Refractive index (@ 514.5 nm)	1.49
Matching temperature (°C)	26

Table 2
Experimental conditions

Re 25,000	--	--	0.24*	0.12	0.0
Re 12,500	0.48	0.36	0.24	0.12	0.0

* Baseline case

Figure 3a shows the isometric view assembly of the rotating turbine blade passage model. The rig was housed between two bearings and was driven by a 30 H.P. ac motor. The speed of rotation was varied by means of a frequency controller. The acrylic model was held in position by four struts. A counter weight was fitted at the opposite end to remove any out-of-balance vibration. Figure 3b shows the fluid handling components of the rig. The fluid entered the rig from the bottom and was delivered to the model by a long duct. A plenum was fitted at the entrance of the model.

The turbine blade passage model geometry is given in Figure 4. The model had a cross-sectional area of one-half of an inch square. The model was fabricated from acrylic and had a W-shaped internal serpentine passage and a rectangular exterior. The four-pass channel with three 180° turns is identical to that of Wagner et al (1991) and was chosen to allow analyses of the velocity measurements in relation to the heat transfer results obtained by Wagner et al (1991). The outside rectangular shape avoids asymmetric refraction of laser beams and the curved inside surfaces did not create any optical refraction because of the identical refractive index of the fluid and the acrylic. RIM enabled the use of LDV to map out the entire flow field and greatly facilitates measurements in the near wall region or regions with large curvature. The RIM fluid is a stress relieving agent and will cause crazing of the model if residual stresses are present. The model was annealed for 36 hours to relieve residual stresses from machining to overcome this problem. The interior surfaces of the model were polished to enhance optical access.

Velocity information was obtained by the laser-Doppler velocimeter shown in Figure 5a. It made use of diffraction grating optics together with an Argon ion laser operating at 200mW and 514.5nm. The optical characteristics of the velocimeter are given in Table 3. The velocity components were obtained by off-axis forward scattering with the measurement volume projected into the rotating passage by a mirror at 45° with respect to the laser axis. The optics were mounted on a mechanism that traversed the measurement volume in three orthogonal directions with a maximum uncertainty of 0.02mm. The output of the photomultiplier was processed by a TSI 1990C counter. The counter and the shaft encoder were interfaced to a microcomputer, which recorded the angular position for every validated Doppler burst. The results at each angular position were then ensemble-averaged to yield mean and rms velocity profiles as a function of passage angle. The processing software continuously displayed the sample size curve during the data acquisition process and allowed the user to terminate the procedure after a statistically meaningful sample was attained. The mean and rms velocities in each ensemble-average was evaluated with statistical uncertainties of less than 2% and 5%, respectively.

Figure 4 shows the measurement locations of the experimental investigation. Measurements were obtained at eleven axial locations at x/D = 1.0, 6.4, 15.0, 18.0, 21.0, 23.0, 25.0, 33.2, 39.3, 41.3 and 43.3 at Reynolds numbers (Re) of 25,000 and 12,500. It should be noted that the streamwise distance x is defined as the distance along the centerline of the passage. Experiments at the higher Re were conducted with Rotation numbers of 0.12 and 0.24 and those with the lower Re, at R_O = 0.12, 0.24, 0.36 and 0.48. Measurements for the baseline case (Re = 25,000 and Ro = 0.24) were obtained at 9 vertical locations from -0.8 H to +0.8 H at regular intervals of 0.2 H. Measurements for the

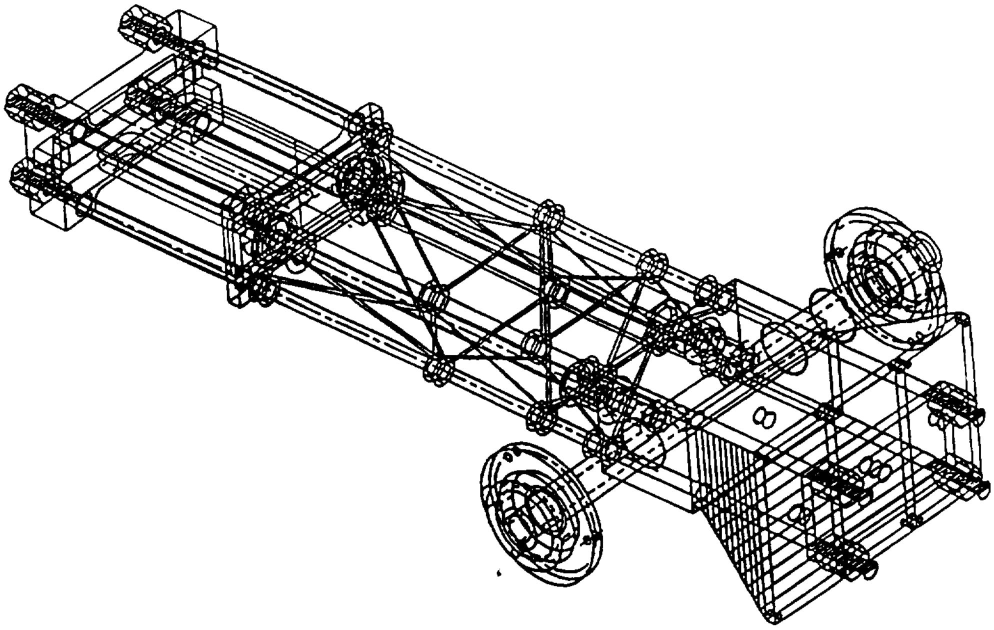

Figure 3a Isometric view assembly of the turbine-blade passage rig.

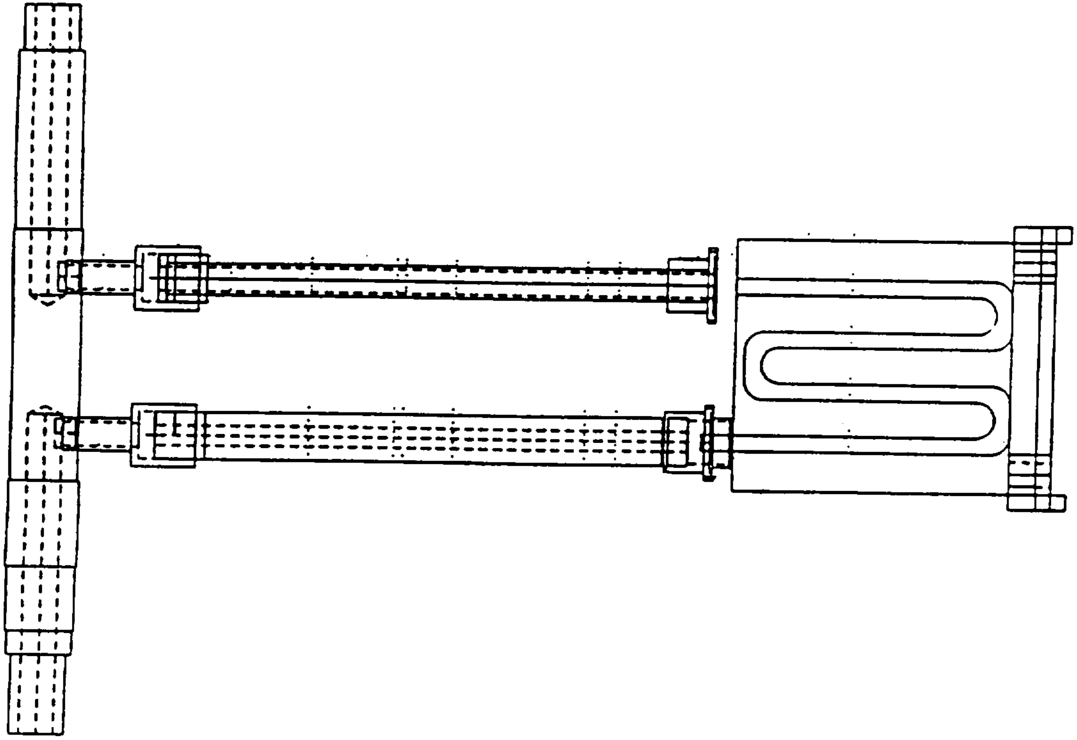

Figure 3b Fluid handling components of the turbine-blade passage rig.

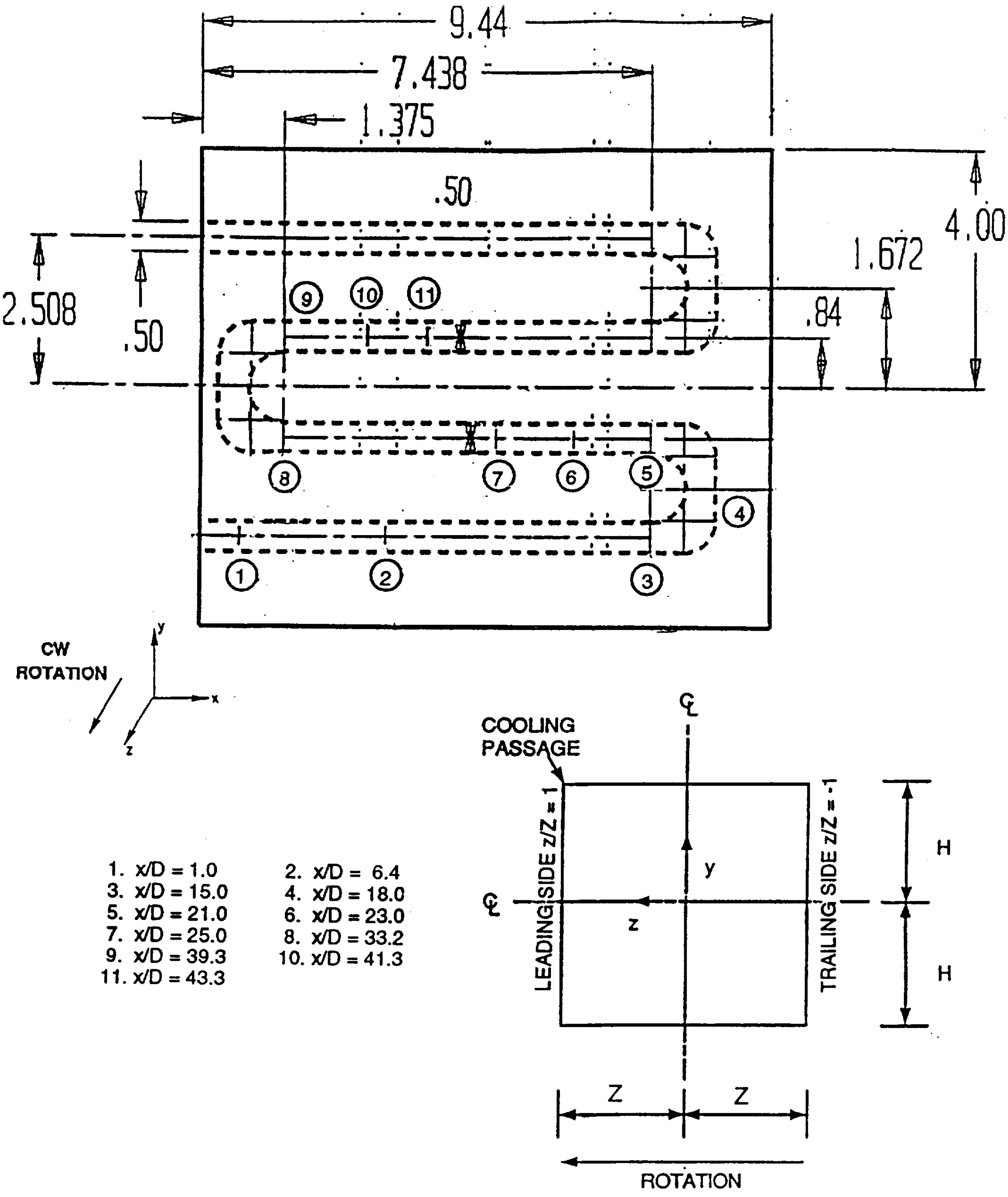
9.44
7.438
1.375
.50
4.00
1.672
.84
2.508
.50
⑨ ⑩ ⑪
⑧ ⑦ ⑥ ⑤
④
① ② ③
CW ROTATION
y
x
z
COOLING PASSAGE
℄
℄
LEADING SIDE z/Z = 1
TRAILING SIDE z/Z = -1
y
z
H
H
Z
Z
ROTATION
1. x/D = 1.0
2. x/D = 6.4
3. x/D = 15.0
4. x/D = 18.0
5. x/D = 21.0
6. x/D = 23.0
7. x/D = 25.0
8. x/D = 33.2
9. x/D = 39.3
10. x/D = 41.3
11. x/D = 43.3

Figure 4. Measureing Locations and Coordinate System.

Table 3
Optical characteristics of the laser-Doppler velocimeter

Half angle of the beam interaction (°)	4.85
Fringe spacing (μm)	3.04
Number of fringes without frequency shift	51.0
Diameter of control volume at $1/e^2$ intensity (μm)	42.0
Length of control volume at $1/e^2$ intensity (μm)	743
Maximum frequency shift (MHz)	9.0
Frequency to velocity conversion (ms^{-1}/MHz)	3.04

remaining cases were obtained at 5 vertical locations from -0.8 H to +0.8 H at regular intervals of 0.4 H. For the baseline case, the mean and rms velocities were ensemble-averaged over pre-selected angle windows of 0.018° ±2% by means of an index and a TTL pulse train from an encoder with 5000 pulses per revolution and external quadrupling. This angular resolution corresponds to a spatial resolution of roughly 0.20 mm ± 2% at radial positions between 0.587 and 0.767m. For the remaining cases, measurements were ensemble-averaged over windows of 0.036° ± 2%. The corresponding spatial resolution between the radial positions was roughly 0.40 mm ± 2%. For Re of 25,000, the mean and rms quantities were normalized by a bulk mean velocity (U_b) of 3.44 and for Re of 12,500, 1.72 m/s.

Figure 5b shows some preliminary velocity measurements obtained at x/D = 21.0 and the corresponding sampling size per 0.018° averaging window for three vertical locations. The sample size per averaging window also corresponds to the data arrival rate for that specific angular position. The distinct feature of the figures is that the similarity between the data arrival rate and the velocity profiles is not observed. The sharp drops in the sample size curves near the walls are due to reduction in data rates, which are common phenomena in laser-Doppler velocimetry because of reduction in signal-to-noise ratio (SNR) near the wall. The troughs in the sample size curves in the center of the passage stem from variation in optical quality over the passage. These results illustrate the velocity and optical biasing effects that conventional population averaging would introduce in the statistics of such samples. The ensemble averaging performed here removes these biasing effects.

3. Computational Procedures

3.1 Overview

The governing equations of continuity, momentum, and energy were solved using the Navier-Stokes code of Rhie (1986). This is a pressure-based implicit procedure which solves the full Navier-Stokes equations in general coordinates, thus allowing the use of body-fitted coordinate systems. In Rhie's approach, the preliminary velocity field is first obtained from the momentum equations with a preliminary pressure field. Since this preliminary velocity field does not satisfy the continuity equation, pressure correction equations are solved to establish a new velocity field which does satisfy the continuity equation. The momentum and continuity equations are coupled through this pressure correction procedure. Then, the energy and turbulent scalar equations are solved in turn. Two near-wall shear-stress treatments were evaluated in conjunction with the two-equation k-ε formulation of turbulence. In one case, the governing equations near the wall were solved by employing generalized wall functions which assume that the boundary layer velocity profile has the universal "law-of-the-wall" profile (Launder and Spaulding, 1974). In the other case, the two-layer wall integration method was used in which the governing equations are solved to the wall (Dash et al., 1983). Near the wall, the classical

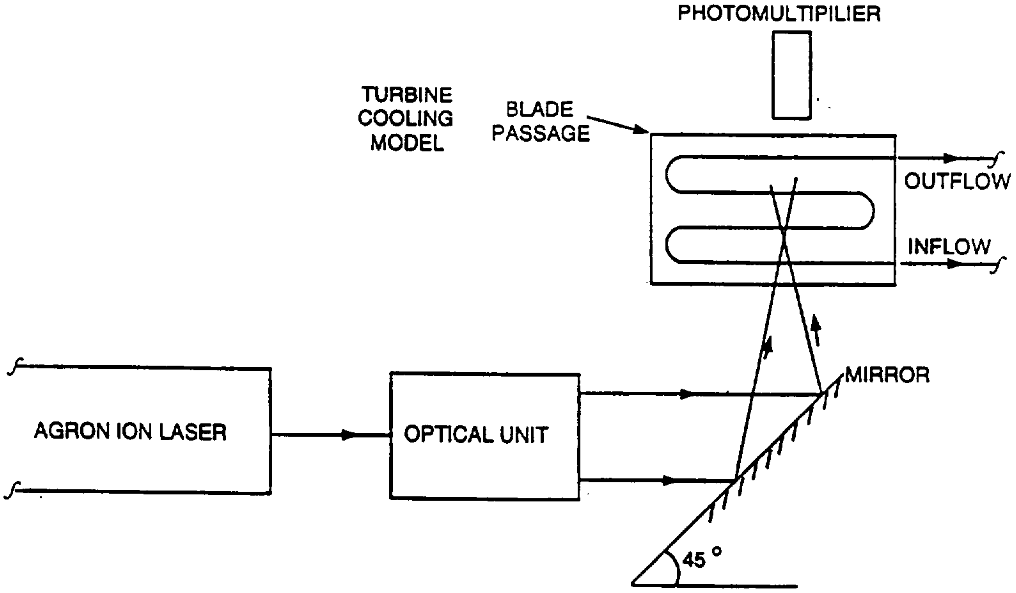
PHOTOMULTIPILIER
TURBINE COOLING MODEL
BLADE PASSAGE
OUTFLOW
INFLOW
MIRROR
AGRON ION LASER
OPTICAL UNIT
45 °

Figure 5a Laser-Doppler velocimeter setup.

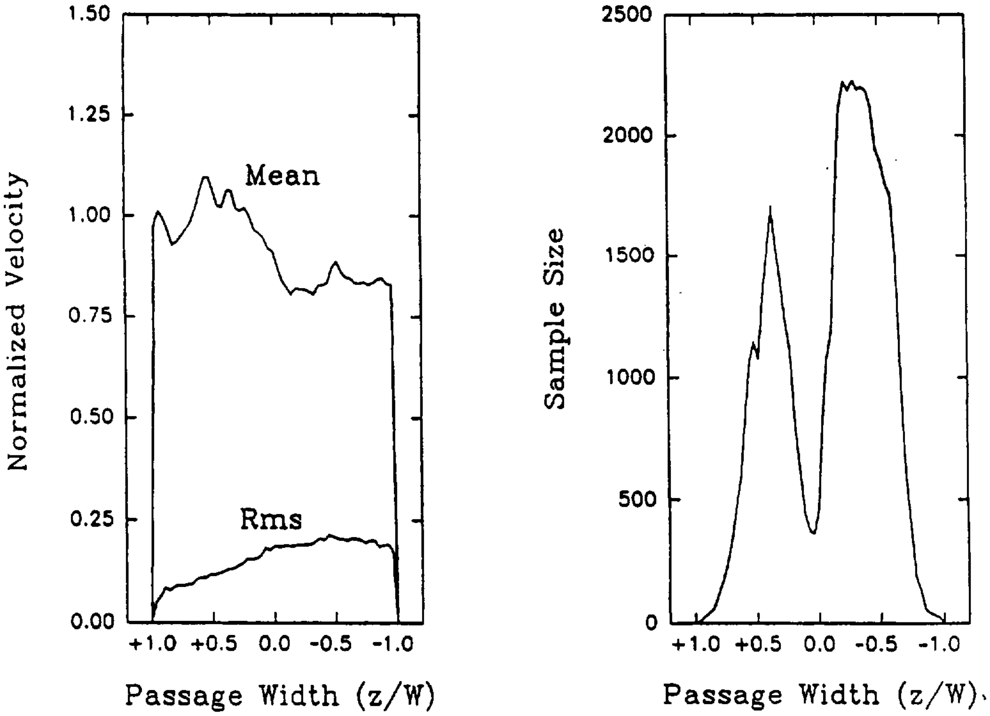

Figure 5b Sample size curve and velocity profile at x/D = 21.0.

Van-Driest mixing length formulation was used. This region was patched with two-equation k-ε turbulence model at $y^+ = 50$.

Three incompressible flow simulations were made of the flow field and heat transfer in the rotating serpentine passage. In all cases, the Reynolds number was nominally 25,000 and the Rotation number, Ro, was 0.24. In two cases, wall functions were employed; these cases had differing inlet boundary conditions. In the third case, the two-layer wall integration method was used. Comparisons of these first two simulations provide information on inlet boundary condition sensitivity. Comparison between the wall functions and wall integration cases, with the same inlet conditions, provide insight into the ability of the two near-wall turbulence models to accurately predict the flow field in the regions with large velocity gradients. All three simulations can be directly compared to the velocity measurements.

3.2 Grid Generation and Flow Field Initialization

3.2.1 Grid Generation

The computational model for the wall function simulations consists of all four passes of the serpentine model. Since initial velocity measurements were made at $x/D = 6.4$, the inlet plane was specified to coincide with this measurement plane. 228 streamwise grid planes define the computational domain with a non-uniform cross-stream mesh of 27 x 27 points as shown in Figure 6(a). This simulation, with wall functions and the inlet plane located at $x/D = 6.4$, will be referred to as Case A. A preliminary grid study of the first two legs of the model in the stationary frame was conducted to insure that the selected grid spacing would be valid for the wall function formulation of the k - ε turbulence model.

Since later velocity measurements were made at $x/D = 1.0$, an additional simulation was made with wall functions with the inlet plane at this location, Case B. The grids of Case A and Case B are identical from $x/D = 6.4$ to the exit of the duct. Seventeen evenly spaced grid planes were added to the Case A grid to span the duct from $x/D = 1.0$ to $x/D = 6.4$ to obtain the Case B grid.

In order to solve the governing equations in the boundary layer for the wall integration method, Case C, extremely tight grid spacing was defined near the walls using a hyperbolic tangent stretching function. The distance between the wall and the first grid point off the wall is 0.0002in which corresponds to $y^+ \approx 0.5$. Additional grid points were added to the central region of each cross-stream grid plane using a geometric stretching function, resulting in a relatively uniform mesh in this region. Further grid refinements were made in the streamwise direction, particularly in the turn region, Figure 6(b). Since the flow is highly three-dimensional in this region, it was felt that more grid planes would better resolve the flow field. Due to the grid refinements in all three directions, the new computational mesh was limited to the first two legs of the serpentine passage. The

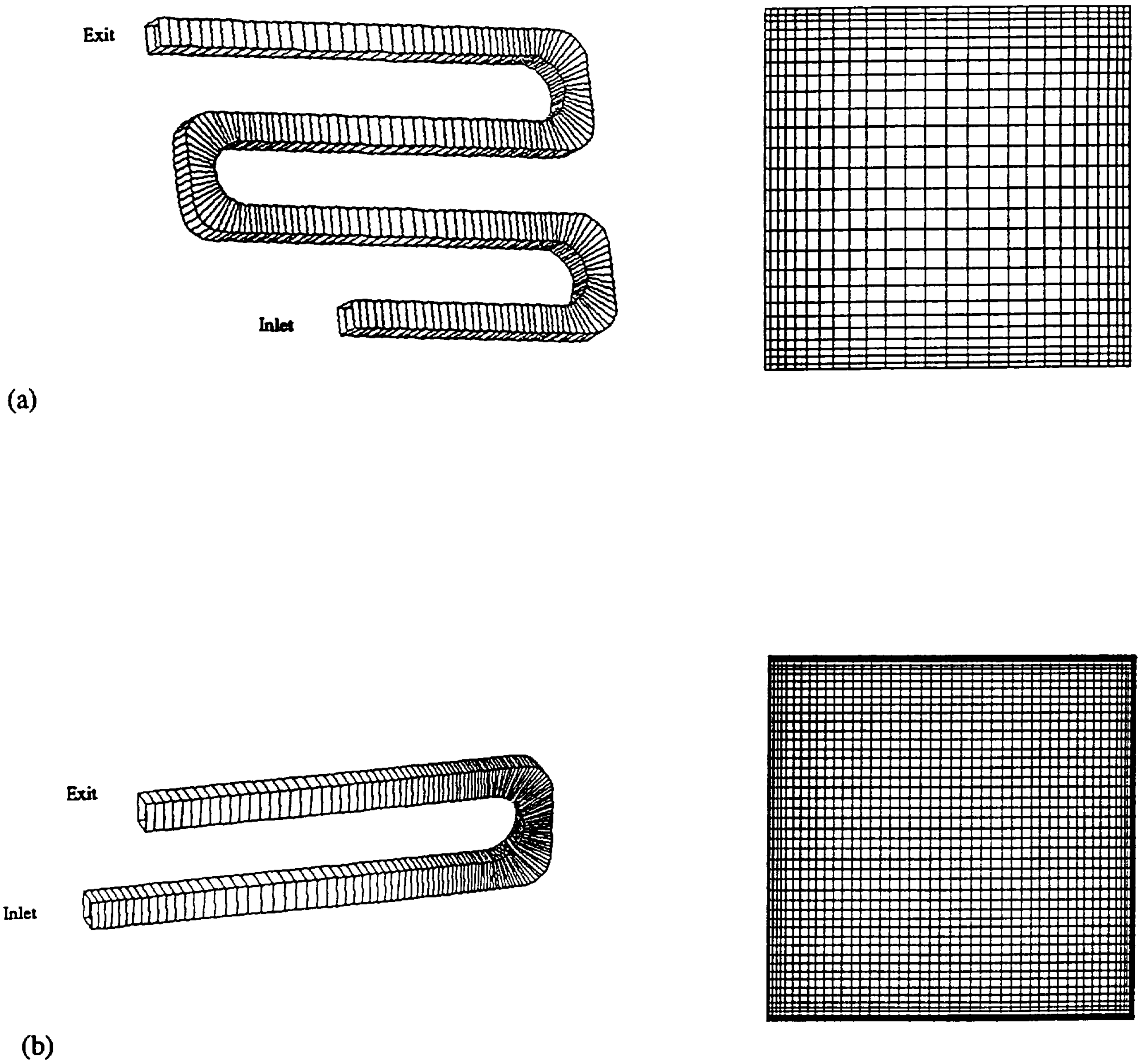

Case A - inlet plane at x/D=6.4
Case B - inlet plane at x/D=1.0
Case C - inlet plane at x/D=1.0;
dense grid near wall and first turn

Figure 6 Computational mesh for (a) wall function simulations (cases A and B) and (b) two-layer wall integration simulation (case C)

computational domain extends from x/D = 1.0 in the first passage to the entrance of the second turn with grid dimensions of 166 x 59 x 59.

3.2.2 Flow Field Initialization

The same general procedure was used to initialize the flow field in all three cases. In the core region of the duct, from $-1.0 < z/Z < 1.0$ and $-0.8 < y/H < 0.8$, the available measured velocities were mapped onto the computational mesh using a two-dimensional interpolation routine. Previous computations were used to complete the inlet profile specification in the vertical direction from $0.8 < y/H < 1.0$ and $-1.0 < y/H < -0.8$.

For Case A, only the streamwise velocity measurements were completed at the time the computation was initiated. Predicted streamwise velocity from a previous computation in a straight rotating duct was used to obtain a realistic boundary layer on the upper and lower walls, y/H = 1.0 and y/H = -1.0. The inlet velocity profile is shown in Figure 7. The slight discontinuity of the velocity contours in the corners of the duct is due to a mismatch between the data and the previous computation. This discontinuity disappears within two streamwise grid planes. It is important to note that the measurements used to initialize the Case A computation were acquired with a screen in the inlet plenum while subsequent data were acquired without the screens. Since no data was available for Case A, the secondary flow was assumed to be small and the tangential and radial velocities were set to zero.

For Cases B and C, the measured streamwise and tangential velocity components at x/D = 1.0 were used, in conjunction with a predicted flow field from a simulation of the inlet plenum, to specify the inlet boundary conditions. Flow through the plenum was simulated to characterize the inlet velocity profile, since data was available for only two of the three velocity components. Results from this study are documented in Section 4.2.

As stated above, the measurements were used where available to specify the inlet velocity profile with predictions used to complete the flow field definition. Streamwise velocities profiles for y/H = -0.96, -0.90, 0.90, and 0.96 were extracted from the predicted flow field and combined with the measurements for $-0.8 < y/H < 0.8$ at x/D = 1.0 and interpolated onto the computational mesh. Due to the very good agreement between the inlet plenum predictions and the measurements at this location, x/D = 1.0, the streamwise velocity gradients are smooth, as shown in Figure 8.

A similar procedure was used to initialize the tangential velocity component. Due to limitation of optical access, it was not possible to acquire tangential velocities very near the leading and trailing surfaces. The locations in which no data was acquired are shown in Figure 9(a) in dark blue. Measurements were linearly extrapolated to the wall for each vertical measurement location. The predictions and measurements were compared via line plots for all channel heights (y/H = -0.8, -0.6, -0.4, -0.2, 0, 0.2, 0.4, 0.6, 0.8). These comparisons indicated that secondary flow was underpredicted by a factor of five at x/D = 1.0. Therefore, the predicted tangential and radial velocity components were scaled by a

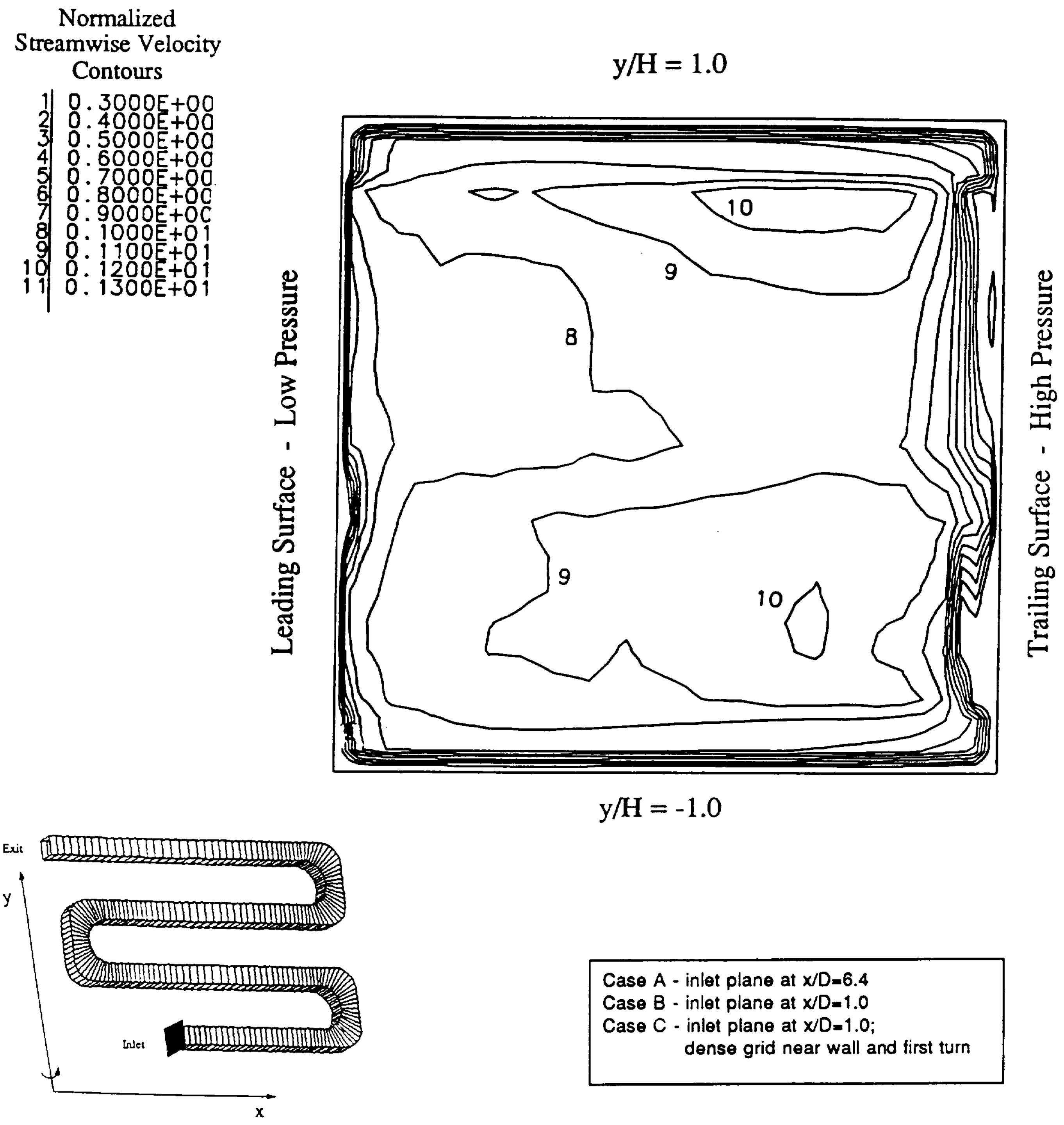

Figure 7 Streamwise Velocity Initialization for case A

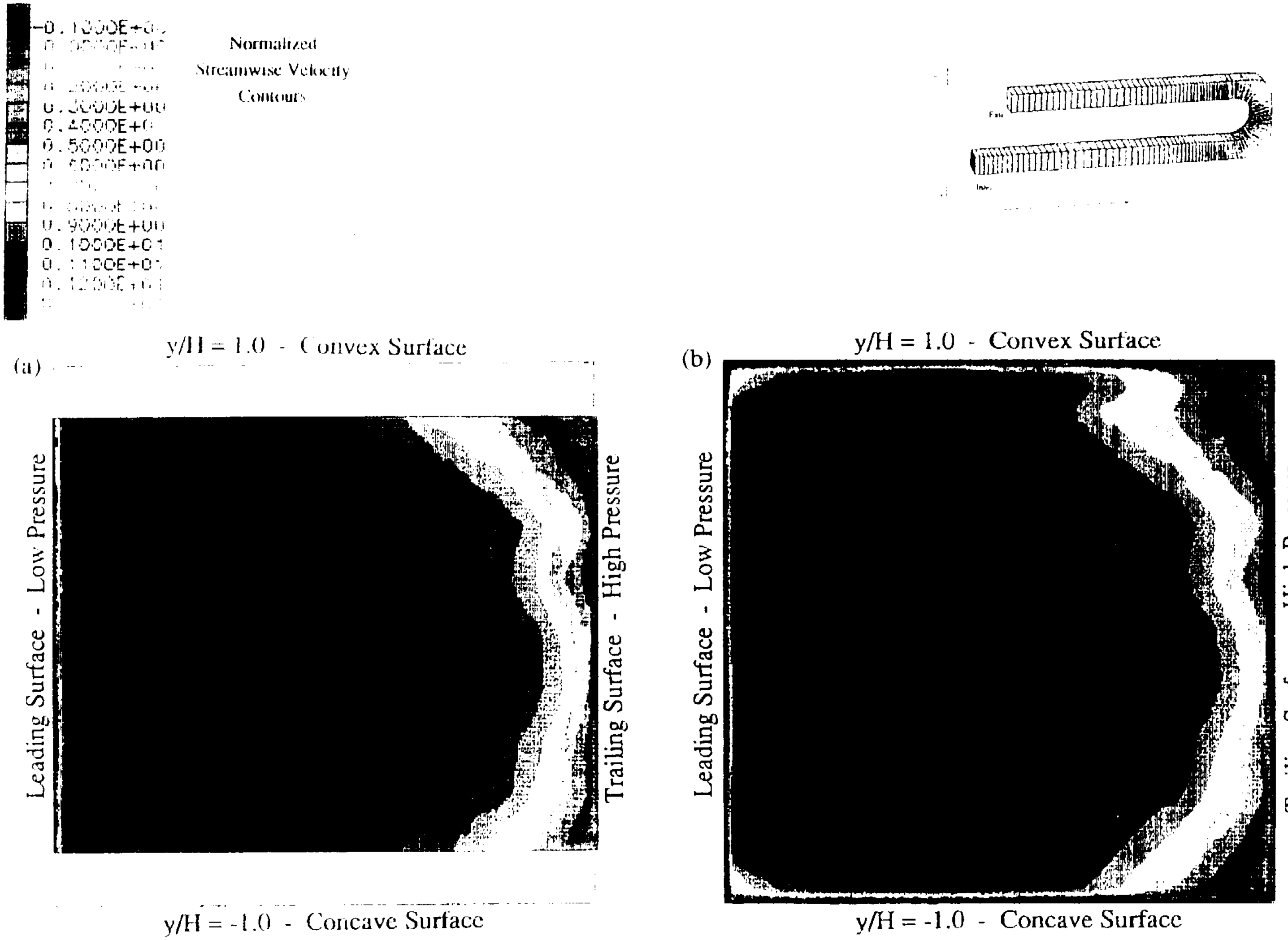

Figure 8 Comparison of normalized streamwise velocity contour (a) measurements versus (b) computationally imposed condition at inlet plane, x/D =1.0 for cases B and C

PRECEDING PAGE BLANK NOT FILMED
PAGE 18 INTENTIONALLY BLANK

factor of five so that they could be used in conjunction with the measurements to initialize the flow field. The measured tangential velocity for $-0.8 < y/H < 0.8$ was combined with the scaled predictions near the walls, $y/H \leq -0.9$ and $y/H \geq 0.9$ and interpolated onto the computational mesh. The differences between the measured tangential velocity profiles and the predictions resulted in some discontinuities in the prescribed inlet boundary condition, Figure 9(b). However, the impact on the downstream flow field predictions is expected to be small.

Since it was not possible to measure the radial velocity component at the inlet, the scaled radial velocity component previously obtained from a numerical simulation was scaled and then was interpolated onto the mesh and is shown in Figure 10. The scale factor was obtained as the ratio of the measured to the previously obtained (via computations) tangential velocity field. Details are given in Section 4.2. The resulting inlet secondary flow field is shown in Figure 11 for reference. The Coriolis induced vortices are not symmetric at the inlet and this is consistent with the measured tangential velocity component.

The measured rms streamwise velocity component at the inlet was used as a basis for initialization of the turbulent kinetic energy (k) and the turbulent energy dissipation (ε). The turbulent kinetic energy at the inlet was assumed to be isotropic with $k = 1.5\ u'^2$ and the streamwise rms velocity was assumed to be constant from $y/H = -0.8$ to $y/H = -1.0$ and y/H 0.8 to $y/H = 1.0$. In order to initialize the turbulent energy dissipation, the turbulent length scale, l was assumed to be three percent of the hydraulic diameter of the channel. In addition, the one-equation turbulence model was assumed to be valid in this region with $\varepsilon = C_\mu\ k^{1.5}/\ l$ where $C_\mu = 0.09$. These assumptions are based on fully developed channel flow and are in agreement with results from the inlet plenum computations. Contours plots of k and ε applied to the inlet plane of the computations are shown in Figure 12.

Inlet boundary conditions were specified as non-dimensional quantities. The dimensionalizing values for velocity and density corresponded to the average inlet values for the experiment. Using the average inlet velocity from the first set of measurements and the density of the RIM fluid, the experimental Reynolds number was computed to be 24,500. This Reynolds number was held for all of the incompressible simulations. The Rotation number was set to match the experiments with $Ro = 0.24$. In order to compare the predicted heat transfer with the Wagner et. al (1991) data, the Prandtl number was set to $Pr = 0.7$.

4. PRELIMINARY RESULTS

Figure 4 shows the coordinate system used in presenting the results. The region between the passage entrance and the first turn will be referred to as the first passage in later discussion and that between the first and second turn, the second passage. Streamwise distance (x) from the entrance is normalized by the equivalent hydraulic diameter (D).

PAGE 20 INTENTIONALLY BLANK

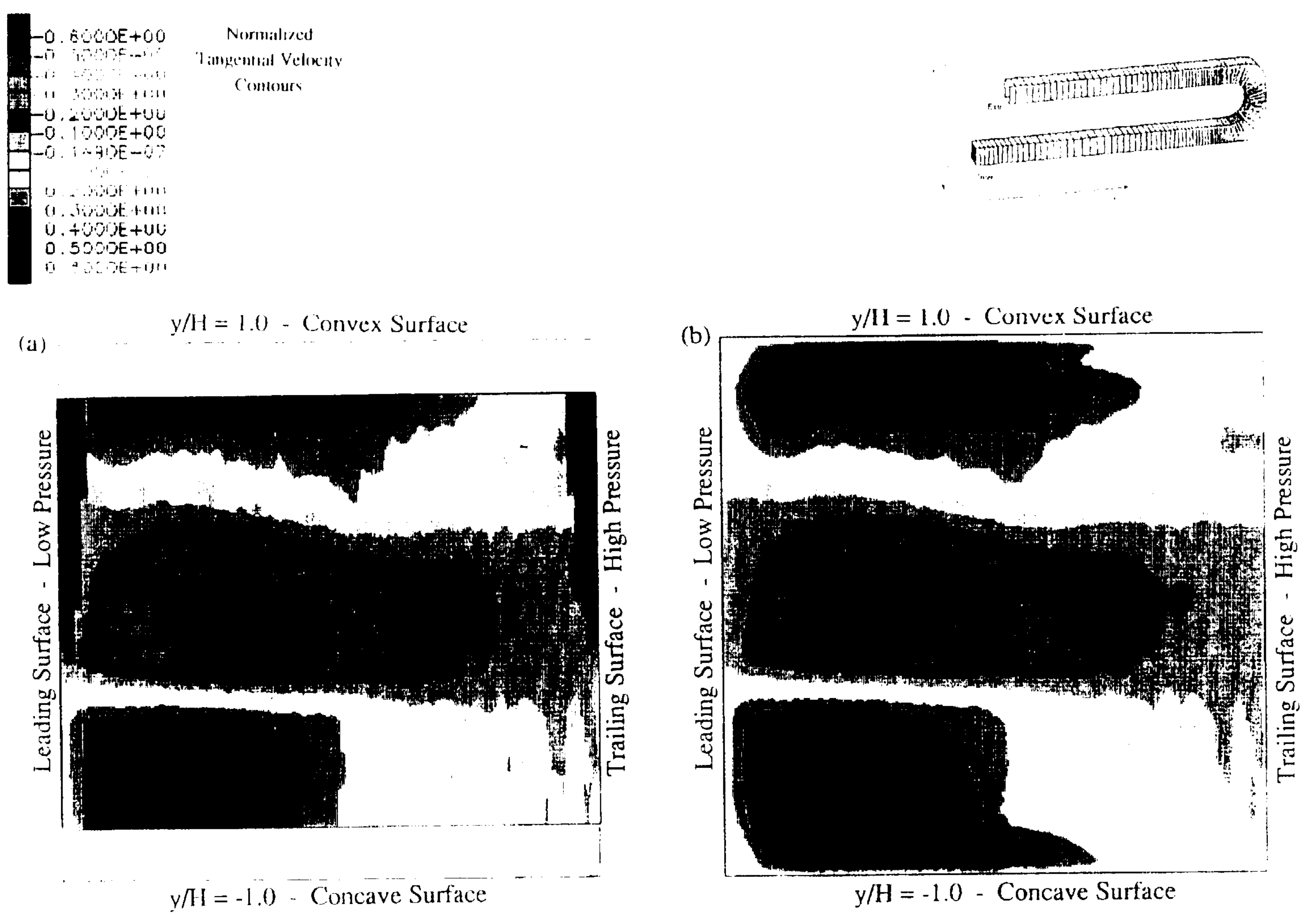

Figure 9 Comparison of normalized tangential velocity contour (a) measurements versus (b) computationally imposed condition at inlet plane, x/D =1.0 for cases B and C

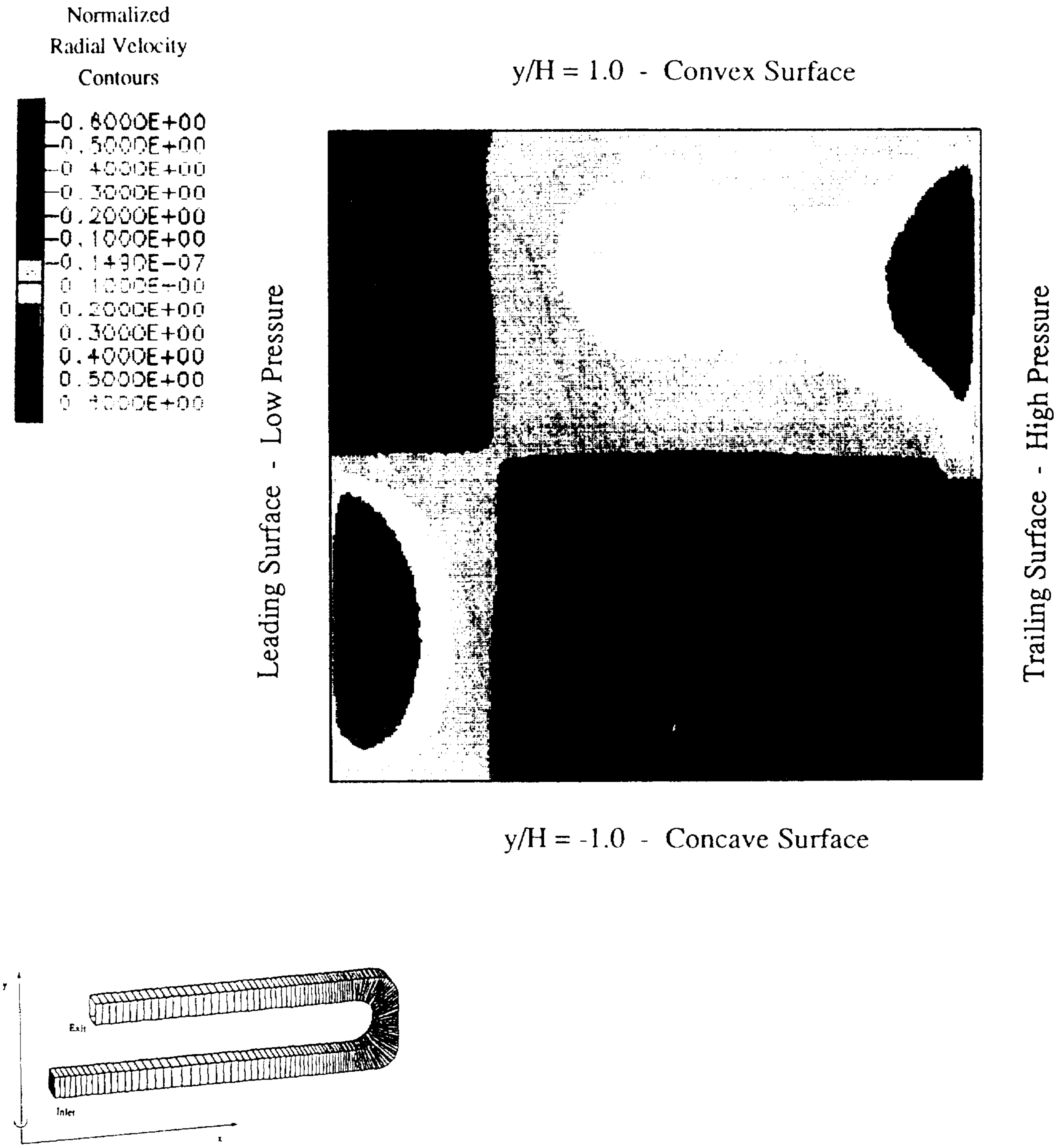

Figure 10 Computationally imposed cross-stream velocity contour at inlet plane, x/D=1.0 for cases B and C

PRECEDING PAGE BLANK NOT FILMED

PAGE 24 INTENTIONALLY BLANK

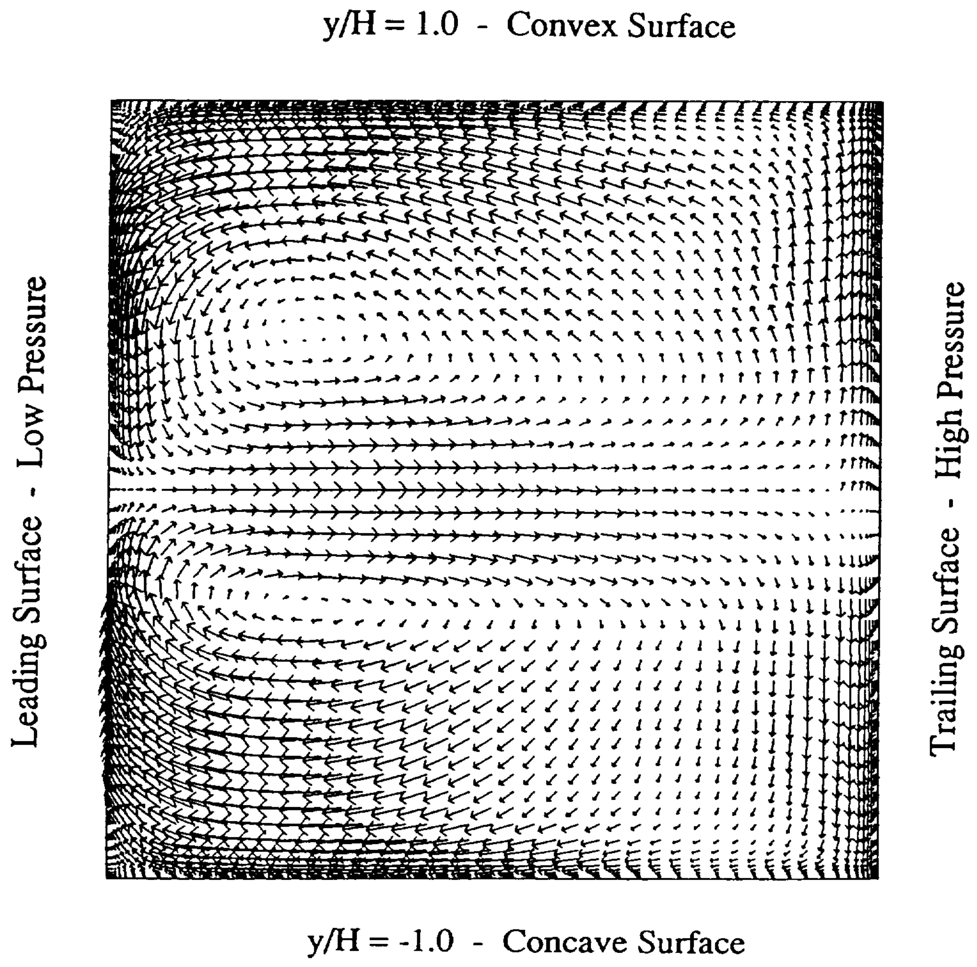

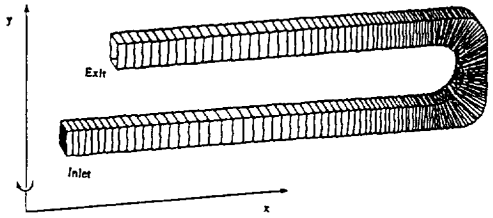

Case A - inlet plane at x/D=6.4
Case B - inlet plane at x/D=1.0
Case C - inlet plane at x/D=1.0;
dense grid near wall and first turn

Figure 11 Secondary flow velocity vectors resulting from imposed inlet velocity boundary condition for cases B and C

PRECEDING PAGE BLANK NOT FILMED

PAGE 26 INTENTIONALLY BLANK

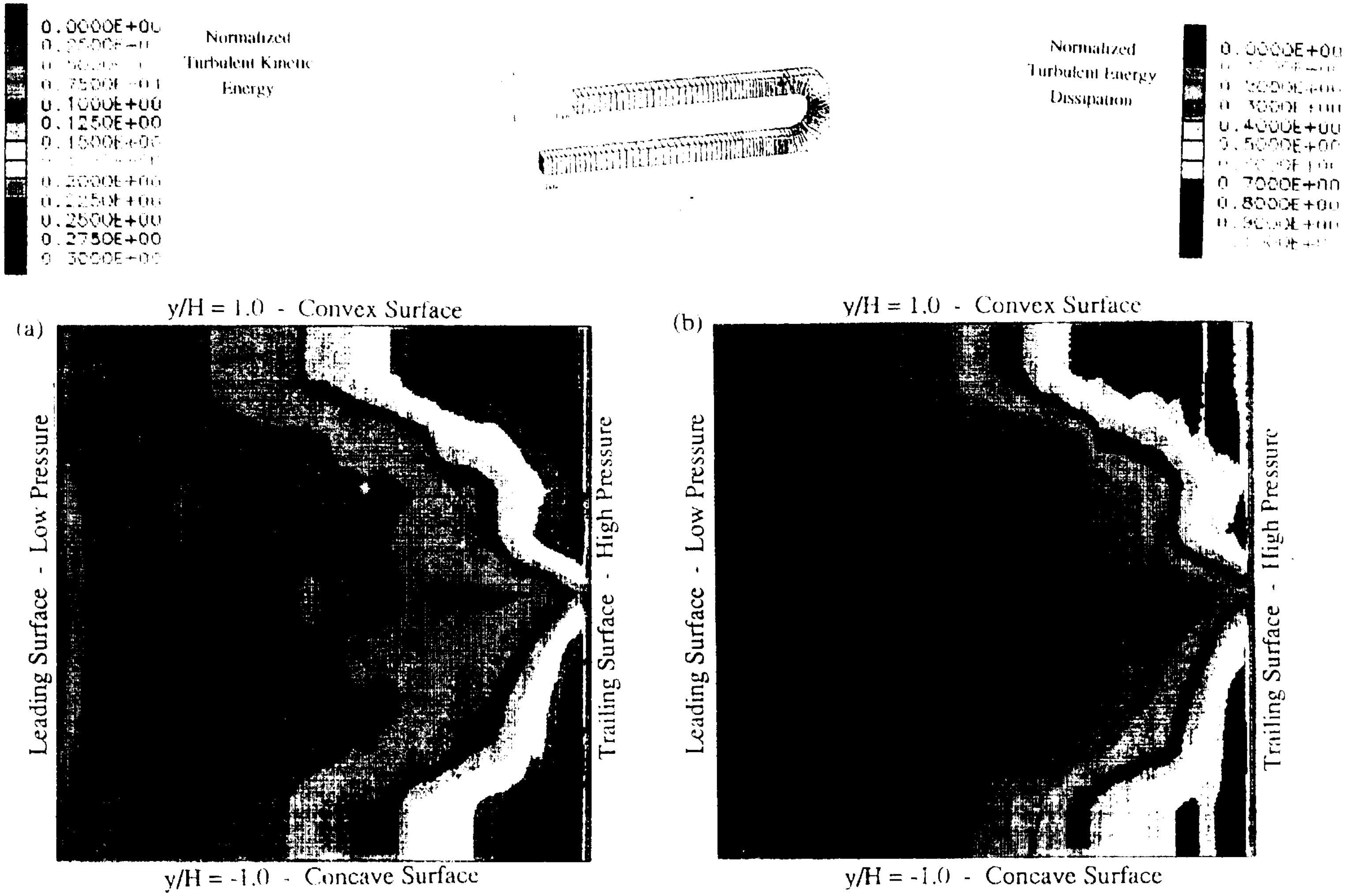

Figure 12 Turbulence quantities imposed at the inlet plane (a) turbulent kinetic energy and (b) turbulent energy dissipation

PAGE 28 INTENTIONALLY BLANK

Vertical (y) and tangential (z) distances are normalized by the half passage height (H) and width (Z), respectively. The coordinate system used to present the results in the straight section is: x is positive along the streamwise direction, y is positive against gravity and z is positive in the direction of rotation; and at the turns, the concave surface is positive. Streamwise velocity (U) is positive radially outward. Cross-stream velocity (V) is positive against gravity in the straight section of the passage and at the turn, radially outward. Tangential velocity (W) is positive in the direction of rotation.

4.1 Stationary results

Mean and rms streamwise data obtained at x/D of 1.0, 6.4, 15.0, 21.1, 23.0, 25.0, 33.2, 39.3, 41.3 and 43.3 at Re of 25,000 and 12,500 are shown in Figures 13a and 13b. These measurements are obtained to provide reference conditions to quantify the effect of rotation. Figures 13a(i) and 13b(i) show that the inlet flow is symmetric for both Re. The flow is fully developed at x/D =6.4, Figures 13a(ii) and 13b(ii). The effect of the turn can be seen in Figures 13a(iii) and 13b(iii). The flow rate on the inside of the turn is higher because fluid is being drawn to the suction side. The low velocity at y/H = -0.8 indicates growth of the boundary layer. The effect is more noticeable for the lower Re, Figure 13b(iii). The scattering in the velocity profile at y/H = -0.8, Figure 13b(iii), indicates that the viscous effect is breaking away from the wall. The same trend is also evident in the second passage, Figures 13b(v) and 13b(vi). The near-wall flow associated with the cross-stream pressure gradient of a turn is indicated by increases in cross-flow near the two walls (z/Z <-0.6 and z/Z >0.6) at all y/H at the exit of the turn, Figures 13a(iv) and 13b(iv). The signature of the near-wall secondary flow is still evident in the profiles at 2D downstream of the turn, Figures 13a(v) and 13b(v). Substantial variation in the vertical direction can be seen in the profiles at x/D = 21.0, Figures 13a(iv) and 13b(iv), as the cross-flow is being convected to the pressure surface; i.e., the outer surface. This vertical variation is dampened at 4D downstream of the turn, Figures 13a(vi) and 13b(vi). At x/D = 23.0 and 25.0, Figures (v) and (vi) of 13a and 13b, near-wall measurements could not be obtained at the trailing wall because of the blockage formed by the leakage of glue into the model during fabrication. Comparison of (vii) and (x) of Figures 13a and 13b shows that, consistent with the results obtained at the first turn, the effect of Re in the range 12,500 to 25,000 is small. The velocity profiles of flow entering and exiting the second turn, Figures (vii) to (x) of 13a and 13b, are similar to those obtained in the first turn, Figures (iii) to (vi) of 13a and 13b. Thus, any differences between velocity characteristics of the flow entering the first and second turns in the presence of rotation are attributed to Coriolis effects.

Figures 14a and 14b show that the turbulent intensity in the first passage is approximately 10% for both Re. The inviscid entrance core is indicated by a reduction in turbulent fluctuation from 10% to 5% at x/D = 1.0, Figures 14a(i) and 14b(i). The turn generates a substantial amount of turbulence. The average rms values at the exit of the turn and 2D downstream of the exit (x/D = 21.0 and 23.0, Figures (iv) and (v) of 14a and 14b) are approximately 15%. The turbulence generated by the turn is quickly damped in the second passage. At 4D downstream of the turn, x/D =25.0 (Figures (vi) of 14a-14b), the average rms values have been reduced to 12% for both Re. The turbulent intensities at y/H = -0.8 at x/D = 15.0, 21.0 and 25.0, Figures (iii), (v) and (vi) of 14b, increase sharply to

PAGE 30 INTENTIONALLY BLANK

PRECEDING PAGE BLANK NOT FILMED

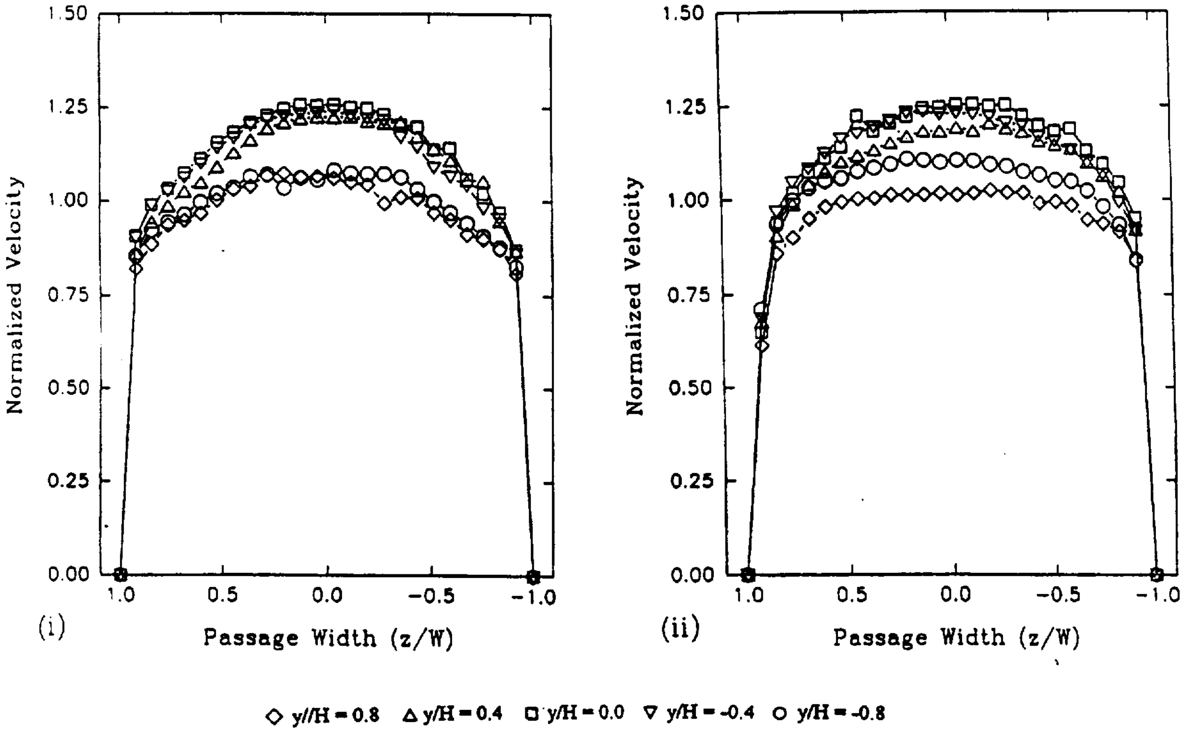

Figure 13a Streamwise mean velocity profiles obtained at Re = 25,000 and Ro = 0.0. (i) x/D = 1.0. (ii) x/D = 6.4.

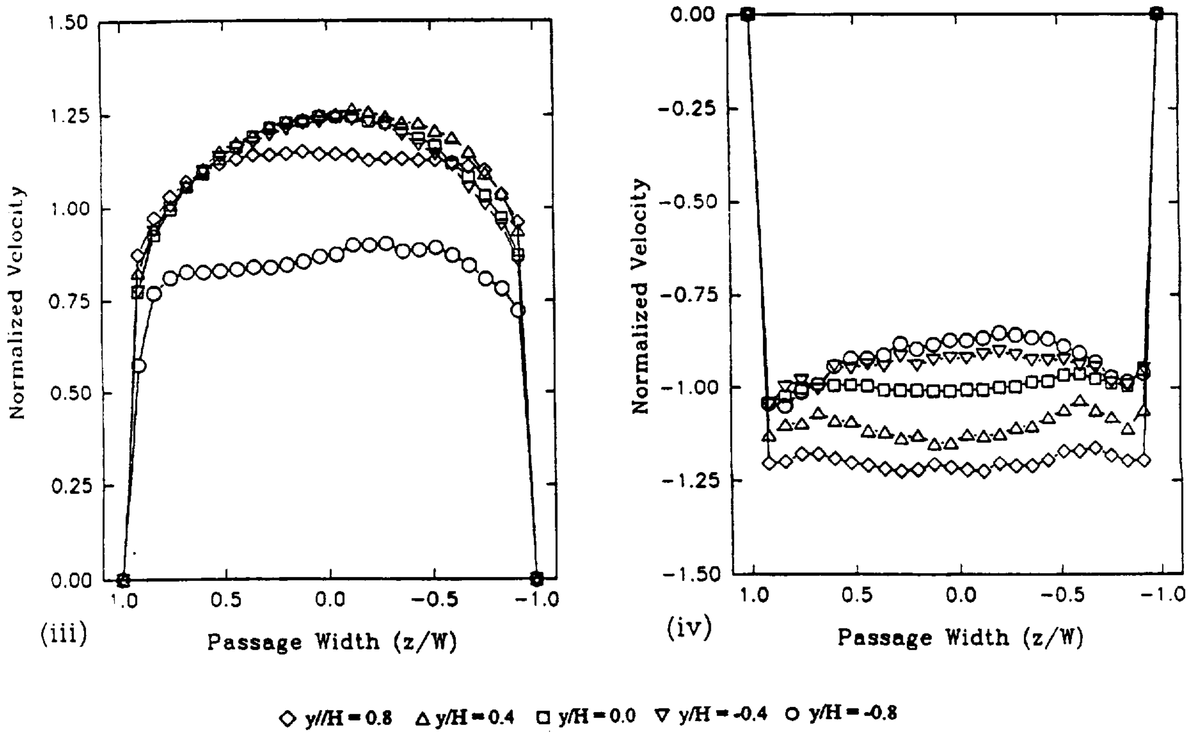

Figure 13a Continued. (iii) x/D = 15.0. (iv) x/D = 21.0.

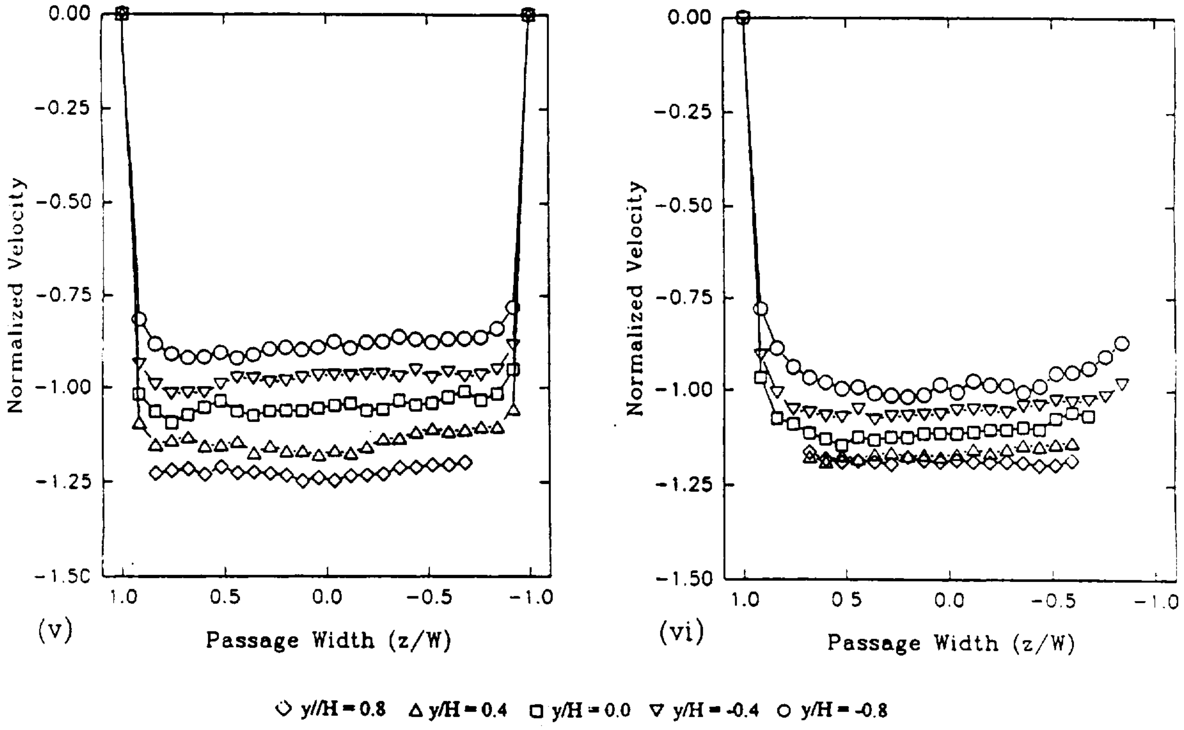

(v) (vi)

Figure 13a Continued. (v) x/D = 23.0. (vi) x/D = 25.0.

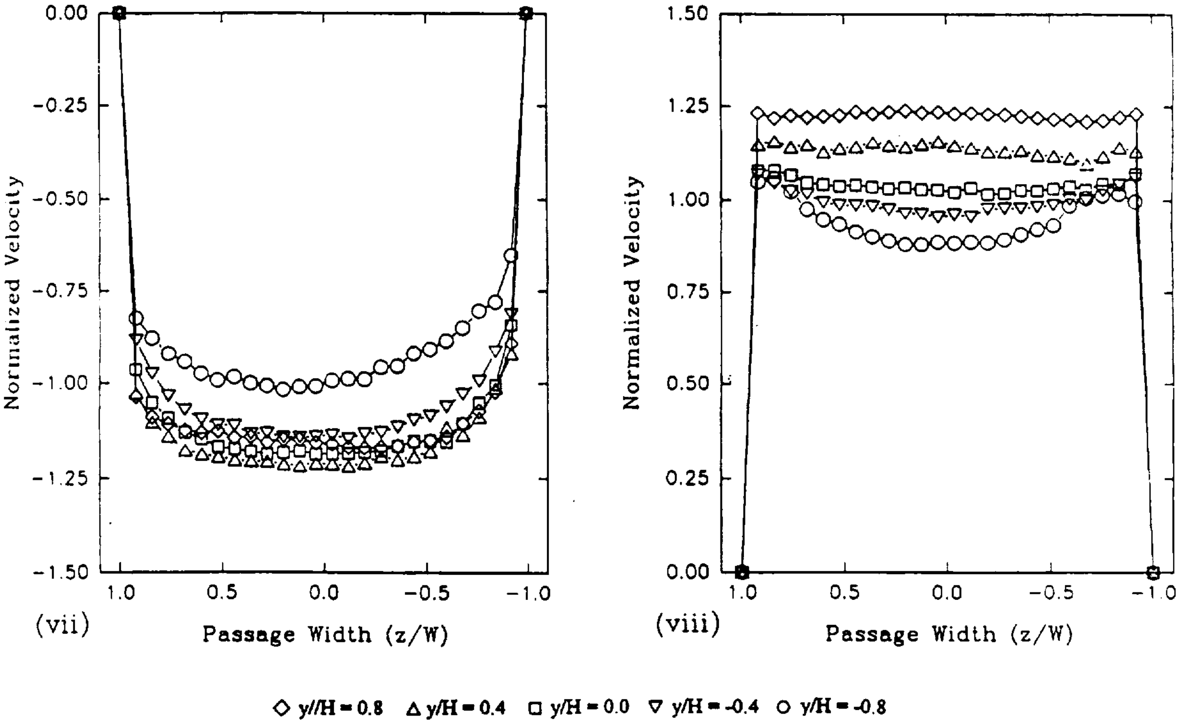

(vii) (viii)

Figure 13a Continued. (vii) x/D = 33.2. (viii) x/D = 39.3.

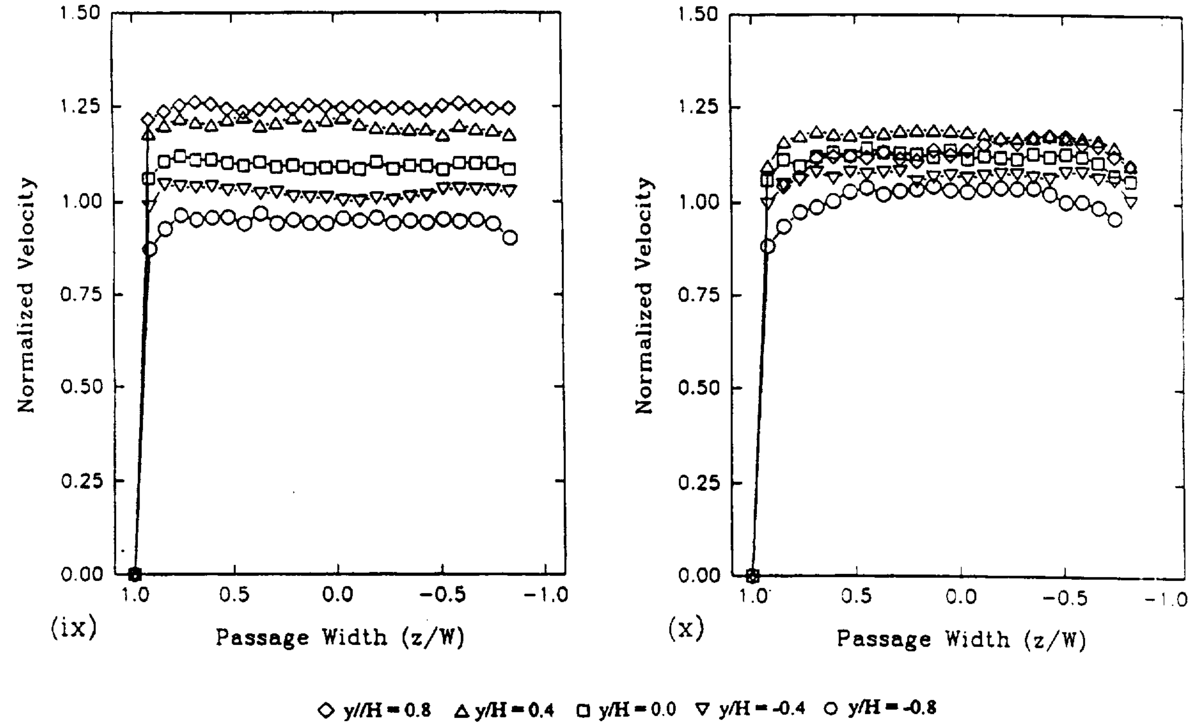

Figure 13a Concluded. (ix) x/D = 41.3. (x) x/D = 43.3.

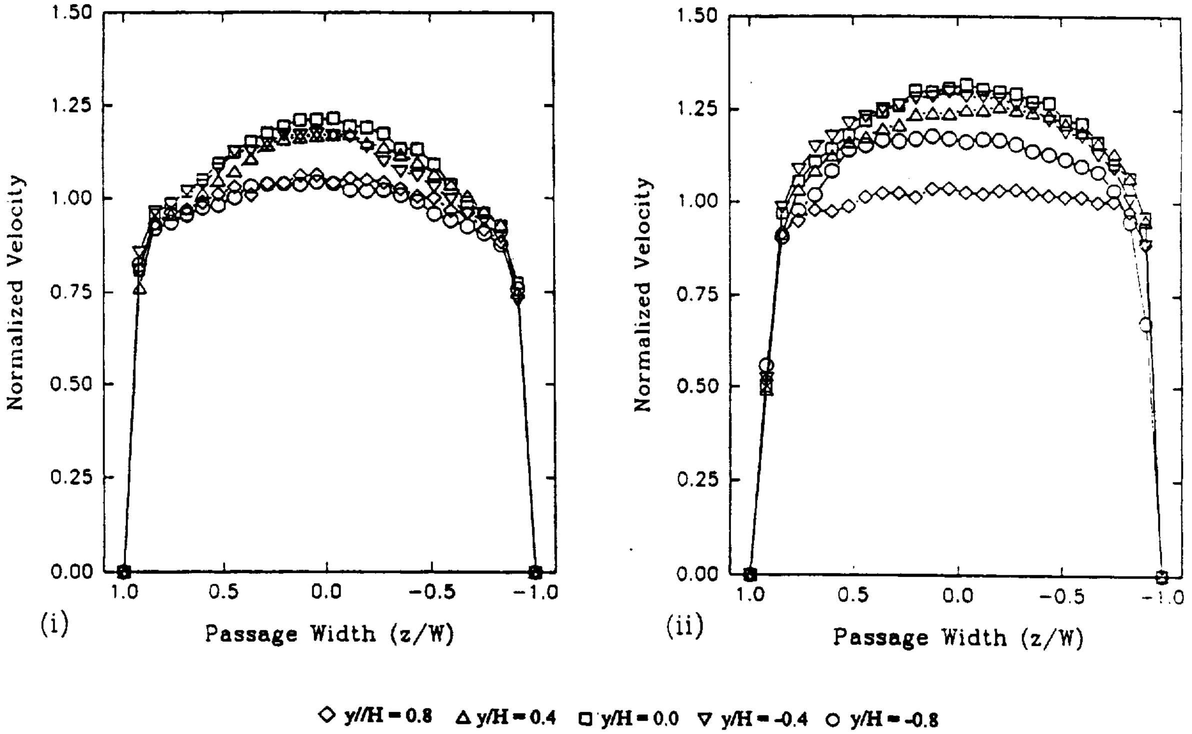

Figure 13b Streamwise mean velocity profiles obtained at Re = 12,500 and Ro = 0.0. (i) x/D = 1.0. (ii) x/D = 6.4.

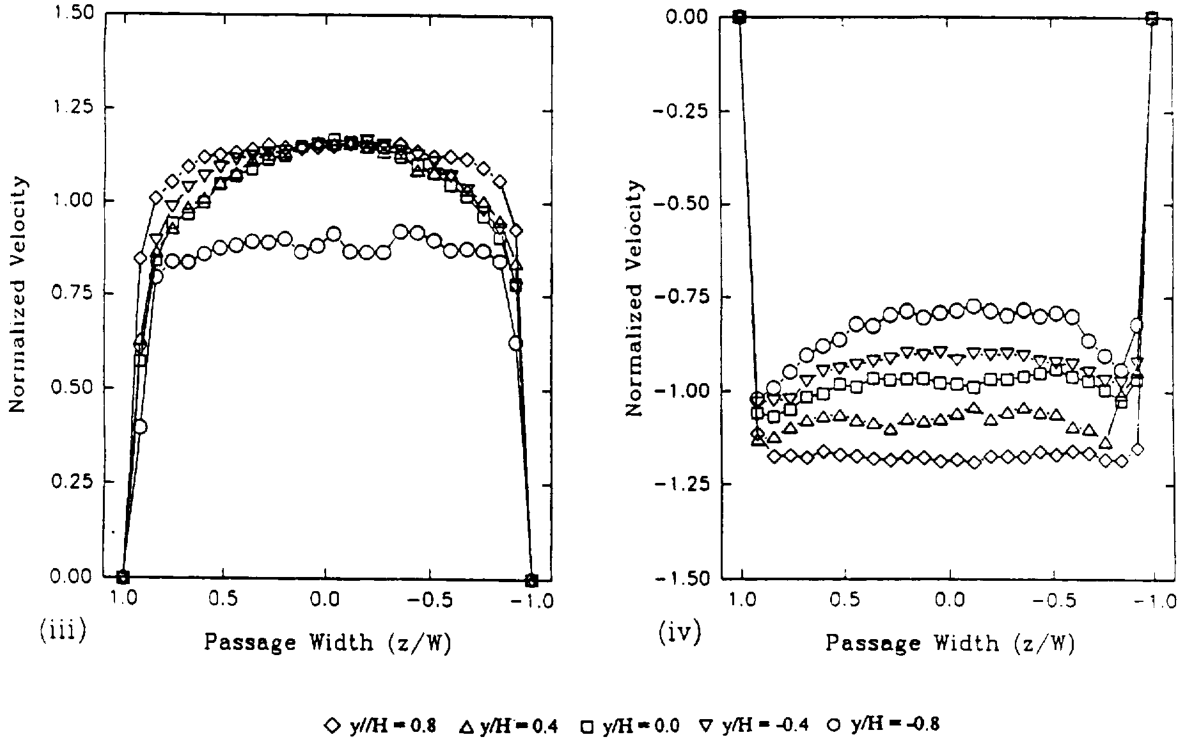

Figure 13b Continued. (iii) x/D = 15.0. (iv) x/D = 21.0.

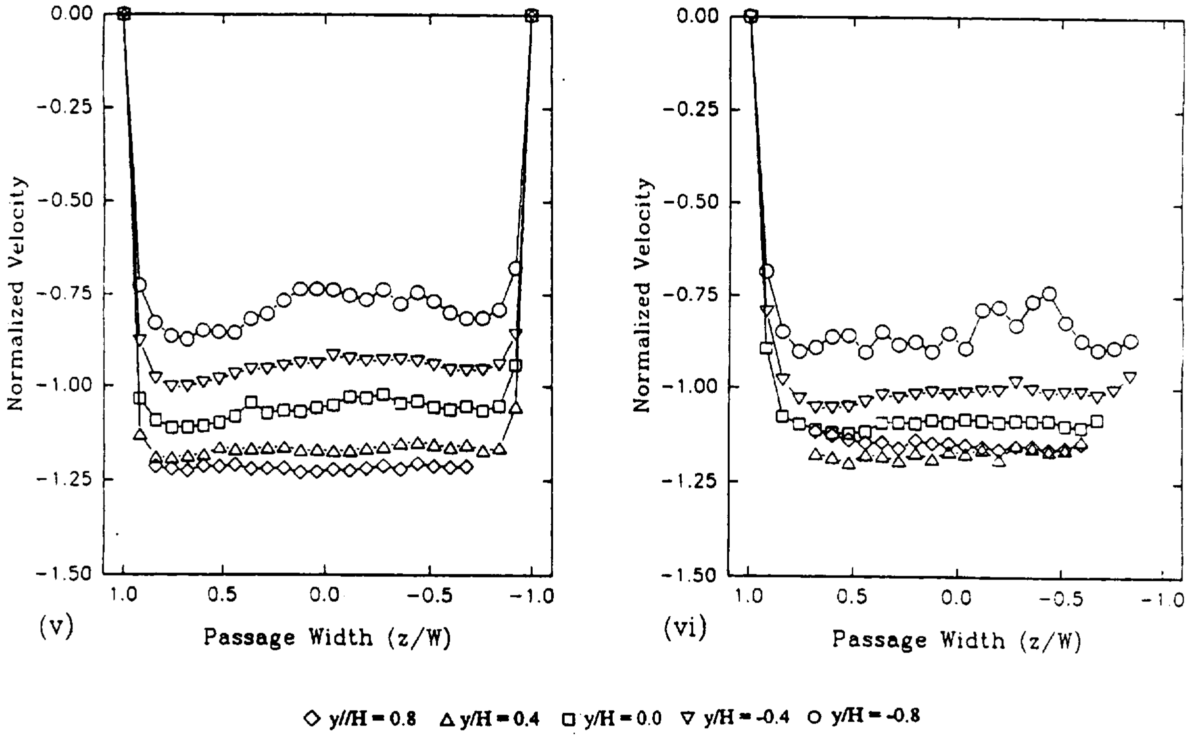

Figure 13b Continued. (v) x/D = 23.0. (vi) x/D = 25.0.

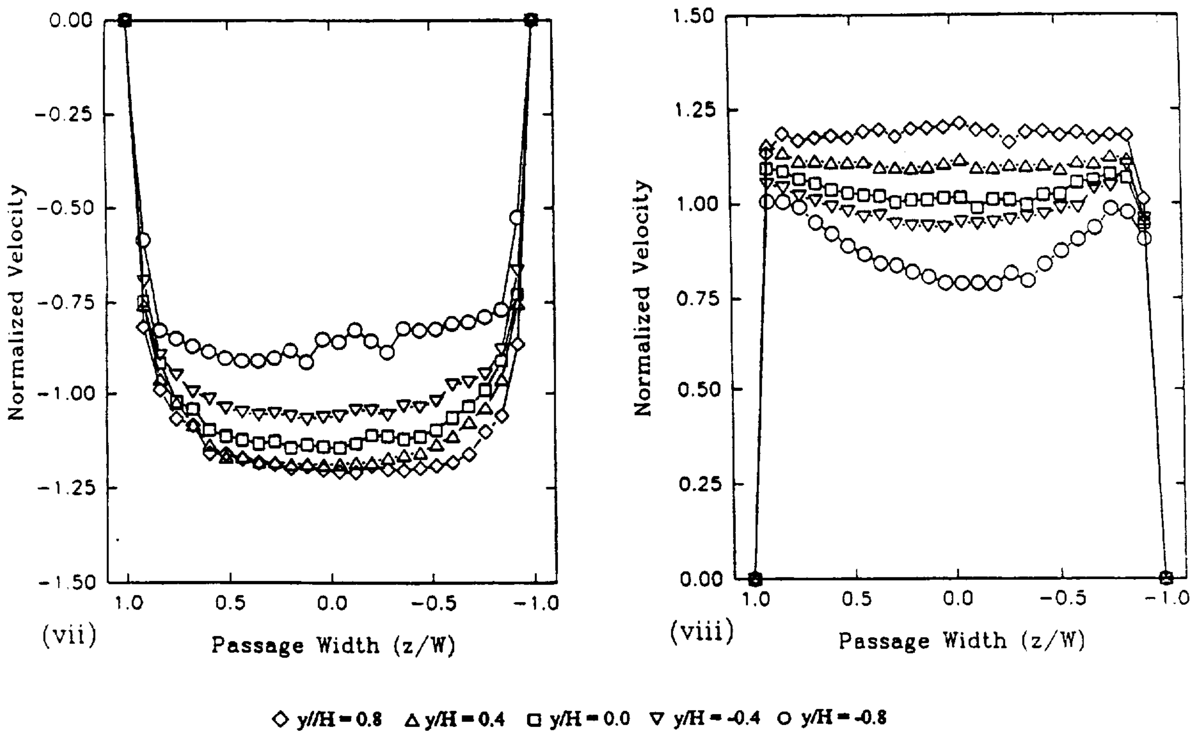

Figure 13b Continued. (vii) x/D = 33.2. (viii) x/D = 39.3.

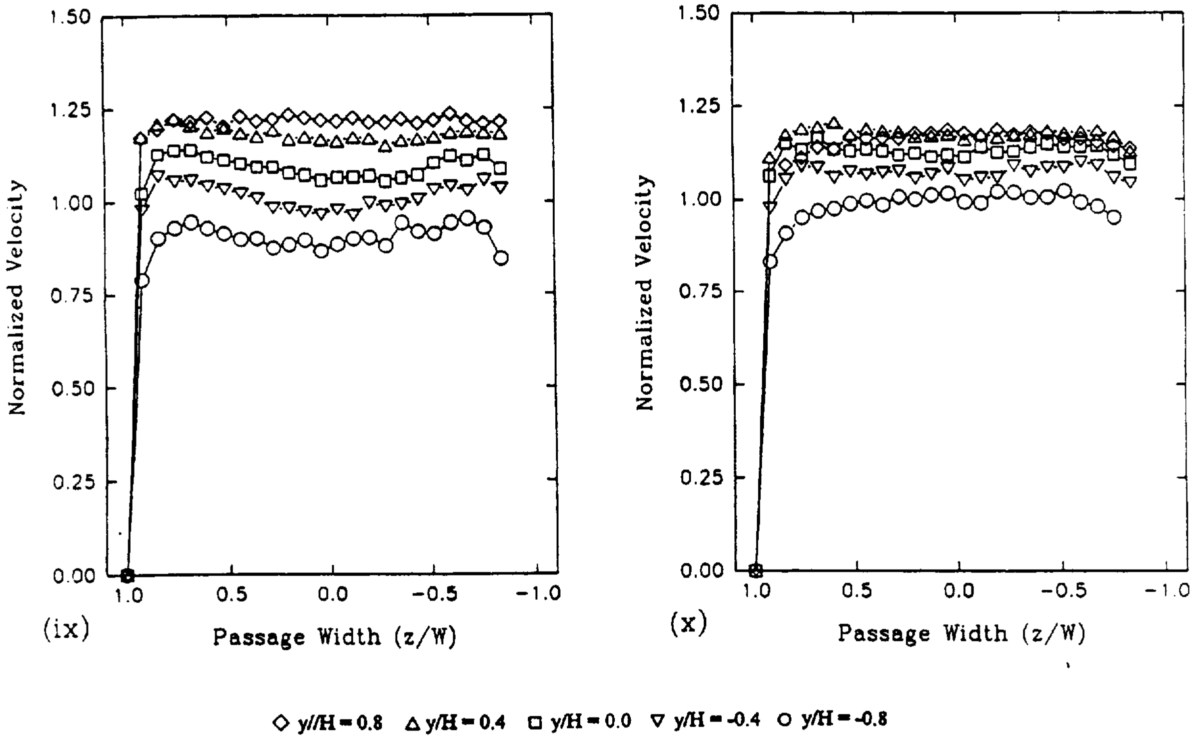

Figure 13b Concluded. (ix) x/D = 41.3. (x) x/D = 43.3.

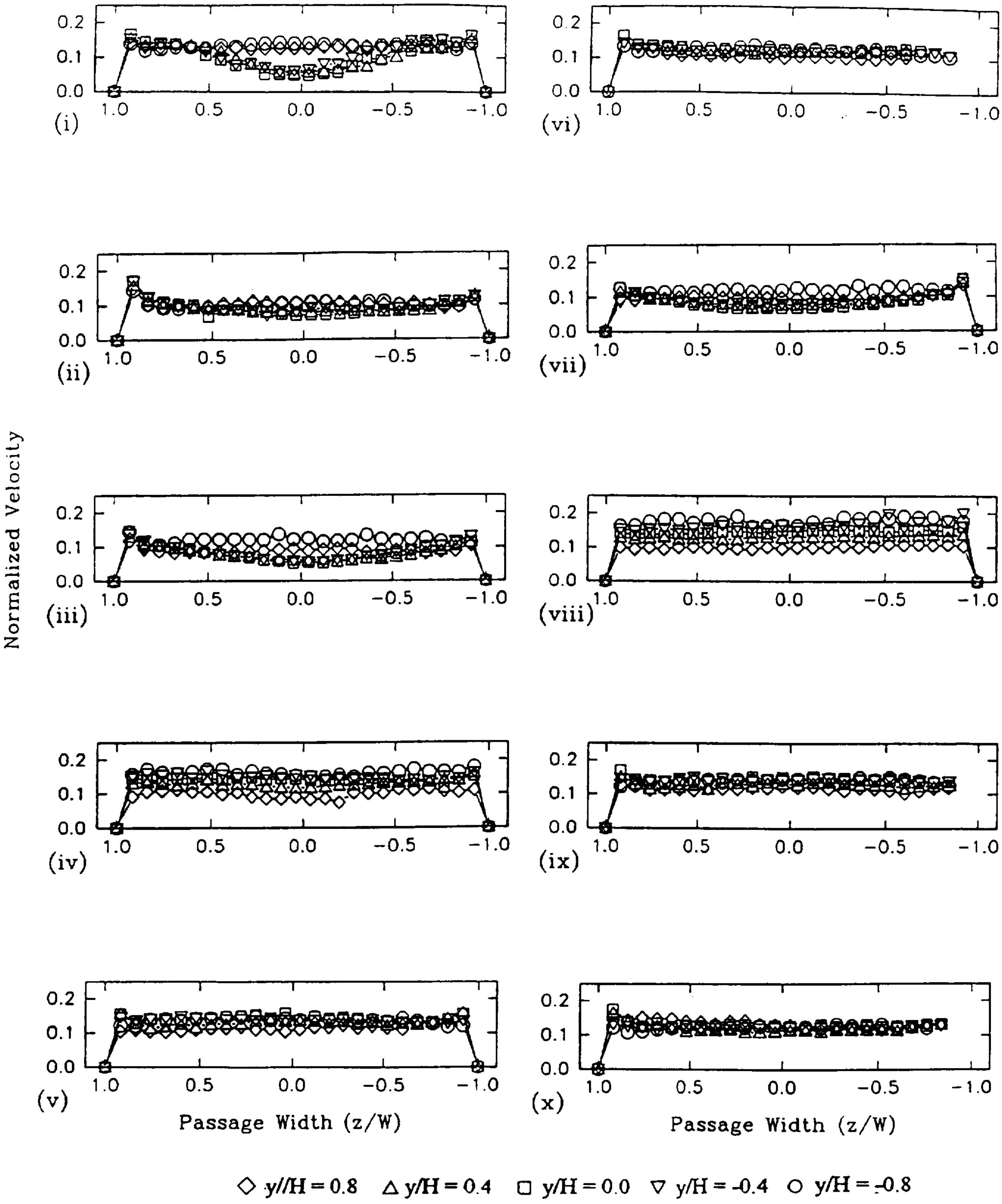

Figure 14a Streamwise rms velocity profiles obtained at Re = 25,000 and Ro = 0.0.
(i) x/D = 1.0 (ii) x/D = 6.4 (iii) x/D = 15.0 (iv) x/D = 21.0
(v) x/D = 23.0 (vi) x/D = 25.0 (vii) x/D = 33.2 (viii) x/D = 39.3
(ix) x/D = 41.3 (x) x/D = 43.3

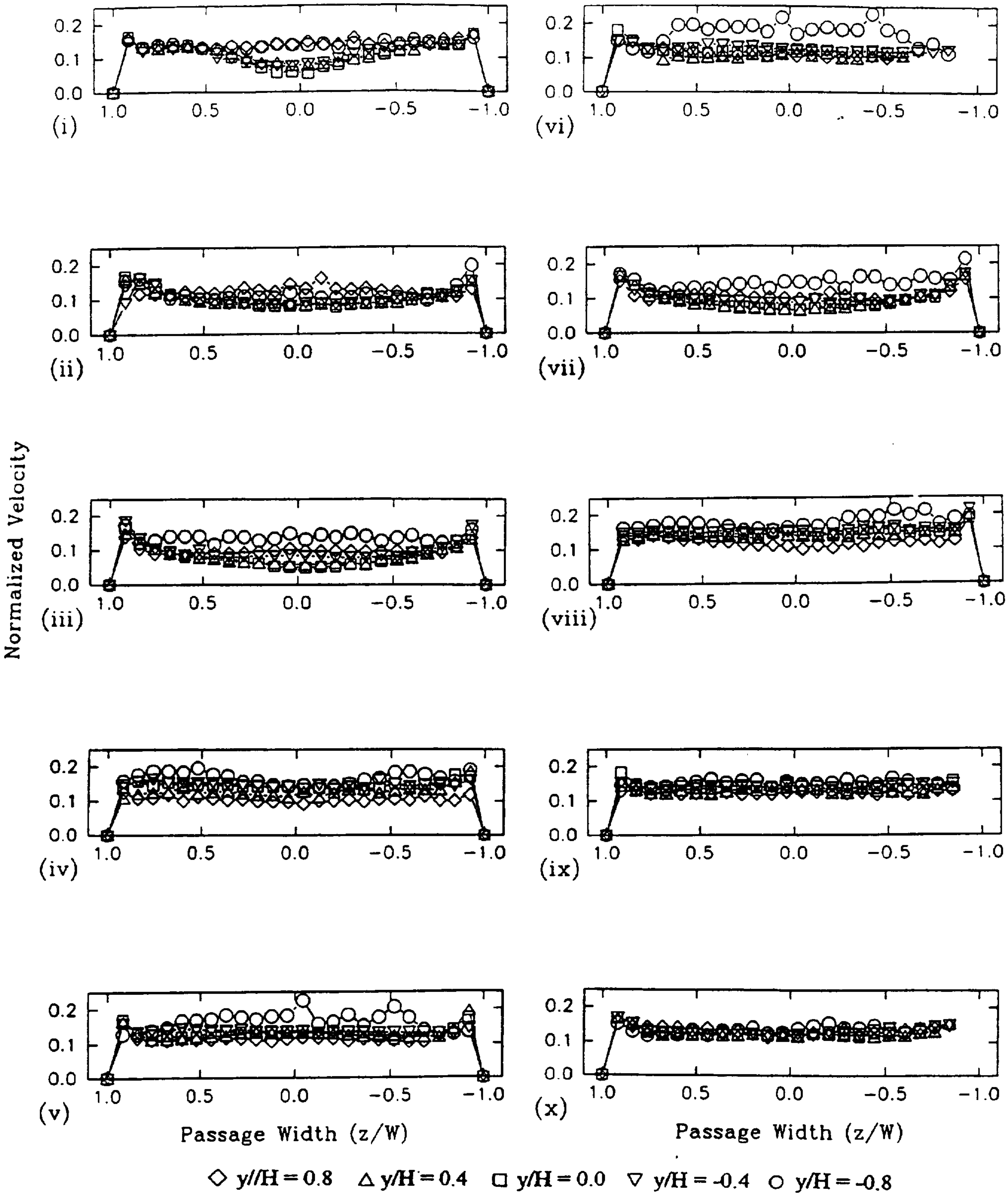

Figure 14b Streamwise rms velocity profiles obtained at Re = 12,500 and Ro = 0.0.

(i) x/D = 1.0 (ii) x/D = 6.4 (iii) x/D = 15.0 (iv) x/D = 21.0
(v) x/D = 23.0 (vi) x/D = 25.0 (vii) x/D = 33.2 (viii) x/D = 39.3
(ix) x/D = 41.3 (x) x/D = 43.3

approximately 20% for Re = 12,500. The secondary flow associated with the turn induces a convection of fluid to the upper wall and speeds up the growth of boundary layer on the lower wall. The turbulent intensities near the lower wall are much higher than those at mid-passage for the lower Re as the cross-flow has a lower momentum which leads to the viscous effect breaking away from the wall. The turbulent intensities obtained in the second turn, Figures (vii) to (x) of 14a and 14b, are similar to those obtained in the first turn, Figures (iii) and (iv) of 14a and 14b.

Mean and rms cross-stream and tangential velocities at x/D = 18.0 are shown in Figures 15a, 15b, 16a and 16b. The mean cross-stream velocities at Re = 25,000, Figure 15a(i), show that the turn is centrifuging the cross-flow to the concave outer surface and this gives rise to positive cross-stream velocity achieving $0.5U_b$. The centripetal pressure gradient is driving the low momentum near-wall fluid toward the inner convex surface, resulting in negative cross-stream velocities reaching $0.75U_b$ near the two walls. Figure 15a(ii) shows that the turbulence intensities in the core flow ($-0.5 < z/Z < 0.5$) are of the order of 15% but those of the near-wall secondary flow ($z/Z < -0.5$ and $z/Z > 0.5$) are of the order of 30%. Thus, the centripetal pressure gradient is also a source of turbulence. The normalized mean and rms velocities at Re = 12,500, Figures 15b(i) and (ii), are similar to those of Re = 25,000, Figures 15a(i) and (ii). Superpositioning the mean velocities of the cross-stream component (Figure 15a(i)) and the tangential component (Figure 16a(i)) yields the expected double vortex associated with a turn. The tangential convection of the vortex is stronger for the higher Re, Figure 16a(i) and 16b(i). The rms tangential velocities at x/D = 18.0 at Re =25,000 are shown in Figure 16a(ii). The rms quantities in the center of the turn (y/H = -0.4 and 0.0) are similar to those of the cross-stream component, both in terms of profiles and magnitude, suggesting that the turbulence is isotropic. The fluctuations near the outer concave surface are damped by the wall. They are lower and have become more uniform. The maximum turbulence intensity of the tangential component approaches $0.4U_b$ and occurs near the middle of the inner turn, y/H = -0.8, where the tangentially opposed convected flows collide. The profiles of the rms tangential velocity for the lower Re, Figure 16b(ii), are similar to those of Re = 25,000 (Figure 16a(ii)), but the magnitudes are smaller at all y/H due to a weaker tangential convection. The sharp increase in heat transfer at the turn in stationary condition, Wagner et al (1991), is attributed to an increase in secondary flow and turbulence.

4.2 Computational Inlet Flow Field Study

Due to the optical limitations, experimental data could only be acquired for the streamwise and tangential velocity components. Therefore, a simulation of the inlet plenum was initiated to provide the complete flow field at x/D = 1.0 in the serpentine passage. The entire length of the inlet transfer tube and the first passage of the duct were not modeled in order to limit the computational mesh. However, fifteen hydraulic diameters of the inlet transfer tube were modeled to provide a reasonable development length prior to the plenum, as shown in Figure 17. A flat streamwise velocity profile with no tangential or radially velocity components was specified at the inlet plane. The grid of the first passage of the serpentine extended nine hydraulic diameters downstream of the

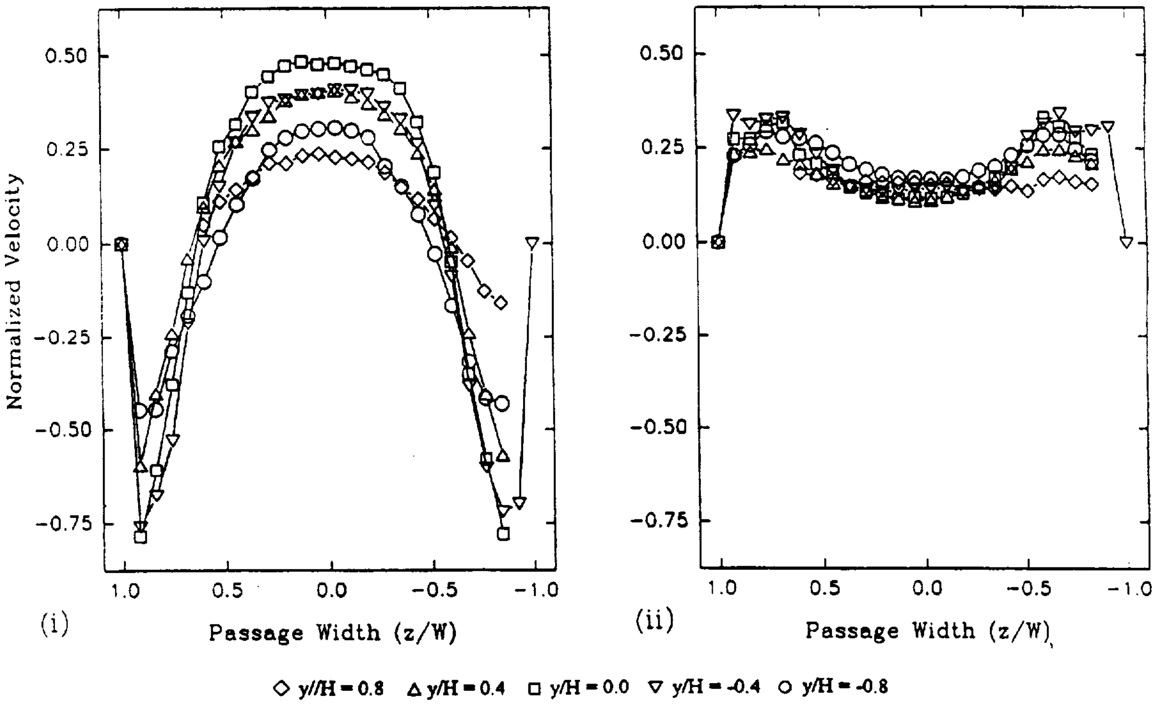

Figure 15a Cross-stream mean and rms velocity profiles at x/D = 18.0,
Re = 25,000 and Ro = 0.0
(i) Mean velocity (ii) Rms velocity

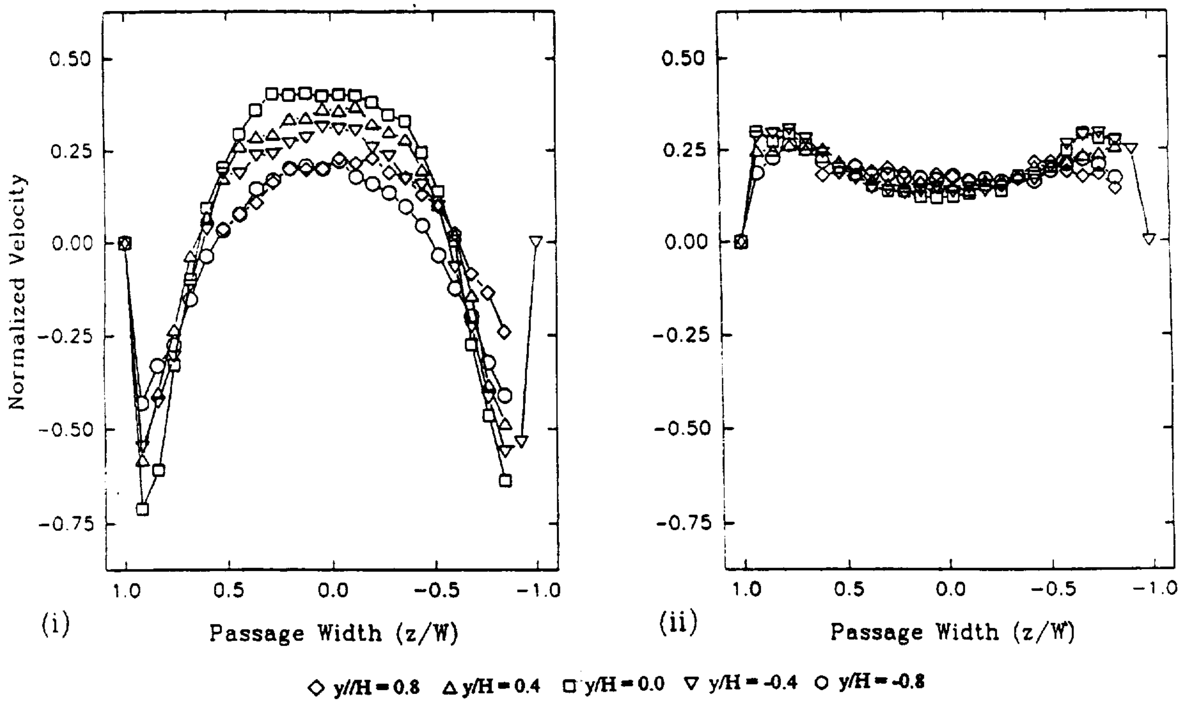

Figure 15b Cross-stream mean and rms velocity profiles at x/D = 18.0,
Re = 12,500 and Ro = 0.0
(i) Mean velocity (ii) Rms velocity

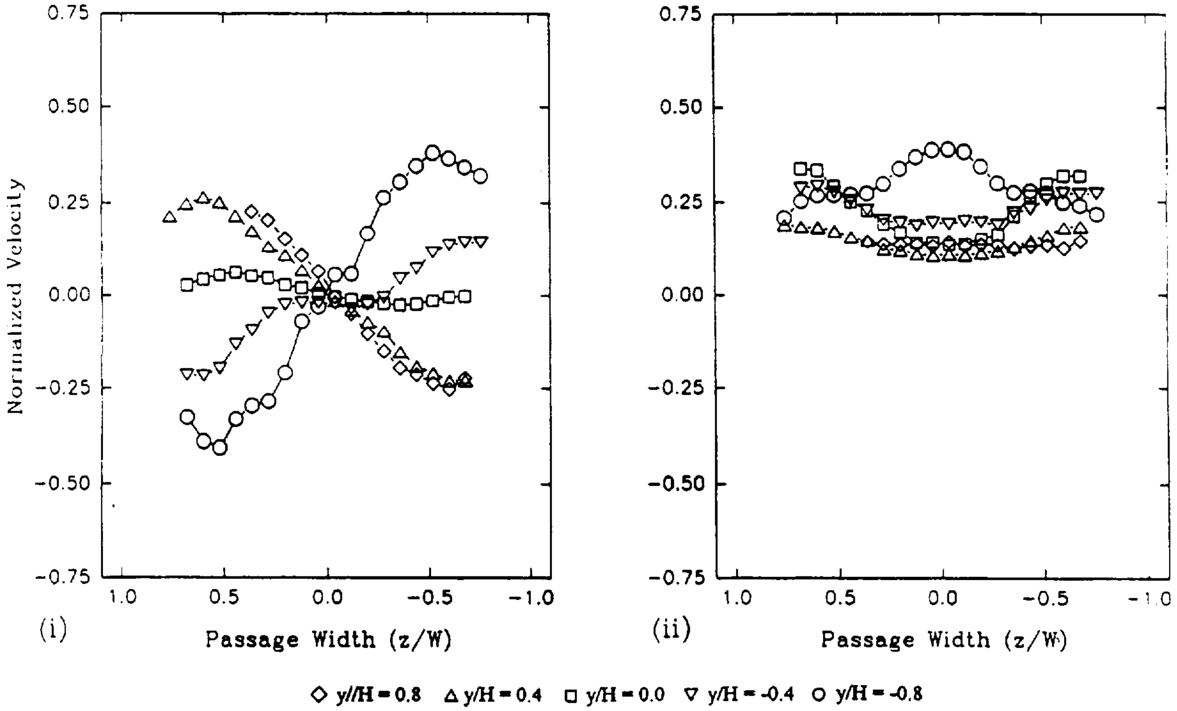

Figure 16a Tangential mean and rms velocity profiles at x/D = 18.0,
Re = 25,000 and Ro = 0.0
(i) Mean velocity (ii) Rms velocity

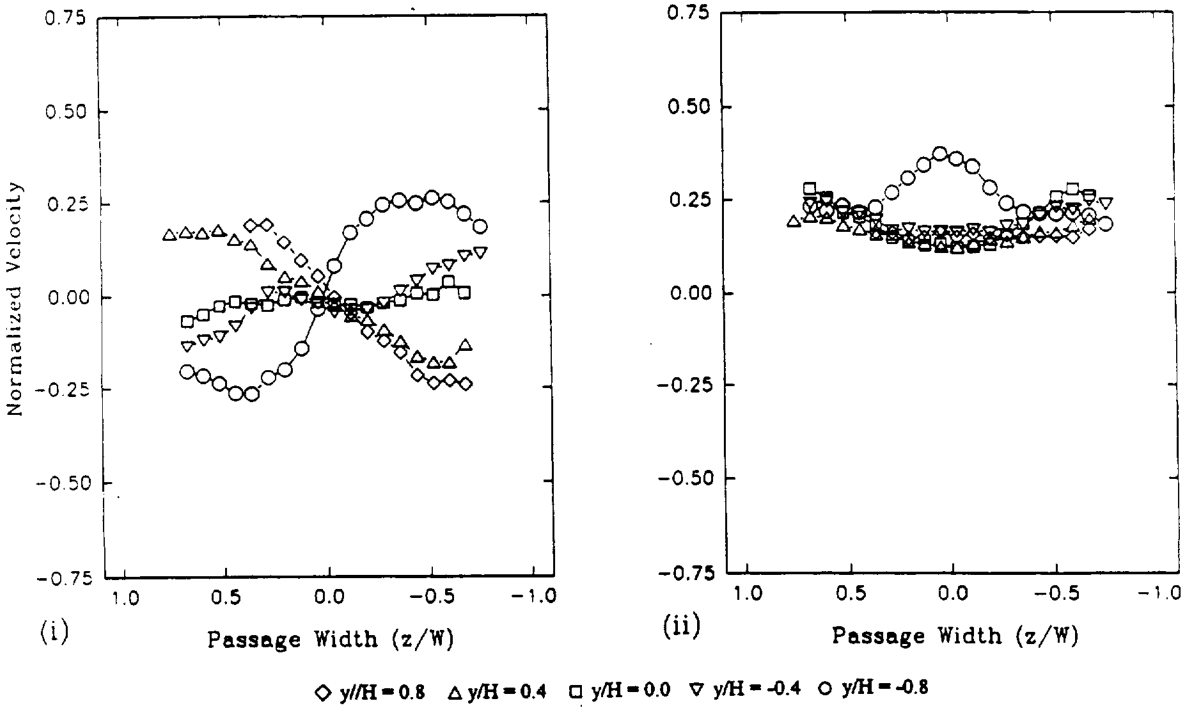

Figure 16b Tangential mean and rms velocity profiles at x/D = 18.0,
Re = 12,500 and Ro = 0.0
(i) Mean velocity (ii) Rms velocity

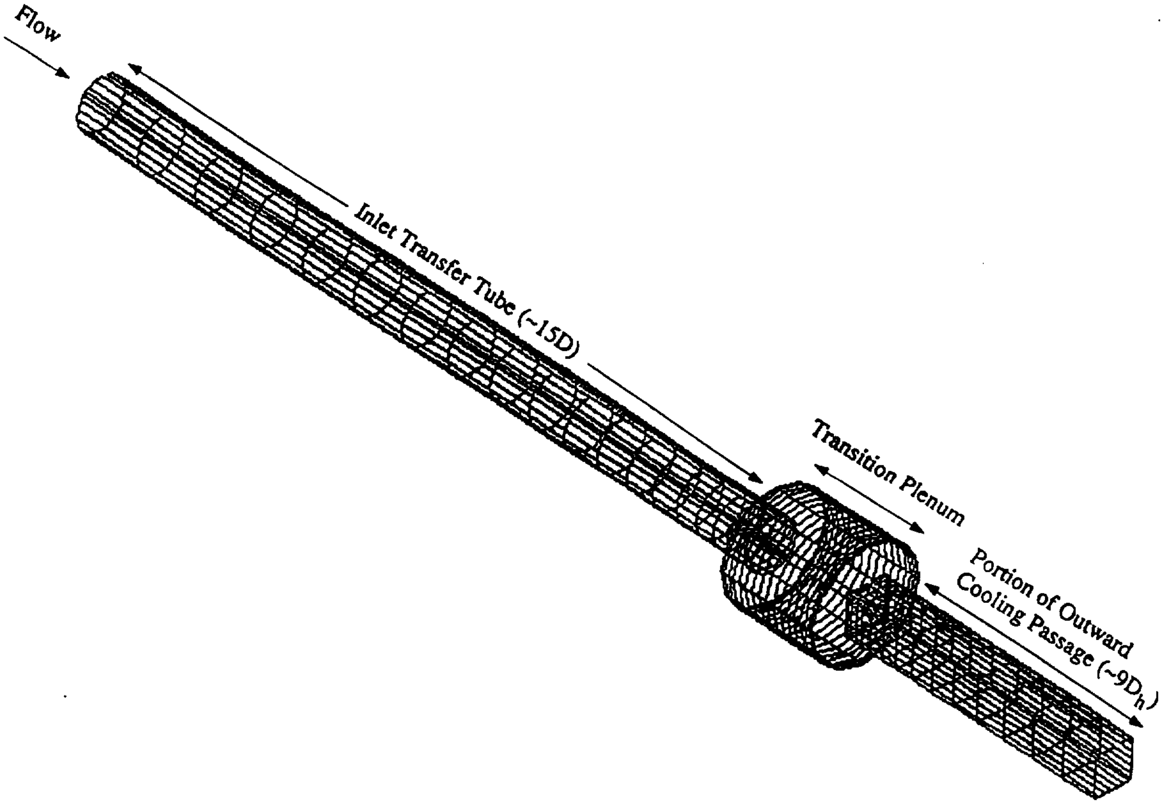
Flow
Inlet Transfer Tube (~15D)
Transition Plenum
Portion of Outward Cooling Passage (~9D_h)

Figure 17 Circumferential grid for the experimental inlet plenum simulation

plenum so that comparisons between the predictions and the measurements could be made at x/D = 1.0 and x/D = 6.4.

A streakline plot 'of a cross-section of the plenum region which extends from leading to trailing surface along the centerline is show in Figure 18a. This figure demonstrates the complexity of the flow field within the plenum. The flow is asymmetric from leading to trailing surface due to the Coriolis force. The sudden expansion generates a recirculation cell at the trailing surface. Conversely, significant reverse flow occurs along the entire length of the leading surface. Streaklines for the cross-section which is rotated 90° relative to Figure 18a are shown in Figure 18b. In the square cross-sectioned passage, the figure extends from y/H = -1.0 to y/H = 1.0. As expected, the computed streaklines are symmetric from side to side. It is interesting to note the region of relatively low velocity fluid in the center of the plenum which can be seen in both Figures 18a and 18b.

In the first passage of the serpentine duct, excellent agreement exists between the measured and computed streamwise velocity at x/D = 1.0, Figure 19a. The flow non-uniformities generated within the plenum skew the high velocity fluid toward the leading surface. The predicted tangential velocity component agrees qualitatively with the data, Figure 19b. Both indicate that the largest tangential velocity occurs along the side walls near the leading surface. However, the measured velocity is approximately five times larger than predictions.

At x/D = 6.4, both the measured streamwise velocity and the predictions show some movement of the high velocity fluid from the leading surface toward the trailing surface due the Coriolis force, Figure 20a. At this location, the measurements show a significant reduction in the strength of the secondary flow. On the other hand, the predicted tangential velocity magnitude remained approximately the same. As a result, the comparison of the tangential velocity components improve, Figure 20b. Since good qualitative agreement existed between the measured and predicted flow field, particularly at x/D = 1.0, the predicted flow field was used in conjunction with the measurements to specify the inlet conditions for the serpentine passage simulations. Good quantitative agreement existed between the measured and computed streamwise velocity component.

Therefore, the streamwise velocity was initialized with the measurements except in the near wall regions where the computations were used. This procedure could not be used for the tangential component. Although the measured tangential velocity was approximately five times the computed, the distributions were very similar. Therefore, the tangential velocity was set from the measurements except in the near wall region where it was taken from these computations scaled up by a factor of five. The radial component was taken from these computations again scaled up by a factor of five.

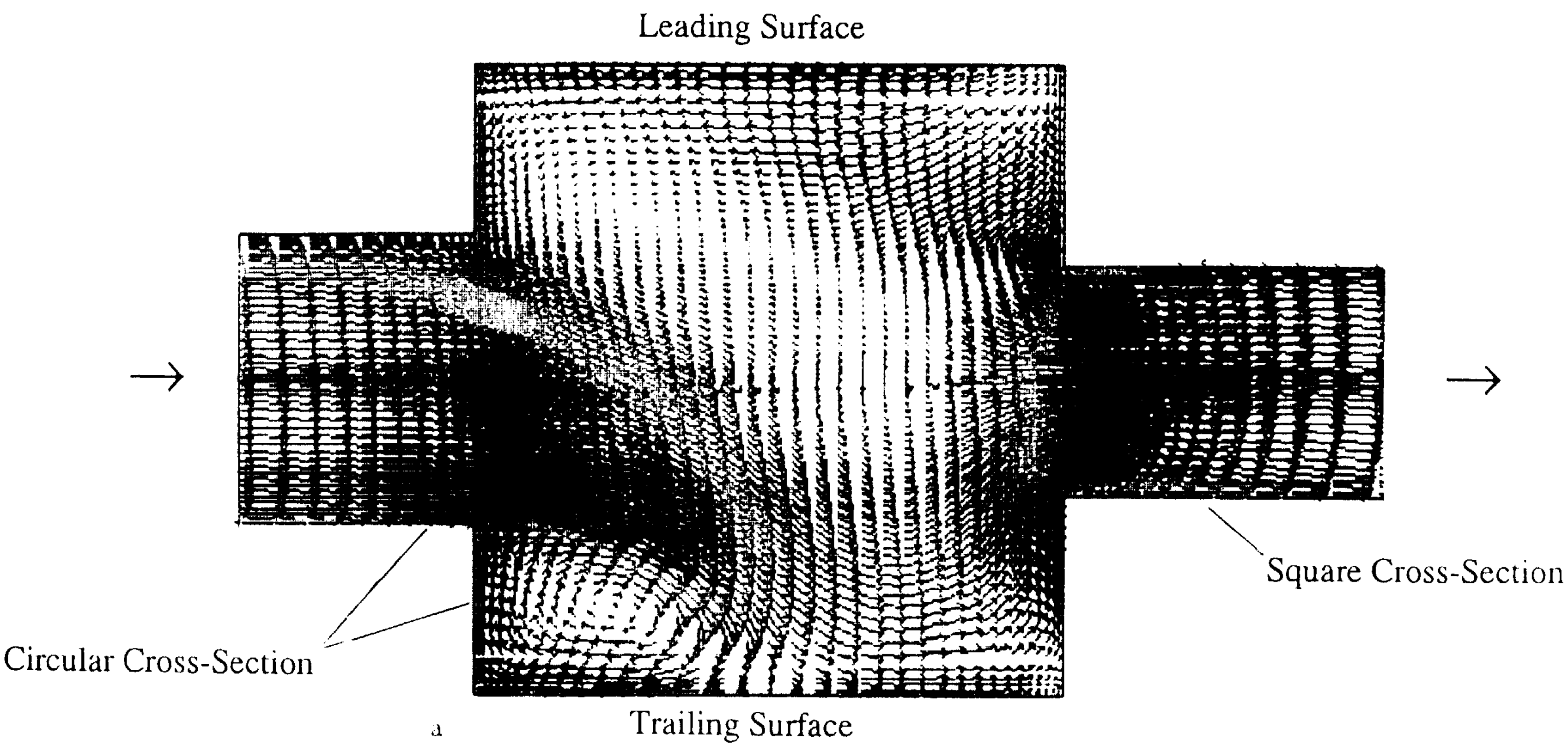

Figure 18 Streakline plots within the plenum; (a) highlights the non-uniform flow distribution from the leading to trailing edges

PAGE 44 INTENTIONALLY BLANK

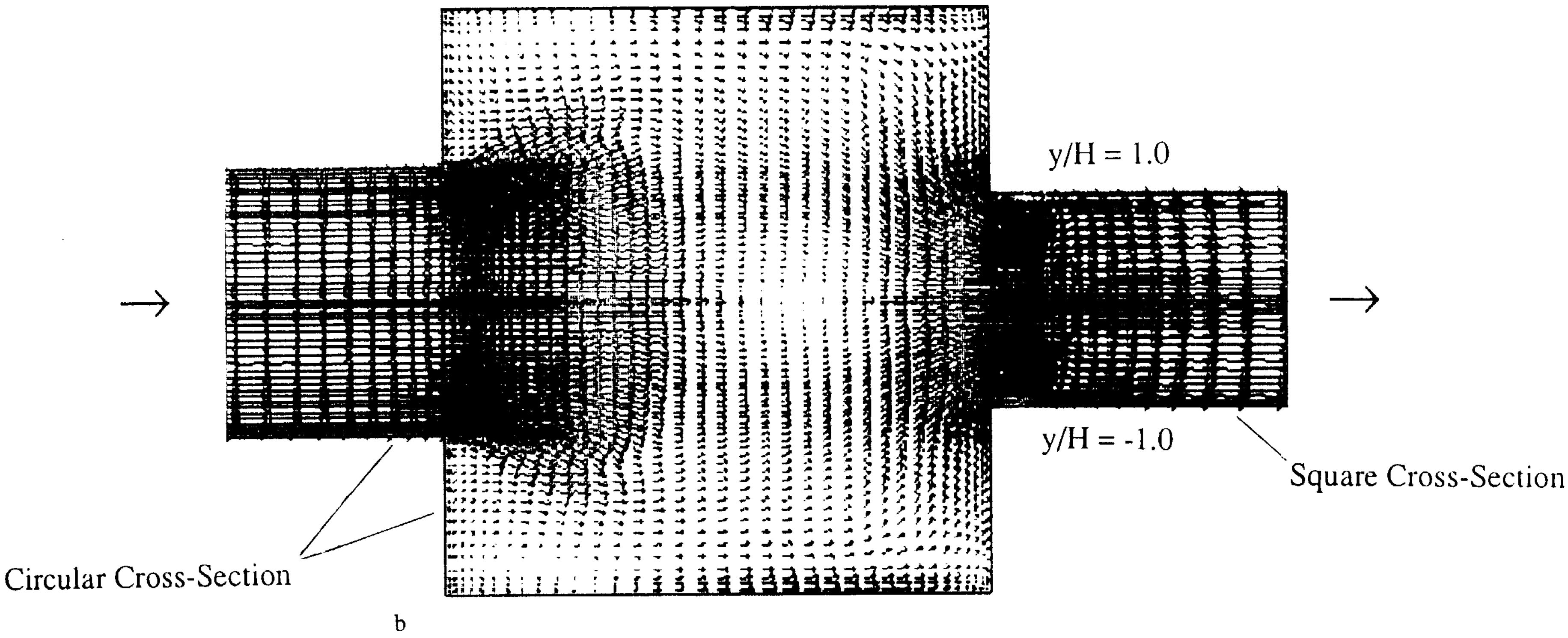

Figure 18 Streakline plots within the plenum; (b) shows the cross-stream direction flow symmetries

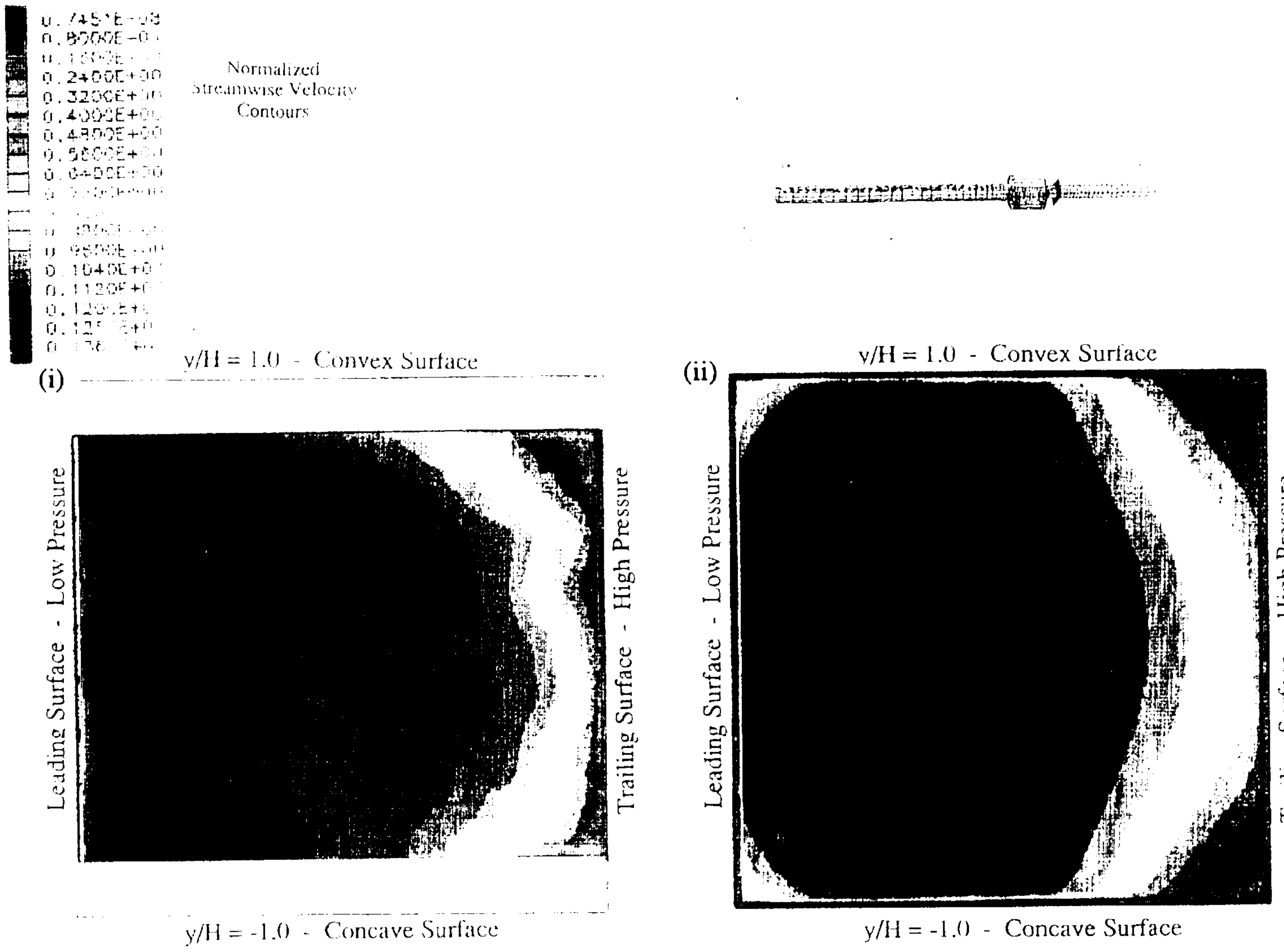

Figure 19a Streamwise velocity comparison at x/D = 1.0 between (i) measurements and (ii) incompressible flow predictions

PAGE 48 INTENTIONALLY BLANK

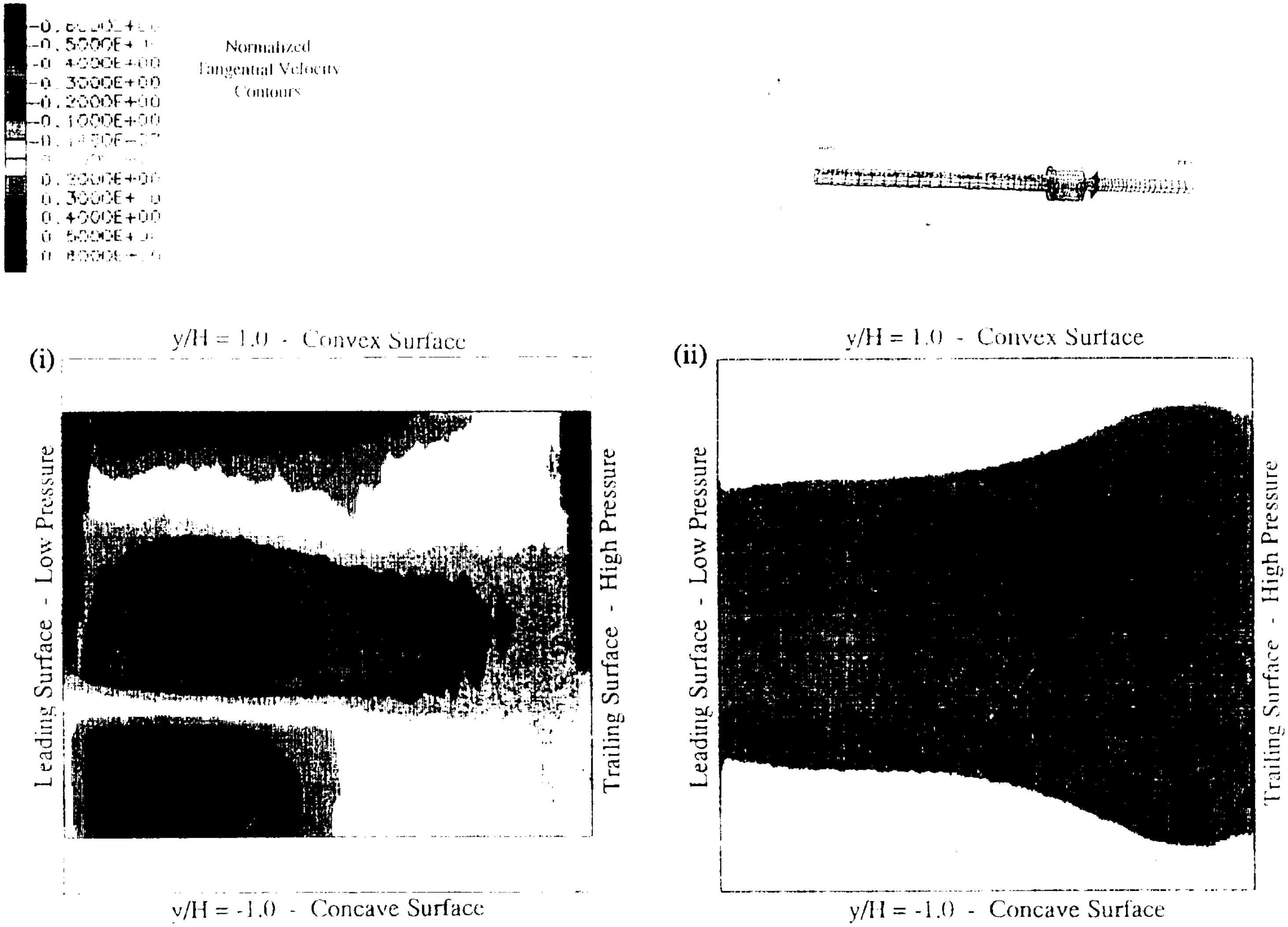

Figure 19b Tangential velocity comparison at x/D = 1.0 between (i) measurements and (ii) incompressible flow predictions

PAGE 50 INTENTIONALLY BLANK

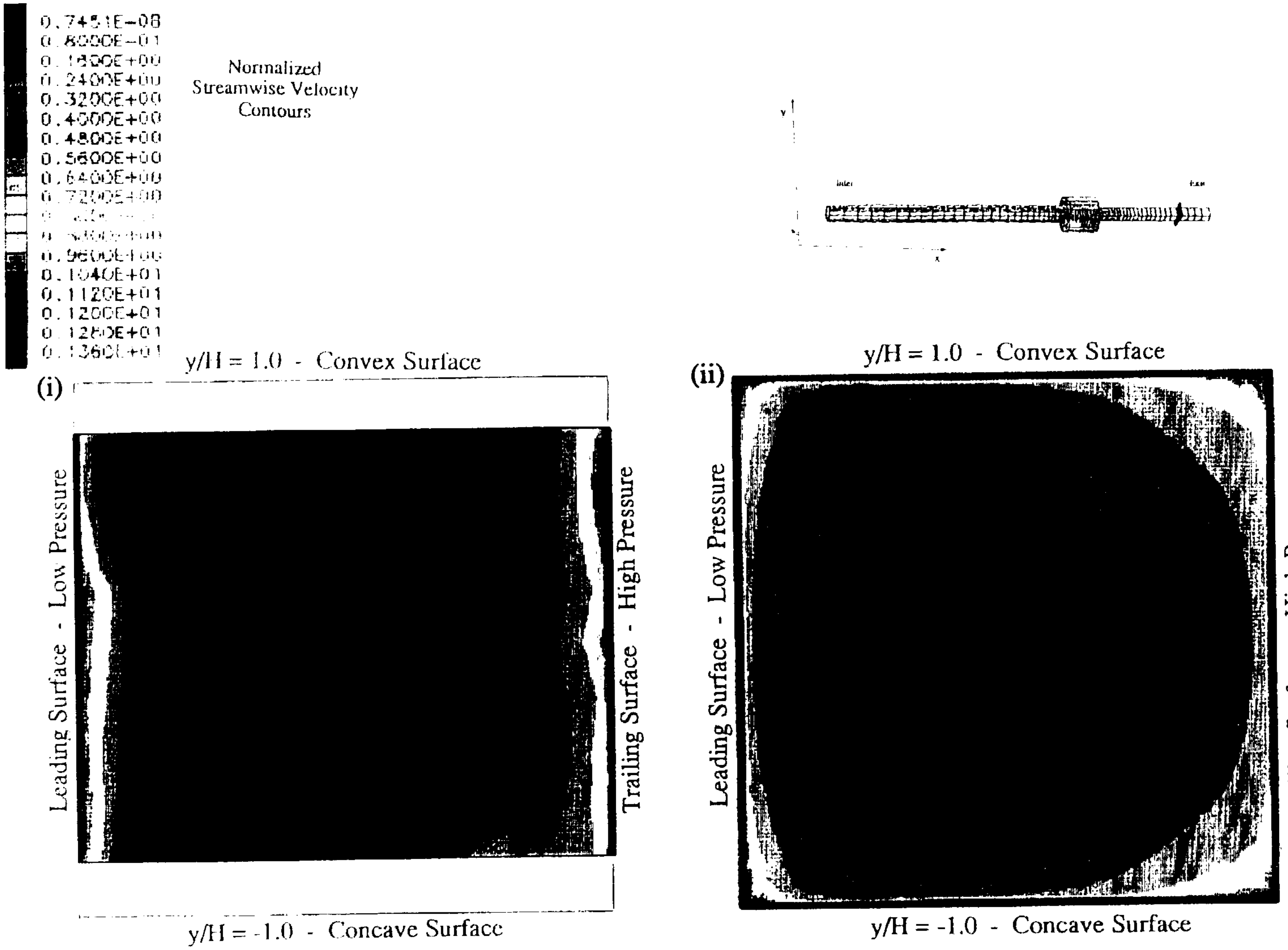

Figure 20a **Streamwise velocity comparison at x/D = 6.4 between (i) measurements and (ii) incompressible flow predictions**

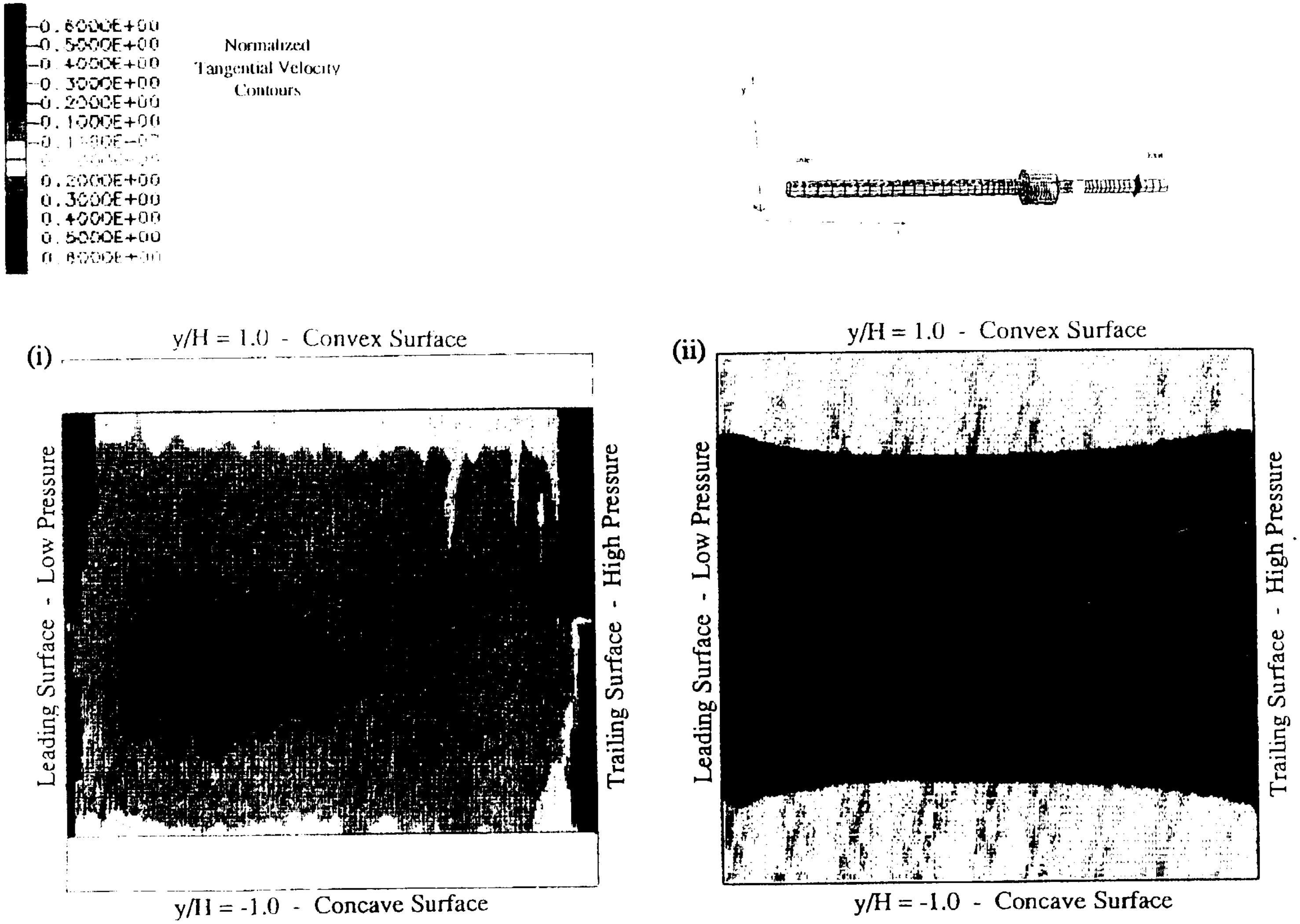

Figure 20b Tangential velocity comparison at x/D = 6.4 between (i) measurements and (ii) incompressible flow predictions

5. RESULTS AND DISCUSSIONS

5.1 Baseline Condition measurements (Re = 25,000 & Ro = 0.24)

The velocity contours obtained in the first passage at x/D = 1.0 are shown in Figures 21. Contrary to the expected result associated with rotation, the shape of the contours (Figure 21(i)) show that the streamwise velocities on the low pressure (leading) side are higher than those on the high pressure (trailing) side. This profile results from the entrance effects associated with the plenum. The velocities of Figure 18 show that the high velocity flow discharged from the high pressure (trailing) side of the delivery pipe is deflected onto the low pressure (leading) side of the model upon impact with the plenum wall. Thus, the flow entering the model is angled toward the low pressure (leading) side and this consequently gives rise to the high velocity region close to the low pressure side at x/D = 1.0. Superimposing the streamwise (Figure 21(i)) and tangential (Figure 21(ii)) velocities confirms that the inlet flows near the upper and lower wall are directed toward the low pressure (leading) side. Figure 21(ii) show that there are substantial secondary flows in the tangential direction with maximum positive velocities approaching $0.6U_b$ and the absolute value of the maximum negative velocity exceeding $0.35U_b$. The positive velocities occur near the upper and lower wall and the negative velocities occur near the center of the passage. The strong positive tangential velocities suggest the high velocity flow discharged from the high pressure (trailing) side of the delivery pipe induce secondary jets upon impact with the plenum wall. The secondary jets sweep along the plenum wall and are reinforced by the cross-stream pressure gradient induced by Coriolis forces in driving near-wall flow toward the low pressure (leading) side. The two wall-jets are turned toward the center of the passage on impact with the low pressure (leading) surface after they enter the square passage. The collision of the two wall-jets near the center of the passage gives rise to the negative tangential velocities at x/D = 1.0. The double vortex at x/D = 1.0 is driven mainly by the entrance effect rather than by the Coriolis effect.

Turbulent fluctuations of the streamwise and tangential velocities are shown in Figures 22(i) and (ii). The rms streamwise velocities, Figure 22(i), show that the fluctuation on the low pressure (leading) side, $z/Z > 0$, are very uniform for all y/H and are of the order of $0.2U_b$. The turbulence intensities increase to 0.3 or $0.4U_b$ on the high pressure (trailing) side. The increase is more noticeable in the profiles near the upper and lower wall, y/H = ± 0.8. The rms tangential velocities, Figure 22(ii), show that there is substantial scattering in the rms values and the overall rms level increases with rotation. The latter suggests an increase in turbulent fluctuation which is not observed in the rms quantities of the streamwise velocities, Figure 22(i). Rms quantities of the tangential velocity contain fluctuations due to speed variation of the model, as well as fluid turbulence. A 1% variation in the speed of rotation will lead to variations in excess $0.1U_b$ of in the normalized rms quantities: a 1% variation in the speed of rotation (40m/s) is 0.4m/s and $0.1U_b$ at Re = 25,000 is 0.34m/s. Since the actual fluid turbulence is swamped by apparent fluctuations due to speed variation, rms values of the tangential component will not be presented. Random variation in the speed of rotation will not affect the mean value.

PAGE 56 INTENTIONALLY BLANK

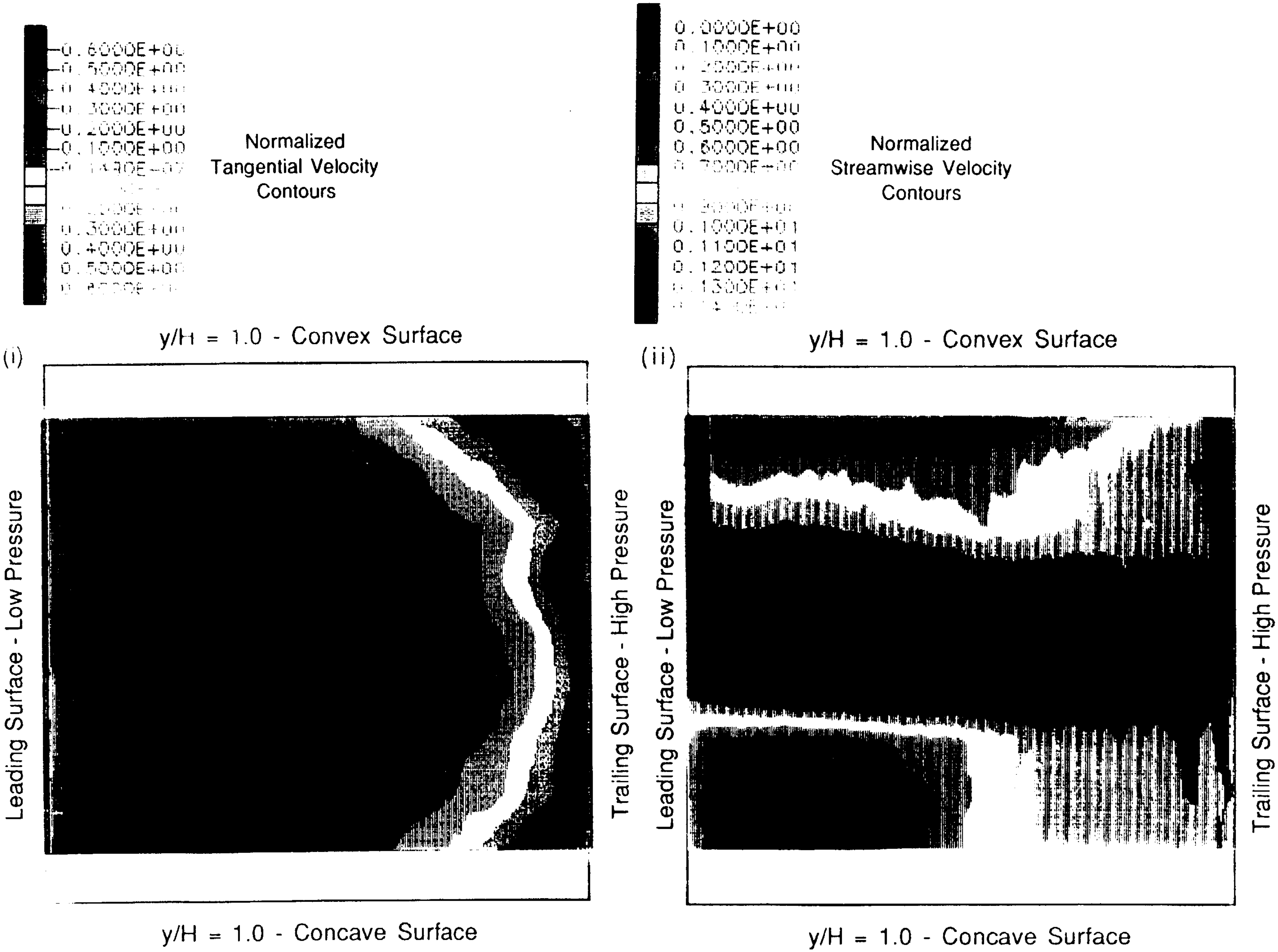

Figure 21 Mean velocity contours at x/D = 1.0, Re = 25,000 and Ro = 0.24.
(i) Streamwise velocity (ii) Tangential velocity

PAGE 58 INTENTIONALLY BLANK

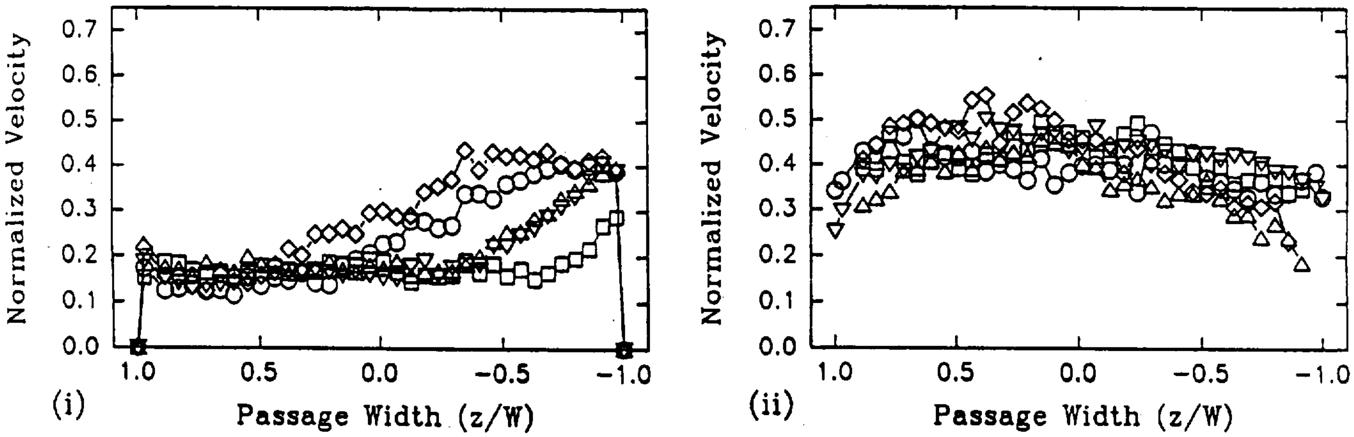

(i)

(ii)

Figure 22 Rms velocity at x/D = 1.0, Re = 25,000 and Ro = 0.24 .
(i) Streamwise velocity (ii) Tangential velocity

PAGE 60 INTENTIONALLY BLANK

The velocity contours obtained at x/D = 6.4 are shown in Figure 23. Comparison of the streamwise velocities obtained at x/D = 1.0 and 6.4, Figures 21(i) and 23(i), shows that the high velocity region is drifting away from the low pressure (leading) side of the passage. However, it is still close to the low pressure (leading) side. The entrance effect is dissipating and the cross-flow is being convected toward the high pressure (trailing) side. Figure 23(ii) shows positive tangential velocities near the upper and lower walls and negative velocities near the center. The cross-stream pressure gradient induced by Coriolis forces is driving the low momentum near-wall flow toward the low pressure (leading) side. The fluid in the center of the passage is drawn to the high pressure (trailing) side to fill the velocity deficit. Thus, the double vortex associated with Coriolis effect has already been established at x/D = 6.4. Comparison of the tangential velocities obtained at x/D = 1.0 and 6.4, Figures 21(ii) and 23(ii), shows that, at x/D =6.4, the positive near-wall convections in the tangential direction occur much closer to the walls. For example, positive velocities occur at y/H = ±0.8 only at x/D = 6.4 in contrast to those which occur at as deep as y/H = ±0.4 at x/D = 1.0. The maximum positive and negative tangential velocities decay from ±0.6U_b at x/D = 1.0 to ±0.12U_b at x/D = 6.4. The strength of double vortex associated with Coriolis effects should increase with increasing radius but the results show that its strength has decreased. The reduction in the strength of the double vortex between x/D = 1.0 and 6.4 confirms that the strong recirculation at the inlet stems mainly from the effect of plenum. It is also evident that the large secondary flow generated by the entrance effect is dissipating rapidly. The influence of the entrance effect on the tangential velocity is smaller than that on the streamwise velocity. The streamwise velocities, Figure 22(i), show that the entrance effect is still evident in the skewing of the velocity profile toward the leading surface at x/D = 6.4. The net velocity in the tangential direction is negative, indicating that there is a net convection from low pressure (leading) to high pressure (trailing) side.

Figure 24 shows the velocity contours obtained at the entrance to the first turn, x/D = 15.0. The double vortex associated with the Coriolis effect is clearly evident in the streamwise velocity contour, Figure 24(i). The high velocity region is shifting toward the high pressure (trailing) side confirming that the double vortex gives rise to a net convection from the low pressure (leading) to the high pressure (trailing) side. The high velocity region is close to the upper wall, indicating convection to the inner, convex low pressure surface. The convection of the cross-flow to the upper wall gives rise to expansion of the lower cell of the vortex, Figure 24(ii). The high negative tangential velocity region, -0.1U_b, shifts from the center of the passage to the upper half, indicating expansion of the lower cell of the vortex. Furthermore, the high positive tangential velocity, 0.1U_b, near the lower wall is evident at y/H = -0.8 but not at y/H = 0.8. The high positive tangential velocity region at the lower wall extends deeper into the passage than that at the upper wall.

The heat transfer results of Wagner et al (1991) show the heat transfer on the high pressure (trailing) and low pressure (leading) surfaces of the first passage decreases initially and then increases towards the end. The high heat transfer in the entrance region is attributed to entrance effects since this heat transfer occurs for stationary and rotation cases. The initial reduction in heat transfer in the first half of the passage is attributed to boundary layer effects. The growth of boundary layer suppresses heat transfer. Coriolis forces

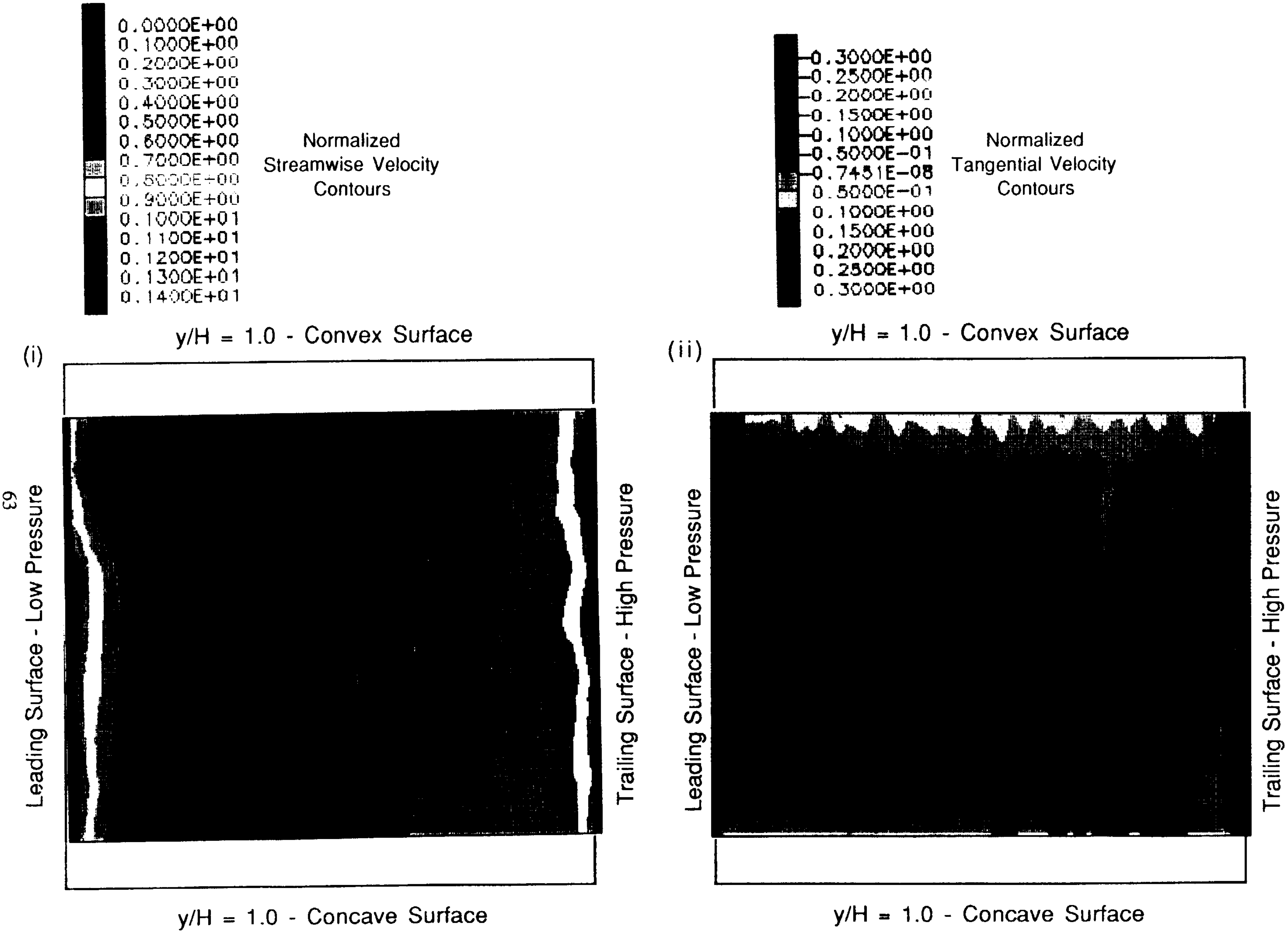

Figure 23 Mean velocity contours at x/D = 6.4, Re = 25,000 and Ro = 0.24.
(i) Streamwise velocity (ii) Tangential velocity

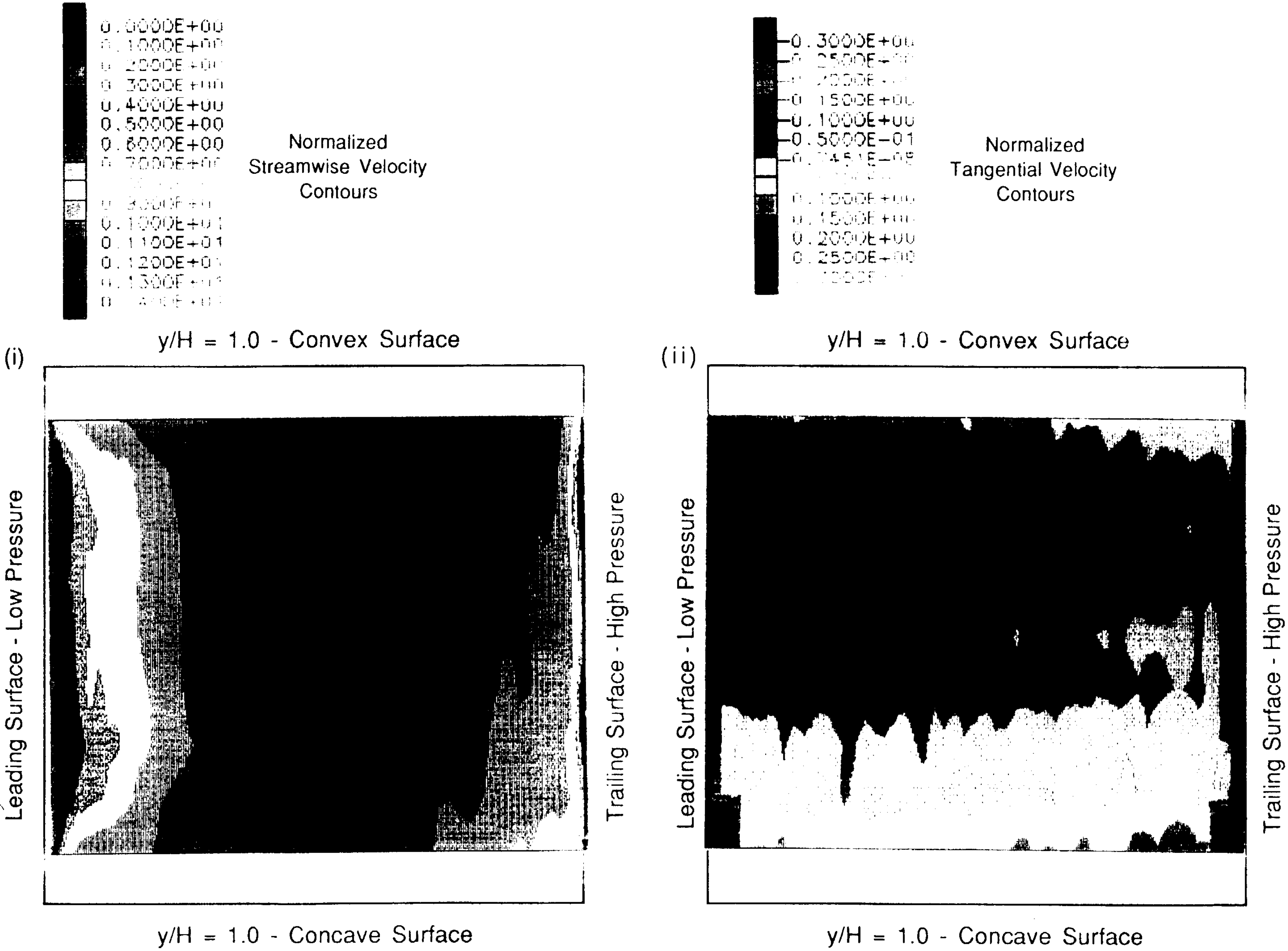

Figure 24 Mean velocity contours at x/D = 15.0, Re = 25,000 and Ro = 0.24.
(i) Streamwise velocity (ii) Tangential velocity

increase the growth of the boundary layer on the low pressure (leading) side and suppress that on the high pressure (trailing) side. The reduction in heat transfer on the low pressure (leading) side in the presence of rotation is more severe than that of the stationary case partly because of a more rapid growth of the boundary layer. The reduction in heat transfer on the high pressure (trailing) side in the presence of rotation is less than that of the stationary case partly because of a slower growth of the boundary layer. The measurements show that the double vortex associated with Coriolis effect has been established downstream of $x/D = 6.4$. There is a net convection from the low pressure (leading) to high pressure (trailing) side in the latter half of the first passage due to Coriolis effect. Thus, the streamwise velocities on the high pressure (trailing) side increase steadily. The increase in heat transfer on the high pressure (trailing) side stems partly from an increase in convective cooling due to increasing velocity. Measurements show an increase in velocity to $1.2U_b$ along the high pressure surface. Assuming μ and ρ are constant, the an increase in velocity leads to an increase in Re by 20%. This increase in Re yields an increase in Nu (heat transfer) by 16% assuming $Nu = f(Re^{0.8})$. However, the heat transfer results of Wagner et al (1991) show an increase in heat transfer of 100% at the end of the first passage. Compressible flow simulation results (Section 5.5) show that the total effect of Coriolis and buoyancy forces lead to an increase in velocity to $1.4U_b$ along the high pressure surface. Assuming μ and ρ are constant, the increase in velocity leads to an increase in Re by 40%. This increase in Re yields an increase in Nu by 30% from the $Nu\text{-}Re^{0.8}$ relationship and still does not account for an increase in heat transfer of 100% shown in the results of Wagner et al (1991). The convection of cool fluid from the center of the passage toward the high pressure (trailing) surface by Coriolis induced secondary flows greatly increase the temperature difference between the wall and the coolant. Therefore, both the increase in velocity and the convection of the cool fluid toward the high pressure (trailing) surface contribute to the increase in heat transfer. Secondary flow plays an important role in the heat transfer. The heat transfer simulation (Section 5.2.2) and compressible flow simulation (Section 5.5) show that secondary flow accounts for another 40% increase in heat transfer. The tangential velocities close to the high pressure (trailing) surface are small. However, one can expect the secondary motion due to Coriolis forces to be vertical near the low pressure (leading) and high pressure (trailing) surfaces. No vertical velocity can be obtained in the straight section of the passage due to rig constraints but cross-stream velocities obtained at the turn confirmed that these velocities are strong near the high pressure (trailing) and low pressure (leading) surfaces. Furthermore, one can expect that the vertical velocities near the high pressure (trailing) and low (leading) pressure surfaces to be of magnitude similar to those of the tangential velocities near the upper and lower walls. The tangential velocity measurements at $y/H = \pm 0.8$ are of the order of $0.1U_b$ and the computational analyses show that the velocities closer to the wall are even higher. The secondary flows in the vertical direction on the high pressure (trailing) and low pressure (leading) surfaces could exceed $0.1U_b$. The streamwise and tangential velocities explain partially the heat transfer characteristics observed in Wagner et al (1991) and they also indicate the importance of obtaining all three velocity components in future investigations. The same tangential convection that increases the streamwise velocity along the high pressure (trailing) surface causes a velocity deficit on the low pressure (leading) side. Thus, the convective heat transfer on the low pressure (leading) surface decreases. The increase in

66 [illegible]

heat transfer on the low pressure (leading) surface in the latter half of the first passage is likely to be associated with enhanced mixing between the near-wall fluid and the cross-flow which is generated by the development of strong secondary flow toward the end of the passage. The tangential velocities close to the upper and lower walls are of the order of $0.1U_b$. Vertical velocities of similar magnitude could be expected along the low pressure (leading) surface.

Figures 25(i) and (ii) show the contours of the cross-stream and tangential velocities in the first turn, x/D = 18.0. Swirl is presence in the turn. Figure 25(i) show that the cross-stream velocities at the high pressure side (trailing side, negative z/Z) on the inside of the turn, negative y/H, are positive and are of the order of 0.8 to $0.95U_b$. The secondary flow is almost as strong as the streamwise velocity and the cross-flow is convected to the outside of the turn by centrifugal force. Fluid is drawn in from the low pressure (leading) side to fill the velocity deficit. This is evident in the tangential velocities at the inside of the turn (Figure 25(ii) $-0.4 > y/H > -0.8$). Negative velocities are present across the entire passage width. The absolute maximum negative tangential velocity achieves $0.65U_b$. Figures 25(ii) show that the velocity between y/H = 0.2 to y/H = -0.8 are all positive and are of the order of $0.2U_b$. Fluid drawn across the convex surface of the turn and swept along the high pressure (trailing) surface is convected back to the low pressure (leading) side at the concave surface. Figures 25(i) show regions of negative cross-stream velocities near the leading surface, $0.5 < z/Z < 1.0$, in a large region of the turn, $0.4 > y/H > -0.8$. This is due to the effect of the cross-stream pressure gradient. The convection of fluid from low pressure (leading) to high pressure (trailing) side in the first passage leads to thickening of the boundary layer on the low pressure side. The flow on the low pressure (leading) side of the turn has a lower momentum and is more sensitive to cross-stream pressure gradient induced by the turn. Clockwise rotation of the model generates a clockwise swirl (view toward the downstream direction) in the first turn. Swirl increases the residence time of the coolant and generates strong cross-stream gradients which would augment heat transfer. The positive cross-stream velocity near the low pressure surface (leading surface, $z/Z < -0.75$) and close to the outer wall (y/H = 0.6 and 0.8) Figures 25(i), indicate the possibility of a small corner recirculation zone in this region.

The results of Wagner et al. (1990) and other researchers such as Yang et al (1992) showed that the heat transfer characteristics were enhanced up to 100% at the turn. In addition to the swirling motion generated by the combination of the turn and rotation, the turn alone is expected to create a substantial pressure drop in the cross-flow, which is highly beneficial to mixing and augmentation of heat transfer. It is evident from the present velocity measurements that the pressure drop results in secondary flows of the order of up to 95% U_b. The cross-flow negotiates the turn at speeds of up to 50% higher than those in the straight passage and consequently would result in a sharp increase in convective heat transfer.

Figure 26(i) shows the streamwise rms velocities at the inlet of the turn (x/D = 15.0). The normalized turbulence intensities at the inlet of the turn are of the order of $0.1U_b$ in the center of the passage. They are of the order of 0.15 to $0.2U_b$ near the lower wall. The

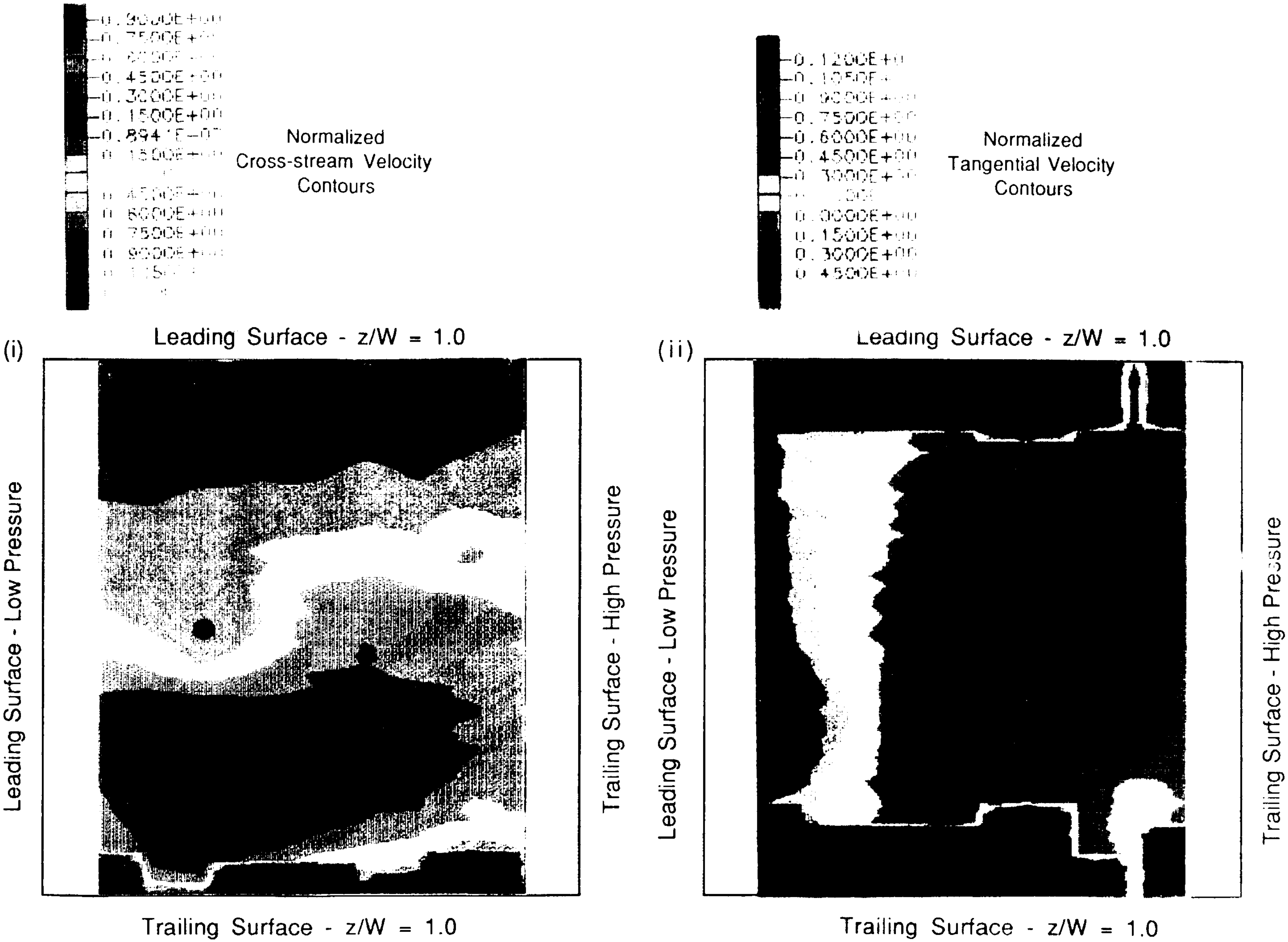

Figure 25 Mean velocity contours at x/D = 18.0, Re = 25,000 and Ro = 0.24
(i) Cross-stream velocity (ii) Tangenual velocity

convection of fluid toward the upper wall enhances the growth of the boundary layer near the lower wall. The viscous effect is breaking away from the lower wall and this gives rise to sharp increases in the turbulence quantities. Near the low pressure (leading) and the high pressure (trailing) surfaces, the effect of the boundary layer increases the turbulence level; however, the results here may contain some noise since spikes are not present in all the profiles. Contamination of data near the wall due to reduced SNR is a commonly occurring phenomenon in LDV. Figures 26(ii) shows the cross-stream rms velocities at the turn (x/D = 18.0). The turbulence intensities of the cross-stream velocity at the outside of the turn (y/H > 0) show that the fluctuations increase almost linearly from near $0.1U_b$ at the low pressure side (leading side, z/Z = 1) to roughly $0.2U_b$ at the high pressure side (high pressure z/Z = -1). However, the cross-stream rms velocity profiles on the inside of the turn (0.2 > y/H > -0.8) show that there are sudden increases in the turbulence level to $0.3U_b$ in the region between the center of the passage, z/Z = 0, to three-quarter of the passage width, z/Z = 0.75. This suggests that there is a local source of turbulence in this region. Inspection of the corresponding velocity profiles, Figure 25(i), indicates that the turbulence is generated by the velocity gradients. Figure 25(i) also shows that the velocity gradients near the high pressure surface (trailing surface, z/Z = -1) induce increases in turbulence levels, Figure 26(ii), but the effect is less noticeable because the nearby wall damps the fluctuations. The general trend of an increase in turbulence intensity from around 10% at the low pressure side (leading side, z/Z = 1) to roughly 20% at the high pressure (trailing side, z/Z = -1) is also evident in the inside of the turn (negative y/H), Figure 26(ii). The rms quantities of the cross-stream velocity in the first turn are generally are higher than those of the streamwise velocity at the inlet of the turn. This result suggests that, as expected, the turn is a major source of turbulence as well as secondary flows. Figures 26(iii) and 26(iv) shows the streamwise rms velocity at the exit (x/D = 21.0) and 4D downstream of the first turn (x/D = 25.0). The cross-stream rms velocity profiles at the turn (Figure 26(ii)) and the streamwise rms velocity profiles at the exit are similar in shape and magnitude. Thus, the turbulence fluctuations are isotropic. The turbulence fluctuations at the first turn (Figure 26(ii)) and the exit of the turn (Figure 26(iii)) are of similar magnitude but those 4D downstream of the turn (Figure 26(iv)) are 50 to 100% lower that those at the turn. These results confirm that the turn is a major source of turbulence. The large fluctuations in the turn allow interfaces between the hot fluid and the cold cross-flow to be rapidly distorted and increased in area many times, so that molecular diffusion (which is the only mechanism responsible for mixing even in turbulent flow) is much more effective and rapid mixing and diffusion of the near-wall hot fluid is induced. The sharp increase of heat transfer, more than 100%, reported in Wagner et al. (1991) and Yang et al. (1992) is attributed to a combination of increase in flow speed, turbulence and swirl.

Figures 27 and 28 show the velocity contours at the exit of the first turn (x/D = 21.0) and 2D downstream of the first turn (x/D = 23.0), respectively. The streamwise velocity contours at x/D =21.0, Figure 27(i), show the complexity of the flow at the exit of the first turn due to interaction of secondary flow induced by the turn and by rotation. The double peak velocity characteristics with high velocities near the high pressure (leading) and low pressure (trailing) sides near the concave surface (the pressure surface of the turn) are consistent with the velocity contours exiting a turn. The high pressure and low pressure

70 [illegible] BLANK

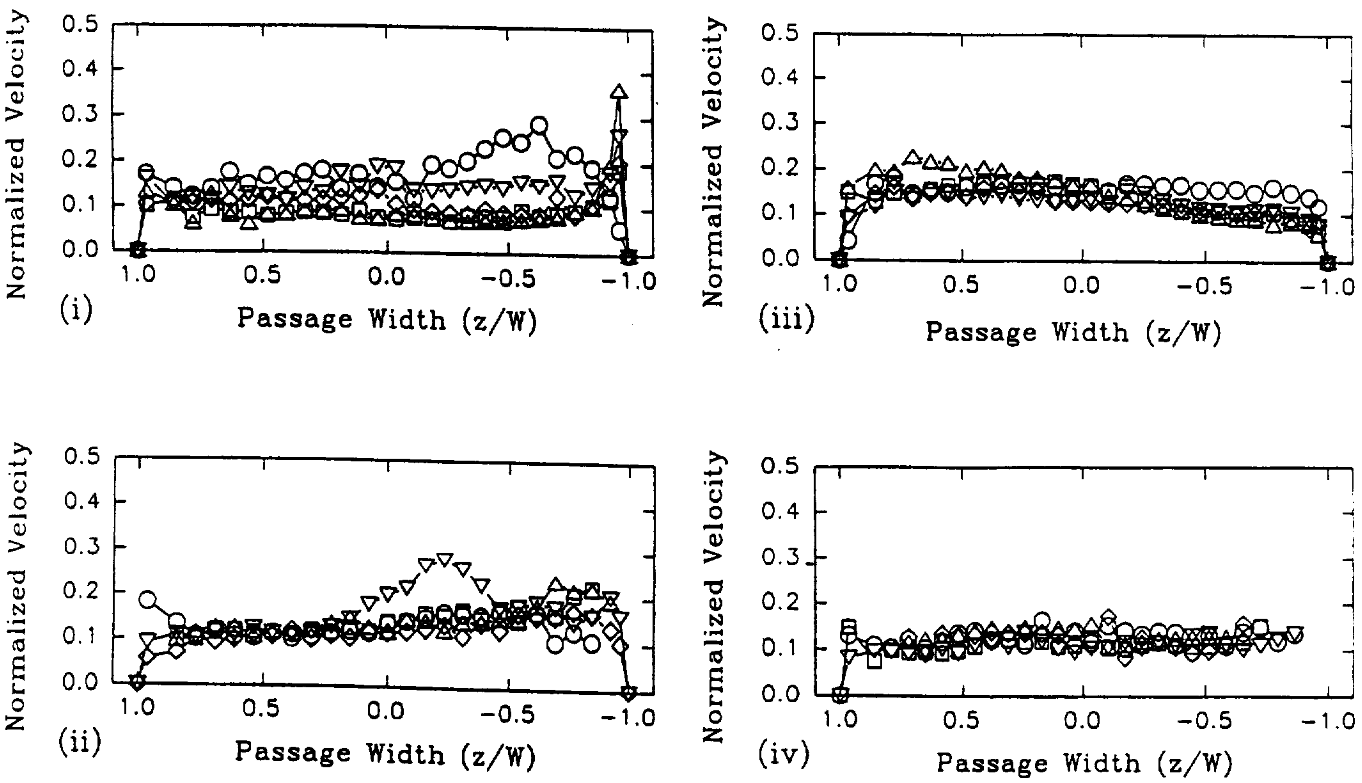

Figure 26 Rms velocity along the cooling passage, Re = 25,000 and Ro = 0.24.
(i) Streamwise rms velocities x/D = 15.0
(ii) Cross-stream rms velocity x/D = 18.0
(iii) Streamwise rms velocities x/D = 21.0
(iv) Streamwise rms velocities x/D = 25.0

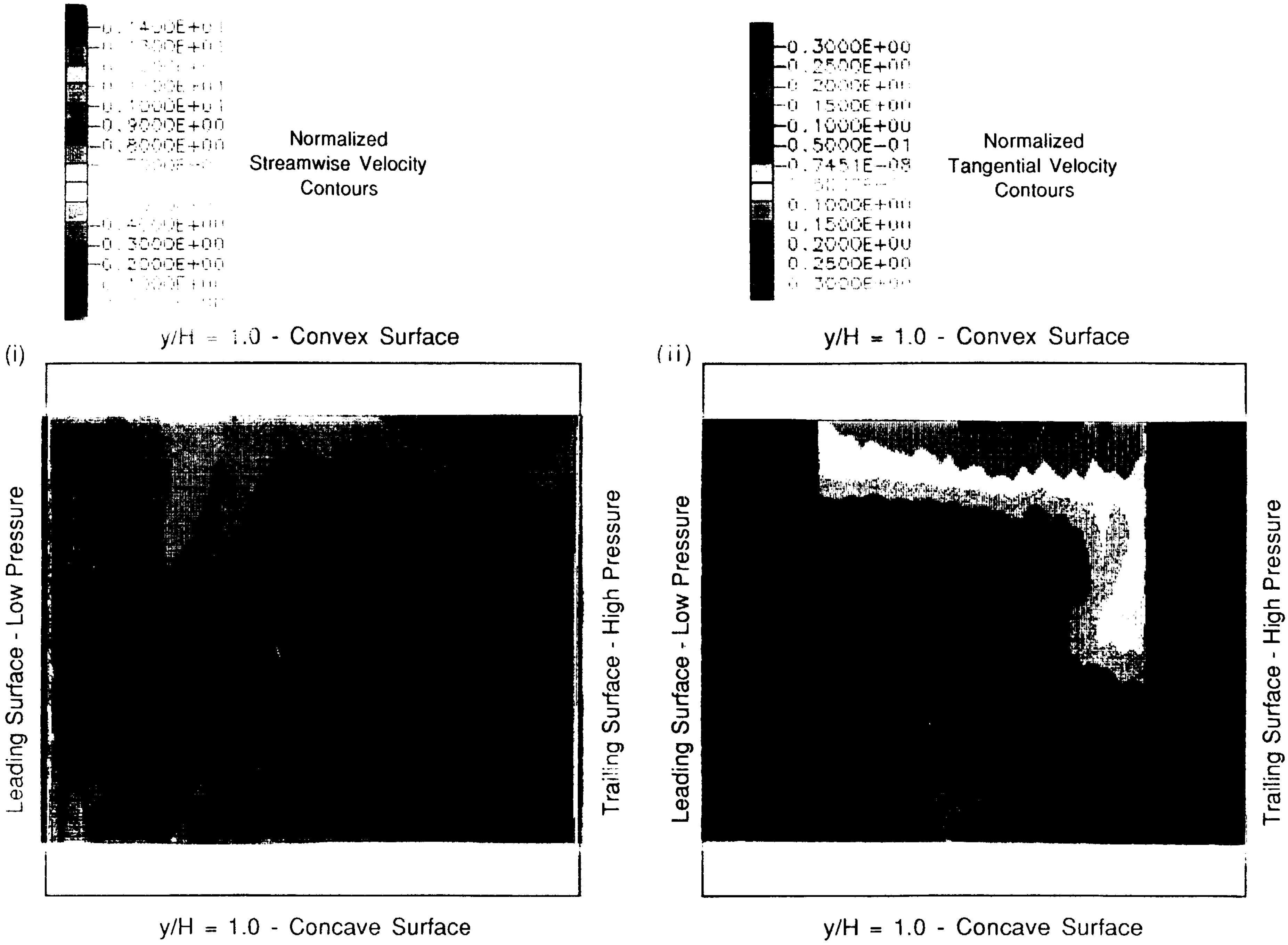

Figure 27 Mean velocity contours at $x/D = 21.0$, $Re = 25{,}000$ and $Ro = 0.24$.
(i) Streamwise velocity (ii) Tangential velocity

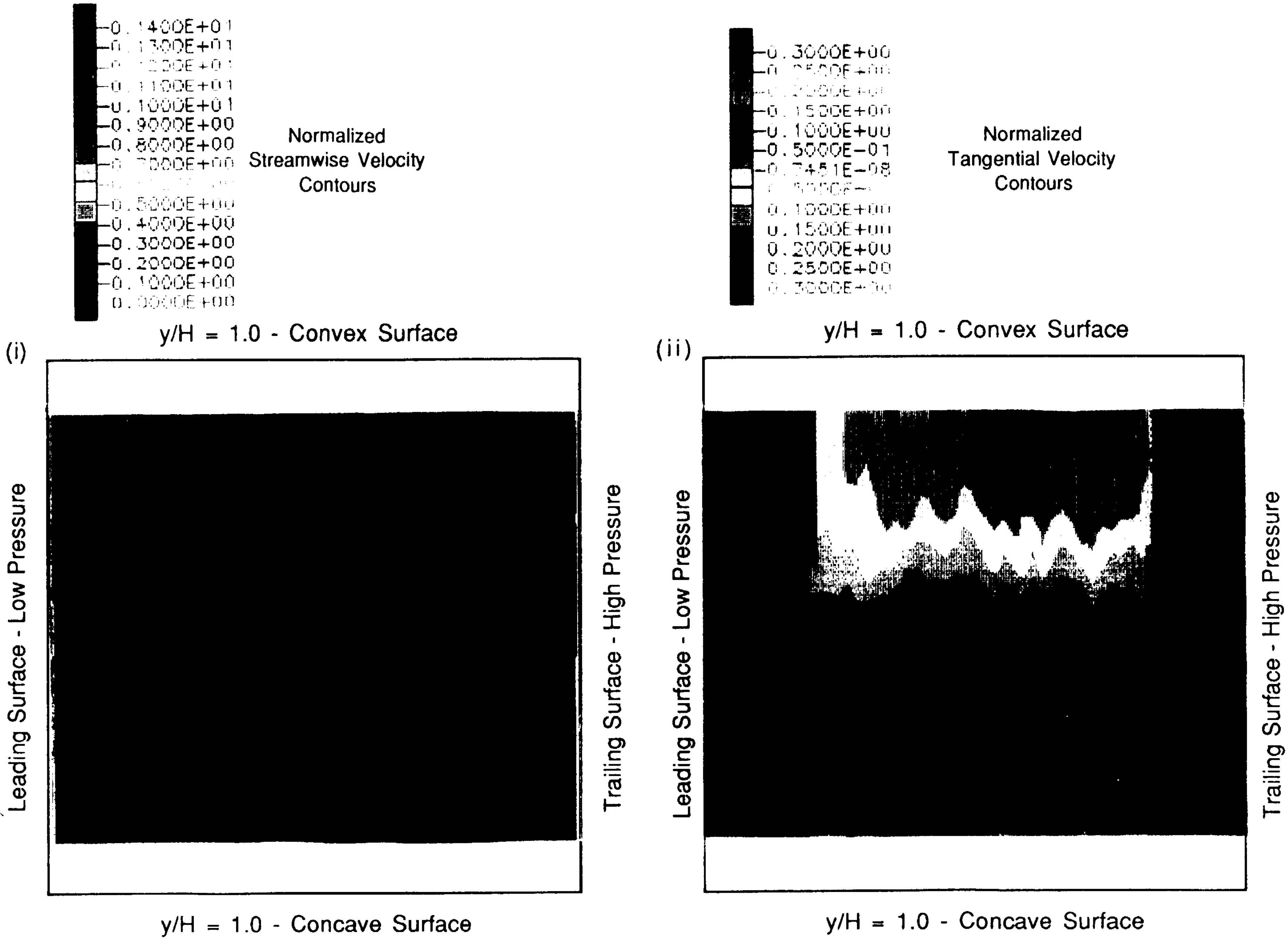

Figure 28 Mean velocity contours at x/D = 23.0, Re = 25,000 and Ro = 0.24.
(i) Streamwise velocity (ii) Tangential velocity

PAGE 74 [illegible]

surfaces are reversed in the first and second passages. The flow direction is reversed due to radially inward flow in the second passage as opposed to radially outward flow in the first passage. Thus, the direction of the Coriolis induced secondary flow is reversed. The shapes of the high velocity contours ($U > 1.2U_b$) are distorted with the maximum velocity region ($U > 1.3U_b$) shifted to the low pressure (trailing) side. The distortion stems from Coriolis effects induced by rotation. The general flow characteristics associated with the interaction of the secondary flows induced by the turn and rotation is still evident in the velocity contours 2D downstream of the first turn, Figure 28(i). Both the vertical and lateral variations in the streamwise velocity are reduced. It is also evident from Figure 28(i) that the velocities close to the low pressure (trailing) and high pressure (leading) surfaces are high. These high velocity regions near the walls increase convective cooling and suppress the growth of boundary layers. The heat transfer between the walls and the coolant is more efficient in this region. The high heat transfer reported in Wagner et al (1991) at 2D downstream of the turn is partly due to increases in the near-wall velocities. The tangential and cross-stream velocities in the turn presented in Figure 25 (described above) show that the flow exiting the first turn produces a clockwise swirl. The presence of swirl at the exit induces rapid mixing. The streamwise velocities at 2D downstream of the exit of the turn, Figure 28(i) are more uniform than those at the exit, Figure 27(i). Figures 27(ii) and 28(ii) show the tangential velocities at the exit of the first turn ($x/D = 21.0$) and 2D downstream of the first turn ($x/D = 23.0$), respectively. In both cases, the tangential velocity in the lower half of the passage (negative y/H) is negative, indicating convection from the high pressure (leading) surface to low pressure (trailing) surface. However, the tangential velocity in the upper half of the passage (positive y/H) is positive, indicating convection from the low pressure (trailing) surface to high pressure (leading) surface. The positive and negative tangential velocities indicate that the cross-flow at the exit of the turn still possesses a clockwise swirl. Thus, the augmentation of heat transfer by swirl is expected to extend to at least 2D downstream of the turn. Contrary to the results obtained at the exit of the second turn ($x/D = 39.3$), which have very little or no scattering, the data obtained at the exit of the first turn ($x/D = 21.0$) show more scatter. The scattering of the data is likely to be due to local imperfections in the model.

The velocity streamwise contours at 4D downstream of the first turn, $x/D = 25.0$ (Figure 29(i)) shows high velocities close to the high pressure (leading) surface. Rotation induces a net tangential convection from the low pressure (trailing) to the high pressure (leading) side in the second passage since the Coriolis effect on radially inward flows is opposite to that on radially outward flows. Figure 29(ii) shows that negative tangential velocities occur near the upper ($y/H > 0.6$) and lower ($y/H < -0.6$) walls at 4D downstream of the second turn ($x/D = 25.0$). Thus, in the near-wall region, the tangential convection is from high pressure (leading) surface to low pressure (trailing) surface. The tangential velocities in the center of the passage (y/H between ± 0.4) are positive indicating convection from the low pressure (trailing) to the high pressure (leading) surface. Thus, the double vortex characteristics associated with the Coriolis effect have already been re-established at 4D downstream of the first turn. The convection in the tangential direction is reversed because of the reversal in the direction of the Coriolis forces. The double vortex has been established at 4D downstream of the first turn and the clockwise generated by the turn and

76

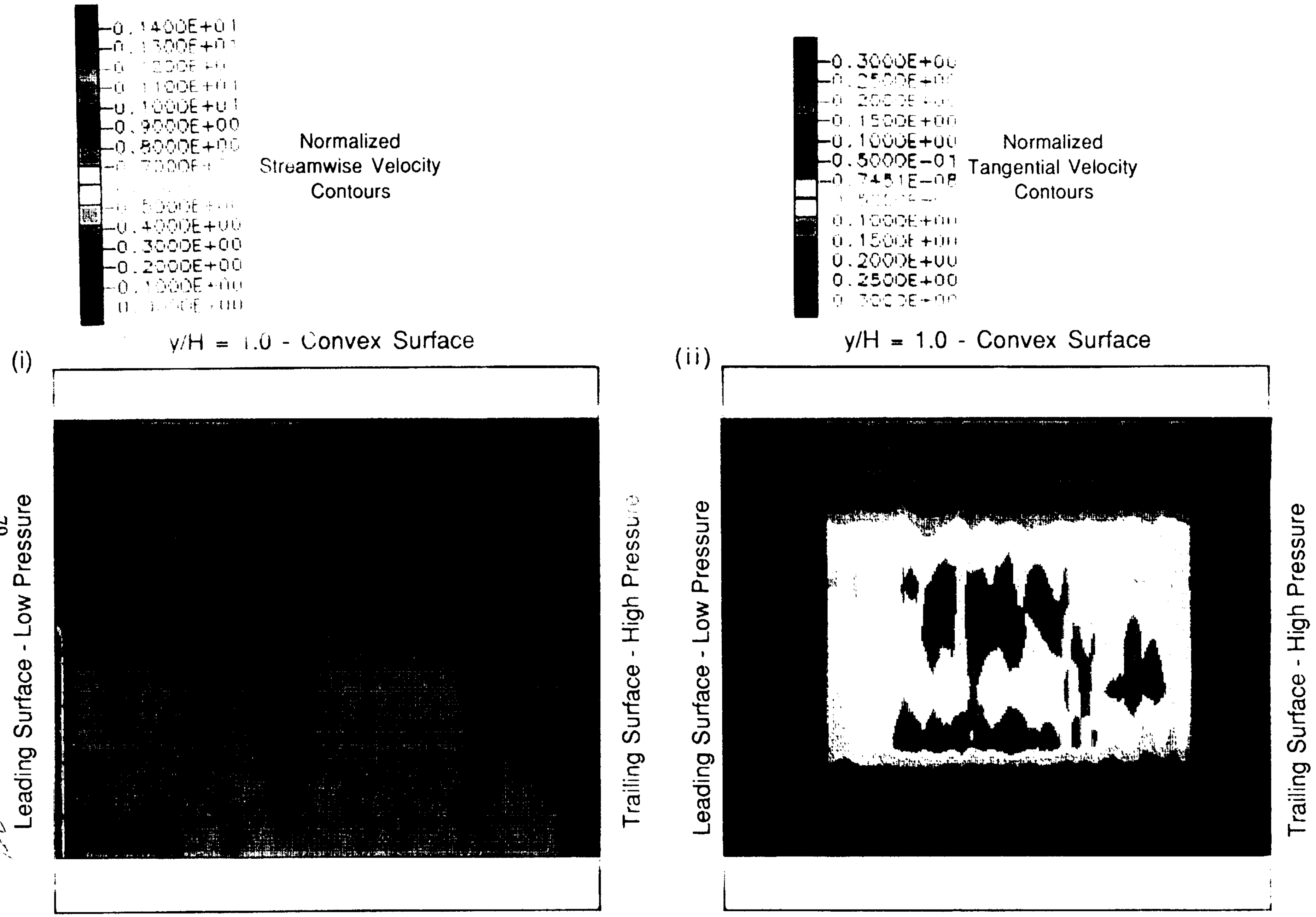

Figure 29 Mean velocity contours at x/D = 25.0, Re = 25,000 and Ro = 0.24.
(i) Streamwise velocity (ii) Tangential velocity

PAGE 78 INTENTIONALLY BLANK

rotation has been dissipated. The streamwise and tangential velocities at 2D and 4D downstream of the first turn show that the effect of the turn extends beyond 2D downstream of the turn but does not extend beyond 4D.

The streamwise velocity contour at the entrance to the second turn (x/D = 33.2), Figure 30(i), shows that the high velocities are on the high pressure (leading) side. Similar to the first turn, the mean velocity increases with increasing y/H because of cross-stream convection to the convex surface of the turn. Figure 30(ii) show the tangential velocity at the entrance to the second turn (x/D = 33.2). Similar to the first passage, the secondary flows on the low pressure surface (leading surface for the first passage and trailing surface for the second) are stronger than those on the pressure side (trailing surface for the first passage and leading surface for the second). Comparison of Figures 24(ii), 29(ii) and 30(ii) shows that the magnitudes of the tangential velocities increase with distance downstream. The tangential velocities in the proximity of the turn, Figure 27(ii) and 28(ii), are higher than those at the entrance of the turn, Figure 24(ii), and along the second passage, Figures 29(ii) and 30(ii). The secondary flow induced by the turn is stronger than that induced by Coriolis effects because of the high pressure drop. The magnitude of the secondary flow diminishes with distance away from the turn. Similar to the velocity characteristics at the entrance of the first turn, the double vortex at the entrance of the second turn is also distorted by the secondary flow induced by the turn, Figure 30(ii).

The heat transfer results of Wagner et al (1991) indicated that, with rotation, the heat transfer in the first, outward flowing passage increases and decreases by 100% and 60% for the high pressure and low pressure surfaces, respectively, compared to the heat transfer with the stationary case. The effect of rotation on heat transfer in the second, inward flowing passage is significantly different compared to the first, outward flowing passage. The heat transfer increases only by 10 to 20 % on the high pressure surfaces compared to stationary results. The heat transfer on the low pressure surface decreases by 5 to 30 % compared to the stationary values. The effects of buoyancy on heat transfer without the complication of Coriolis generated secondary flow have been studied in vertical stationary ducts with parallel and counter flow configurations by Eckert et al (1964) and Metais and Eckert (1964). Based on their results, buoyancy forces would be expected to cause significant changes in the heat transfer in turbine coolant passages and be strongly dependent on flow direction (radially inward vs. radially outward). For heated stationary vertical plates, the gravitational forces induce a buoyancy effect which causes the higher temperature fluid, i.e. less dense fluid, to rise. Similarly, the centrifugal force in a heated rotating passage induces a buoyancy effect against the centrifugal force.

With rotation the buoyancy forces on fluids with densities lower than that of the bulk density is radially inward but the buoyancy force on fluids with densities higher than that of the bulk density is radially outward. In the first passage, Coriolis forces increase the velocity (convective heat transfer) on the high pressure (trailing) surface and convect cool core fluid to the high pressure side. The density difference between the cool fluid accumulating on the high pressure side and the cross-flow induces radially outward secondary flows. Thus, buoyancy forces tend to increase the velocity (convective heat

PAGE 80 INTENTIONALLY BLANK

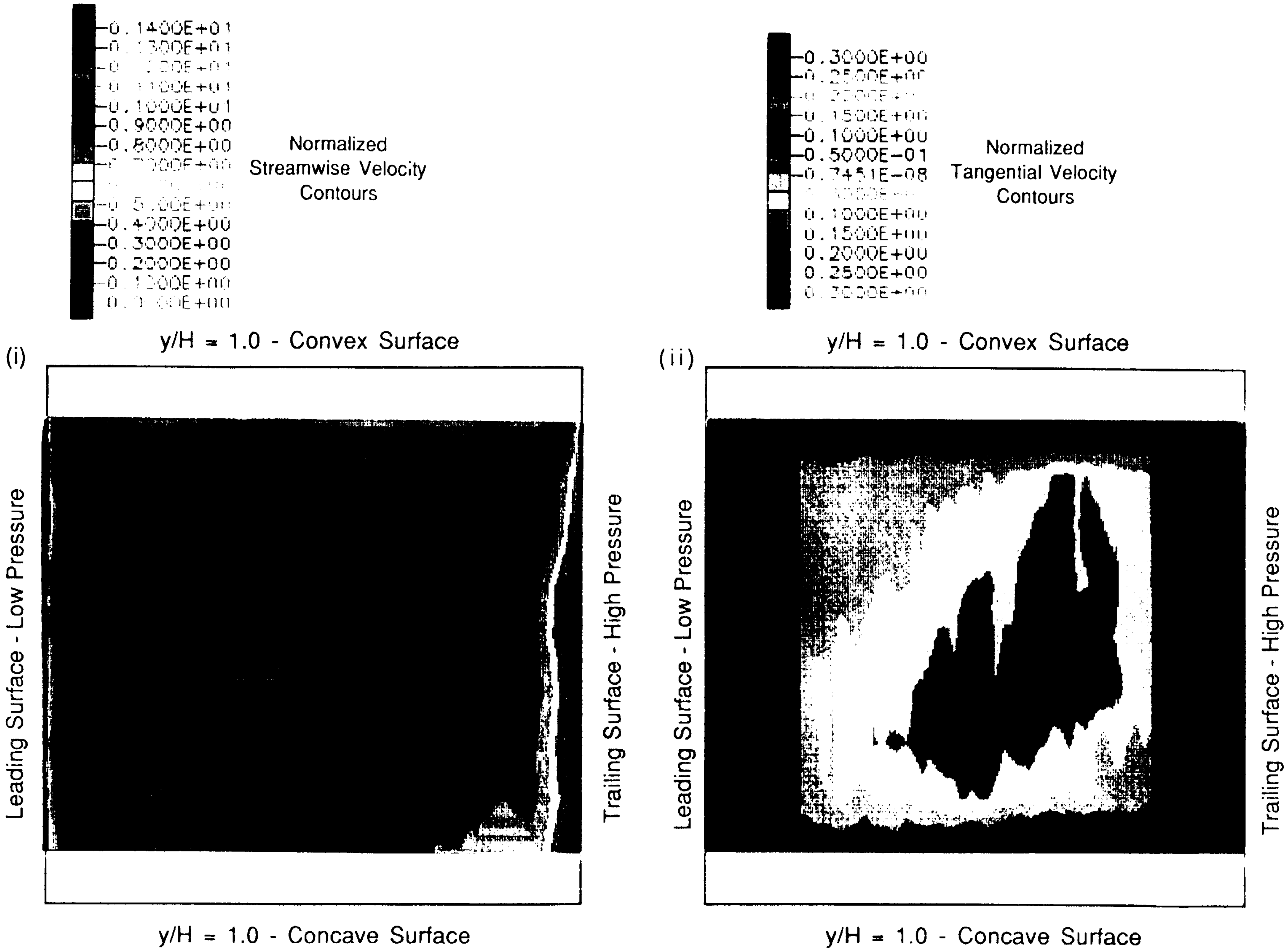

Figure 30 Mean velocity contours at x/D = 33.2, Re = 25,000 and Ro = 0.24.
(i) Streamwise velocity (ii) Tangential velocity

PAGE 82 INTENTIONALLY BLANK

transfer) on the high pressure side. The heat transfer observed in the presence of rotation is much higher than that of the stationary case, Wagner et al (1991), because Coriolis and buoyancy forces reinforce each other. Coriolis forces reduce the flow velocity (convective heat transfer) on the low pressure (leading) side. In addition, the Coriolis forces induce tangential convections along the upper and lower walls. Surface heat transfer from the walls to the fluid increase the temperature of the near-wall fluid. Thus, the Coriolis forces accumulate hot fluid along the low pressure surface as well as reduce the velocity on the low pressure side. Buoyancy forces on fluids with densities lower than that of the bulk density are radially inward. The secondary flows induced by buoyancy forces along the low pressure surface are radially inward. This further reduces the streamwise velocities and inhibits the heat transfer on the low pressure side.

In the second radially inward flow passage, buoyancy effects associated with centrifugal forces remain unchanged but the direction of the Coriolis forces are reversed. Coriolis forces increase the flow velocity (convective heat transfer) along the high pressure (leading) side and convection of cool fluid to the high pressure side. The temperature of the fluid near the high pressure (leading) surface is lower than that of the bulk temperature. The secondary flows induced by buoyancy forces associated with the density difference between the fluids along the high pressure (leading) surface and in the center of the passage is radially outward. Thus, the secondary flows induced by buoyancy forces reduce the increases in flow velocity associated with Coriolis effects. This reduces the flow velocities and offsets the increase in heat transfer induced by Coriolis effects. Coriolis forces reduce the flow velocities and convective heat transfer on the low pressure (trailing) side. However, the accumulation of hot fluids along the low pressure (trailing) side gives rise to radially inward secondary flows, induced by buoyancy forces, which tends to increase the velocity near the low pressure surface. This will increase the velocity on the low pressure (trailing) side and offset some of the reduction in heat transfer associated with Coriolis effects. The variations in heat transfer on the high pressure and low pressure sides of the second passage associated with rotation are less than those in the first passage. In the first passage, increases in heat transfer associated with Coriolis effects are always reinforced by buoyancy effects. In the second passage, Coriolis and buoyancy effects work against each other. When Coriolis forces decrease the heat transfer, buoyancy forces increase it and vice versa. In the second passage, Coriolis forces are expected to increase the heat transfer on the high pressure side but decrease that on the low pressure side and the effect of the buoyancy forces is expected to be the opposite. Similar to the first passage, the streamwise velocity measurements show an increase in velocity to $1.2U_b$ along the high pressure surface. Assuming μ and ρ are constant, the increase in velocity leads to an increase in Re by 20%. This increase in Re yields an increase in Nu (heat transfer) by 16% from the $Nu\text{-}Re^{0.8}$. The results of Wagner et al (1991) show that the heat transfer on the high pressure in the second passage side increases by 10 to 20% in the presence of rotation and that on the low pressure side decreases. Heat transfer in turbine blade cooling passages is determined by Coriolis, buoyancy and secondary flow effects. The apparent agreement in the heat transfer results observed by Wagner et al (1991) and those deduced from Coriolis effects the stems from buoyancy and secondary flow effects offsetting each other. In the second passage, buoyancy effects opposed Coriolis and secondary flow effects. The secondary flows

PAGE 84 INTENTIONALLY BLANK

induced by Coriolis forces continue to affect the heat transfer characteristics in the second passage. Disregarding the effect of the turn, the tangential velocities along the first and second passage (Figure 24(ii), 29(ii) and 30(ii)) show that the secondary flows in the second radially inward flow passage are stronger than those in the first radially outward passage. However, the influence of the secondary flow induced by the Coriolis force on heat transfer in the second passage is smaller than that in the first passage. The bulk temperature of the fluid increases with distance downstream. The impact of convection of the core fluid to the high pressure surface on heat transfer reduces because of reduction in temperature difference between the wall and the fluid. Although the present effort is isothermal and incompressible, it has explained many of the heat transfer results observed by Wagner et al (1991). Buoyancy and secondary flow effects are strong in the first passage because the temperature differences are high. However, it should be noted that in the case of actual flow passages where trip strips are used to increase mixing, the effect of buoyancy is shown to decrease (Wagner et al 1991a, Johnson et al 1992) compared to the importance of buoyancy in this smooth passage.

Figures 31(i) to (iii) show the streamwise velocity contours obtained at exit of the second turn (x/D = 39.3), at 2D (x/D = 41.3) and 4D (x/D = 43.3) downstream of the second turn. No tangential velocity measurements were obtained at these locations because the optical access for this component is more restricted. However, the direction of the tangential velocity can be deduced from the streamwise velocity component. At the exit of the second turn, Figure 31(i), the velocities close to the lower wall (y/H = -0.6 and -0.8) are skewed toward the low pressure (leading) side but those in the remainder of the passage are skewed toward the high pressure (trailing) side, indicating positive tangential convection close to the lower wall and negative tangential convection in the remainder of the passage. This trend is consistent with that of a counterclockwise swirl expected from the flow exiting the second turn. Since clockwise rotation of the rig generated clockwise swirl in the flow exiting the first turn, a counterclockwise swirl is expected in the flow exiting the second turn because the direction of the cross-flow is reversed and thus the direction of the secondary flow induced by the Coriolis effect. The signature of the secondary flow associated with the turn and rotation is clearly evident in the velocity contours at the exit of the second turn, Figure 31(i). The high velocities at the exit of the second turn occur at the concave surface and are consistent with Coriolis induced secondary flows. Figure 31(i) show that there are substantial vertical variations in the streamwise velocities near the low pressure surface (leading side, $z/Z > 0.5$) and in the center of the passage ($-0.5 < z/Z < 0.5$). In both of these locations, the variations are of the order of $0.5U_b$ over a distance of 10mm. These large variations are associated with the strong secondary flow induced by a combination of the turn and rotation. Figure 31(ii) shows the streamwise velocity contours at 2D downstream of the second turn, x/D = 41.3. The signature of the secondary flow associated with the turn and rotation is still evident at 2D downstream with a general shift in the direction of the high velocity region toward the high pressure (trailing) side because cross-stream convection in the tangential direction is reversed as the flow exited the turn. The Coriolis effect in the third radially outward flow passage induces a net tangential convection from low pressure (leading) to high pressure (trailing) surfaces. Comparison of Figures 31(i) and 31(ii) shows that the velocity distribution at 2D downstream of the second turn is more

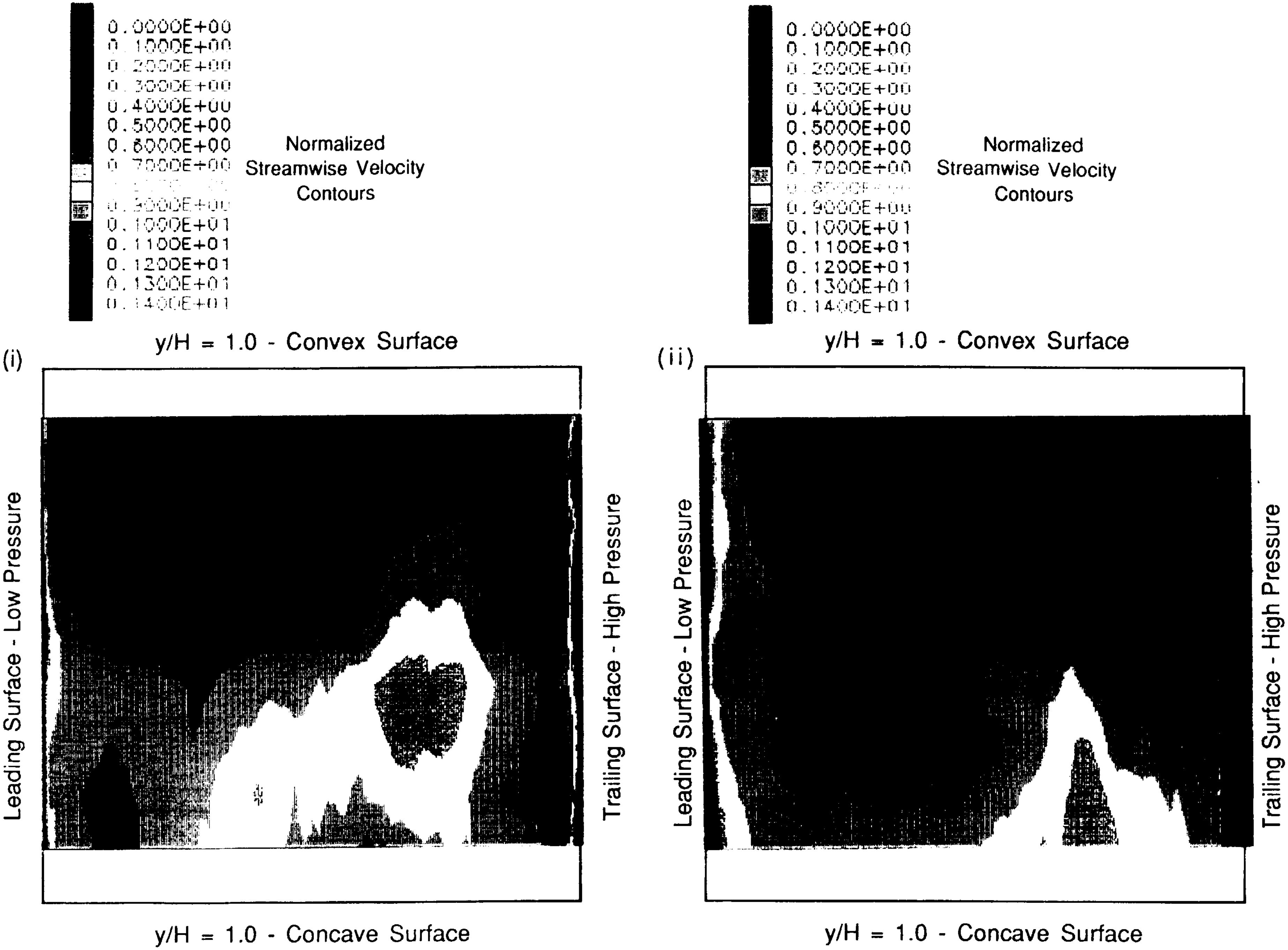

Figure 31 Streamwise mean velocity in the third passage, Re = 25,000 and Ro = 0.24.
(i) x/D = 39.3 (ii) x/D = 41.3

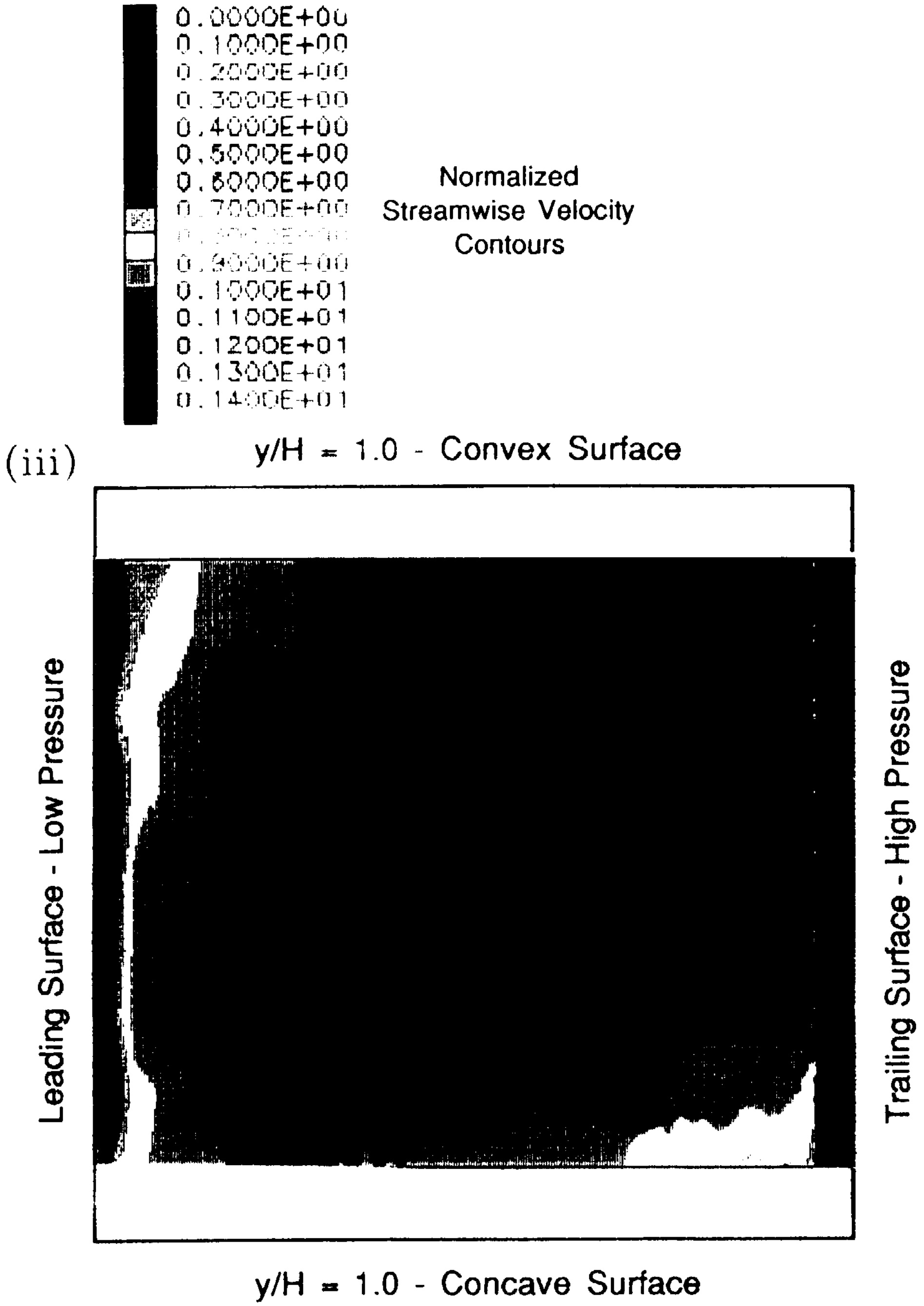

Figure 31 Continued. (iii) x/D = 43.3.

uniform than that at the exit of the turn. The secondary flows and velocity gradient generated by the second turn is dissipating.

Comparison of Figures 31(i) and 26(i) shows that the cross-flows exiting the first and second turns are relatively uniform on the high pressure side (leading side for the second passage and trailing side for the third) but there is a substantial cross-flow variation in the vertical direction on the low pressure side. However, the maximum absolute velocity at the exit of the second turn is approximately $0.12U_b$ higher than that at the first turn. Thus, the velocities at the exit of the first and second turn are nearly mirror images to each other but with substantial differences in magnitude. Furthermore, the near wall-flow at the exit of the second turn is stronger than that of the first turn. Comparison of the velocity contours at 2D downstream of the first ($x/D = 23.0$) and second turns ($x/D = 41.3$), Figures 31(ii) and 27(i), shows the same features as those at the exit of the two turns ($x/D = 21.0$ and 39.3): the velocity contours at 2D downstream of the first and second turns are nearly the mirror images of each other in shape but different in magnitude. Although the velocities coming out of both turn have gradients of similar magnitude, the velocity contours at 2D downstream of the second turn, Figure 30(ii), have much steeper gradients than those at 2D downstream of the first turn, Figure 27(i). The secondary flow at the exit of the first turn is dissipating at a quicker rate than that at the exit of the second turn. For example, at $z/Z = -0.5$ at 2D downstream of the second turn (Figure 31(ii)), the variation in streamwise velocity over 10mm is approximately $0.4U_b$ and that at $z/Z = 0.5$ at 2D downstream of the first turn (Figure 27(i)) is $0.25U_b$: $z/Z = -0.5$ and 0.5 are chosen for the comparison because the high pressure side in the third passage is the trailing side and that in the second passage is the leading side. This probably stems from the difference between radially outward and inward flow. It is also evident from Figures 31(ii) and 27(i) that there are larger discrepancies in the velocity measurements near the upper and lower walls ($y/H = \pm 0.8$) than in the remainder of the passage. These discrepancies are attributed to differences in surface roughness, as well as positional uncertainty. The near wall flow is dependent on surface roughness for $Re < 10^7$. Positional uncertainty has a greater effect on the near wall measurement because of the presence of steep gradients. The control volume size for the measurements is approximately 0.9 mm in the vertical direction and can be aligned to a precision of 0.2 mm. Near-wall measurements show that velocity can vary from zero to 100% U_b within 0.8 mm from the wall. Thus, a positional uncertainty of ±0.2 mm can give rise to a statistical uncertainty of $\pm 0.08U_b$.

Figure 31(iii) show the streamwise velocities at 4D downstream of the second turn, $x/D = 43.3$. The velocities close to the lower wall ($y/H = -0.6$ and -0.8) are skewed toward the low pressure (leading) side but those in the remainder of the passage are skewed toward the high pressure (trailing) side. Contrary to the results obtained in the first turn, Figure 26(i), which show that the effect of the clockwise swirl associated with the turn and rotation does not exist beyond 4D downstream of the turn, the counterclockwise swirl, evident in the velocity profiles at the exit of the second turn ($x/D = 39.3$), is still evident at 4D downstream of the turn. The influence of the swirl induced by a combination of rotation and the turn may extend beyond 4D downstream of the turn for $Ro > 0.24$. Thus, augmentation of heat transfer associated with swirl may also extend beyond 4D downstream of the turn for Ro > 0.24.

No velocity data is available at the second turn because of rig constraints. The heat transfer results of Wagner et al (1991) do not include any data downstream of x/D = 36.0. No comparison can be made between the velocity and heat transfer measurements downstream of x/D = 33.2. The implications of the flow characteristics on heat transfer downstream of x/D = 33.2 are considered in the computation studies in Sections 5.2 and 5.5.

5.2 Baseline Simulations

5.2.1 Flow Simulations

The velocity measurements have shown that the Coriolis force acts on the low momentum fluid near upper and lower walls resulting in a migration of fluid from the high pressure surface to the low pressure surface. In the center of the duct, high momentum fluid moves from the low to high pressure surface. Thus, the Coriolis induced double vortex results in migration of the high momentum fluid in the center of the duct toward the trailing surface, the high pressure surface for radially outward flow.

Under the present effort the classical Coriolis induced flow was both measured and predicted 6.4 diameters downstream of the inlet plenum as shown in Figure 32. As discussed in Section 2.2, Case A was initiated at x/D = 6.4. Cases B and C were initiated at x/D = 1.0 with Case C having high near wall resolution.. Comparisons are shown only for Case B and C since this location was specified as the inlet plane for Case A. Excellent agreement exists between measured and predicted streamwise velocity, Figure 32a. The high velocity fluid which was present at the leading surface of the duct at the plenum exit has started to migrate toward the trailing surface. In addition, both the measurements and the predictions show that the boundary layer is starting to thicken on the leading surface. Since the predictions for both the two-layer wall integration, Case C, and the wall function, Case B, simulations are almost identical, both near wall shear-stress treatments adequately resolve the flow field in the first leg of the rotating serpentine passage.

The tangential velocity component shows the classical secondary flow field, Figure 32b. The tangential velocity is positive near the upper, y/H = 1.0, and the lower, y/H = -1.0, surfaces indicating that fluid moves from the high pressure, trailing, surface toward the low pressure, leading, surface. The vortex is completed with fluid moving from the leading toward the trailing surface in the center of the duct. The predicted tangential velocity is also in excellent agreement with the data at x/D = 6.4.

For flow entering the first turn, the measured streamwise velocity component is compared with predictions for all three incompressible flow simulations in Figure 33a. At this location, the highest velocity fluid resides near the convex surface, y/H = 1.0. The effect

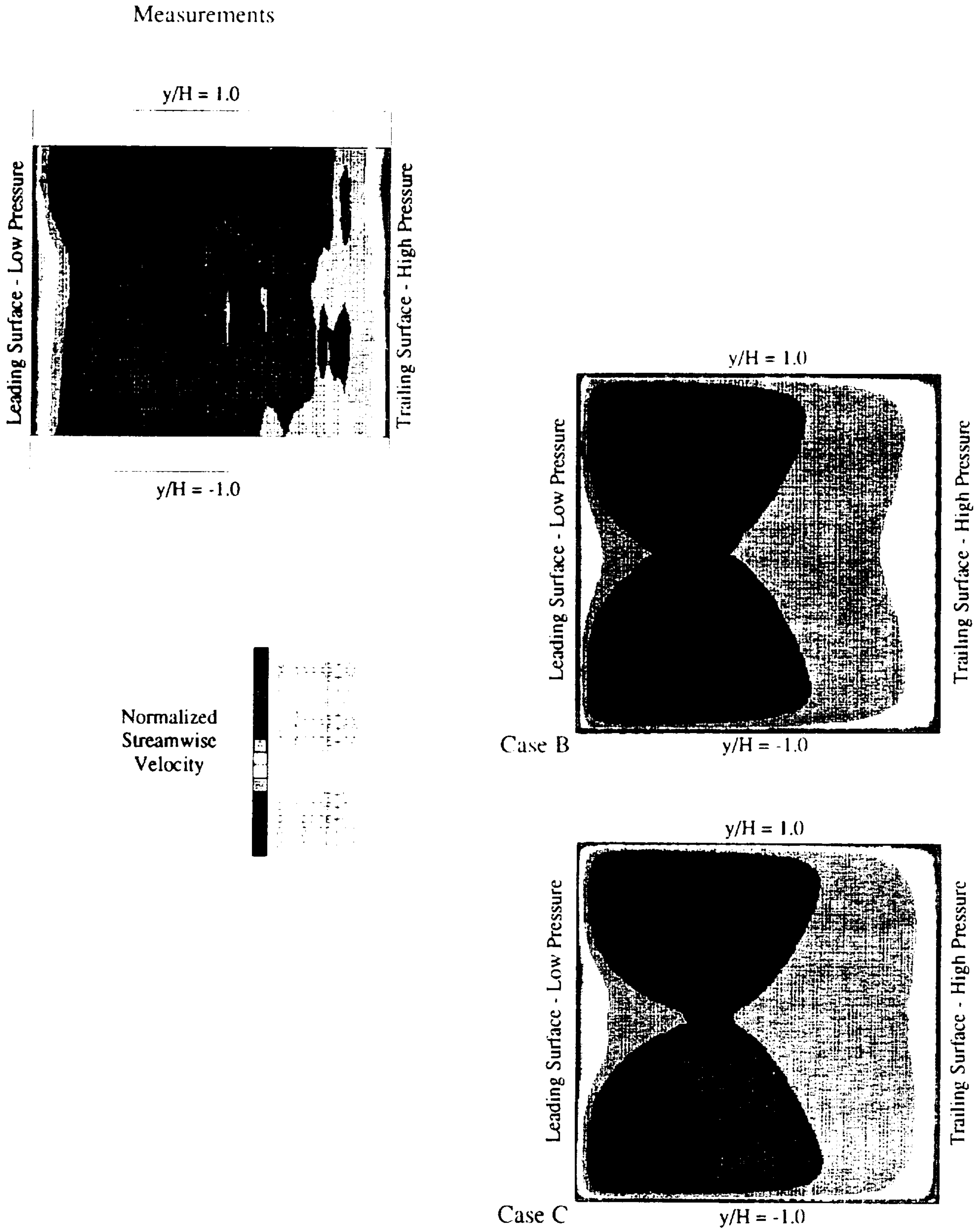

Figure 32a Streamwise velocity comparisons between measurements and predictions from cases B and C at x/D =6.4

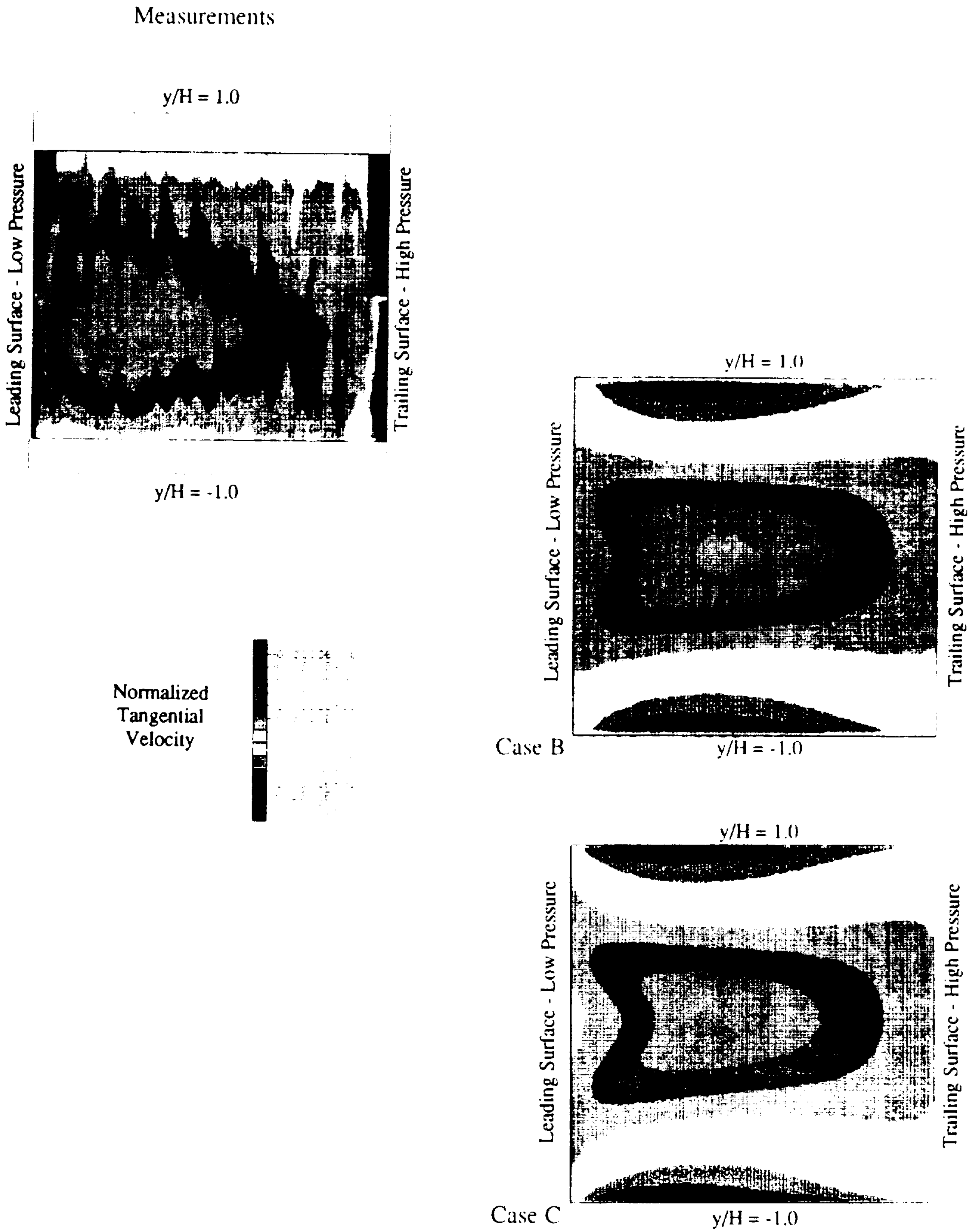

Figure 32b Tangential velocity comparisons between measurements and predictions from Cases B and C at x/D =6.4

PRECEDING PAGE BLANK NOT FILMED

PAGE 94 INTENTIONALLY BLANK

of the turn is apparent at this location since high velocity fluid would be anticipated at the convex surface from inviscid flow theory. The migration of fluid toward the high pressure, trailing, surface causes low momentum fluid to accumulate near the low pressure surface resulting in a relatively thick boundary layer. This phenomenon was experimentally measured and predicted in all three simulations; the shape of the velocity contours was extremely well predicted near the low pressure surface. The sensitivity of the predictions to inlet boundary conditions is demonstrated in Figure 33a. Both the wall function and two-layer wall integration with the complete inlet boundary condition specification, Cases B and C, show excellent agreement with data at x/D = 15.0. Since the same grid distribution was used for both wall function predictions, Cases A and B, the differences in predicted streamwise velocity at this location can be directly attributed to the differing inlet profiles.

Prediction of the tangential velocity component further emphasizes the importance of correct specification of inlet boundary conditions on the ability of the Navier-Stokes code to predict the secondary flow field within the rotating duct. The Coriolis induced movement of fluid from the high pressure surface toward the low pressure surface along the walls at y/H = 1.0 and y/H = -1.0 was predicted in all three simulations. Although the tangential velocity magnitude was correctly predicted, a much more complicated tangential velocity field was predicted for Case A as shown in Figure 33b. (The dark blue color on the contour plots of data indicate that no measurement was made at these locations.) For Cases B and C, in which the computations were initialized with large secondary flow at x/D = 1.0, the agreement between the measurements and predictions is greatly improved in the center region of the duct. Near the convex surface, y/H = 1.0, the data and predictions both seem to indicate that the Coriolis induced movement of fluid is confined to a region from y/H = 0.8 to y/H = 1.0, where no measurements were made. In contrast, near the concave surface, measurements show that positive tangential velocity penetrates further into the central region of the duct. However, the predicted positive tangential velocity is confined to the region very near the wall. The wall integration simulations, Case C, would closely resemble measurements if the positive tangential velocity associated with the Coriolis induced vortex near the concave wall extended further into the duct.

Due to the pressure gradient in the turn, the concave surface becomes the high pressure surface and the convex surface is the low pressure surface. Flow field development, as flow enters the turn, is illustrated through tangential velocity predictions in Figure 34. At x/D = 15.6, positive tangential velocity at the upper and lower surfaces and the negative tangential velocity in the central region of the duct which are indicative of the Coriolis induced double vortex has undergone changes due to the new pressure field in the turn. The pressure gradient in the turn causes the low momentum fluid near the leading surface to move from the high pressure, concave, surface toward the low pressure, convex, surface. Since this fluid migration is in the same direction as the Coriolis induced vortex in the lower half of the duct, this vortex grows in size. In contrast, the vortex in the upper half of the duct has reduced greatly in size as indicated by the small region of positive tangential velocity at the intersection of z/Z = -1.0 and the convex surface.

PAGE 96 INTENTIONALLY BLANK

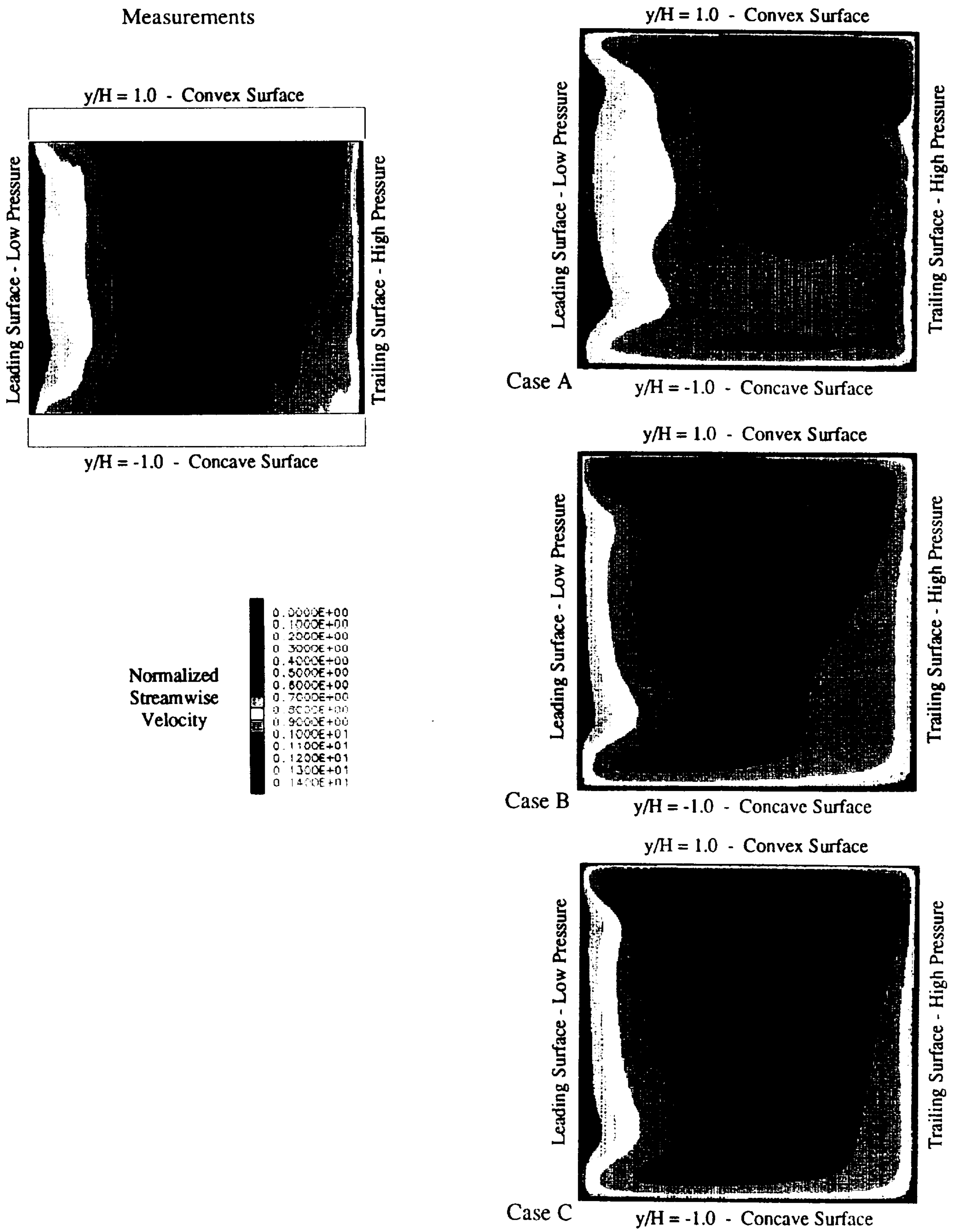

Figure 33a Streamwise velocity comparison between measurements and predictions at x/D = 15.0

PAGE 98 INTENTIONALLY BLANK

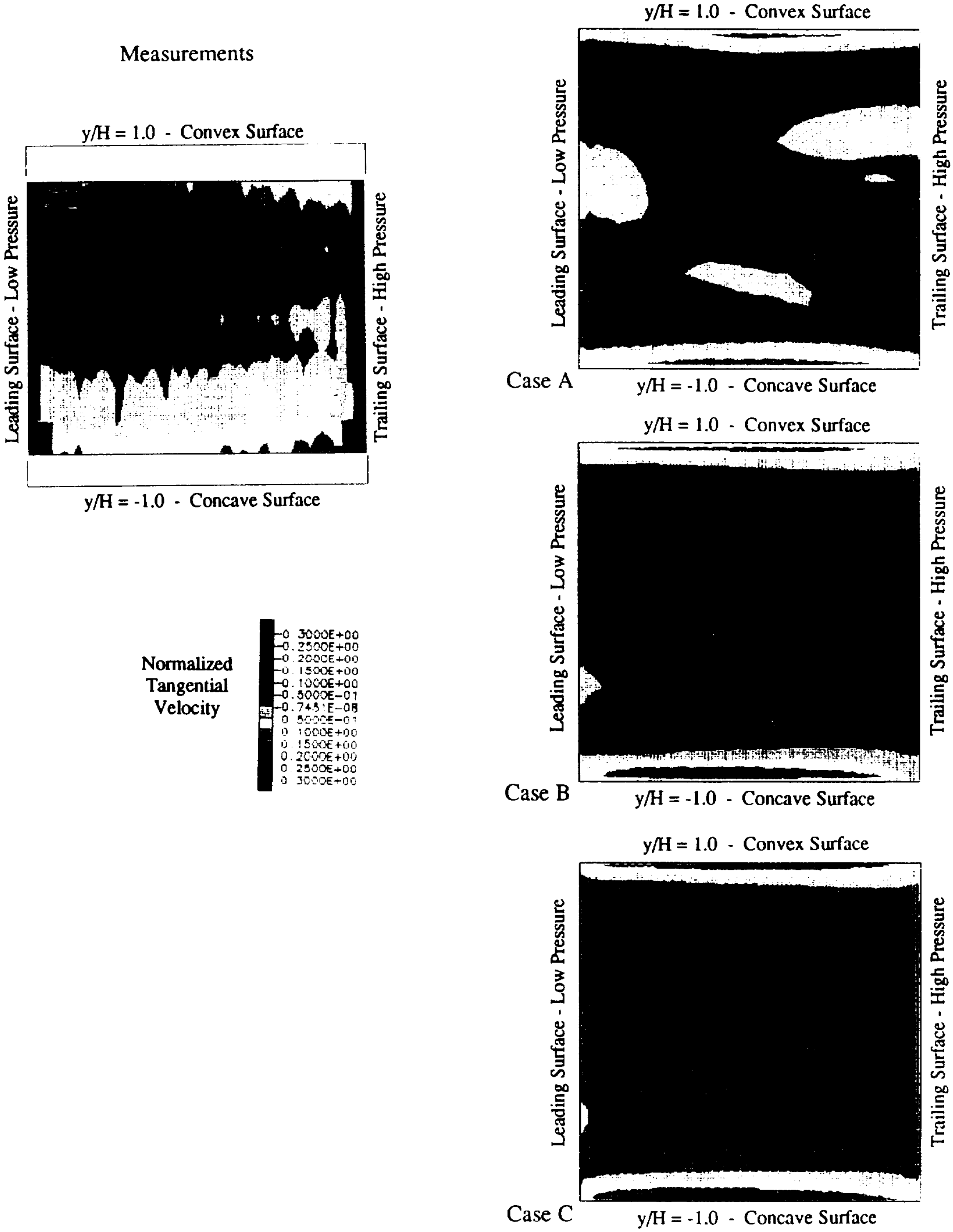

Figure 33b Tangential velocity comparison between measurements and predictions at x/D = 15.0

PRECEDING PAGE BLANK NOT FILMED

PAGE 100 INTENTIONALLY BLANK

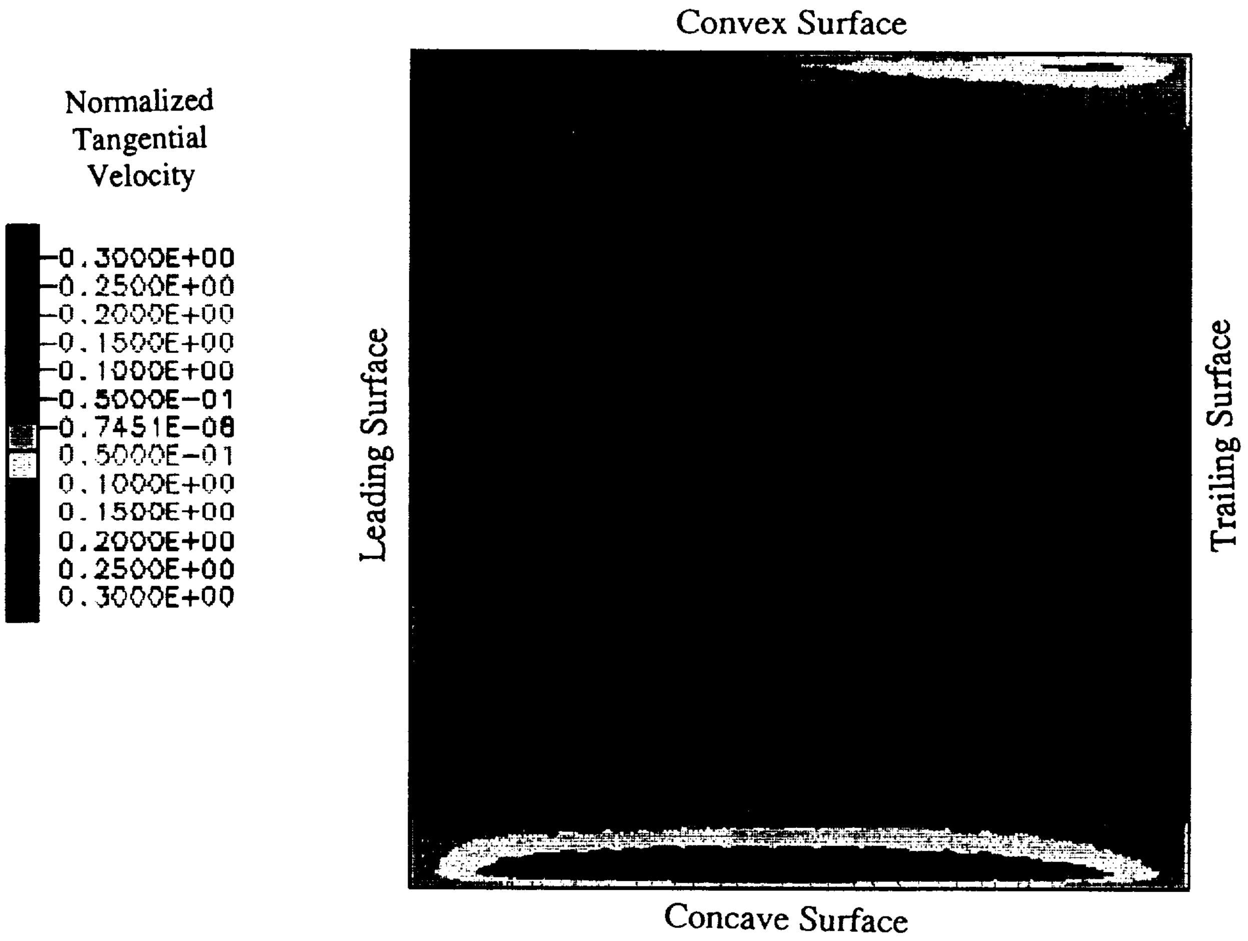

Figure 34 Tangential velocity contour at x/D = 15.6 shows flow field changes as the flow progresses through the first bend

The tangential and radial velocity components are compared with measurements at the 90° location of the first turn, x/D = 18.0 in Figures 35. These comparisons indicate that both velocity components show the same overall flow features as the measurements. The simulations tend to overpredict the tangential velocity component and underpredict the radial velocity component. At this location, the contour plots indicate that one large vortex is present. In this view the secondary flow moves counter clockwise with fluid moving from the trailing toward the leading side near the concave surface and returning to the trailing side near the convex surface. The strength of this secondary flow is much greater than the tangential velocity component measured upstream of the turn. Both the data and the predictions indicate that a small vortex exists in the corner between the concave and trailing surfaces. It is interesting to note that radial velocity component is underpredicted to a greater degree in Cases B and C, which was initialized with all known information at x/D = 1.0. However, the location of high velocity is more accurately predicted in Case C in which the two-layer wall integration formulation of the k-ε turbulence model was used. The secondary flow vectors for Case C are shown in Figure 36.

As flow exits the turn, x/D = 21.0, the measurements and the predictions of the streamwise velocity component show the same overall flow features, as shown in Figure 37a. Since the flow is now radially inward, the streamwise velocity is less than zero. The fluid with the highest velocity magnitude occurs near the corner between the concave and trailing surfaces. The data indicate that low velocity fluid is located near the trailing surface at y/H ≈ 0.0. This low velocity fluid is predicted in all three simulations. The differing inlet velocity profiles and differing near wall shear stress treatments in the turbulence model do not result in any significant changes to the predicted streamwise velocity at this location.

The tangential velocity component for fluid exiting the turn, x/D = 21.0, is compared with predictions in Figure 37b. Although, the magnitude of the tangential velocity component in all three simulations was approximately the same, flow structure differs significantly in Case A as compared with Cases B and C. This result indicates that although the streamwise velocity component was relatively insensitive to the inlet boundary condition at this location, upstream boundary conditions are important to correctly simulate secondary flow even downstream of a turn. With both the wall function and the two-layer wall integration simulation, Cases B and C, the tangential velocity indicates that a fairly high level of swirl is present which is similar to the measurements. However, with wall functions a stronger secondary flow was predicted than was measured. On the other hand, both the tangential velocity magnitude and the shape of the contours are extremely well predicted with the two-layer k-ε turbulence model, Case C. This result seems to indicate that in order to accurately predict the secondary flow in regions of large velocity gradients it is necessary to solve the governing equations to the wall and correctly specify inlet boundary conditions. Secondary flow velocity vectors emphasize the complex structure of the flow at this location, Figure 38. In addition, to the overall swirl which occurs near the duct walls, the predictions indicate the presence of five small vortices.

In the second passage of the duct, streamwise velocity is in radially inward and the Coriolis force acts in the opposite direction. Comparisons of the streamwise and tangential

PAGE 104 INTENTIONALLY BLANK

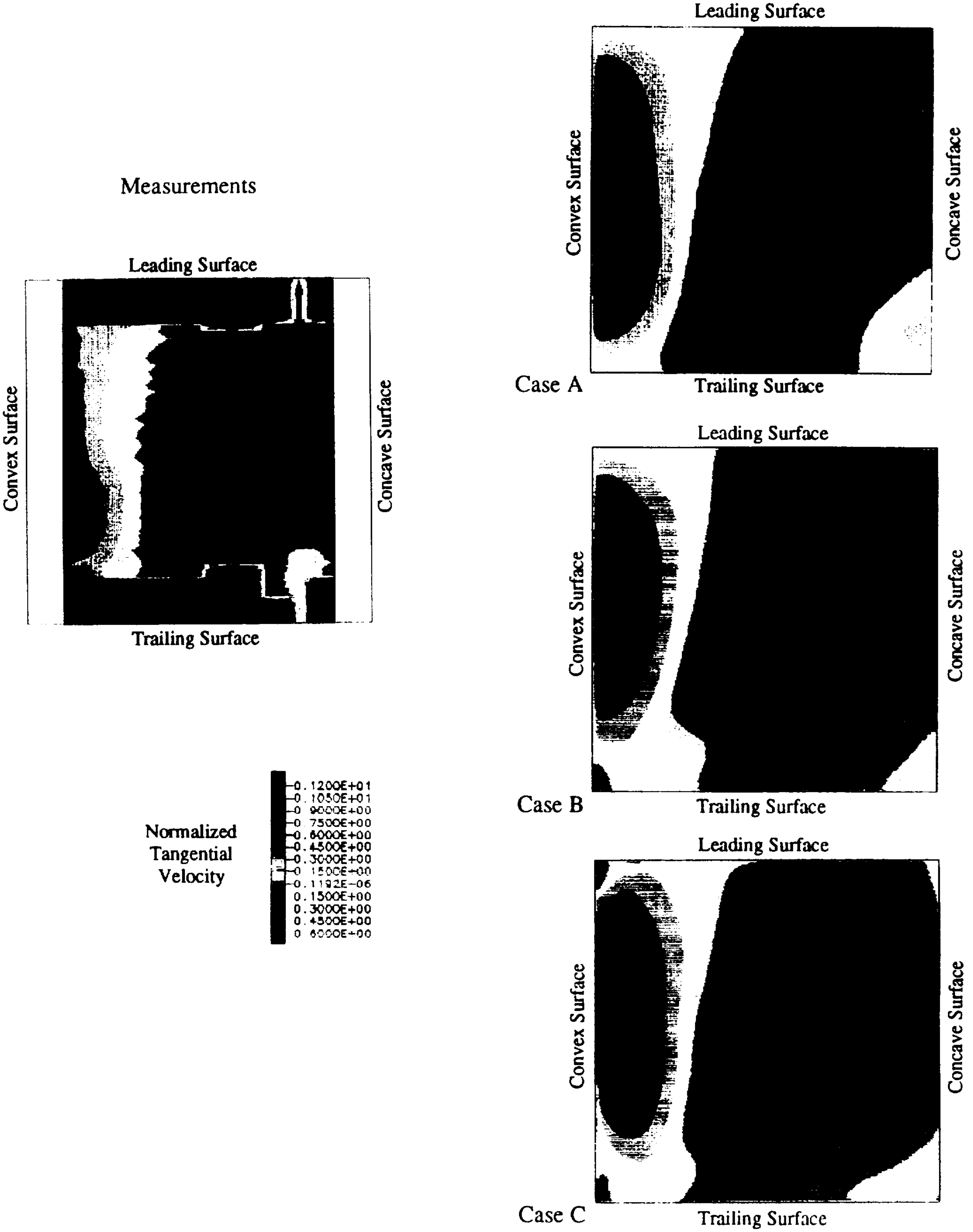

Figure 35a Tangential velocity comparison between measurements and predictions at x/D = 18.0

PRECEDING PAGE BLANK NOT FILMED

PAGE 106 INTENTIONALLY BLANK

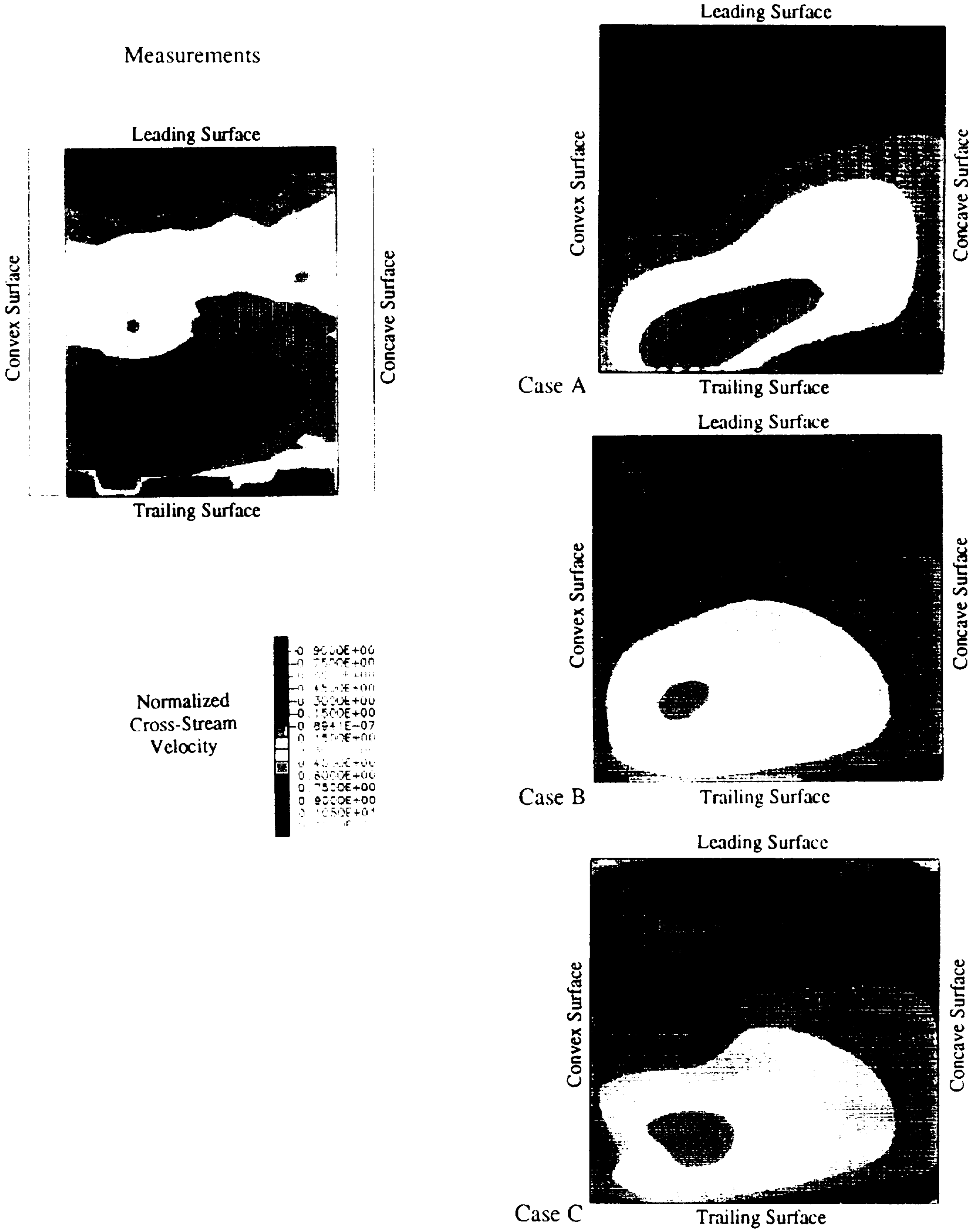

Figure 35b Cross-stream velocity comparison between measurements and predictions at x/D = 18.0

PAGE 108 INTENTIONALLY BLANK

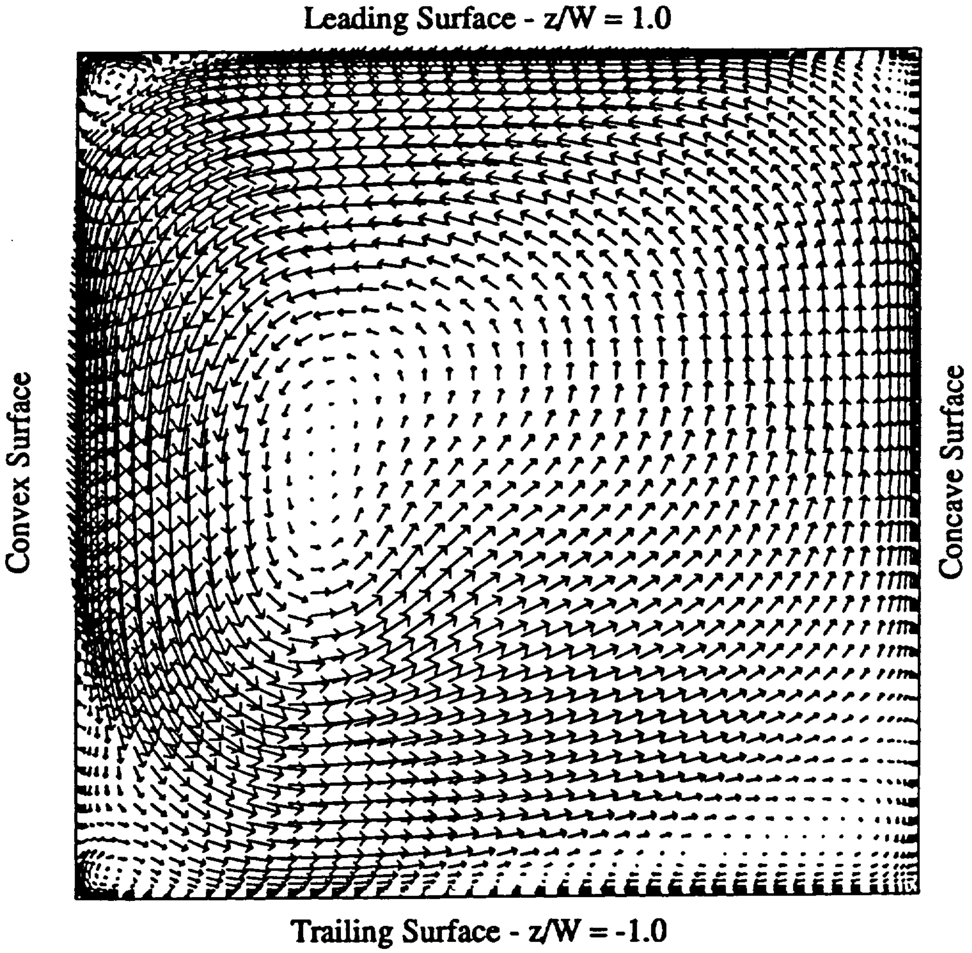

Figure 36 Streaklines at x/D = 18.0 for case C show the one large vortex which is formed at the 90° location of the first turn

PAGE 110 INTENTIONALLY BLANK

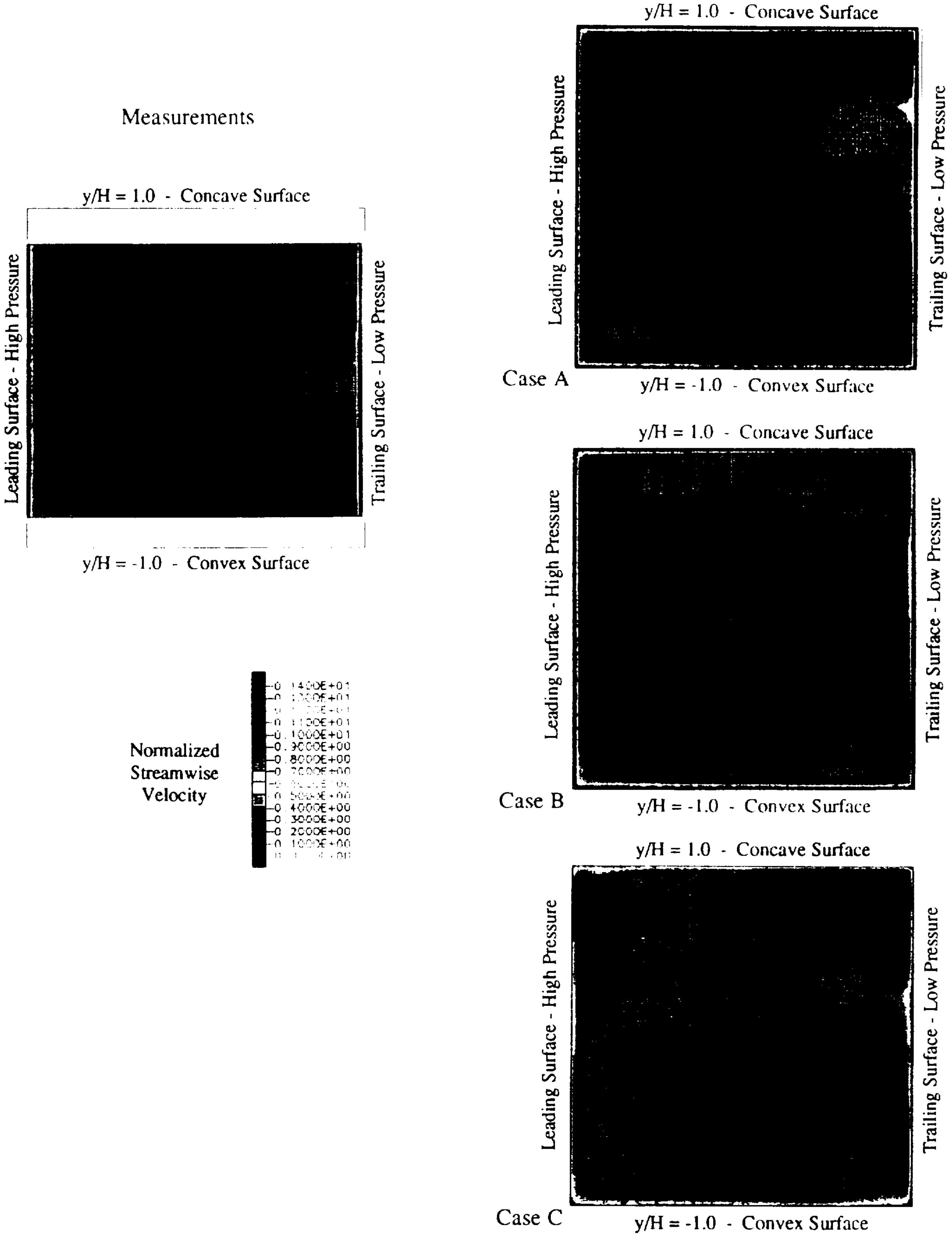

Figure 37a Streamwise velocity comparison between measurements and predictions at x/D = 21.0

PRECEDING PAGE BLANK NOT FILMED

PAGE 112 INTENTIONALLY BLANK

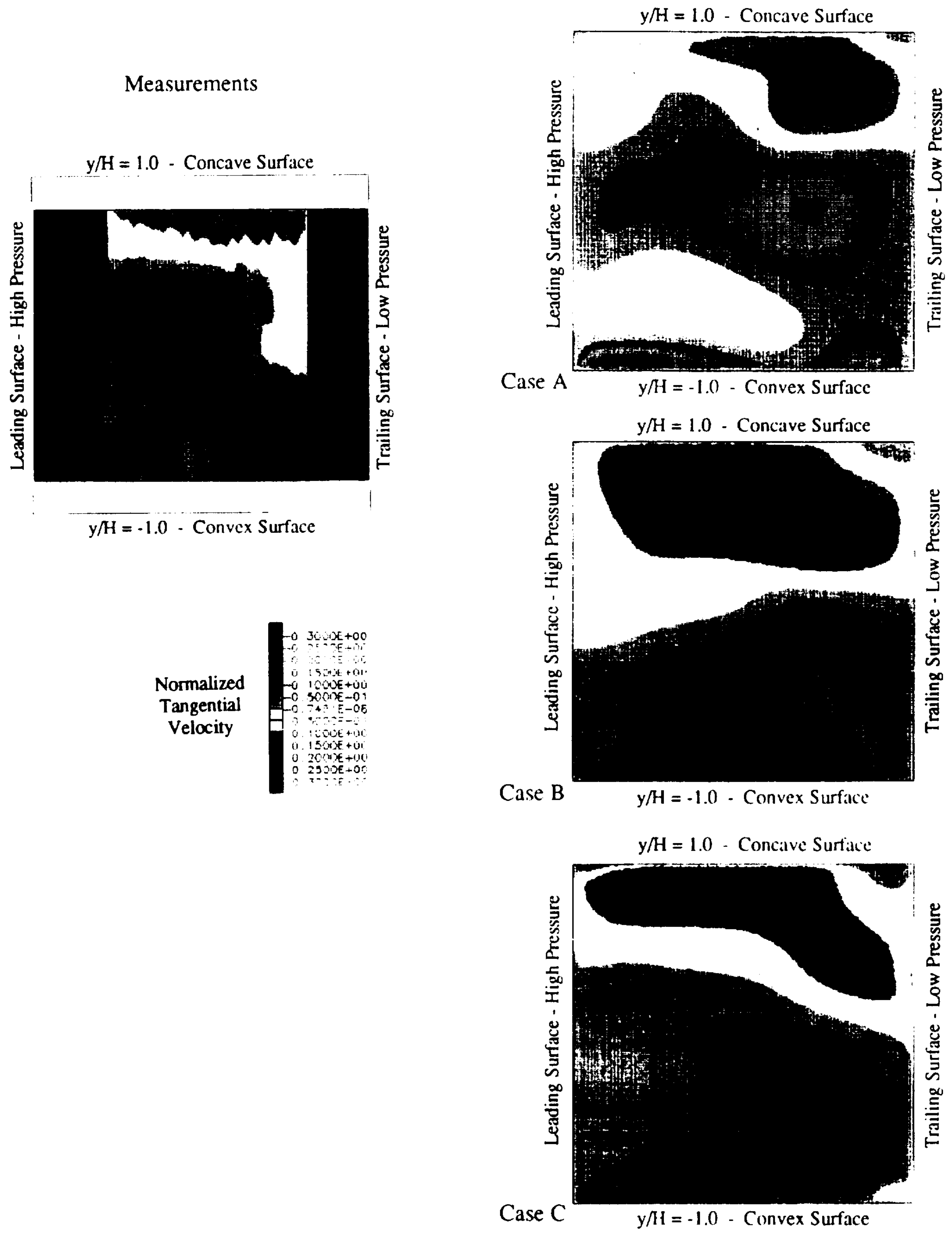

Figure 37b Tangential velocity comparison between measurements and predictions at x/D = 21.0

PRECEDING PAGE BLANK NOT FILMED

PAGE 114 INTENTIONALLY BLANK

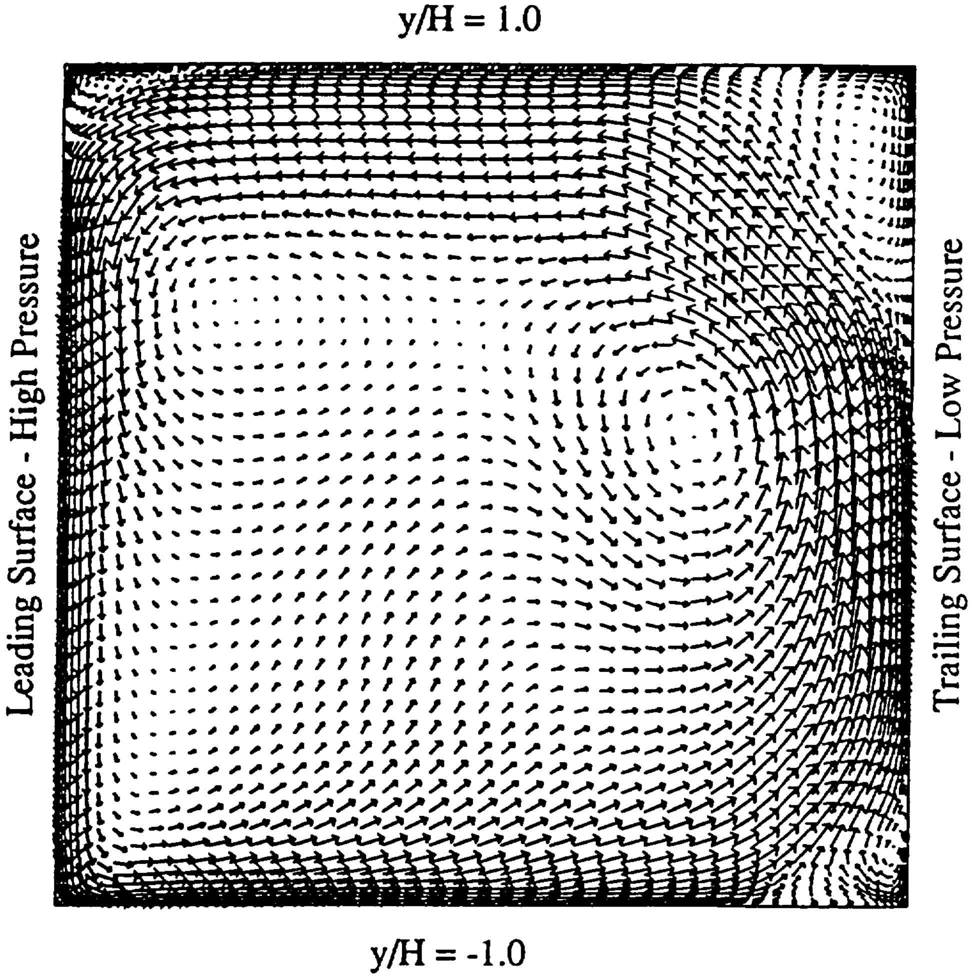

Figure 38 Streaklines of the secondary flow at the exit of the first bend highlight the complex flow structure which develops within the turn

PAGE 116 INTENTIONALLY BLANK

velocity contours at x/D = 25.0 are made in Figure 39. Experimental measurements indicate that the flow field has undergone some fairly significant changes in only four diameters downstream of the turn. The measurements of the streamwise velocity component and the wall integration predictions, Case C, agree to the greatest extent. However, the predictions seem to show slower transition to the fully developed flow field. In both Cases A and B, fairly low streamwise velocities are predicted near the wall located at y/H = 1.0 which is inconsistent with the measurements. The measurements of the tangential velocity component indicate a rather sudden change in the secondary flow structure. At this location, measurements show the classical Coriolis induced vortex. Since the Coriolis force acts in the opposite direction with radially inward flow, low momentum fluid migrates from the leading, high pressure, surface to the trailing, low pressure, surface along the upper and lower walls. The predictions show that the region of positive tangential velocity at the upper wall which was present at x/D = 21.0 is migrating toward the center of the duct Figure 39b.

Good agreement between the data and the two-layer wall integration predictions in the turn maybe due to the fact that the flow in this region may be a pressure dominated flow field. On the other hand, the flow field development downstream of the turn may be more dominated by mixing which may not be as well predicted with the current turbulence models. In summary, the importance of accurately defining inlet boundary conditions in simulations of rotating ducts has been demonstrated. The two-layer wall integration k-ε turbulence model appears to more accurately predict the flow field in the regions with high velocity gradients.

5.2.2 Heat Transfer Simulations

Since the computations were conducted at Reynolds and Rotation numbers that match the conditions of Wagner et al (1991), by also matching the Prandtl number, it is possible to relatively quickly obtain a solution to the energy equation by using the converged flow field as input. Therefore, an assessment of the ability of the Navier-Stokes code to predict heat transfer could be made. It is important to note that the effect of the centrifugal buoyancy forces are not predicted since the computations were performed for incompressible flow.

Nusselt number contours of the leading and trailing surfaces for all three simulations are plotted in Figure 40 with the same scales. Regions of high heat transfer occur in the turns and on the high pressure surfaces; the trailing surface in the passages with radially outward flow and the leading surface in the passages with radially inward flow. The heat transfer on the trailing surface of the second turn is similar to the leading surface of the third turn. The Coriolis force causes low pressure prior to the turn and high pressure beyond the turn for both of these surfaces. Likewise, the distinctive heat transfer contours are similar between the leading surface of the second turn and the trailing surface of the third turn.

Comparisons of the predicted heat transfer for the three simulations yields some interesting observations. Due to the differing inlet velocity profiles for the two wall function

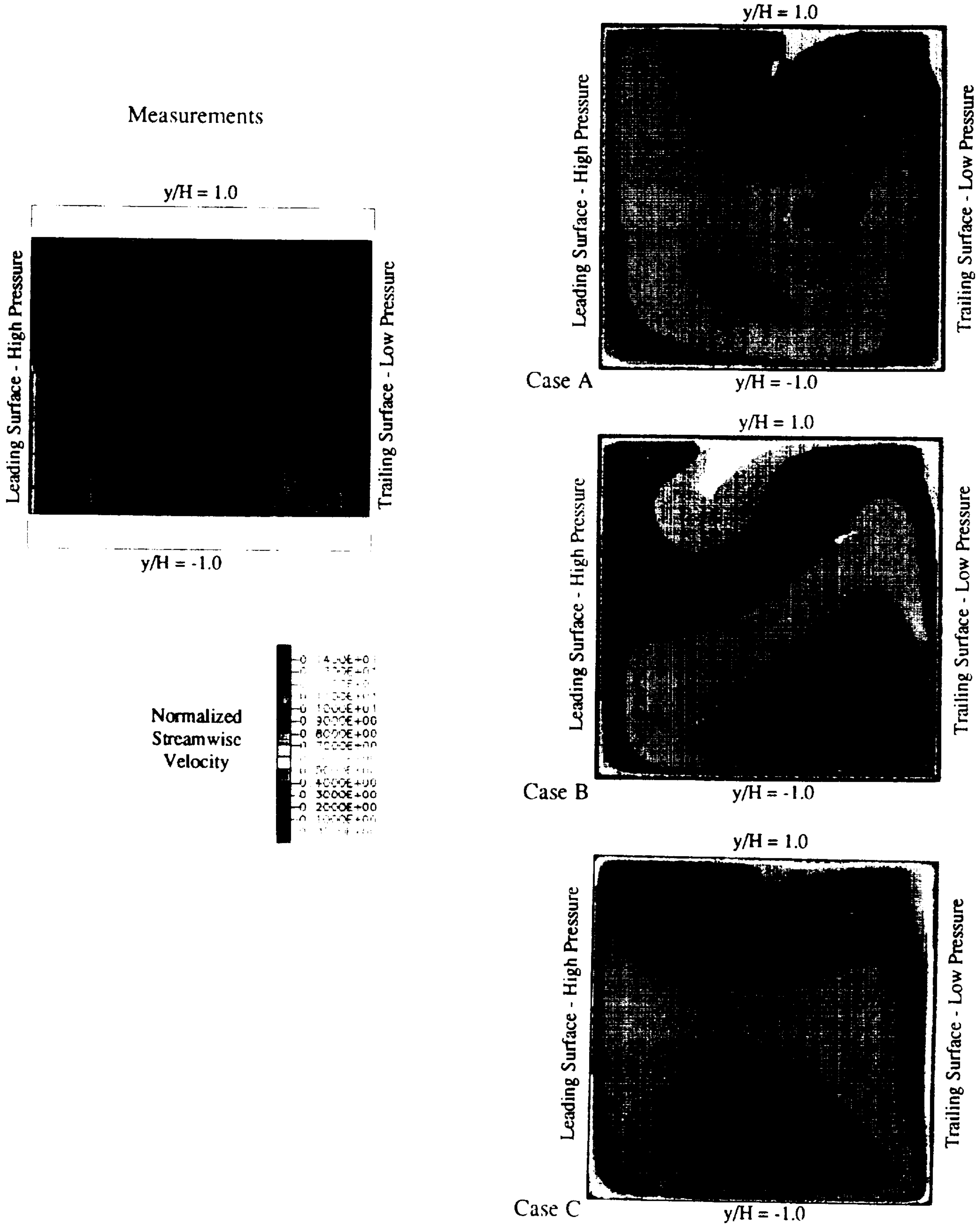

Figure 39a Streamwise velocity comparison between measurements and predictions at x/D = 25.0

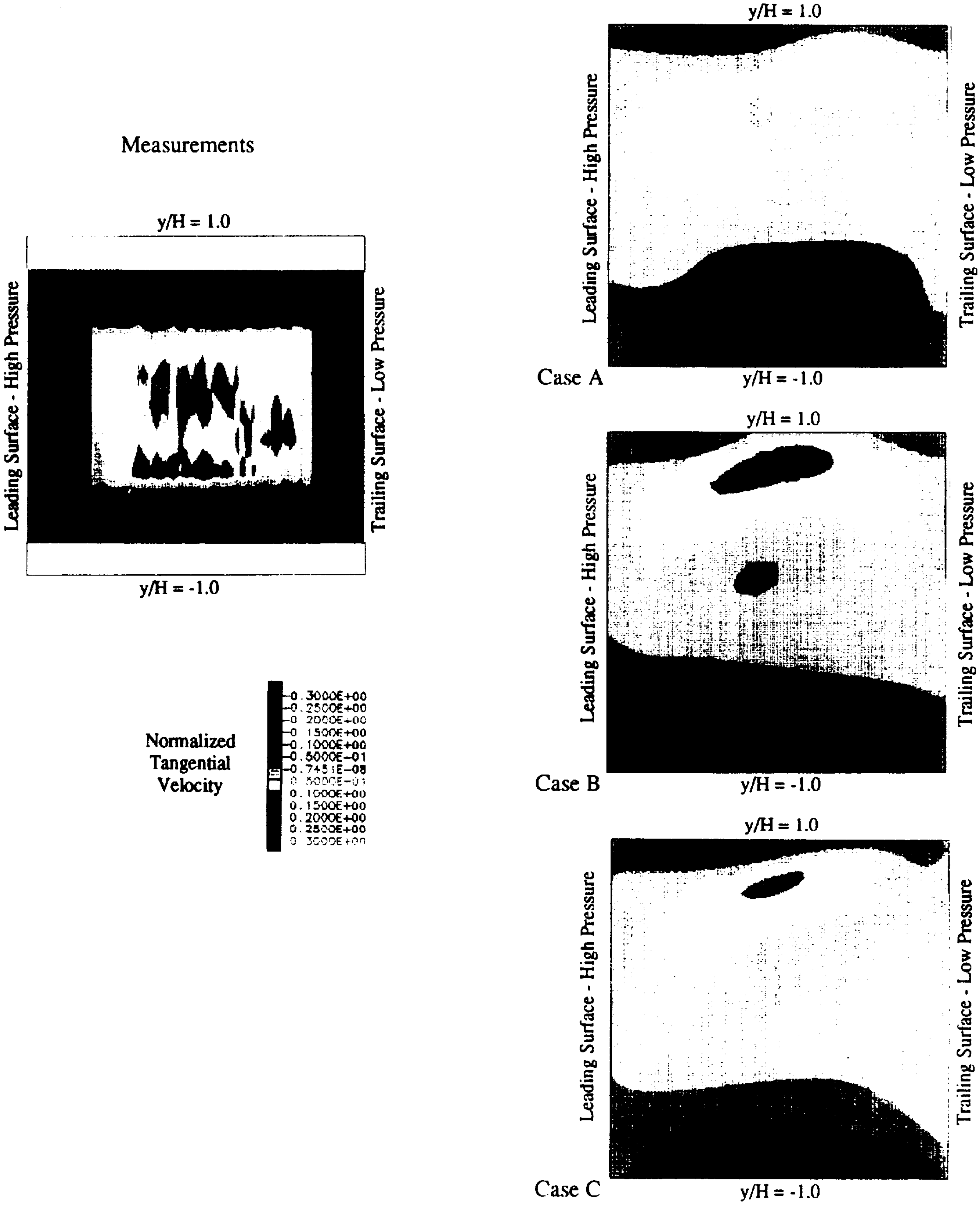

Figure 39b Tangential velocity comparison between measurements and predictions at x/D = 25.0

120

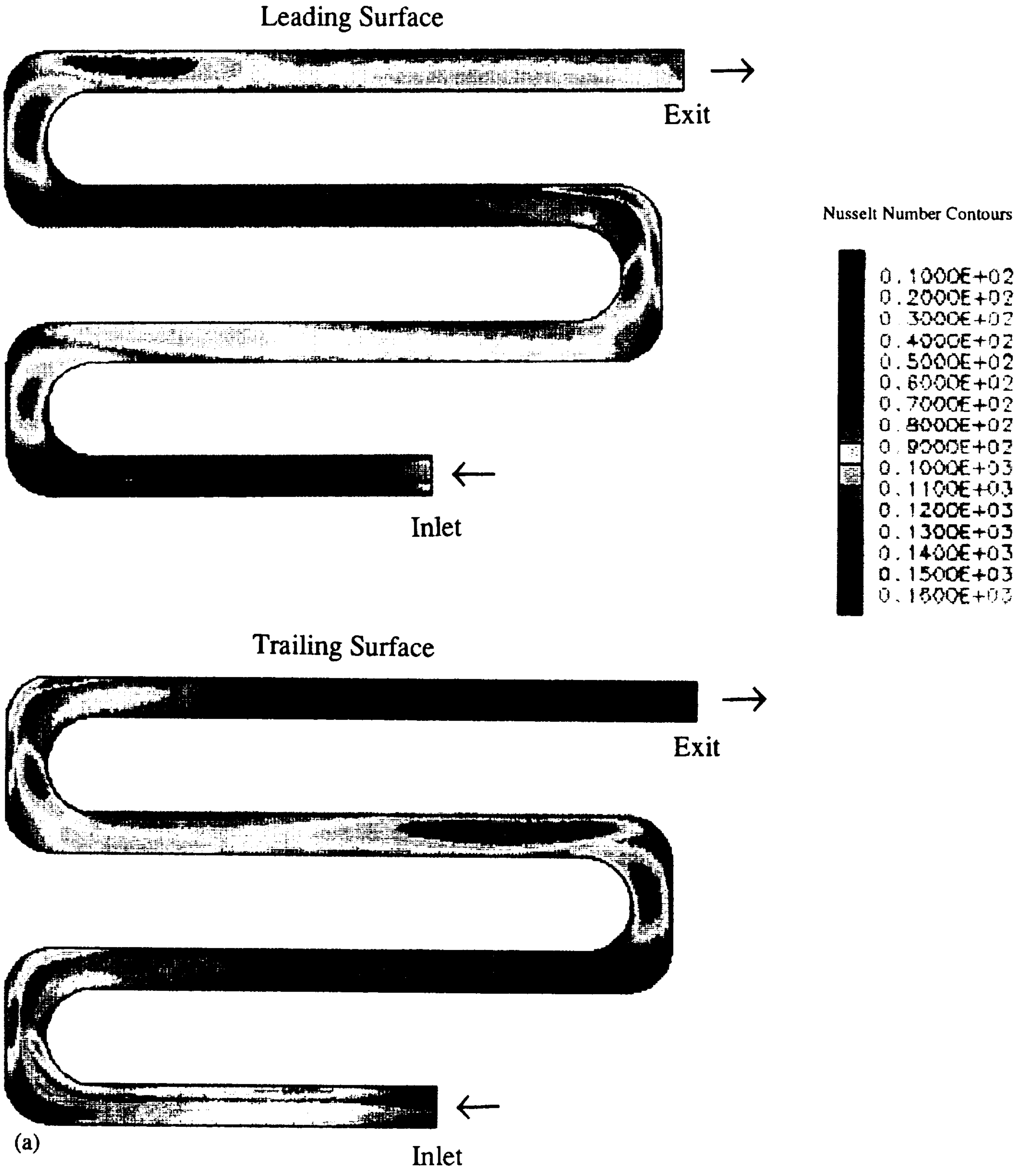

Figure 40 Nusselt number contours show large variations in heat transfer on the leading and trailing surfaces for all incompressible simulations (a) case A

PAGE 122 INTENTIONALLY BLANK

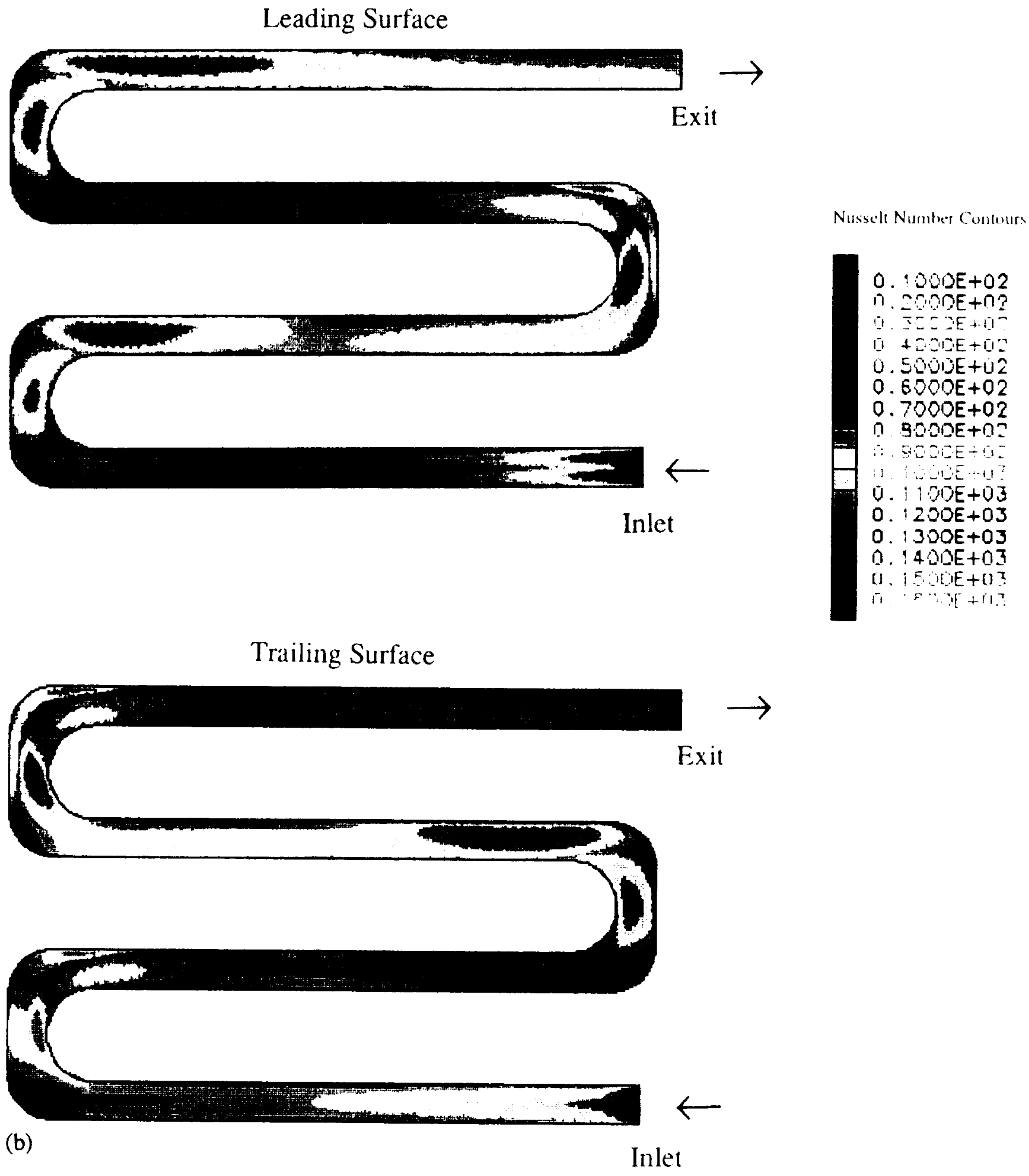

Figure 40 Continued. (b) case B.

PAGE 124 INTENTIONALLY BLANK

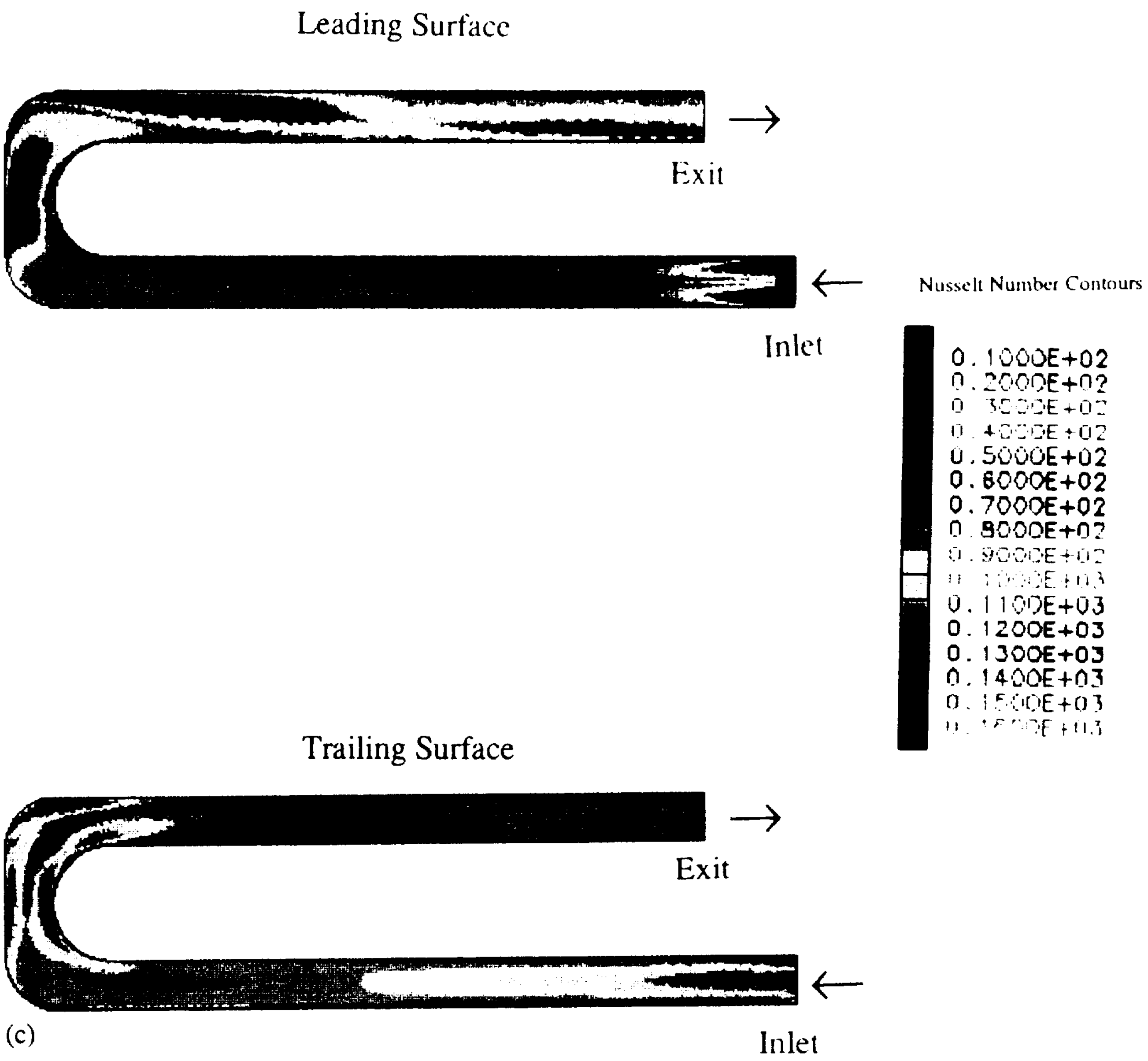

Figure 40 Concluded. (c) case C.

PRECEDING PAGE BLANK NOT FILMED
PAGE 126 INTENTIONALLY BLANK

simulations, Cases A and B, small differences exist in the predicted heat transfer on the leading surface of the first passage. As the flow exits the turn, $x/D = 21$, higher heat transfer is predicted for Case B. Although the contours show very similar gradients for the two wall function cases in the second and third turns, the peak heat transfer differs by approximately 10%. On the trailing surface, comparison between the two wall function cases yield similar results. Beyond the first turn, Nusselt number gradients for the two simulations are similar with some subtle difference is the heat transfer magnitude.

Comparison of Cases B and C, show that larger gradients are predicted with the two-layer wall integration simulation. Enlargements of the Nusselt number contours are shown in Figures 41 with an expanded scale. These figures further emphasize that larger gradients in heat transfer are predicted with the two-layer wall integration simulation, Case C. The velocity vectors at the 90° location of the first turn, Figure 36, provide insight on the impact of the predicted flow field on the heat transfer at this location. On the trailing surface, the main vortex interacts with the corner vortex. This interaction appears to locally suppress the heat transfer in the center of the duct. This phenomenon is clearly shown in the wall integration simulation. However, flow moves from the concave to the convex surface along the entire leading surface resulting in a more uniform heat transfer distribution across the width of the duct. Therefore, the predicted heat transfer is consistent with the flow field. Since overall cooling of turbine airfoils is adequate but local hot spots occur, accurate prediction of these local heat transfer gradients is extremely important to airfoil designers.

The Nusselt number contours on the leading and trailing surfaces were span-averaged and compared with data from Wagner et al (1991). The Nusselt number was non-dimensionalized with the correlation value for fully developed turbulent flow in stationary tube with constant wall temperature, $Nu_{\infty} = 0.021\, Pr^{0.5}\, Re^{0.8} = 57$ (Kays and Crawford, 1980). The high and low pressure surfaces as well as the turn locations are noted in the figures for reference. The Wagner et al (1991) data points are represented by oval symbols; the length of the symbol corresponds to the length of the copper segments in the model and the height corresponds to the uncertainty of the measurement.

In order to isolate the effect of inlet boundary conditions on predicted heat transfer, the span average Nusselt number for Cases A and B are compared with Wagner et al (1991) data in Figure 42. The first leg of the trailing surface shows some fairly significant differences in heat transfer due to the differing inlet velocity profiles. Span-averaged heat transfer plots as well as the contour plots show that the inlet velocity profile influences the predicted heat transfer far downstream; in the second and third passages. Predicted span-average heat transfer collapse only in the fourth passage.

In Figure 43, the predicted span-average Nusselt numbers are compared for Cases B and C. The simulation with the two-layer wall integration turbulence model consistently predicts lower heat transfer on the low pressure surfaces; the leading surface with radially outward flow and the trailing surface with radially inward flow. On the other hand, the span-average Nusselt numbers on the high pressure surface and the first leg are essentially the same. The

PRECEDING PAGE BLANK NOT FILMED PAGE 128 INTENTIONALLY BLANK

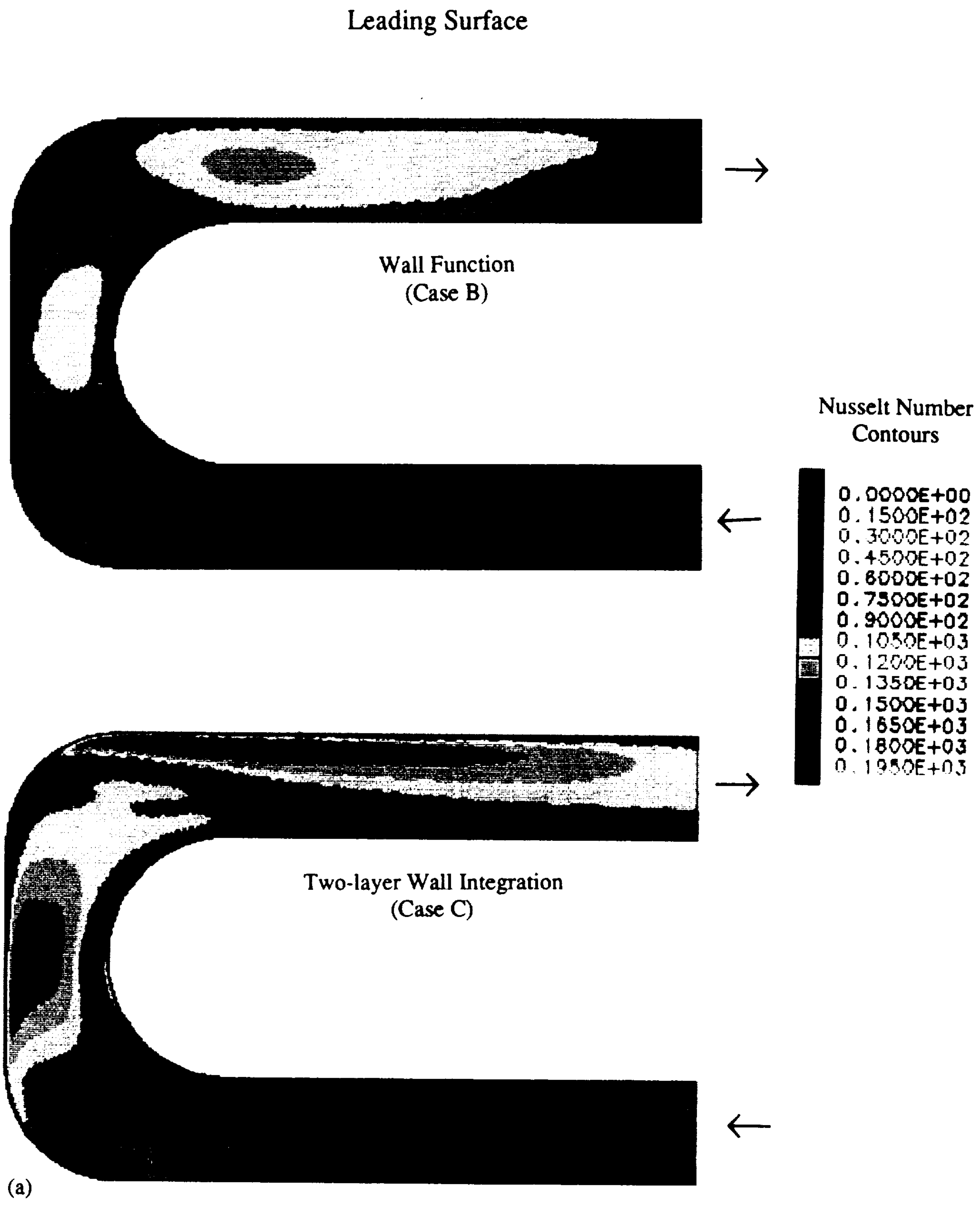

Figure 41 Detailed comparison of heat transfer in the first turn emphasize that high local heat transfer and larger heat transfer gradients are predicted with the two-layer wall integration simulation as compared with the wall function simulation on (a) the leading surface

PRECEDING PAGE BLANK NOT FILMED

PAGE 130 INTENTIONALLY BLANK

Trailing Surface

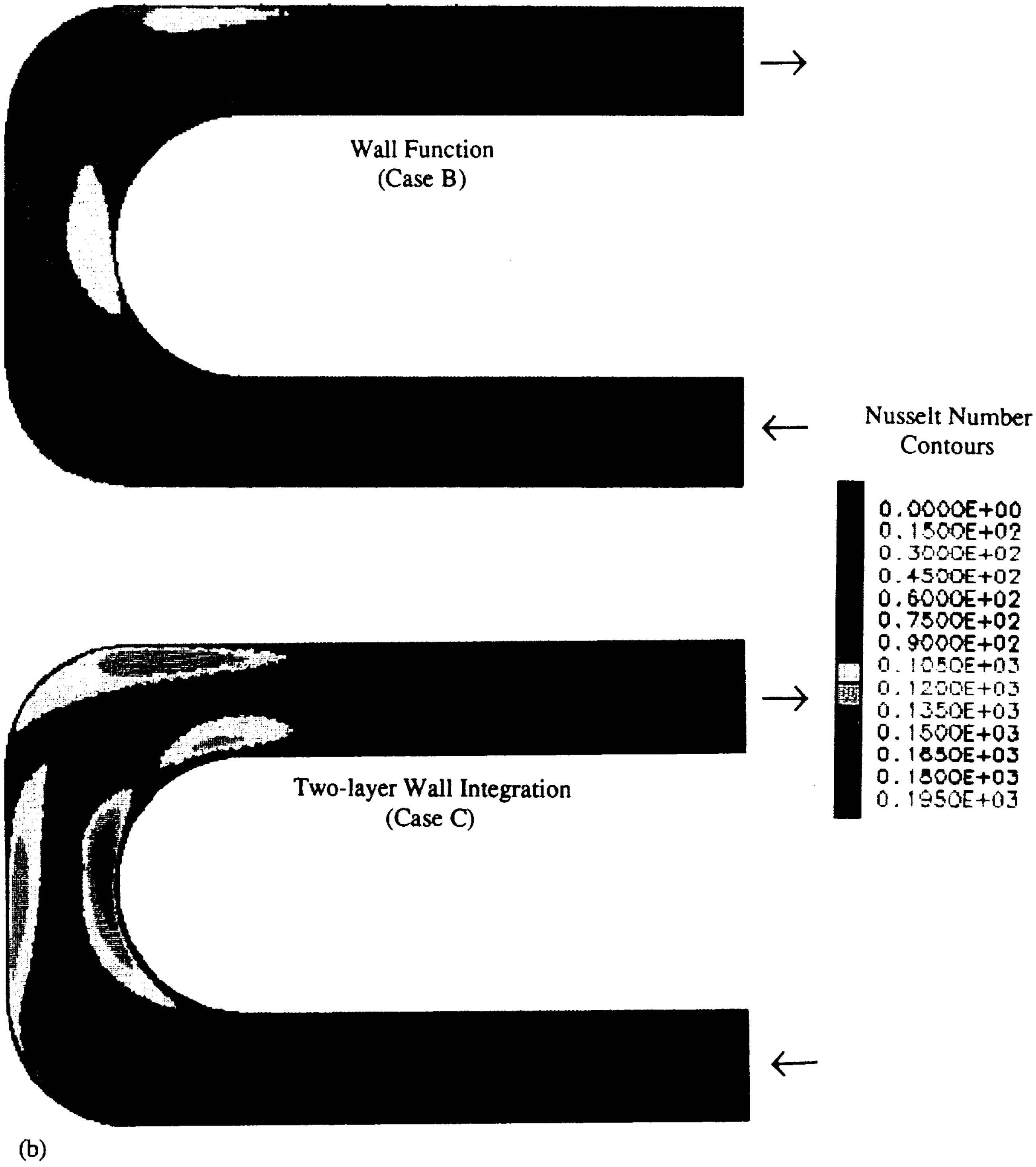

Figure 41 Concluded. (b) trailing surface.

132

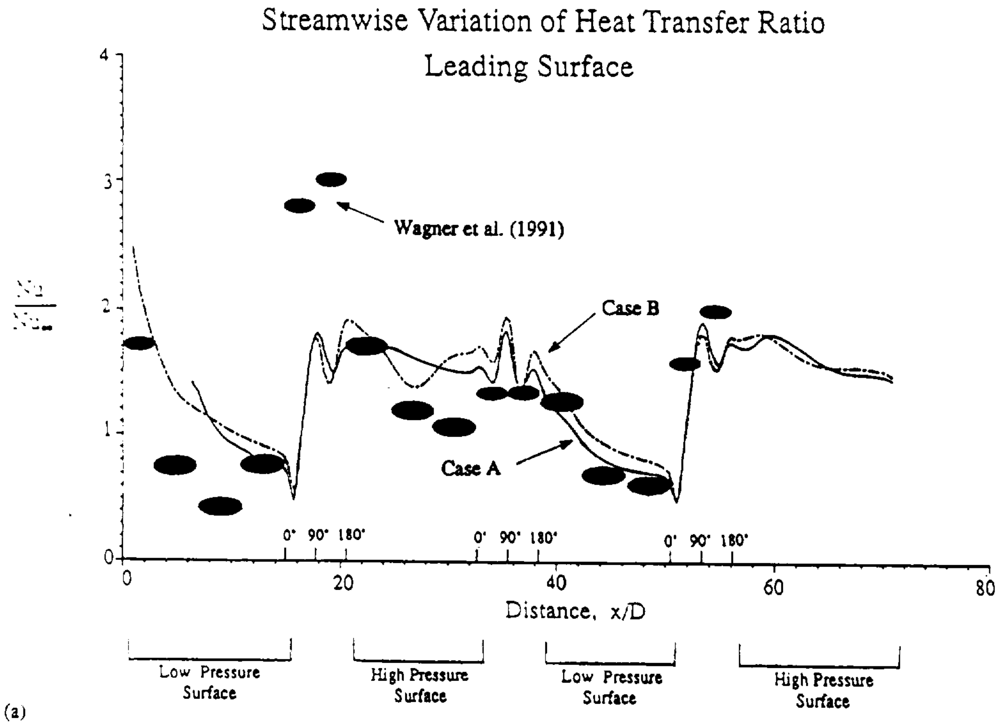

Figure 42 Comparison of span-average heat transfer for the wall function simulations (case A and B) show that the inlet boundary condition influences the predicted heat transfer far downstream on the (a) leading surface

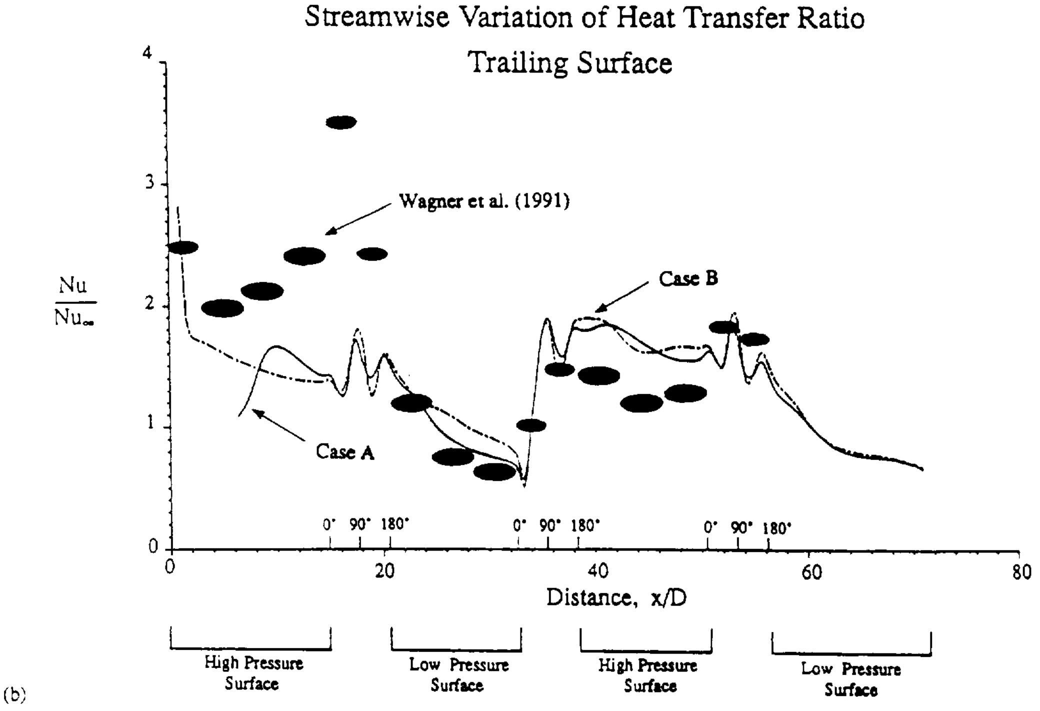

Figure 42 Concluded. (b) trailing surface.

PAGE 134 INTENTIONALLY BLANK

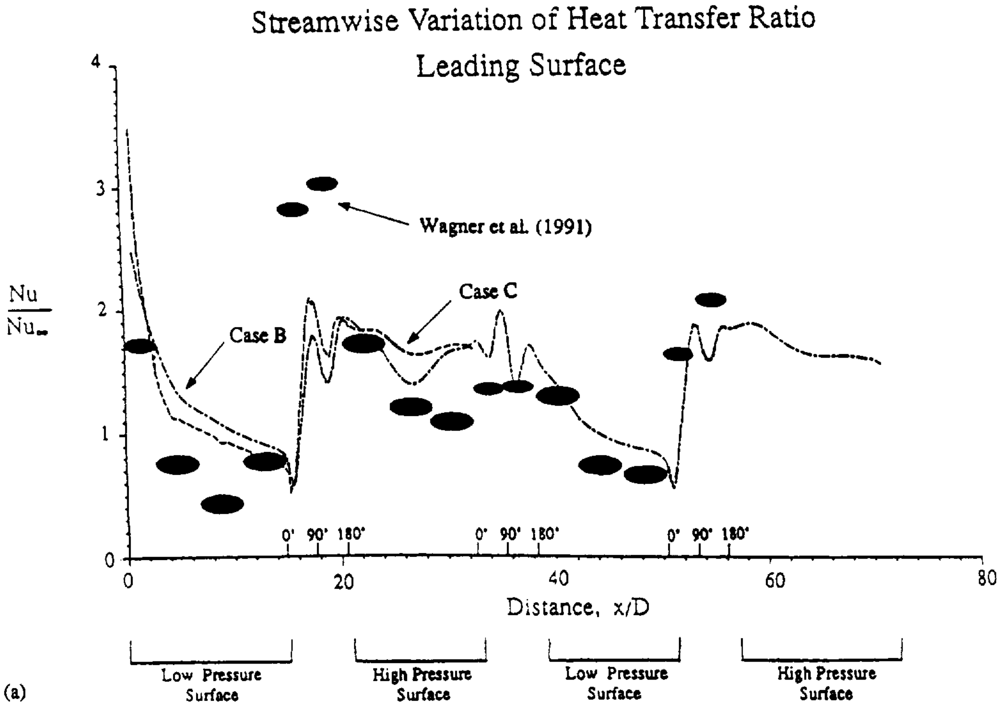

Figure 43 Comparison of the span-averaged heat transfer for Cases B and C with data of Wagner et al (1991) on (a) leading surface

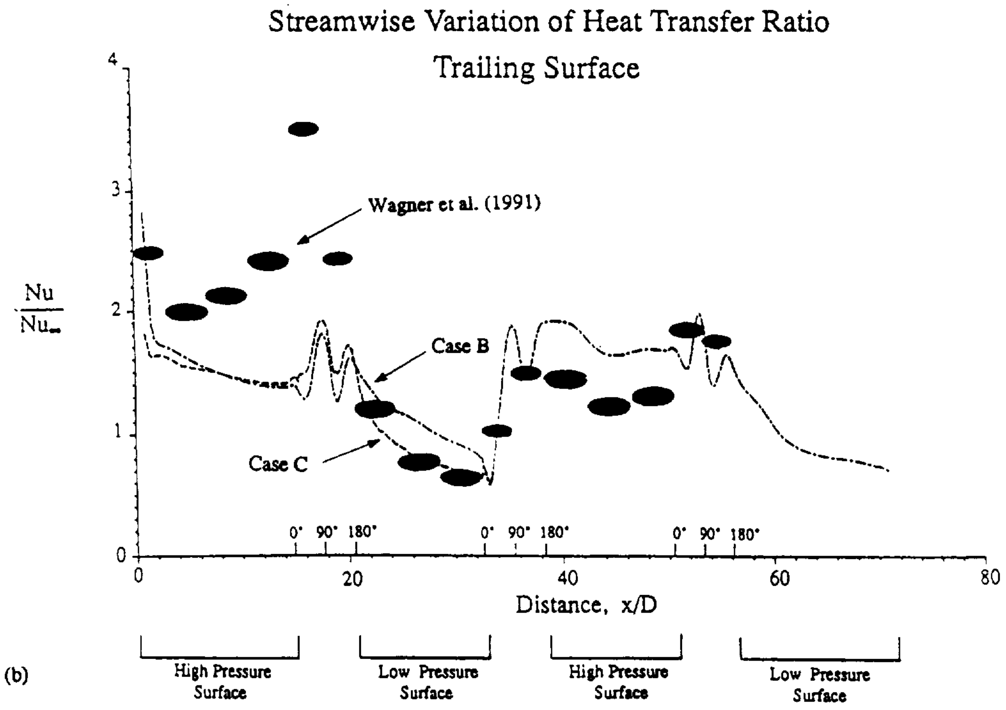

Figure 43 Concluded. (b) trailing surface.

two-layer wall integration case predicts an increase in heat transfer of approximately 15% relative to Case B on the high pressure surface of the second passage.

On the trailing surface of the first passage, the wall integration simulation, Case C, predicts an increase in heat transfer of approximately 40% relative to the stationary fully developed correlation value while the data of Wagner et al (1991) indicate an increase of 100%. (As discussed in Section 5.1, an increase in heat transfer of 15% can be attributed to the increase in the streamwise velocity near the trailing surface.) On the other hand, the simulation is overpredicting heat transfer by approximately 30% on the leading, low pressure surface. Since the buoyancy force and the Coriolis force reinforce one another for radially outward flow, inclusion of the buoyancy force will improve the prediction on both the leading and trailing surfaces of the first passage where the temperature differences (and buoyancy effects) are large.

In the second passage, the effect of buoyancy is not expected to be as large as in the first passage and Figure 43 shows improved agreements between the data of Wagner et al (1991) and the wall integration predictions, Case C. In the first turn, the incompressible flow simulations underpredict the measured heat transfer by 50%. Therefore, the effect of buoyancy may be important in the first turn as well as the first passage.

5.3. The effect of Reynolds number

In addition to the base case experiments discussed in Section 5.1, measurements were made to assess the effect of Reynolds and Rotation numbers. Figures 44a to 46b show the streamwise and tangential velocities obtained along the first passage at x/D = 1.0, 6.4 and 15.0 at Re = 12,500 and 25,000. In all three axial locations, the streamwise velocity profiles obtained at Re = 12,500 ((v) & (vi) of Figures 44a, 45a and 46a) are more parabolic than those at Re = 25,000 ((i) & (ii) of the same figures). This is expected because the boundary layer at a lower Reynolds number is thicker.

Figures 44a(i) and (v) show that, for Ro = 0.24, the flow is skewed toward the low pressure (leading) side at x/D = 1.0 for Re = 12,500 and 25,000. The plenum effect observed in the streamwise velocities obtained with Re = 25,000 and Ro = 0.24 (described in Section 5.1) is also evident in those obtained with Re = 12,500 and Ro = 0.24, Figure 44a(v). Plug-type profiles are evident at the entrance in the center of the passage ($-0.6 < y/H < 0.6$), Figures 44a(ii) & (vi), for Ro = 0.12 because the effect of rotation is small. However, the entrance effect is noticeable near the upper and lower wall ($y/H = \pm 0.8$, Figure 44a(ii) & (iv)). Figures 44b(v) & (vi) show that, at Ro = 0.12, the differences between the tangential velocity obtained Re = 25,000 and 12,500 are small. Increasing Ro to 0.24, Figures 44b(i) & (ii), has no significant effect on the differences between the tangential velocity. Thus, for Ro < 0.24, the effect of Reynolds number on the tangential velocity at the inlet is small for Re in the range 12,500 to 25,000.

Comparisons of the streamwise velocity profiles ((i), (ii), (v) and (vi) of Figure 44a with those of Figure 45a) show skewness to reduce between x/D = 6.4 and 1.0 for all

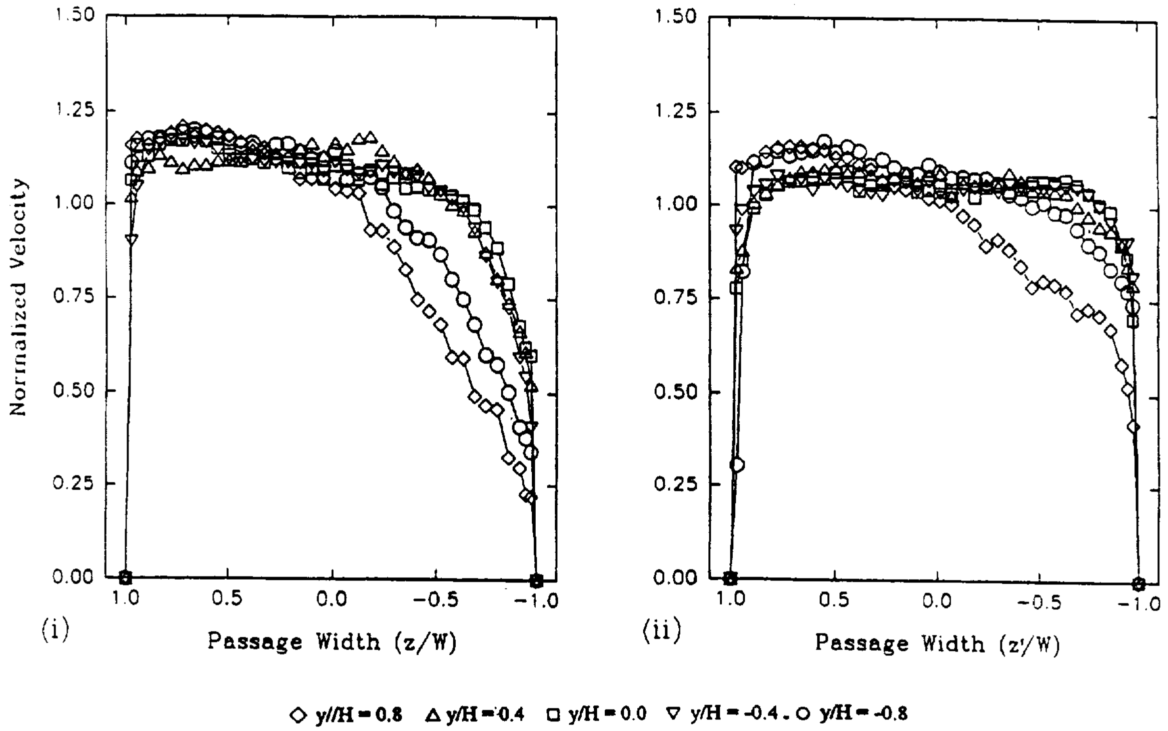

Figure 44a Comparisons of streamwise mean velocities at x/D = 1.0. (i) Re = 25,000 and Ro = 0.24. (ii) Re = 25,000 and Ro = 0.12.

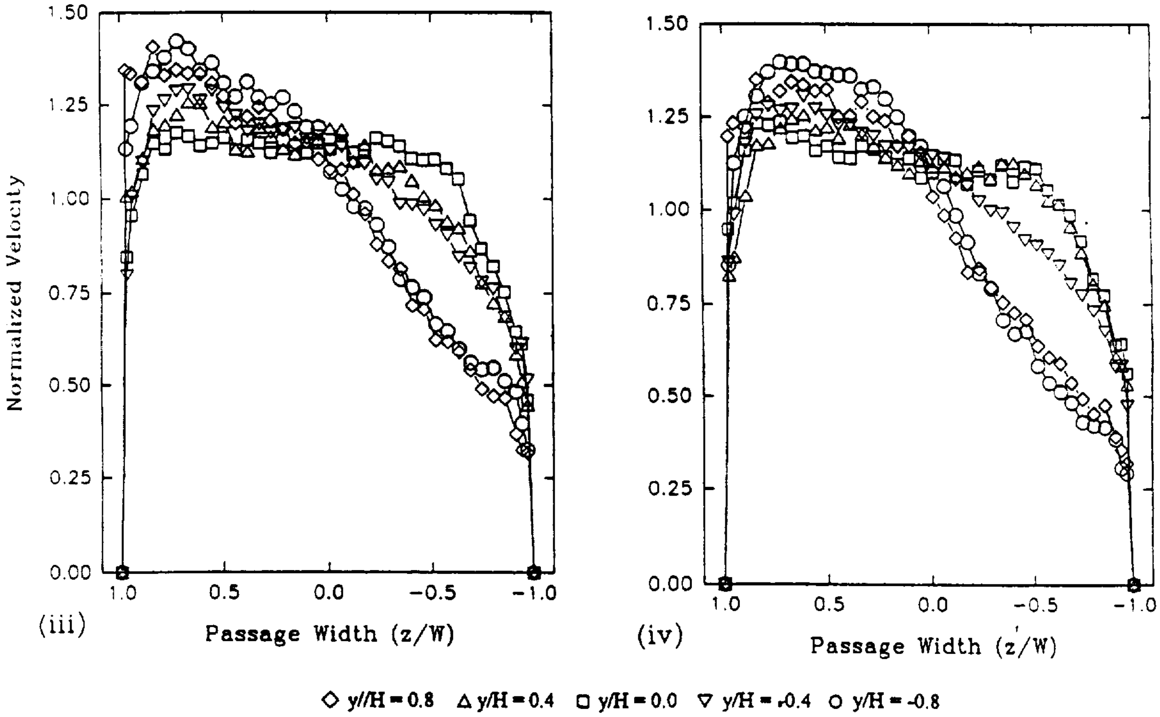

Figure 44a Continued. (iii) Re = 12,500 and Ro = 0.48. (iv) Re = 12,500 and Ro = 0.36.

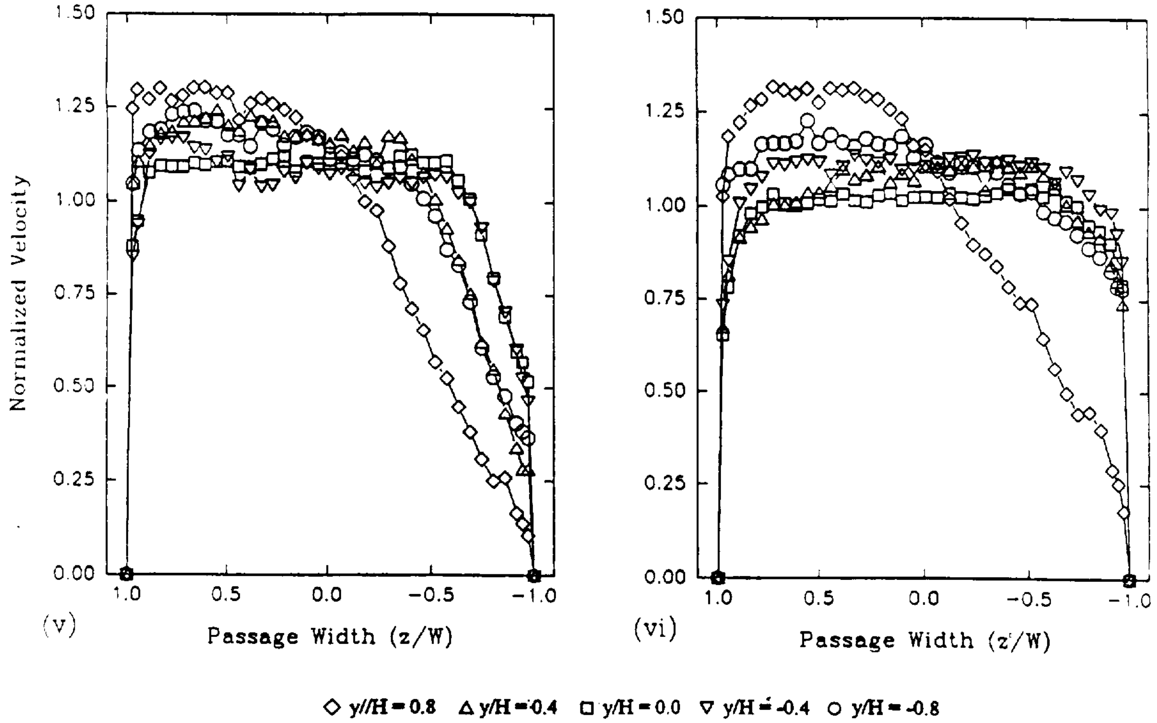

Figure 44a Concluded. (v) Re = 12,500 and Ro = 0.24. (vi) Re = 12,500 and Ro = 0.12.

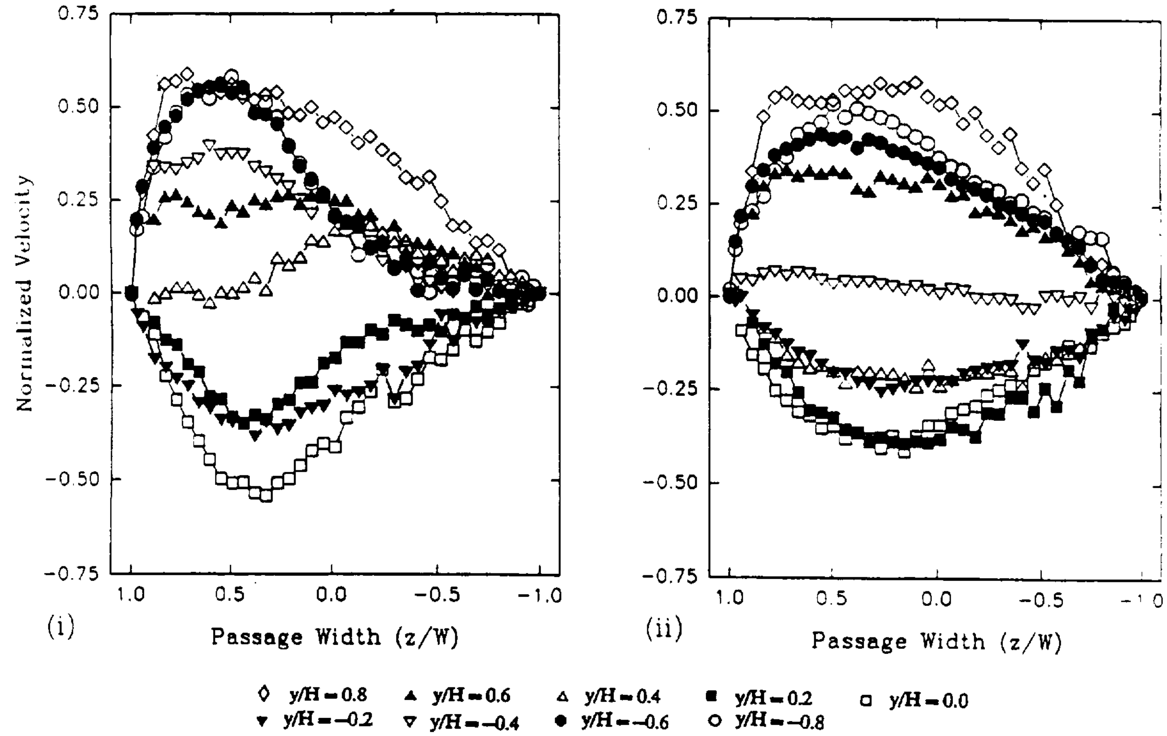

Figure 44b Comparisons of tangential mean velocities at x/D = 1.0. (i) Re = 25,000 and Ro = 0.24. (ii) Re = 25,000 and Ro = 0.12.

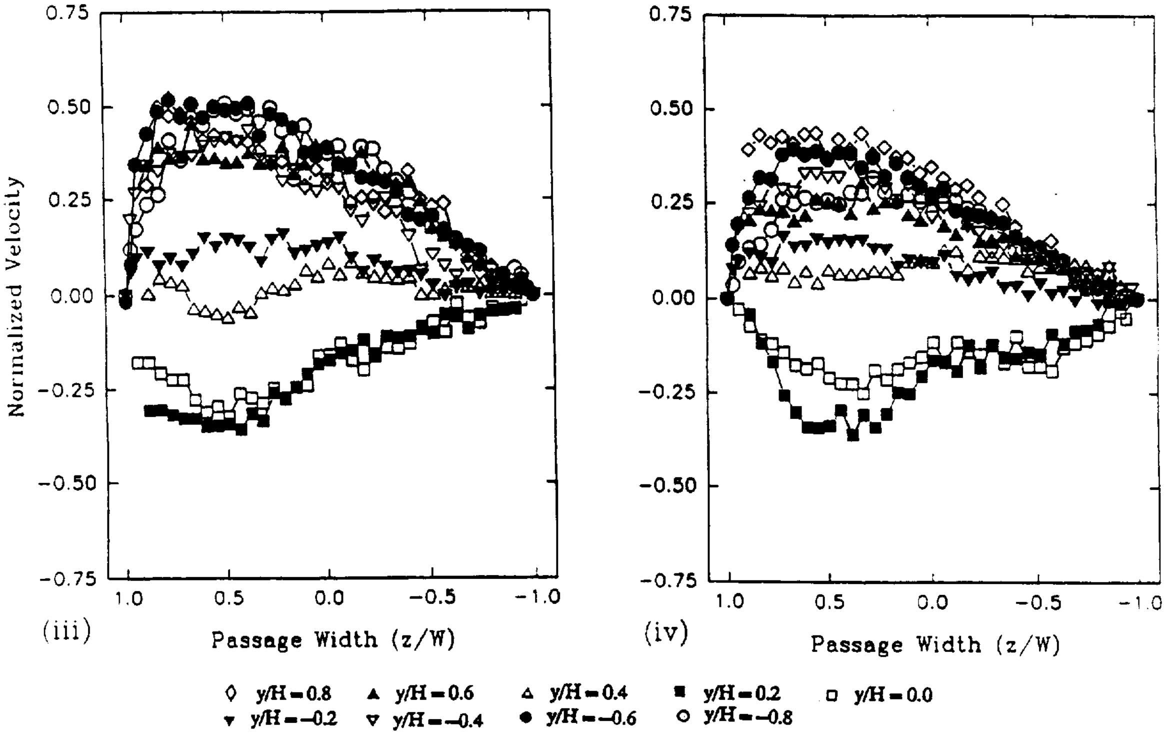

Figure 44b Continued. (iii) Re = 12,500 and Ro = 0.48. (iv) Re = 12,500 and Ro = 0.36.

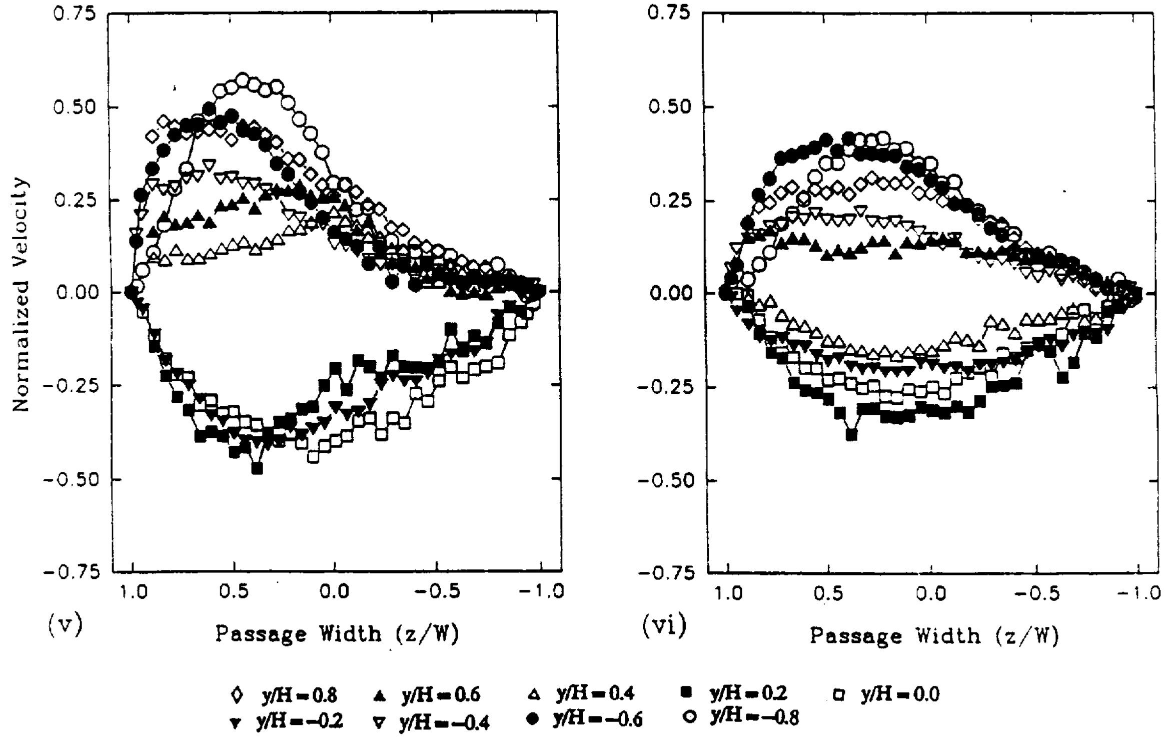

Figure 44b Concluded (v) Re = 12,500 and Ro = 0.24. (vi) Re = 12,500 and Ro = 0.12.

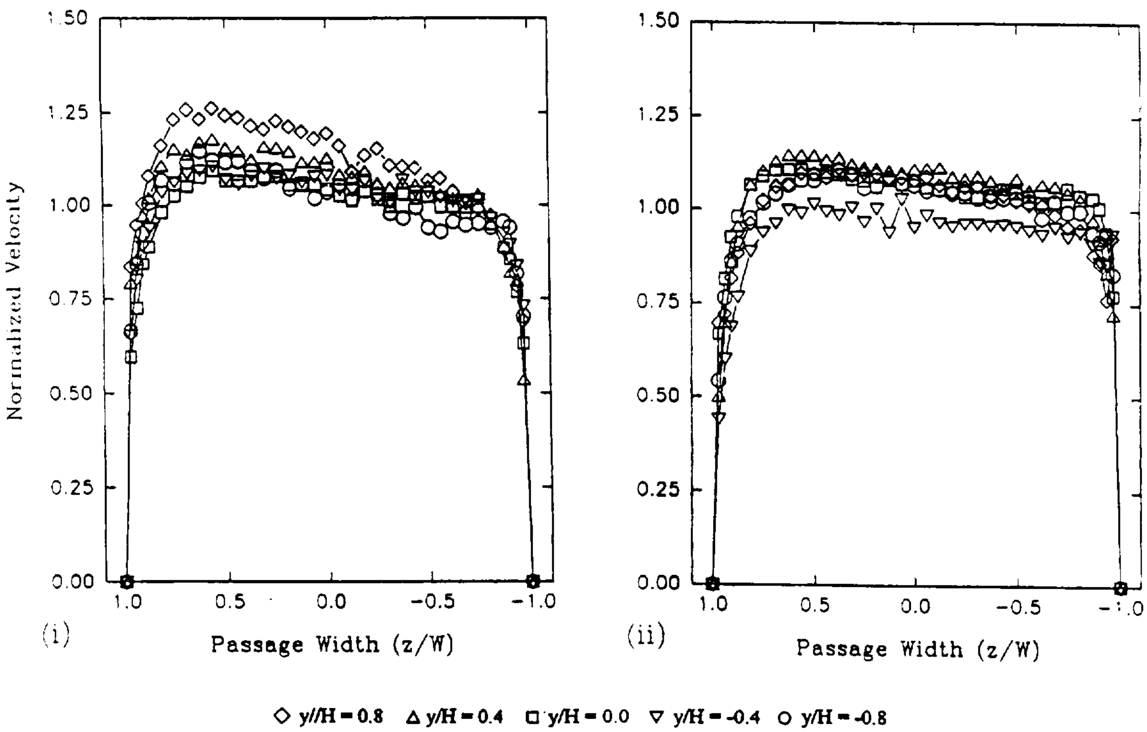

Figure 45a Comparisons of streamwise mean velocities at x/D = 6.4. (i) Re = 25,000 and Ro = 0.24. (ii) Re = 25,000 and Ro = 0.12.

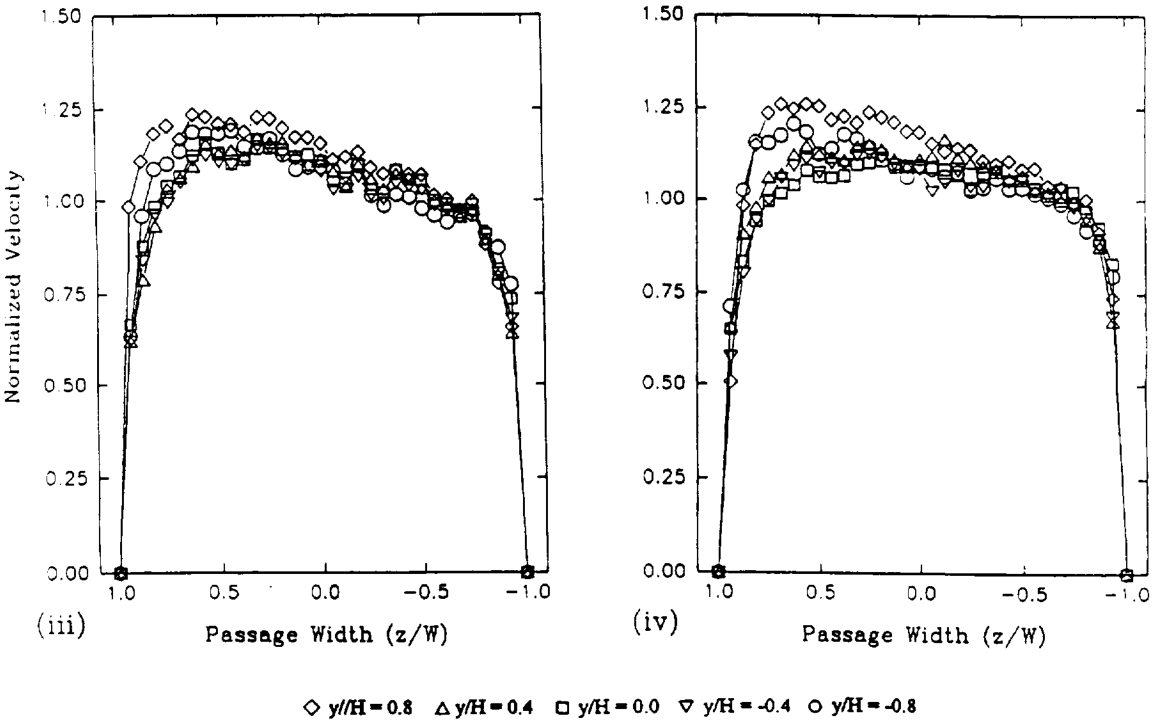

Figure 45a Continued. (iii) Re = 12,500 and Ro = 0.48. (iv) Re = 12,500 and Ro = 0.36.

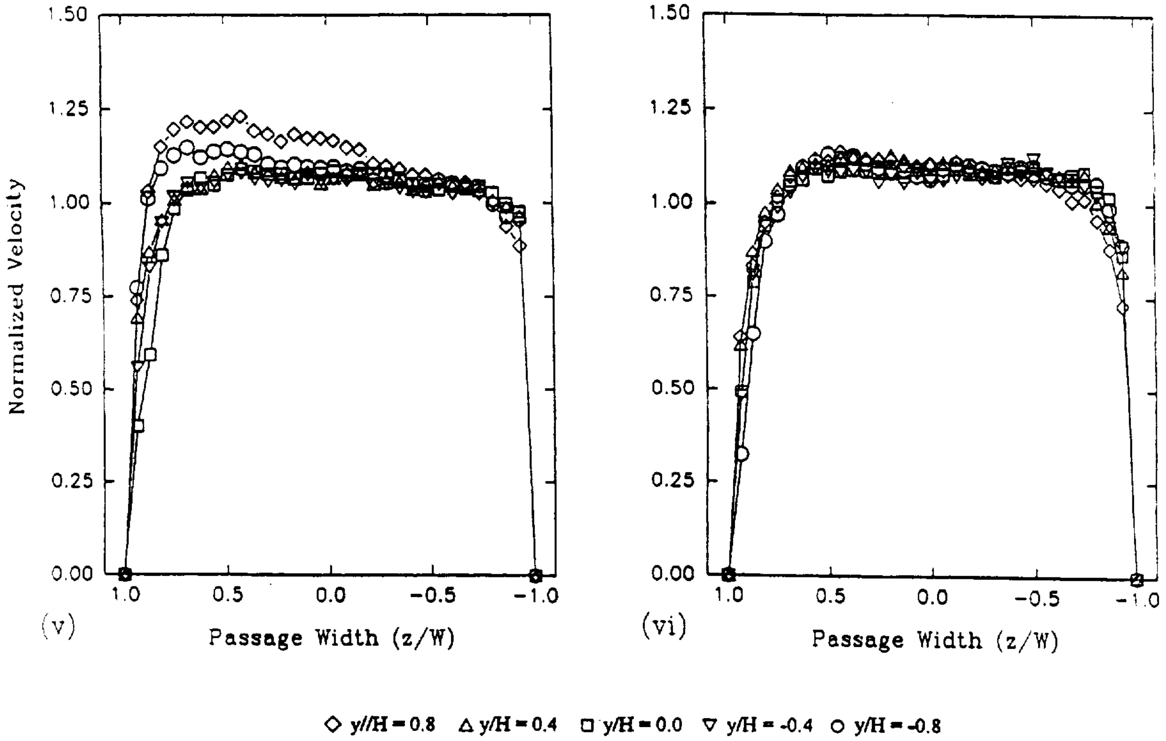

Figure 45a Concluded. (v) 12,500 and Ro = 0.24. (vi) Re = 12,500 and Ro = 0.12.

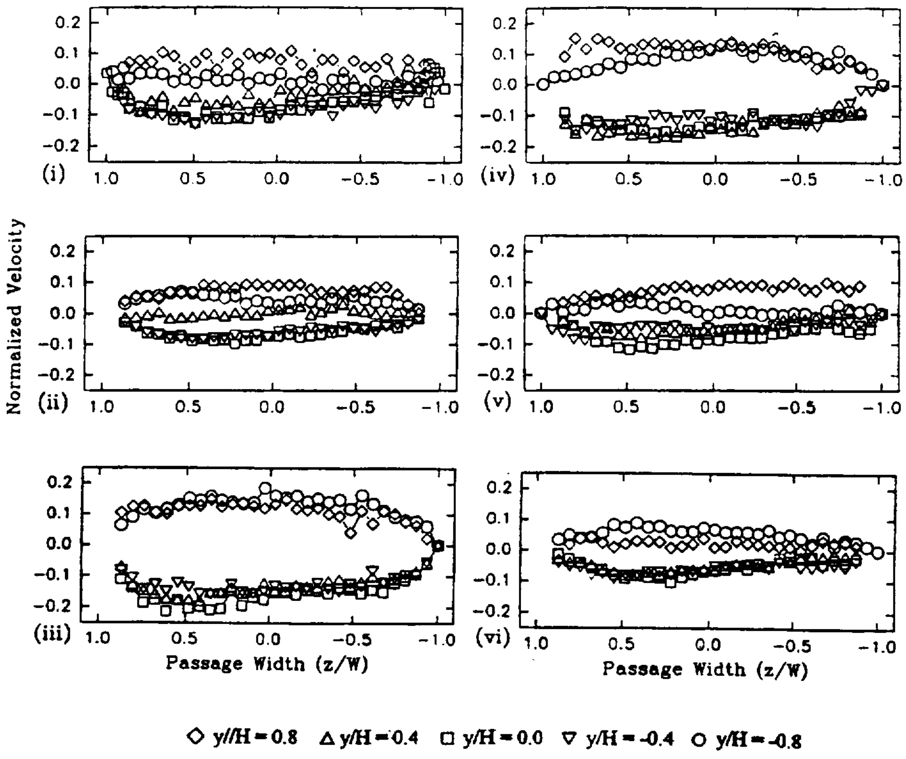

Figure 45b Comparisons of tangential mean velocities at x/D = 64. (i) Re = 25,000 and Ro = 0.24. (ii) Re = 25,000 and Ro = 0.12. (iii) Re = 12,500 and Ro = 0.48. (iv) Re = 12,500 and Ro = 0.36. (v) Re = 12,500 and Ro = 0.24. (vi) Re = 12,500 and Ro = 0.12.

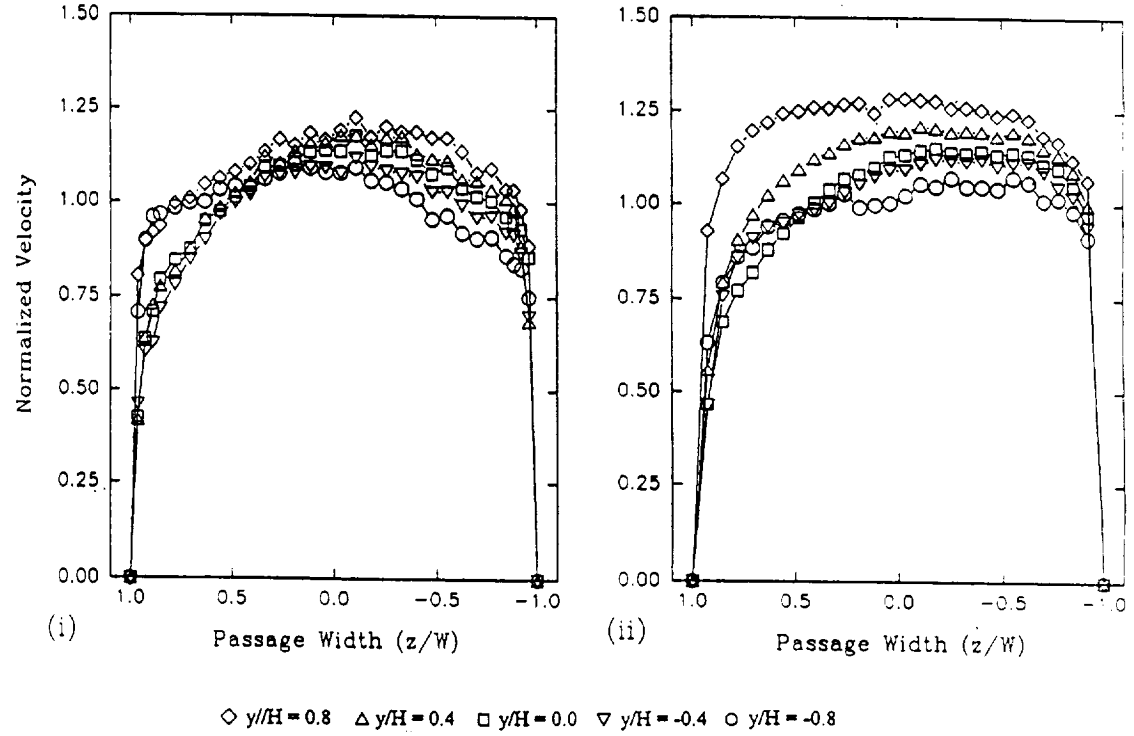

Figure 46a Comparisons of streamwise mean velocities at x/D = 15.0. (i) Re = 25,000 and Ro = 0.24. (ii) Re = 25,000 and Ro = 0.12.

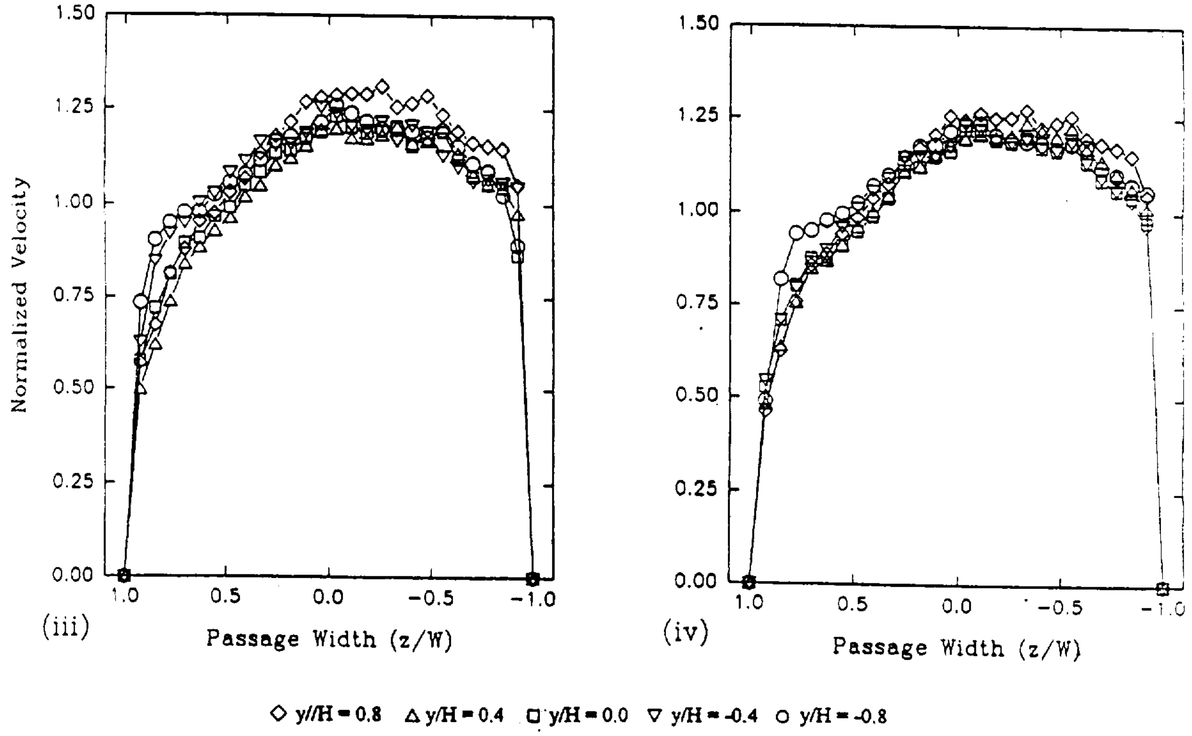

Figure 46a Continued. (iii) Re = 12,500 and Ro = 0.48. (iv) Re = 12,500 and Ro = 0.36.

C-2

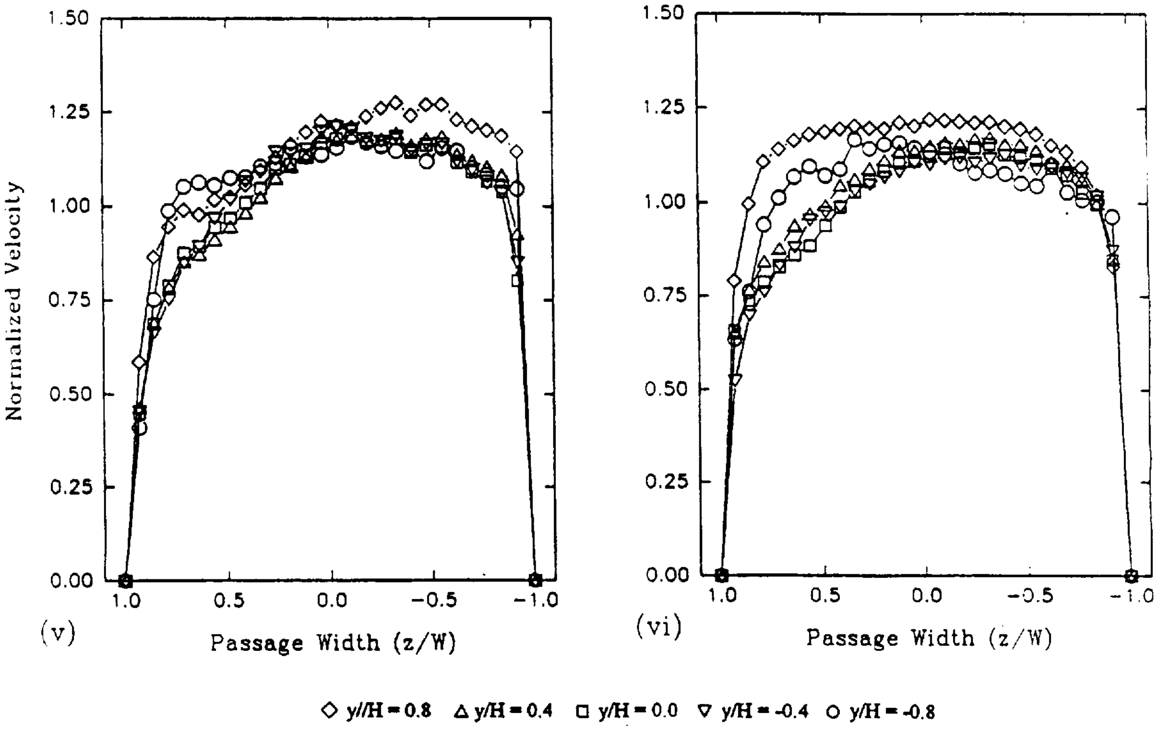

Figure 46a Concluded. (v) Re = 12,500 and Ro = 0.24. (vi) Re = 12,500 and Ro = 0.12.

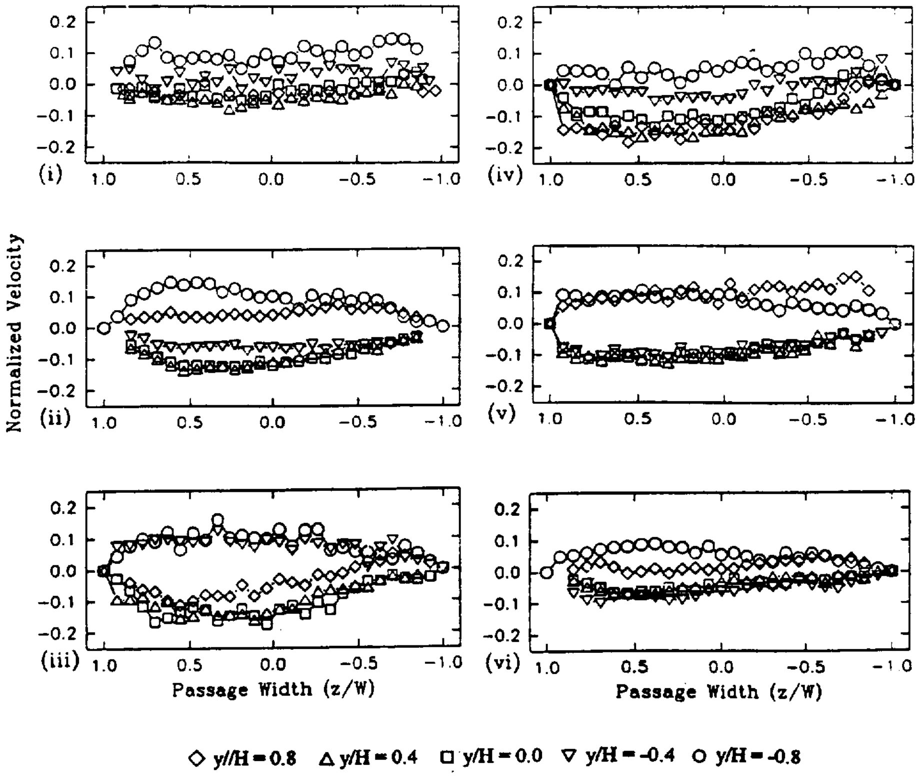

Figure 46b Comparisons of tangential mean velocities at x/D = 15.0. (i) Re = 25,000 and Ro = 0.24. (ii) Re = 25,000 and Ro = 0.12. (iii) Re = 12,500 and Ro = 0.48. (iv) Re = 12,500 and Ro = 0.36. (v) Re = 12,500 and Ro = 0.24. (vi) Re = 12,500 and Ro = 0.12.

conditions. The entrance effect dissipates with distance and this is also evident in the tangential velocity profiles (Figures (i), (ii), (v) and (vi) of Figure 44b with those of Figure 45b) which show reductions of 300% in the maximum tangential velocity.

Figures 46a(i) and (v) show the streamwise velocities obtained at x/D = 15.0 at Ro = 0.24 for Re = 25,000 and 12,500. The streamwise velocity profiles obtained with both Re are skewed towards the high pressure side. The skewness of the velocity profiles at Re = 12,500 is larger than those at Re = 25,000 because of the boundary layer effects. The streamwise velocities obtained at x/D = 15.0 at Ro = 0.12 for both Re are shown in Figures 46a(ii) and 46a(vi). The skewness in the velocity profiles toward the high pressure (trailing) side relative to that at Ro = 0.24 is reduced at Ro = 0.12 for both Re. At Ro = 0.12, the variations in streamwise velocity in the vertical direction are large at Re = 25,000 (Figures 46a(ii)) than at Re = 12,500 (Figure 46a(vi)). The streamwise velocities at y/H = +0.8 at Re = 25,000 (Figure 46a(ii)) are considerably higher than those at (Figure 46a(vi)). The cross-flow at Re = 25,000 negotiates the turn at a higher speed than that at Re = 12,500 and a higher pressure difference between the concave and convex surfaces is required to turn the flow. The convection of cross-flow to the convex surface of the turn is stronger at Re = 25,000 than at Re = 12,500 because the cross-stream pressure gradient induced by the turn is stronger, i.e. the induced secondary flow. The normalized cross-stream and tangential velocities obtained at under stationary condition, Figures 15a (i), 15b(i), 16a(i) and 16b(ii), confirm that the secondary flows at the turn at Re = 25,000 are stronger than those at Re = 12,500. The flow characteristics at the entrance of the turn are substantially affected by the secondary flows at the turn. The flow characteristics at x/D = 15.0 are also affected by secondary flows induced by Coriolis effects. The double vortex associated with Coriolis induced secondary flows is evident in the skewing of the streamwise velocity profiles toward the low pressure (leading) surface near the upper and lower wall at Ro = 0.12 and Re = 12,500, Figure 46a(vi). The double vortex associated with Coriolis induced secondary flows is not evident the streamwise velocity profiles at Ro = 0.12 and Re = 25,000, Figure 46a(ii). The relative strength of the secondary flows induced by the turn to those by Coriolis effects at Re = 25,000 is stronger than that at Re = 12,500 for Ro = 0.12. Figures 46b(i), (ii), (v) and (vi) show the tangential velocity profiles obtained at Re = 12,500 and 25,000 for both Ro. The tangential velocities all differ from one another. The differences stem from rotation as well as from Reynolds number effects. These results will be analyzed in Section 5.4 which considers the effect of rotation.

Figures 47a to 49b show the streamwise and tangential velocities obtained at the exit of the first turn (x/D = 21.0) and at 2D (x/D = 23.0) and 4D (x/D = 25.0) downstream of the first turn at Re of 12,500 and 25,000. Figures 47a(i), (ii), (v) and (vi) show that the streamwise velocities at the exit of the first turn (x/D =21.0) at Re = 12,500 and Ro = 0.12 differs from the remaining three cases. At Re = 25,000, the maximum absolute cross-stream velocity at the turn reaches $0.7U_b$ in the absence of rotation (Figure 15a(i)) and that in the presence of rotation, $0.95U_b$ (Figure 26(i)). The maximum absolute tangential velocity at the turn reaches $0.4U_b$ at Re = 25,000 in the absence of rotation, Figure 16a(i), and that in the presence of rotation, $0.65U_b$ (Figure 26(ii)). Both the maximum cross-stream tangential velocities in the presence of rotation are $0.25U_b$ higher than those in the absence of rotation. It is evident that increasing Ro from 0.0 to 0.24 increases the secondary flows by $0.25U_b$

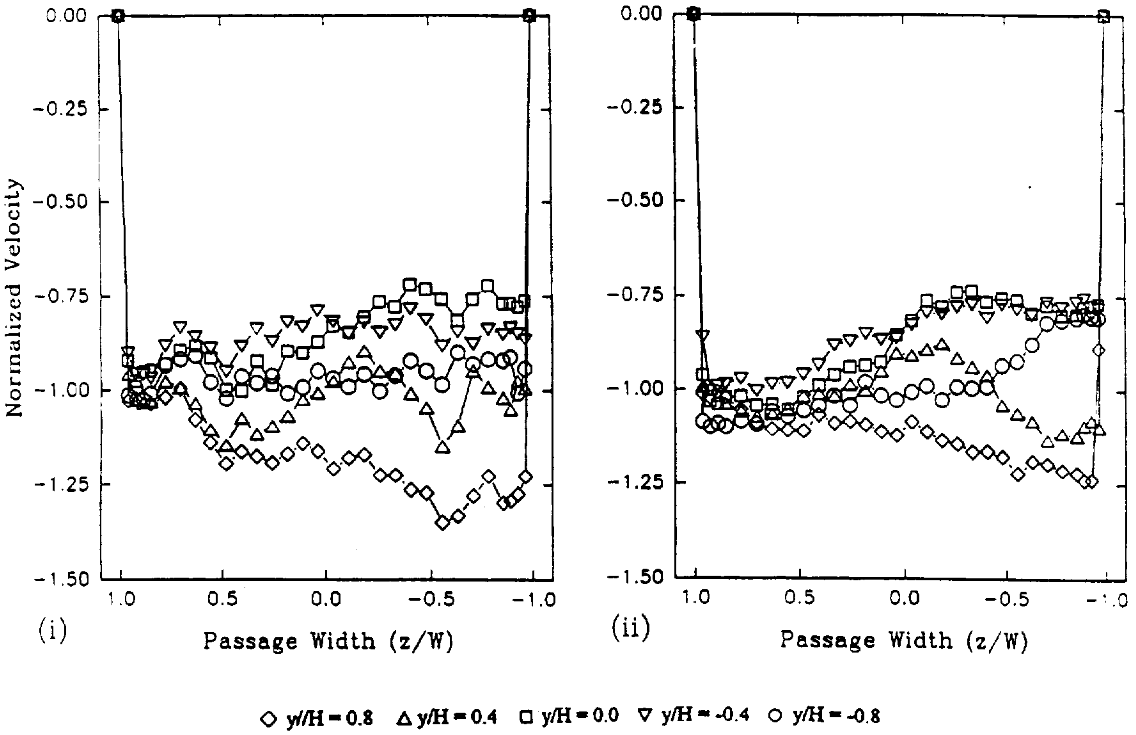

Figure 47a Comparisons of streamwise mean velocities at x/D = 21.0. (i) Re = 25,000 and Ro = 0.24. (ii) Re = 25,000 and Ro = 0.12.

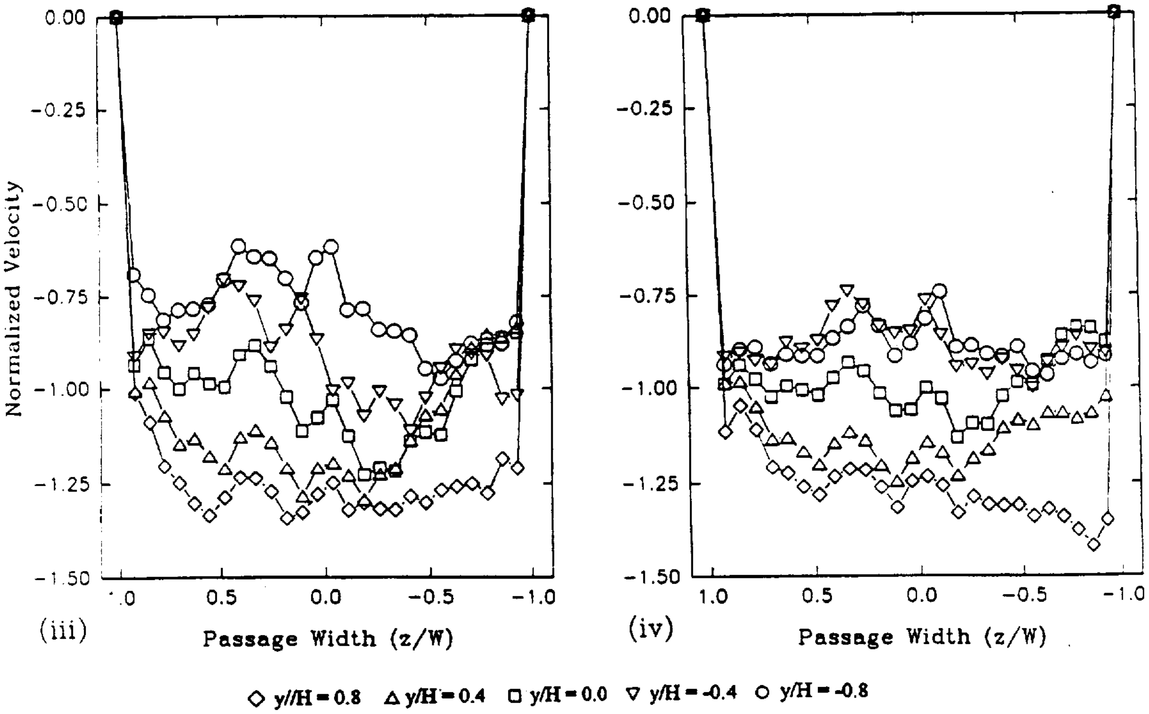

Figure 47a Continued. (iii) Re = 12,500 and Ro = 0.48. (iv) Re = 12,500 and Ro = 0.36.

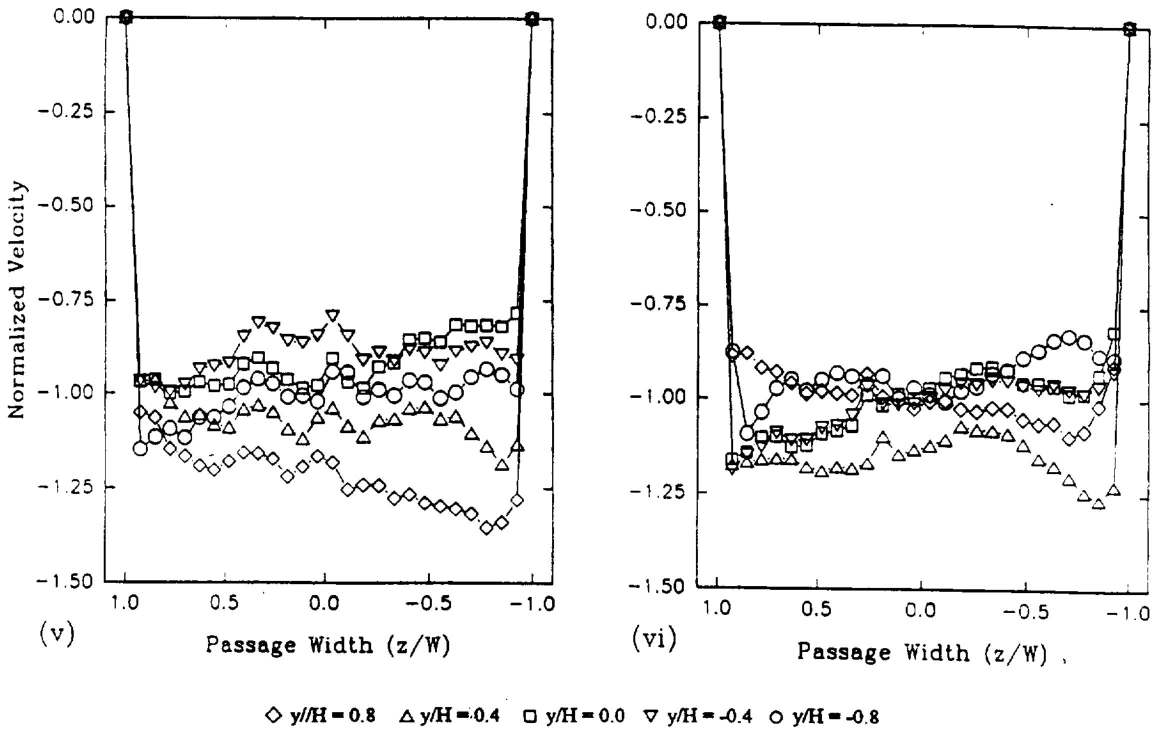

Figure 47a Concluded. (v) Re = 12,500 and Ro = 0.24. (vi) Re = 12,500 and Ro = 0.12.

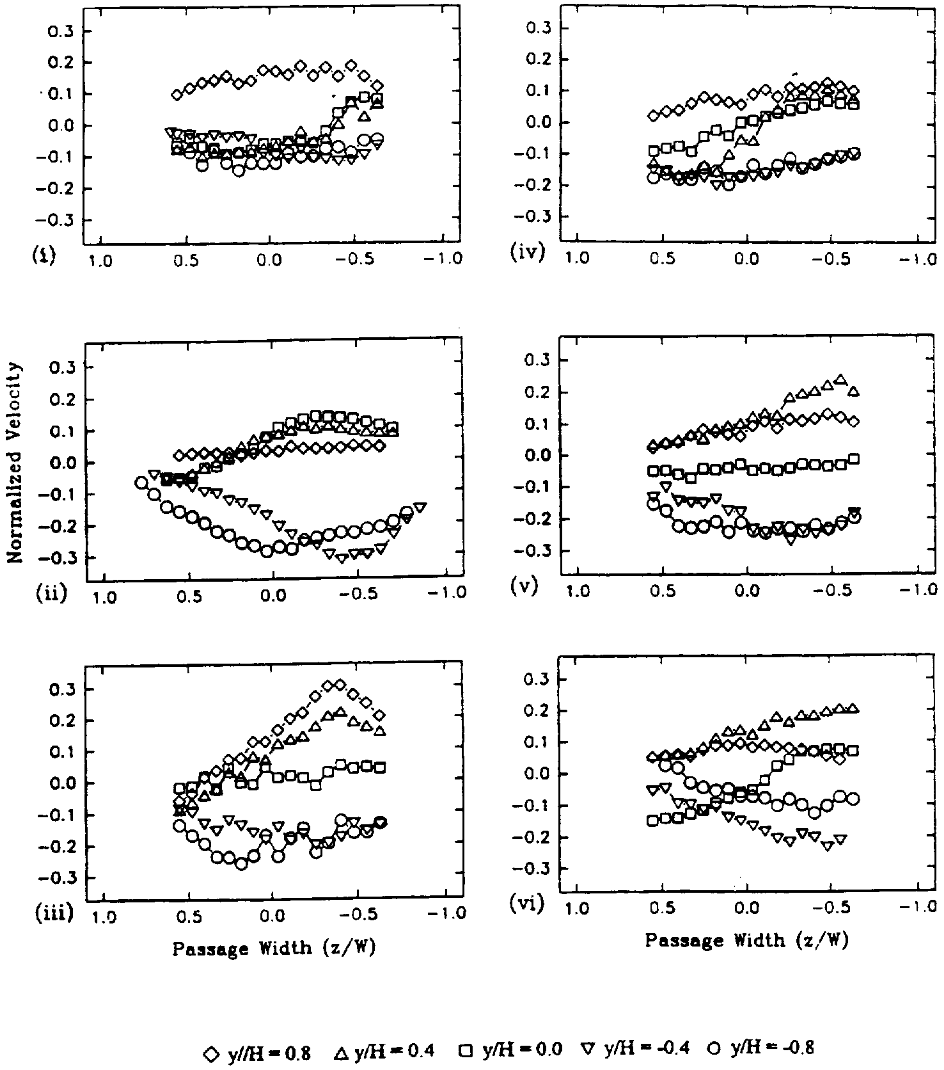

Figure 47b Comparisons of tangential mean velocities at x/D = 21.0. (i) Re = 25,000 and Ro = 0.24. (ii) Re = 25,000 and Ro = 0.12. (iii) Re = 12,500 and Ro = 0.48. (iv) Re = 12,500 and Ro = 0.36. (v) Re = 12,500 and Ro = 0.24. (vi) Re = 12,500 and Ro = 0.12.

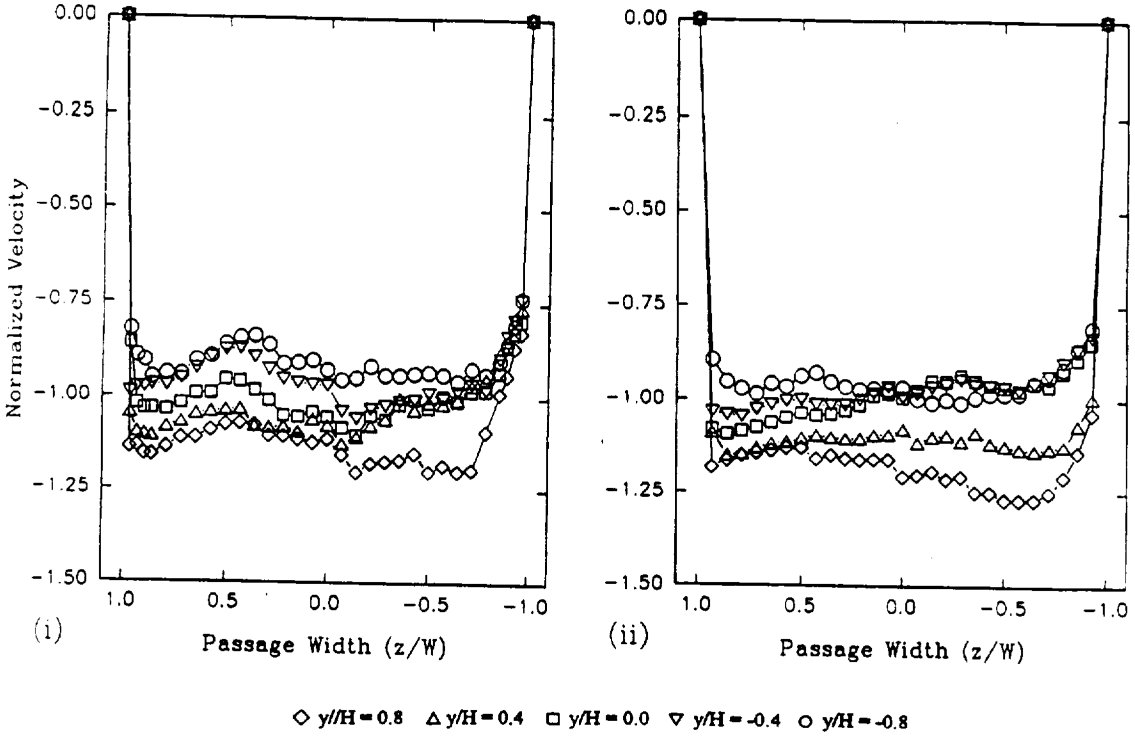

Figure 48a Comparisons of streamwise mean velocities at x/D = 23.0. (i) Re = 25,000 and Ro = 0.24. (ii) Re = 25,000 and Ro = 0.12.

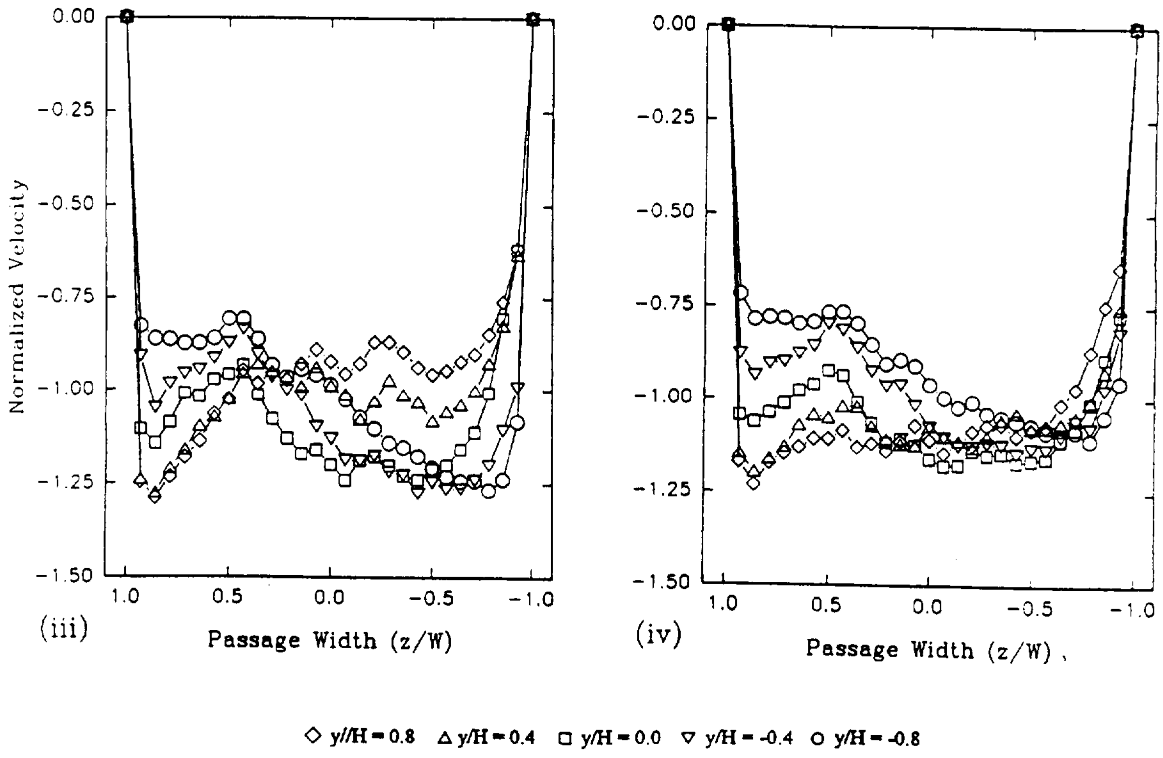

Figure 48a Continued. (iii) Re = 12,500 and Ro = 0.48. (iv) Re = 12,500 and Ro = 0.36.

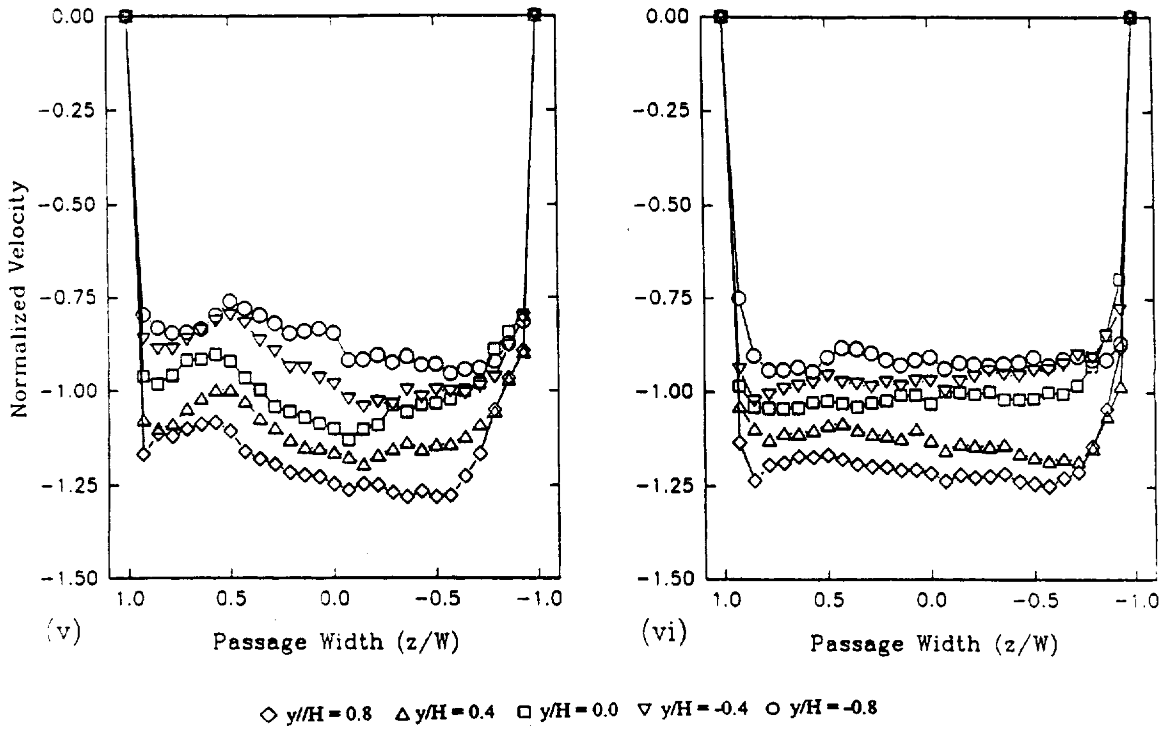

Figure 48a Concluded. (v) Re = 12,500 and Ro = 0.24. (vi) Re = 12,500 and Ro = 0.12.

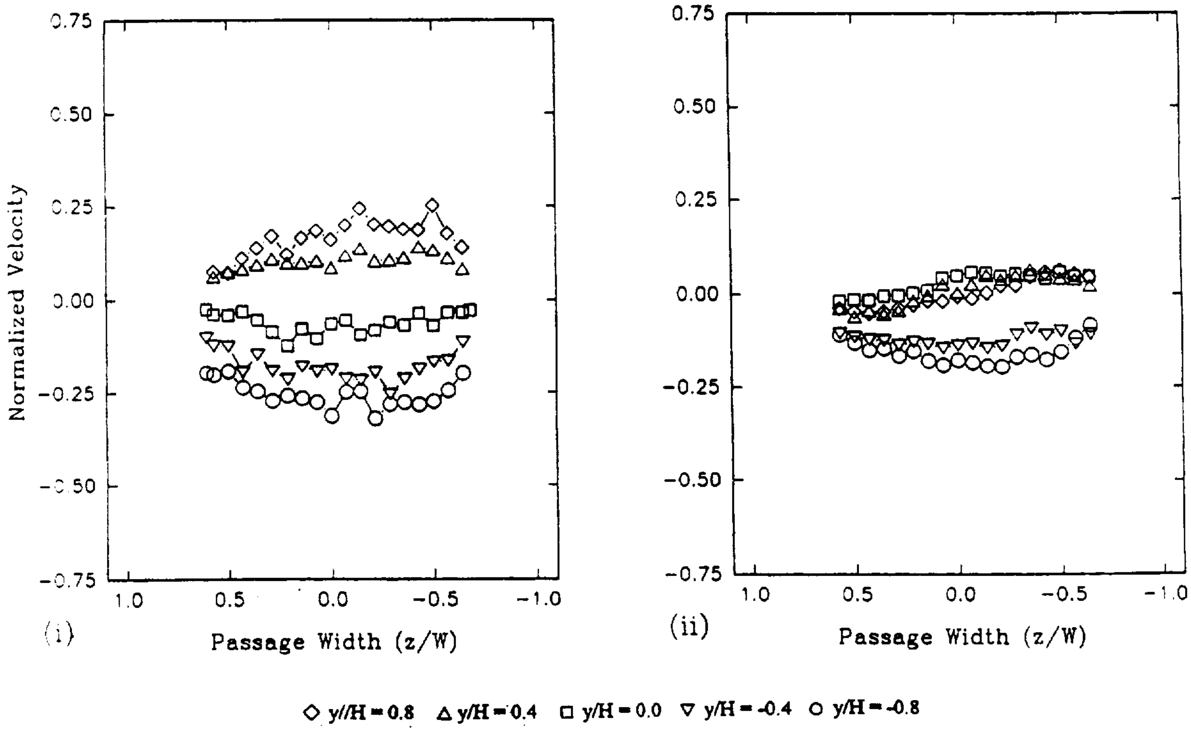

Figure 48b Comparisons of tangential mean velocities at x/D = 23.0. (i) Re = 25,000 and Ro = 0.24. (ii) Re = 25,000 and Ro = 0.12.

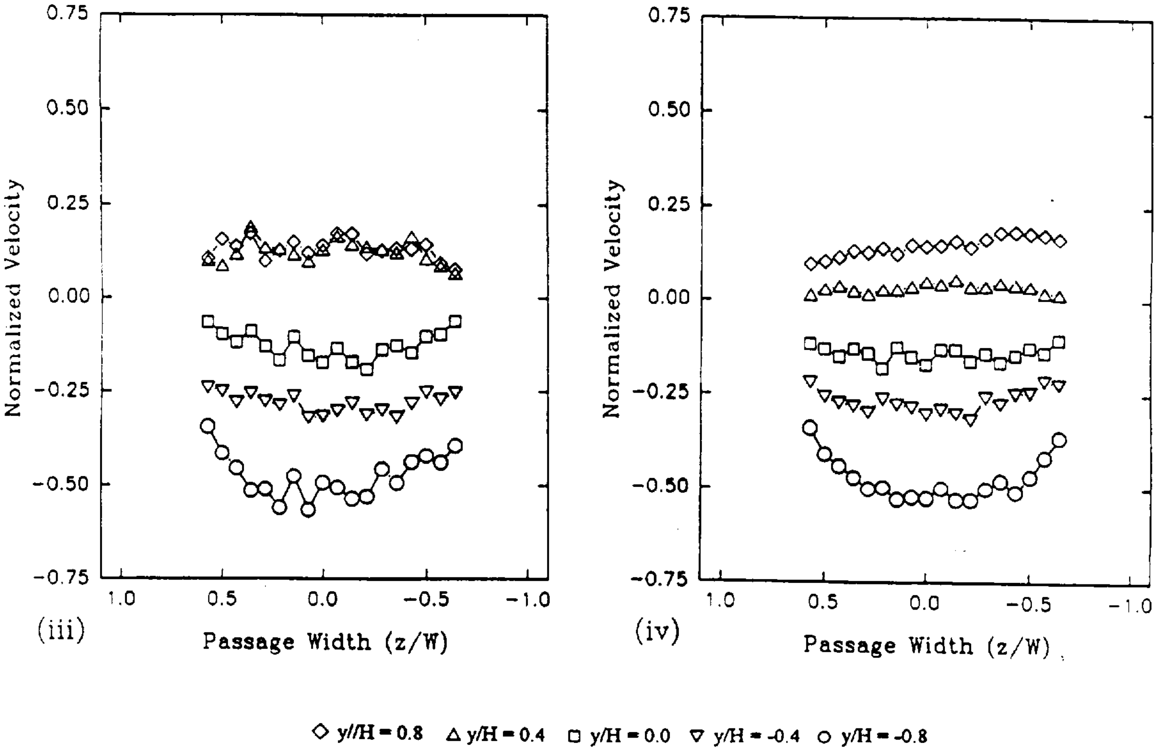

Figure 48b Continued. (iii) Re = 12,500 and Ro = 0.48. (iv) Re = 12,500 and Ro = 0.36.

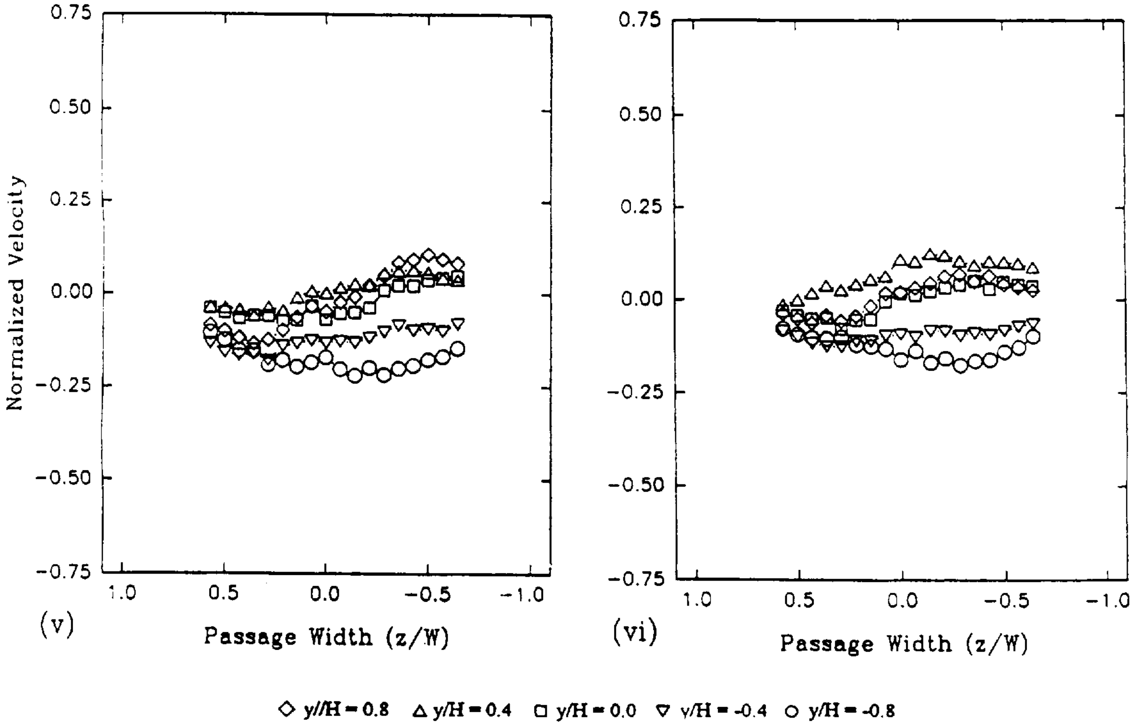

Figure 48b Concluded. (v) Re = 12,500 and Ro = 0.24. (vi) Re = 12,500 and Ro = 0.12.

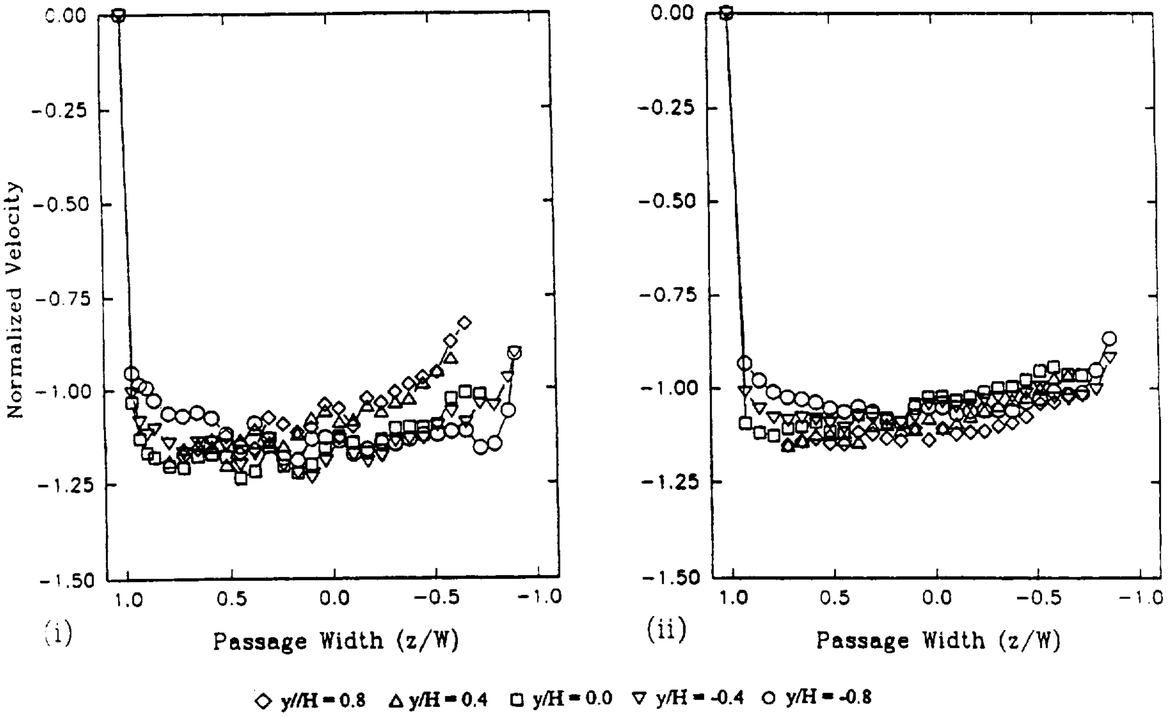

Figure 49a Comparisons of streamwise mean velocities at x/D = 25.0. (i) Re = 25,000 and Ro = 0.24. (ii) Re = 25,000 and Ro = 0.12.

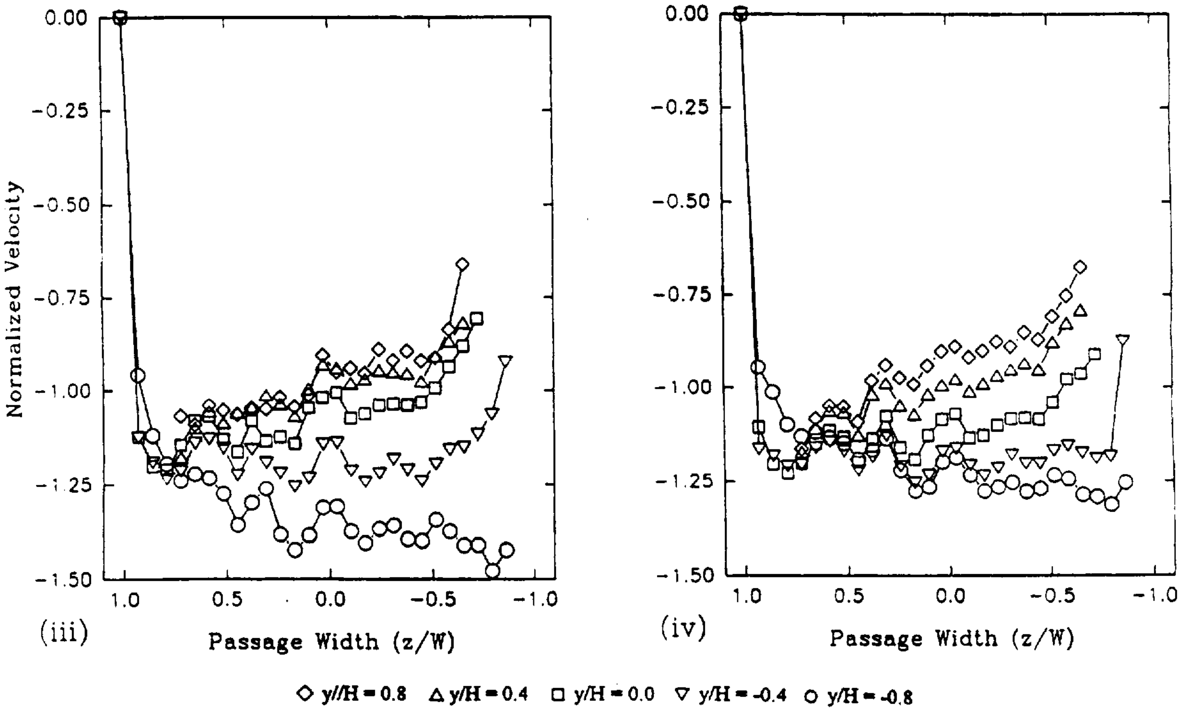

Figure 49a Continued. (iii) Re = 12,500 and Ro = 0.48. (iv) Re = 12,500 and Ro = 0.36.

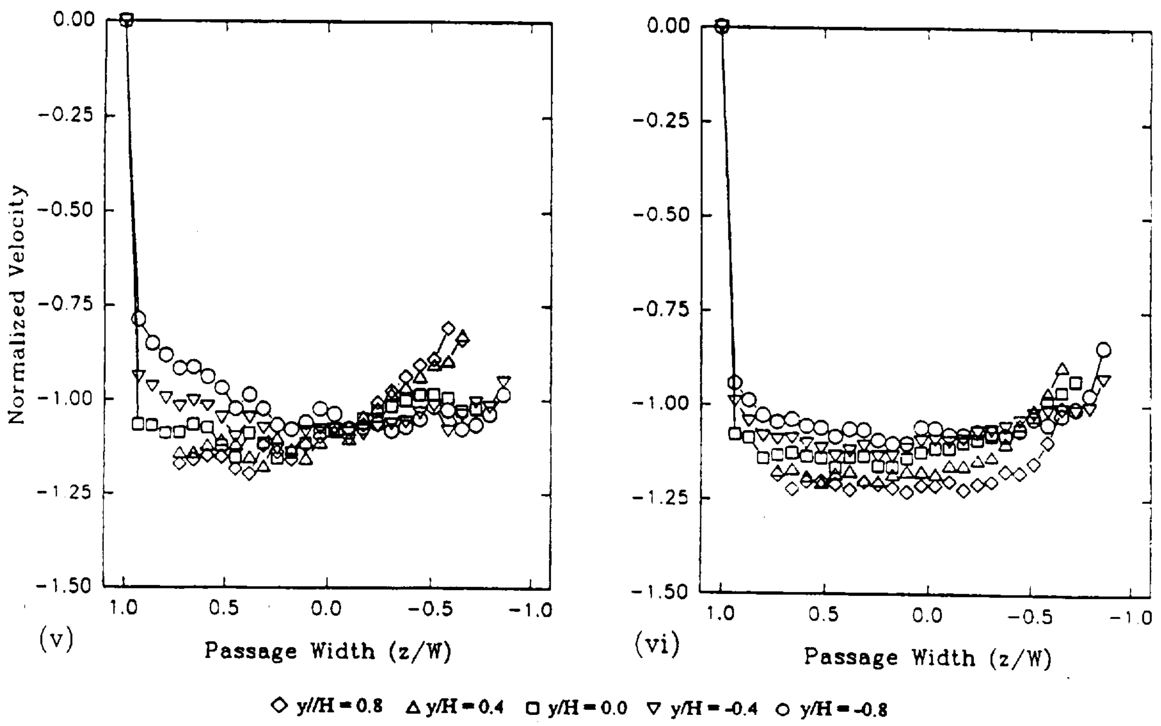

Figure 49a Concluded. (v) Re = 12,500 and Ro = 0.24. (vi) Re = 12,500 and Ro = 0.12.

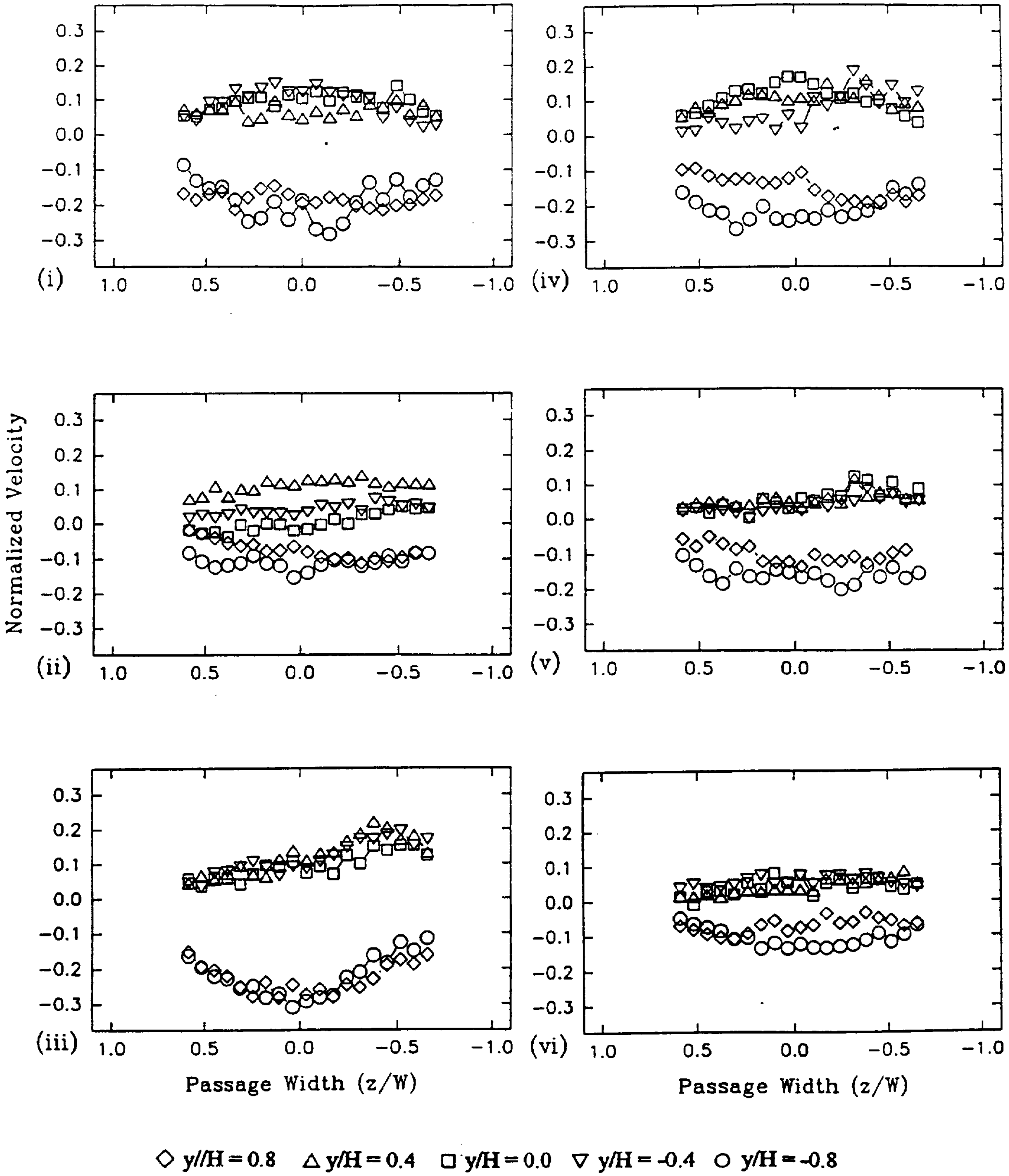

Figure 49b Comparisons of tangential mean velocities at x/D = 25.0.
(i) Re = 25,000 and Ro = 0.24 (ii) Re = 25,000 and Ro = 0.12
(iii) Re = 12,500 and Ro = 0.48 (iv) Re = 12,500 and Ro = 0.36
(v) Re = 12,500 and Ro = 0.24 (vi) Re = 12,500 and Ro = 0.12

and that the secondary flows induced by the turn are stronger than those induced by rotation. Section 5.4 shows that the effect of Ro on the secondary flow characteristics is approximately linear and one can expect reducing Ro from 0.24 to 0.12 reduces the strength of the secondary flow by approximately $0.12U_b$. Figures 47a(i) and (ii) show that reducing the both maximum cross-stream and tangential velocities by $0.12U_b$ does not affect significantly the streamwise velocity characteristics. The flow characteristics at the exit of the first turn (x/D = 21.0) are mainly determined by the secondary flow induced by the turn for Re = 25,000. Comparison of Figures 15a(i) and 15b(i) indicates that reducing Re from 25,000 to 12,000 does not affect the cross-stream velocities significantly. However, the maximum tangential velocity at the turn reduces from $0.4U_b$ to $0.2U_b$ when Re is reduced from 25,000 to 12,000. Reducing Re from 25,000 to 12,500 but keeping Ro constant at 0.24, Figures 47a(i) and (v), does not effect the streamwise velocities at the exit of the first turn significantly. This is expected because the measurements show that only the tangential velocities are affected and the reductions are small. The reduction in the maximum tangential velocity at the turn is of the order of $0.2U_b$. This is less than the total reduction of reducing both the maximum cross-stream and tangential by $0.12U_b$, reducing Ro from 0.24 to 0.12 at Re = 25,000. The differences between the streamwise velocity distributions observed in Figures 47a(i) and (vi) stem from sharp reductions in the tangential velocities for Re = 12,500 and Ro = 0.12.

Figures 48a(i) 48a(ii), 49a(i) and 49a(ii) show that the vertical variations (i.e. velocity gradient) in the streamwise velocity at 2D (x/D =23.0) and 4D (x/D =25.0) downstream of the first turn for the Re = 25,000 are lower than those of Re = 12,500, Figures 48a(v) 48a(vi), 49a(v) and 49a(vi). The profiles with the lower Re are more parabolic and have thicker boundary layers. The tangential velocities of Figures 47b(i) & (ii) show that the secondary flows at Re = 25,000 are weaker that those at Re = 12,500 (Figures 47b(v) & (vi)) at the exit of the first turn. The secondary flows at the turn are generated by cross-stream pressure gradient. They are higher at the lower Re because and the cross-flow has a lower momentum (i.e. a lower inertia). A flow with a lower inertia is expected to response to changes induced by pressure gradient quicker and the resulting secondary flow is also expected to achieve a stronger magnitude. However, Figures 48b(i) & (ii) and 49b(i) & (ii) show that, at 2D and 4D downstream of the first turn, the tangential velocities at Re = 25,000 are stronger than those at Re = 12,500 ((v) and (vi) of Figures 48b and 49b). A flow with a lower inertia is also expected to dissipate quicker than that with a higher inertia and this is evident in the tangential velocities of Figures 48b(i) & (ii) and 49b(i) & (ii). The effect of Reynolds number extends beyond 25D downstream of the inlet.

Figure 50a and 50b shows the streamwise and tangential velocities obtained at x/D = 33.2 at Re of 12,500 and 25,000. Both the streamwise and tangential velocities for Ro < 0.24 ((i), (ii) (v) and (vi) of Figures 50a-50b) are similar at these Re. Similarities are also evident in the streamwise velocities obtained at the exit of the second turn and 2D and 4D downstream of the second turn, i.e. x/D = 39.3, 41.3 and 43.3 ((i), (ii) (v) and (vi) of Figures 51 to 53). The flow at the entrance of the second turn is independent of Re in the range 12,500 to 25,000. The changes in heat transfer result associated with variations in Re downstream of x/D = 33.2 is expected to be smaller than those upstream of x/D = 25.0. The

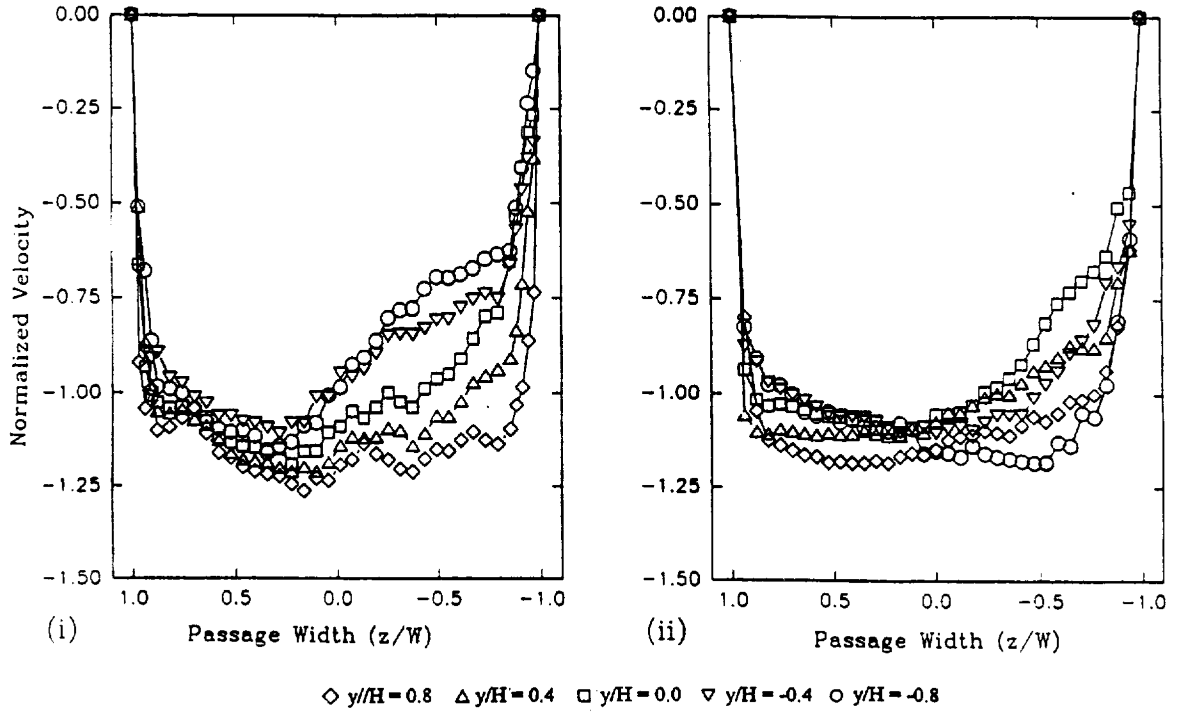

Figure 50a Comparisons of streamwise mean velocities at x/D = 33.2. (i) Re = 25,000 and Ro = 0.24. (ii) Re = 25,000 and Ro = 0.12.

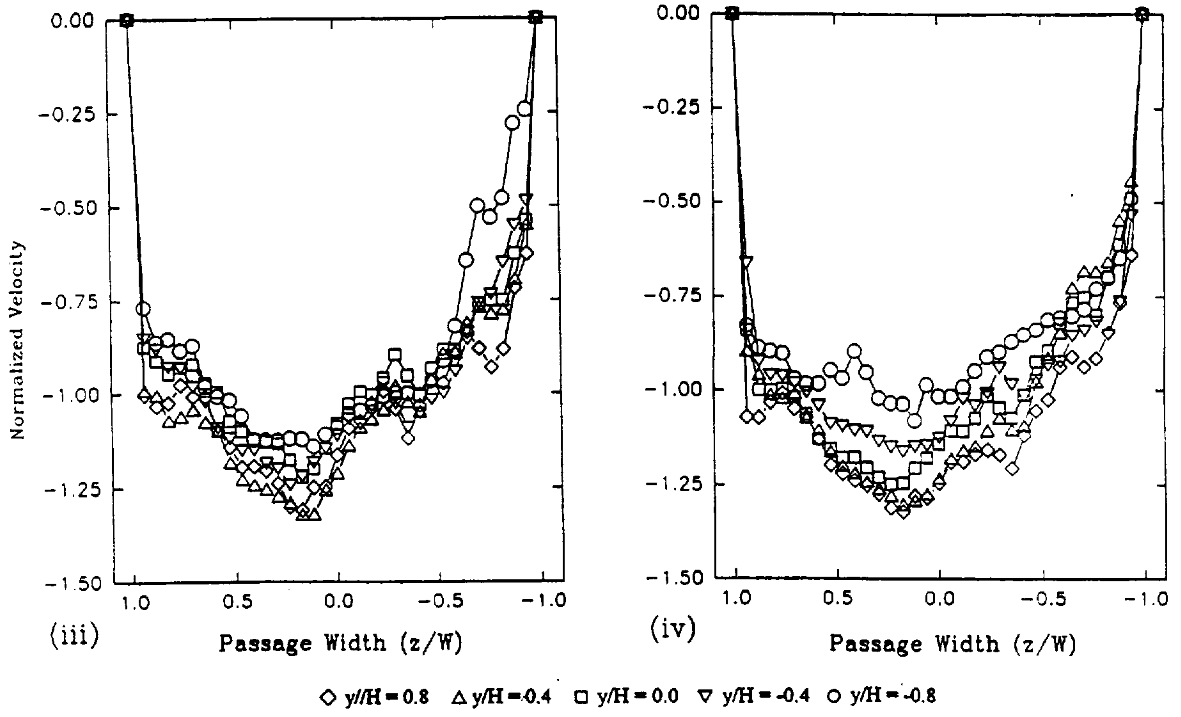

Figure 50a Continued. (iii) Re = 12,500

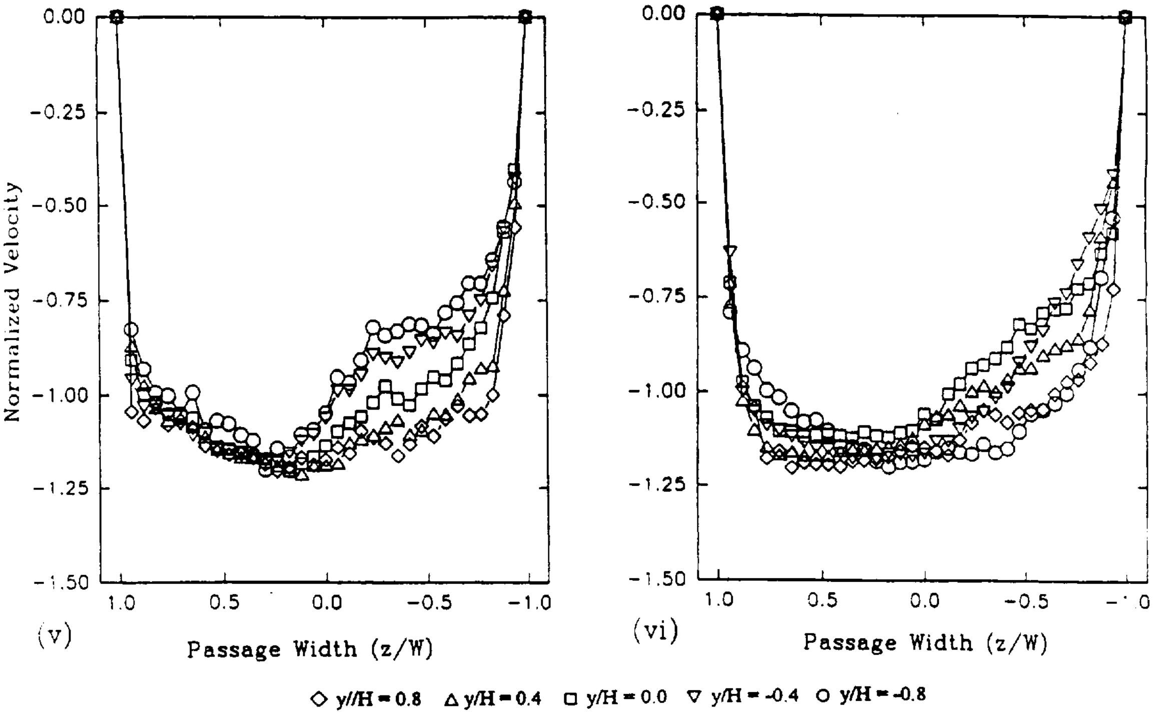

Figure 50a Concluded. (v) Re = 12,500 and Ro = 0.24. (vi) Re = 12,500 and Ro = 0.12.

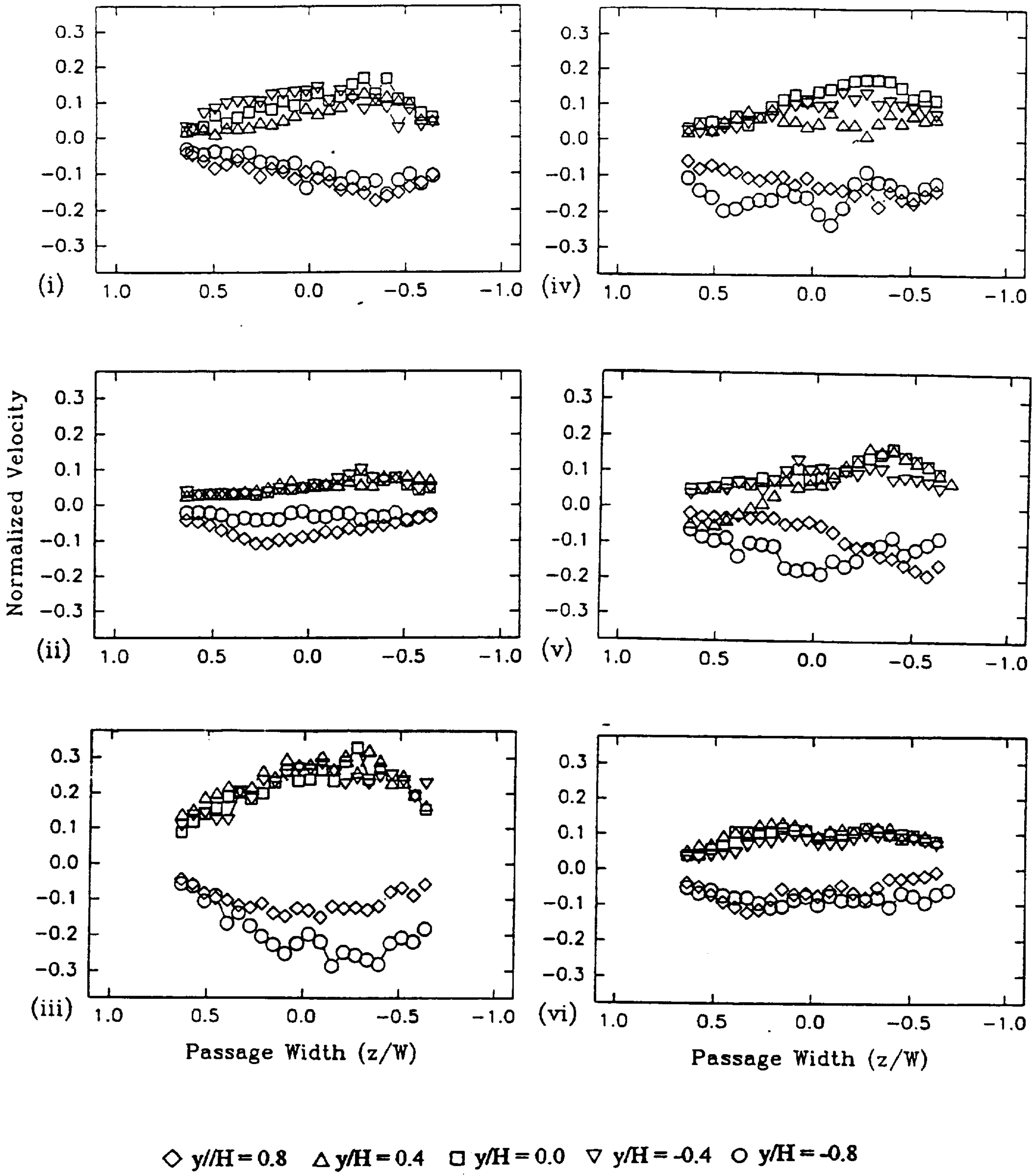

Figure 50b Comparisons of tangential mean velocities at x/D = 33.2.
(i) Re = 25,000 and Ro = 0.24 (ii) Re = 25,000 and Ro = 0.12
(iii) Re = 12,500 and Ro = 0.48 (iv) Re = 12,500 and Ro = 0.36
(v) Re = 12,500 and Ro = 0.24 (vi) Re = 12,500 and Ro = 0.12

velocity characteristics at Re = 12,500 and 25,000 exhibit greater similarity downstream of x/D = 33.2 than those upstream of x/D = 25.0.

5.4. The effect of Rotation number

Figures 44a and 44b show the streamwise and tangential velocities obtained at x/D = 1.0 at different Ro. The entrance effect associated with the plenum described in Section 4.1 is also evident in the streamwise velocities for Ro > 0.24, Figure 44a(i), (iii), (iv) and (v). The skewness of the velocity profile toward the leading side increases with increasing Ro. The effect of rotation at a higher Ro is stronger. Plug-type profiles are evident at the entrance in the center of the passage ($-0.6 < y/H < 0.6$), Figures 44a(ii) and (vi), for Ro = 0.12 because the effect of rotating is small. However, the entrance effect is noticeable near the upper and lower wall. Figures 44b(v) and (vi) show that increasing Ro from 0.12 to 0.24 results in increases in maximum positive tangential velocity from $0.42U_b$ to $0.58\ U_b$ and negative velocity from $0.33U_b$ to $0.42\ U_b$. Further increase in Ro from 0.24 to 0.48, Figures 44b(v) and (iii), does not affect the maximum positive and negative velocities significantly. This result indicates that the effect of rotation is asymptotic.

Figures 45a and 45b show the streamwise and tangential velocities obtained at x/D = 6.4 at different Ro. Comparison of the streamwise velocities at x/D = 1.0 and 6.4 (Figures (i) to (iv) of 44a and 45a) shows that the skewness of the velocity profile at x/D = 6.4 is reduced relative to that at x/D =1.0 and for all Ro. This is due to a net cross-stream convection from low pressure (leading) to high pressure (trailing) side in the tangential direction induced by Coriolis effects. Thus, the entrance effect is dissipating. The magnitude of the secondary flow increases with increasing Ro, Figures 45b(iii) to (vi). For a Re of 12,500, the positive and negative tangential velocities for Ro = 0.48, 0.36, 0.24 and 0.12 are approximately 0.20, 0.15, 0.12 and 0.7 U_b. The effect of rotation is approximately linearly with some small scattering due to variation of the rotational speed of the model. A 1 % variation in the rotational speed can lead to variations in the normalized relative velocities as explained above. The heat transfer results of Bo et al (1991) show that the effect of rotation on heat transfer within the first 10 D is linear. Increasing the Ro from 0.12 to 0.24 increases the heat transfer by a factor of 2. The increase in heat transfer correlates well with the increase in tangential convection, indicating that there is an important relationship between secondary flow and heat transfer in a serpentine passage.

The streamwise and tangential velocity profiles obtained at x/D = 15.0 are shown in Figures 46a and 46b. The streamwise velocities, Figures 46a(i) and 46a(ii), show that there are substantial difference in the velocity profiles obtained at Ro = 0.12 and 0.24 for Re = 25,000. The velocity at the Ro = 0.12 is higher than that at Ro = 0.24 near the upper wall. Fluid is being convected to the convex surface of the turn. The flow at x/D = 15.0 is influenced by the effect of the turn and the effect of rotation. The effect of the turn for Ro = 0.12 is relatively stronger than that for the Ro = 0.24 because rotation effect is lower at the lower Ro. Similar trends are evident in the streamwise velocities obtained at Ro = 0.12 and 0.24 for Re = 12,500. Figures 46a(iii) to 46a(v) show that the velocities obtained at Re =

12,500 for Ro = 0.24, 0.36 and 0.48 are similar. The effect of rotation on the streamwise velocity is asymptotic. The similarity of the streamwise velocity suggests that there should not be a significant difference in the heat transfer characteristics. However, the heat transfer measurements of Wagner, et al. (1991) indicated that the heat transfer continues to increase with Ro. The increase in heat transfer is partly attributed to differences in secondary flow, as evident in the tangential velocity profiles (Figures 46b(iii) and 46b(vi)) and partly attributed to buoyancy effects which are not addressed here.

Figures 45b and 46b show that, between x/D = 6.4 and 15.0, the tangential velocities on the low pressure (leading) side are higher than those on the high pressure (trailing) side at all y/H in all cases. Thus, the secondary flow on the low pressure side is stronger. Wagner et al (1991) show that heat transfer on the low pressure (leading) side is reduced in the first half of the first passage with increasing rotation but it increases toward the end of the passage. They attribute the increase in heat transfer in the latter half of the first passage to development of secondary flow and the current velocity measurements provide clear evidence for this. The tangential velocity profiles of Figures 45b(ii), 45b(vi), 46b(ii) and 46b(vi) show that, for Ro = 0.12, the double vortex observed at x/D = 6.4 is still evident in the results at x/D = 15.0 for both Re. Both the positive and negative tangential velocities for Re = 25,000 and Ro = 0.12 at x/D = 15.0 (Figure 46b(ii)) are higher than those at x/D = 6.4 (Figure 45b(ii)). Thus, the vortex strength at x/D = 15.0 is higher than that at x/D = 6.4, indicating that the secondary flow continues to develop between x/D = 6.4 and 15.0. However, at Ro = 0.12, there is very little difference between in the tangential velocity profiles for Re = 12,500 at both locations, Figures 45b(vi) and 46b(vi). The rotation effect has reached an asymptotic value by x/D = 6.4 for Ro = 0.12. Thus, for Re = 12,500 and Ro = 0.12, variations in heat transfer characteristic between x/D = 6.4 and 15.0 are attributed to changes in the primary flow and buoyancy induced secondary flow between x/D = 6.4 and 15.0. The primary flow continues to develop between x/D = 6.4 and 15.0 as the net tangential velocity is negative for Re = 12,500 and Ro = 0.12 resulting in a steady convection of fluid from low pressure (leading) to high pressure (trailing) side. At x/D = 15.0, the magnitudes of the tangential velocity at Re = 12,500 (Figure 46b(v)) are higher than those at Re = 25,000 (Figure 46b(i)) for Ro = 0.24. The secondary flow is stronger for the lower Re because the cross-flow has lower momentum and is more sensitive to the cross-stream pressure gradient. The double vortex for Re = 12,500 is fairly symmetrical above y/H = 0.0. However, the discussion in Section 4.2 shows that the vortex in the lower half of the passage has expanded into the upper half and that in upper half is being compressed. The tangential velocity in close proximity to the turn is influence by centrifugal effects as well as Coriolis effects. The Reynolds number varies linearly with flow rate while the centrifugal effect is related to the square of the rotation speed. For Re = 12,500, the flow rate and rotational speed are halved. Therefore, the centrifugal effect to Reynolds number effect is halved so the influence of the secondary flow induced by centrifugal effects is less. For Re = 25,000 and Ro = 0.24 and Re = 12,500 and Ro = 0.36, the flow rate is halved and the rotational speed is reduced by 75% so that Reynolds number to centrifugal effect remains the same. The normalized tangential velocities for these two conditions are expected to be similar, as evident in the profiles of Figures 46b(i) and 46b(iv). For high Ro (Ro > 0.24 for Re = 25,000 and Ro > 0.36 for Re =12,500), the tangential velocity characteristics in close proximity to the turn show more influenced due to rotation. At Ro = 0.48, Figure 46b(iii), the effect is even stronger, so that the vortex in the lower half of the passage has extended even deeper into to the upper half than that at Ro = 0.36. Figure 46b(iii) shows that, at Ro = 0.48, the velocities at y/H = -0.8 and -0.4 are both positive. The eye of the vortex (indicated by the change from positive to negative velocity) occurs at approximately y/H = 0.2 for Ro = 0.48, Figure 46b(iii). In contrast, the change from positive to negative velocity (the eye of the vortex) for Ro = 0.36 occurs at y/H = -0.4, Figure 46(iv).

Figures 47a and 48a show the streamwise velocities at the exit of the first turn (x/D = 21.0) and 2D downstream of the first turn (x/D = 23.0), respectively. The streamwise velocities obtained at the exit of the first turn (x/D = 21.0) at various Ro are shown in Figures 47a(i) at 47a(vi). For Ro < 0.36, Figures 47a(i) to 47a(ii) and 47a(iv) to 47a(iv), the velocities on the low pressure (trailing) side are higher than those on the high pressure (leading) side. However, Figure 47a(iii) shows that the velocities on the high pressure (leading) side are higher than those on the low pressure (trailing) side for Ro = 0.48. It is evident from Figures 46a(i) to 46a(vi) that the velocities of cross-flow entering the first turn on the high pressure (trailing) side are higher than those on the low pressure (leading) side. This trend is expected to reverse because Coriolis forces induce a net tangential convection from low pressure to high pressure side. The convection from low pressure to high pressure side corresponds to convection from leading to trailing in the first radially outward flow passage but to convection from trailing to leading in the second radially outward flow passage. The effect of the reversal in the direction of the Coriolis force is the strongest at Ro = 0.48 and its signature is already evident at x/D = 21.0. The streamwise velocities obtained at 2D downstream of the first turn (x/D = 23.0) at various Ro are shown in Figures 48a(i) to 48a(vi). Figures 48a(ii) and 48a(vi) show that the streamwise velocity profiles at Ro = 0.12 are closer to the stationary cases (Figures 13a(v) and 13b(v)) than those at Ro > 0.24 (Figures 48a (i) and 48a(iii) to 48a(v)). The effect of rotation is small for Ro = 0.12. The differences between the profiles at Re = 12,500 and 25,000, Figures 48a(ii) and 48a(vi), are due to Reynolds number effects described in Section 5.3. For Ro > 0.24, Figures 48a(iii) to 48a(v), the velocity profiles posses a double peak structure with high velocities close to the high pressure (leading) and low pressure (trailing) surfaces. The high velocities close to the walls increase convective cooling and suppress the growth of the boundary layer. These increase the rate of heat transfer between the walls and the coolant. Increase in high heat transfer at 2D downstream of the turn is evident in the results of Wagner et al (1991) and is due to a more efficient heat transfer between the wall and the coolant. The heat transfer increases with rotation because the near-wall velocities increase with rotation.

Figures 47b and 48b show the tangential velocities at the exit of the first turn (x/D = 21.0) and 2D downstream of the first turn (x/D = 23.0), respectively. In all cases, (Figure 47b(ii) to 47b(vi) and 48b(ii) to 48b(vi)) the tangential velocity profiles at all y/H are similar to those of the baseline condition (Figures 47b(i) and 48b(i)) at both locations. The clockwise rotation of the rig generates a clockwise swirl at the exit of the first turn which is evident in all cases. The maximum positive and negative velocities occur at different axial location. For example, for Re = 25,000, the positive and negative velocities at Ro = 0.12

(Figure 47b(ii)) are higher than those at Ro = 0.24 (Figure 47b(i)) at x/D = 0.21 and vice versa at x/D = 23.0 (Figures 48b(i) and 48b(ii)). However, the velocity characteristics for Ro = 0.36 and 0.48 (Figures 48b(iii) and 48b(iv)) are very similar at x/D = 23.0 at most y/H locations with maximum negative velocities reaching 0.5 U_b. This results suggests that the rotation effect is asymptotic for Ro > 0.36. Swirl is still evident at 2D downstream of the turn for all Ro, Figures 48b(i) to 48b(vi). Thus, the augmentation of heat transfer by swirl is expected to extend to at least 2D downstream of the turn for all Ro.

The streamwise and tangential velocities obtained at 4D downstream of the first turn (x/D = 25.0) at various Ro are shown in Figures 49a and 49b. The tangential velocity profiles (Figures 49b(i) to 49b(vi)) show that, in all cases, negative velocities occur near the upper and lower walls (y/H = ±0.8). Thus, in the near-wall region, the tangential convection is from leading to trailing side. It is also evident from Figures 49b(i) to 49b(vi) that the tangential velocities in the center of the passage (-0.4 < y/H < 0.4) are positive indicating convection from low pressure (trailing) to high pressure (leading) side in all cases. Thus, the double vortex characteristics associated with the Coriolis effect have already been established at 4D downstream of the turn. The transition from clockwise swirl to double vortex occurs between 2D and 4D downstream of the first turn. The clockwise swirl associated with the interaction of the secondary flow induced by the turn and rotation is clearly evident in the tangential velocity at 2D downstream of the turn described above. Figure 49a(vi) shows that the streamwise velocity profiles obtained with Ro = 0.12 and Re = 12,500 are closer to the stationary references (Figure 13b(vi)) than those at Ro > 0.24, Figures 49a(iii) to 49a(v). The effect of rotation is small for Ro = 0.12 but the signature associated with the Coriolis effect is clearly evident in the skewing of the velocity profiles toward the leading side. For Re =12,500 and Ro > 0.24, Figures 49a(iii) to 49a(v) the velocity variations in the vertical and lateral directions increase with increasing Ro. The lateral velocity gradients in the upper half of the passage are steeper than those in the lower half. The steep velocity gradient in the upper half of the passage is attributed to the reversal in the direction of the tangential convection during the transition from clockwise swirl to double vortex. The direction of the tangential convection in the lower half of the passage remains the same during the transition from clockwise swirl to double vortex so that the velocity gradients are not as steep as those in the upper half. The steepness of the velocity gradients in the lateral direction in the upper and lower half of the passage increases with increasing Ro, Figures 49a(iii) to 49a(vi). The level of swirl and the vortex strength associated with high Rotation numbers are stronger and the changes in tangential velocity are more extreme than those for lower Rotation numbers. Furthermore, the transition from clockwise swirl to double vortex is expected to occur over a longer distance for the high Rotation numbers than low Rotation numbers. The cross-flow at a high Ro process a stronger level of swirl and requires a longer dissipating length than that at a low Ro. Consequently, the transition from clockwise swirl to double vortex occurs at an axial distance close to x/D = 25.0 at a high Ro but at a distance farther upstream (close to x/D = 23.0) at a low Ro. The flow at x/D = 25.0 is less developed for a high Ro than that at a low Ro. The velocity gradients in both the vertical and lateral direction at Ro = 0.12 and 0.24 for Re = 25,000 (Figures 49a(i) and 49a(ii)) are lower than those for Re =12,500 (Figures 49a(v) and 49a(vi)). Increasing Re increases turbulent mixing and reduces the velocity gradient in the mean velocity profile. This effect has already been described in Section 5.3 which considered the influence of Reynolds number. At Re = 25,000, the augmentation of heat transfer associated with the secondary flow induced by the turn is not expected to extend beyond 4D downstream of the turn for Ro < 0.24. The heat transfer characteristic at 4D downstream of the turn is expected to be similar to that in the straight section of the passage. At Re = 12,500, the augmentation of heat transfer associated with the secondary flow induced by the turn may extend beyond 4D downstream of the turn for Ro > 0.24. The heat transfer characteristic at 4D downstream of the turn may be higher than those in the straight section of the passage.

Figures 50a and 50b show the streamwise and tangential velocities at the entrance to the second turn (x/D = 33.2). Figures 50a(v) and 50a(vi) show that increasing the Ro from 0.12 to 0.24 results in reduction in streamwise velocities near the lower wall. This is due to the transition of the double vortex to clockwise swirl which begins at the second turn. The velocity characteristics for Ro = 0.12 and 0.24 are different because the transition is more rapid at Ro = 0.24. Increasing Ro from 0.24 to 0.36, Figures 50a(vi) and 50a(v) gives rise to more acute velocity profiles with steeper velocity gradient in the lateral direction. The net tangential convection associated with the Coriolis effect at Ro = 0.36 is stronger than that at Ro = 0.24. Further increase in Ro from 0.36 to 0.48, Figures 50b(iv) and 50b(iii), does not have any significant effect in the velocity profiles. Consistent with the velocity measurements at the end of the first passage, those at the end of the second passage also show that the effect of rotation on the streamwise velocity is asymptotic. The magnitudes of the tangential velocity, Figures 50a(iii) to 50a(v) on the low pressure (trailing) side is stronger that those on the high pressure (leading) side for Ro > 0.24. Similar to the first passage, the development of secondary flow gives rise to stronger tangential velocity near the low pressure surface. For Ro = 0.48, the magnitudes of the tangential velocity at 4D downstream of the inlet (Figure 49a(iii)) and at the outlet of the second passage (Figure 50a(iii)) are more or less the same. For the remaining 5 cases of Figures 50a(i), 50a(ii) and 50a(iv) to 50a(vi), there are marked reductions in the tangential velocity components, i.e. the strength of the secondary flows. For Ro < 0.36, the magnitude of the secondary flow diminishes with distance away from the turn initially. The discussions above indicate that the secondary flow in the straight section of the passage increase with distance. The secondary flow along the second passage is expected to decrease to a minimum and then increases for Ro < 0.36. At the highest Ro (0.48), the secondary flow induced by rotation is comparable to that induced by the turn and there is little or no reduction in the strength of the secondary flow along the second passage.

The variations in the streamwise and tangential velocity characteristics on the high pressure (leading) and low pressure (trailing) surfaces along the second passage associated with Ro are higher than those along the first passage. Wagner et al (1991) indicate that the heat transfer on the high pressure (trailing) side of the first passage increases by up to 100% as Ro increases from 0.24 to 0.48 but that on the high pressure (leading) side of the second passage increases by less than 30% as Ro increases from 0.24 to 0.48. Heat transfer in a rotating turbine-blade cooling passage is dependent Coriolis induced secondary flows and buoyancy effects. The discussions in Section 5.1 show that the high heat transfer in the first passage is due to Coriolis and buoyancy effects reinforcing one another. The low heat transfer in the second passage is a result of buoyancy forces opposing Coriolis forces.

The streamwise velocities for Ro between 0.12 and 0.48 within 4D downstream of the second turn are shown in Figures 51, 52 and 53. In all cases, they are similar to the mirror images of the streamwise velocities obtained at the same axial location downstream of the first turn, Figures 47a, 48a and 49a. The high pressure and low pressure surfaces in the second and third passages are reversed due to the reversal in flow direction.

5.5 Compressible Flow Simulations

To determine the effect of the centrifugal buoyancy force on the predicted heat transfer, two simulations were initiated with variable density. In addition to the non-dimensional parameters of Reynolds number and Rotation number, it is also important to match the Buoyancy parameter. Therefore, the inlet density, velocity magnitude, and temperature were specified to match the data of Wagner et al (1991) to insure that all of the non-dimensional parameters were consistent between the computations and the heat transfer measurements. In addition, the same computational mesh and initialization procedures were used to initialize both the compressible and incompressible cases. This procedure is described in Section 3.2.2. The first compressible flow case employed wall functions with the inlet plane specified at $x/D = 6.4$. The two-layer wall integration k-ε turbulence model was used with the inlet plane specified at $x/D = 1.0$ in the second simulation.

The incompressible flow computations illustrated the importance of correctly specifying the inlet boundary conditions and the ability of the two-layer turbulence model to accurately predict the flow field in the regions of large gradients. Therefore, emphasis will be placed on the wall integration simulation in the discussion of the results. However, the wall function simulation will be used to discuss the differences in the four passage simulations since the two-layer wall integration simulation was limited to the first two passages of the serpentine model.

To reiterate, the Reynolds number and Rotation number are consistent between the Wagner et al (1991) data, the current velocity measurements, and both the incompressible and compressible flow calculations (nominally, Re = 25,000 and Ro = 0.24). In addition, the heat transfer data of Wagner et al (1991) and the compressible flow predictions have the same density ratio, $\Delta\rho/\rho = 0.07$, and the same buoyancy parameter, $B.P. = (\Delta\rho/\rho)(R/D)(\Omega D/V)^2 = 0.2$.

For radially outward flow, the Coriolis induced secondary flow causes the cooler fluid from the center of the duct to move toward the trailing face and increases the streamwise velocity in this region. The centrifugal buoyancy force is directed radially outward and has a larger magnitude for the cooler, more dense fluid which further increases the velocity near the trailing side. In Figure 54, the centerline velocity for the experimental data is compared with the wall function simulations with the inlet located at $x/D = 6.4$. The

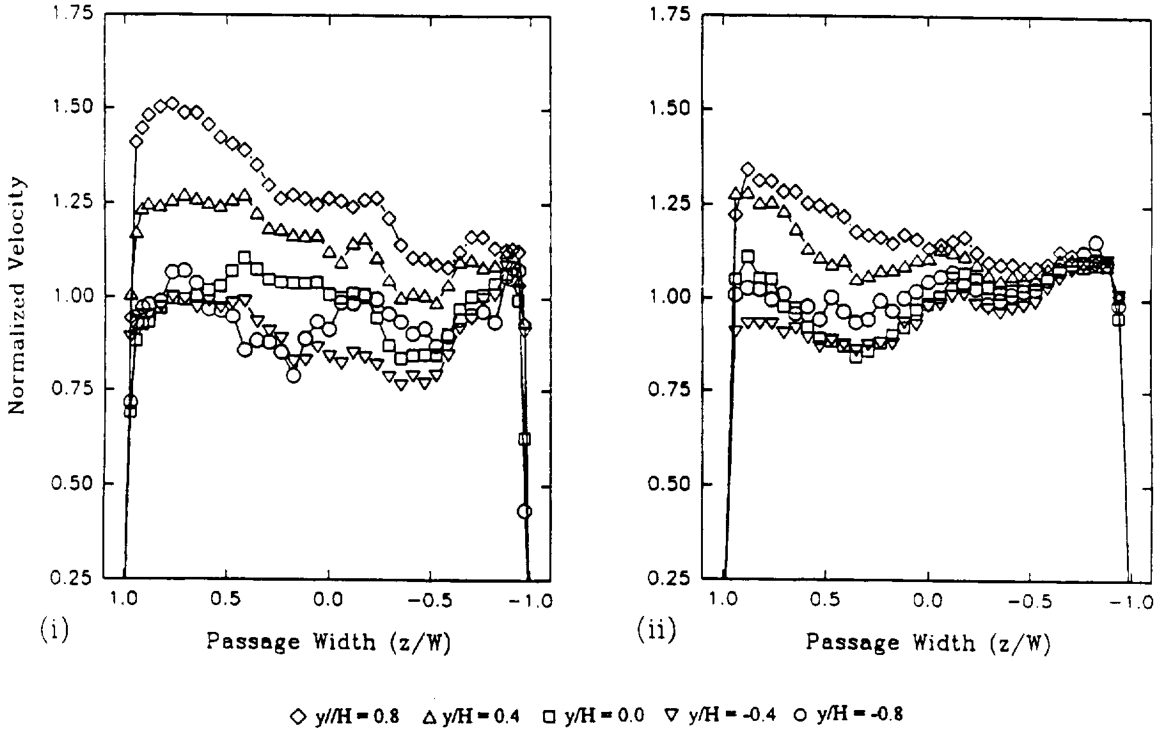

Figure 51 Comparisons of streamwise mean velocities at x/D = 39.3. (i) Re = 25,000 and Ro = 0.24. (ii) Re = 25,000 and Ro = 0.12.

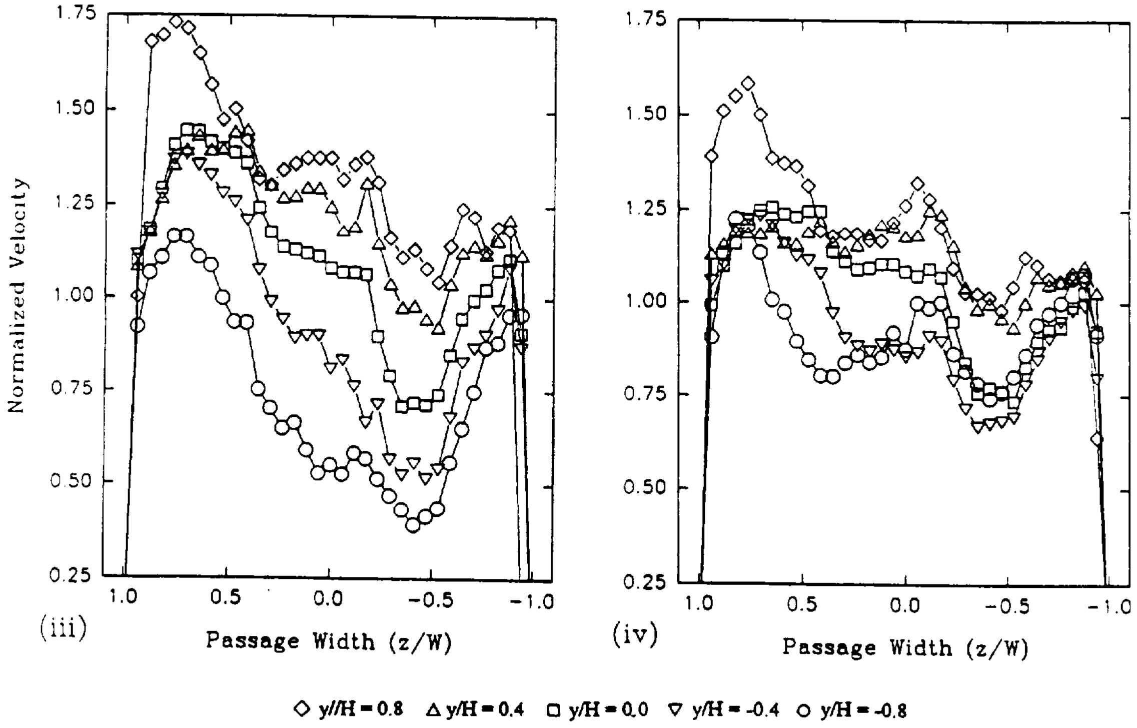

Figure 51 Continued. (iii) Re = 12,500 and Ro = 0.48. (iv) Re = 12,500 and Ro = 0.36.

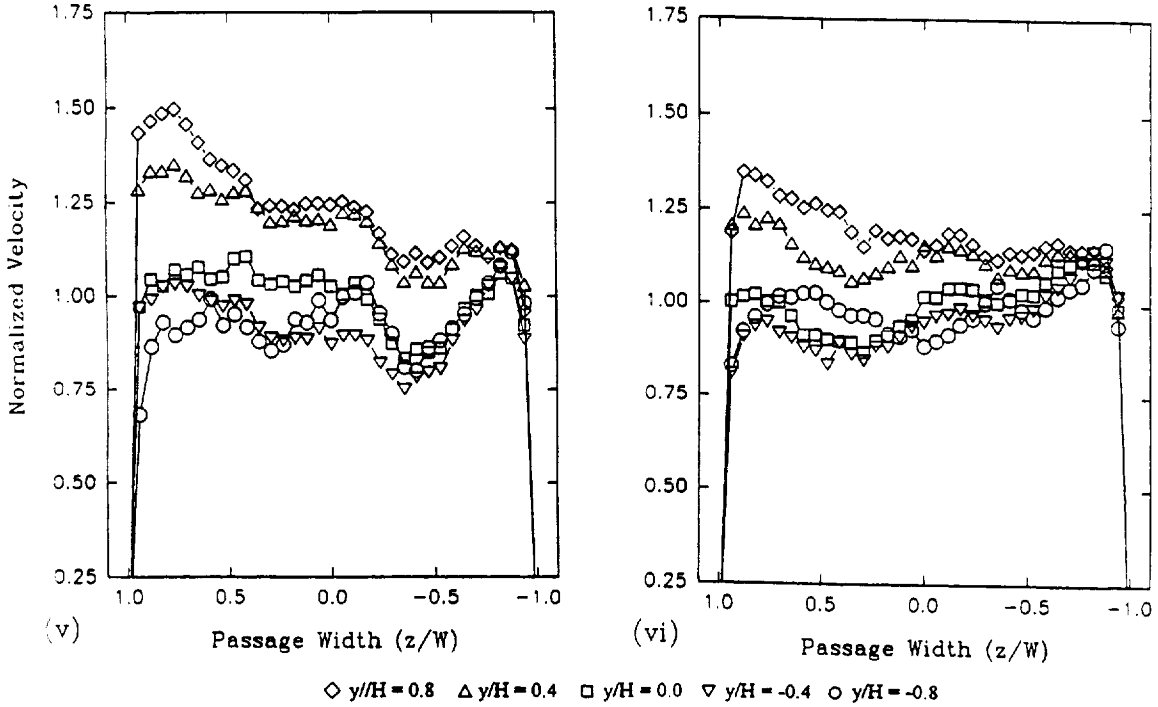

Figure 51 Concluded. (v) Re = 12,500 and Ro = 0.24. (vi) Re = 12,500 and Ro = 0.12.

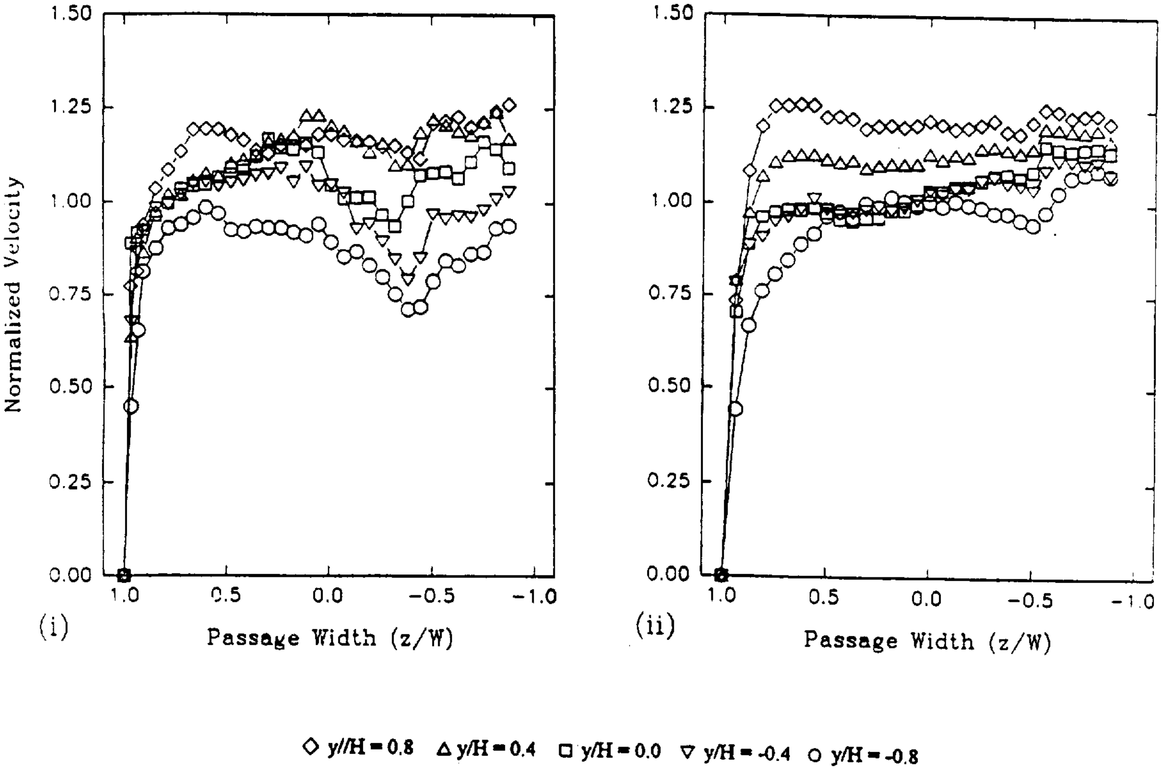

Figure 52 Comparisons of streamwise mean velocities at x/D = 41.3. (i) Re = 25,000 and Ro = 0.24. (ii) Re = 25,000 and Ro = 0.12.

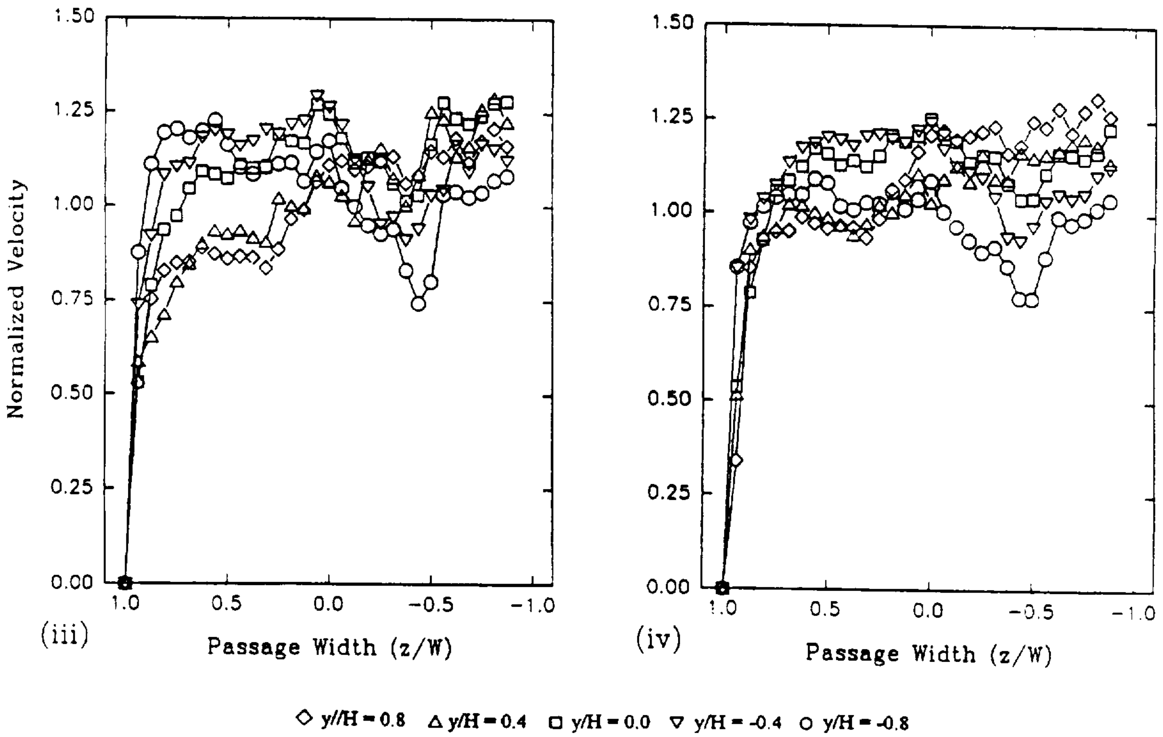

Figure 52 Continued. (iii) Re = 12,500 and Ro = 0.48. (iv) Re = 12,500 and Ro = 0.36.

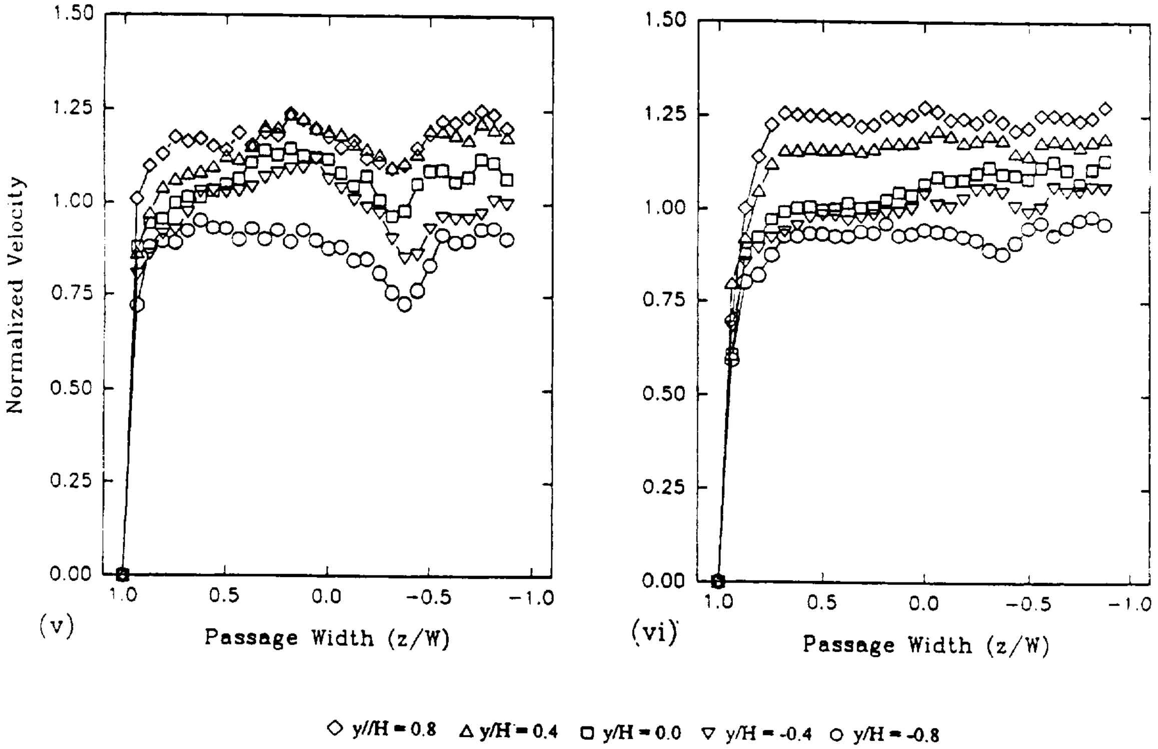

Figure 52 Concluded. (v) Re = 12,500 and Ro = 0.24. (vi) Re = 12,500 and Ro = 0.12.

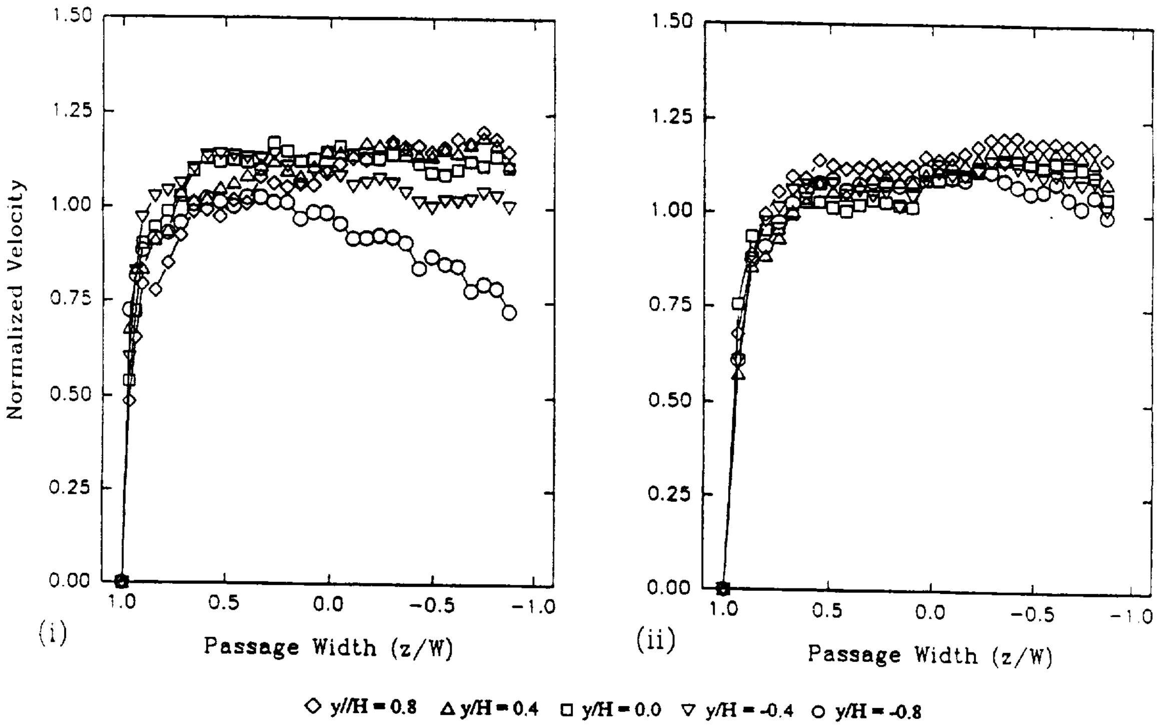

Figure 53 Comparisons of streamwise mean velocities at x/D = 43.3. (i) Re = 25,000 and Ro = 0.24. (ii) Re = 25,000 and Ro = 0.12.

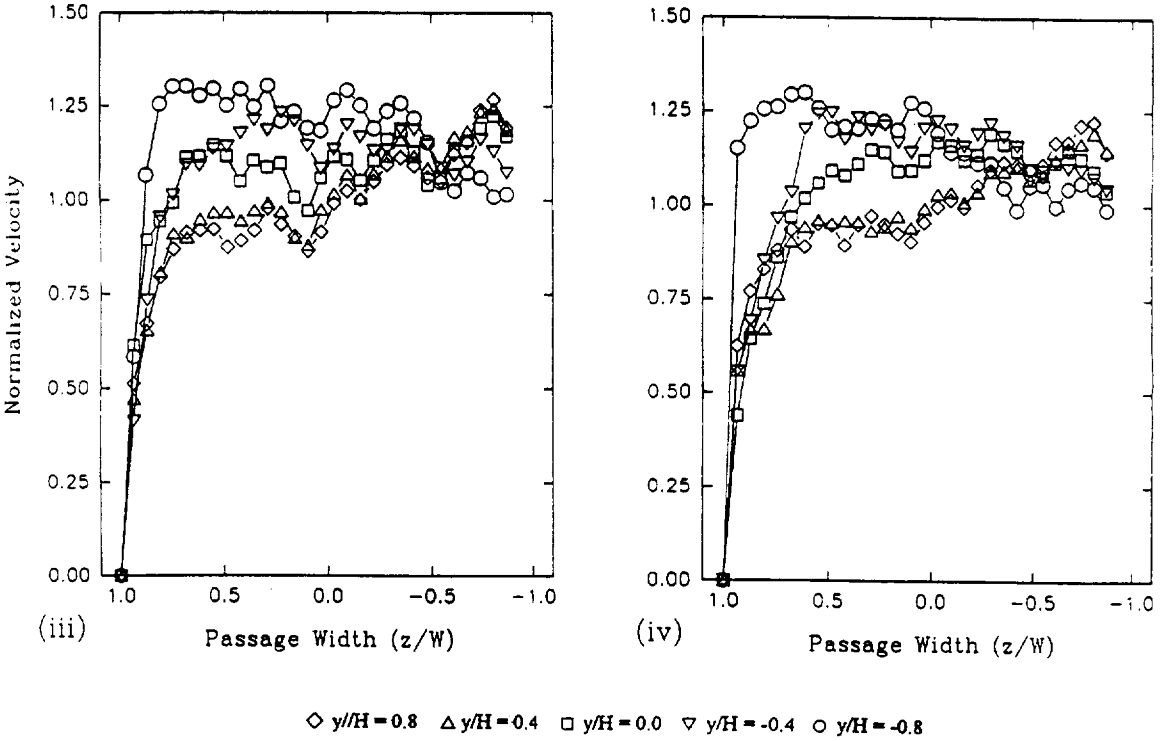

Figure 53 Continued. (iii) Re = 12,500 and Ro = 0.48. (iv) Re = 12,500 and Ro = 0.36.

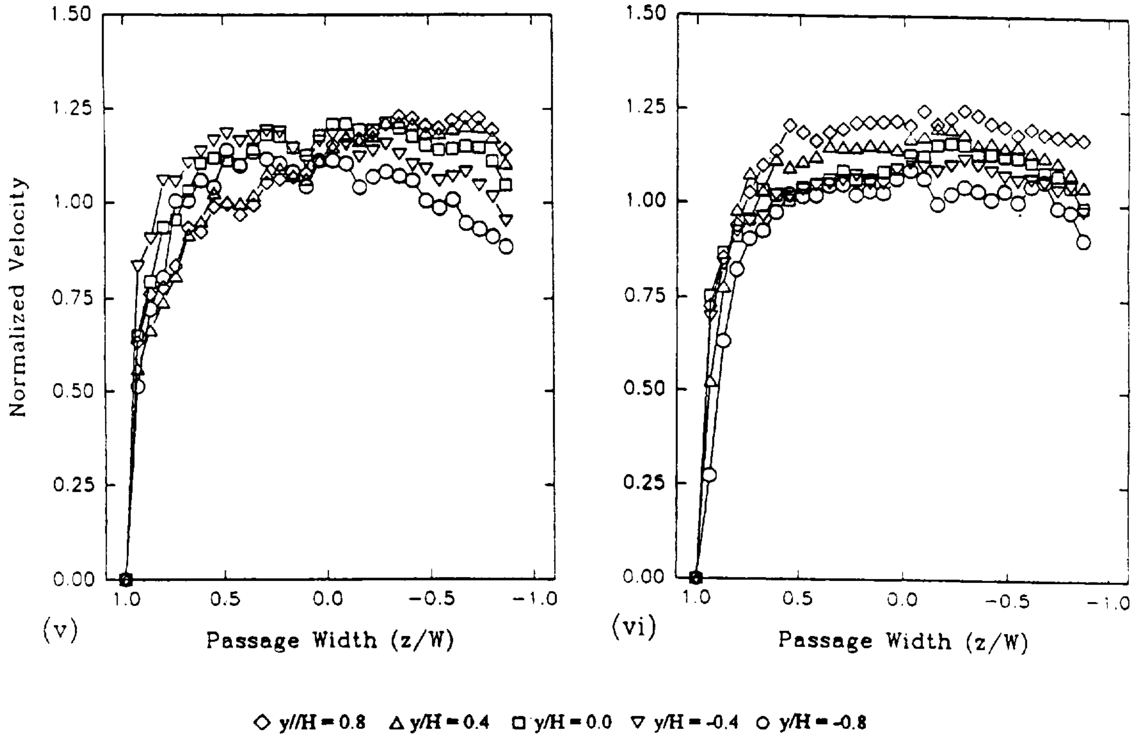

Figure 53 Concluded. (v) Re = 12,500 and Ro = 0.24. (vi) Re = 12,500 and Ro = 0.12.

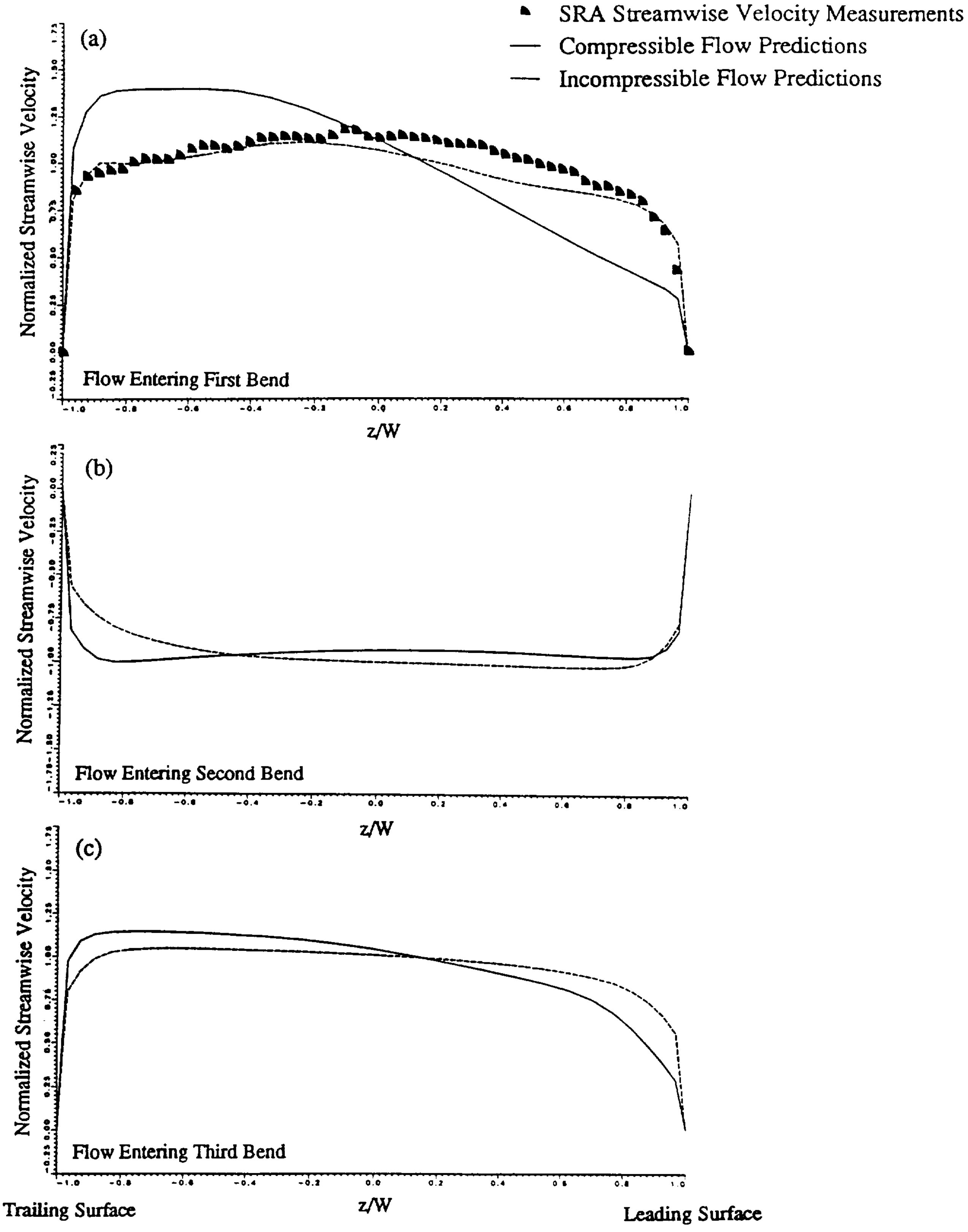

Figure 54 Effect of buoyancy on the centerline velocity

streamwise velocity profile from the trailing to leading surfaces at the centerline of the duct, y/H = 0.0, is shown for flow entering the first turn in Figure 54a. As expected, the centrifugal buoyancy force significantly increases the velocity near the trailing surface resulting in a very thin boundary layer on this wall. Conversely, a much thicker boundary layer develops on the leading surface.

The streamwise velocity profile is also shown for flow entering the second and third turns in Figure 54. For radially inward flow, the Coriolis force acts in the opposite direction causing the cooler fluid to move toward the leading surface. Since the centrifugal buoyancy force is directed radially outward and has a larger effect on the cooler fluid near the leading surface, it tends to decrease the velocity magnitude near the leading surface resulting in a more uniform velocity profile at the duct centerline as shown in Figure 54b. The same flow phenomenon occurs in the first and the third legs of the passage. Therefore, prior to the third turn, the Coriolis and buoyancy induced secondary flows tend to increase the velocity near the trailing surface, Figure 54c. However, the magnitude of the centrifugal buoyancy force is reduced due to a smaller difference between the bulk fluid and the passage wall temperature.

The centerline streamwise velocity profiles indicate that the centrifugal buoyancy force has a significant impact on the flow field in the first leg. Further detail of the streamwise velocity entering the first turn is provided in Figure 55 for the two-layer wall integration simulation. A contour plot of the streamwise velocity shows that reverse flow occurs across the entire leading surface. (The wall function simulation predicted reverse flow in the corners between the side walls and the leading, low pressure, surface.) Prakash and Zerkle (1992) have also predicted reverse flow in a radially rotating duct with outward flow. In their wall function simulations at the same Reynolds number, Re = 25,000 but with a both a larger rotation number, Ro = 0.48 and a larger density ratio, $\Delta\rho/\rho$ = 0.13, reverse flow along the entire leading surface was predicted. Prakash and Zerkle (1992) indicate that at lower buoyancy parameters or lower rotation numbers, the reverse flow either disappeared or was confined to a small region near the leading wall - side wall corner as was predicted in the current simulations.

The tangential velocity contours at the entrance of the first turn, x/D = 15.0, are shown in Figure 55b. As compared to the tangential velocity predicted for the incompressible predictions, Figure 33b, the compressible flow computations show lower tangential velocities near the upper and lower surfaces, y/H = 1.0 and y/H = -1.0, but increased movement of fluid from the leading to the trailing surface in the center of the duct. This is consistent with the increased skew of the streamwise velocity profile due to the centrifugal buoyancy force.

Nusselt number contours of the leading and trailing surfaces are shown in Figure 56 for the wall function simulation with compressible flow. The highest heat transfer was predicted in the first and third turns where the flow is radially outward entering the turn. Although the local heat transfer distribution in the first turn is similar between the incompressible and compressible flow calculations, the centrifugal buoyancy force in the

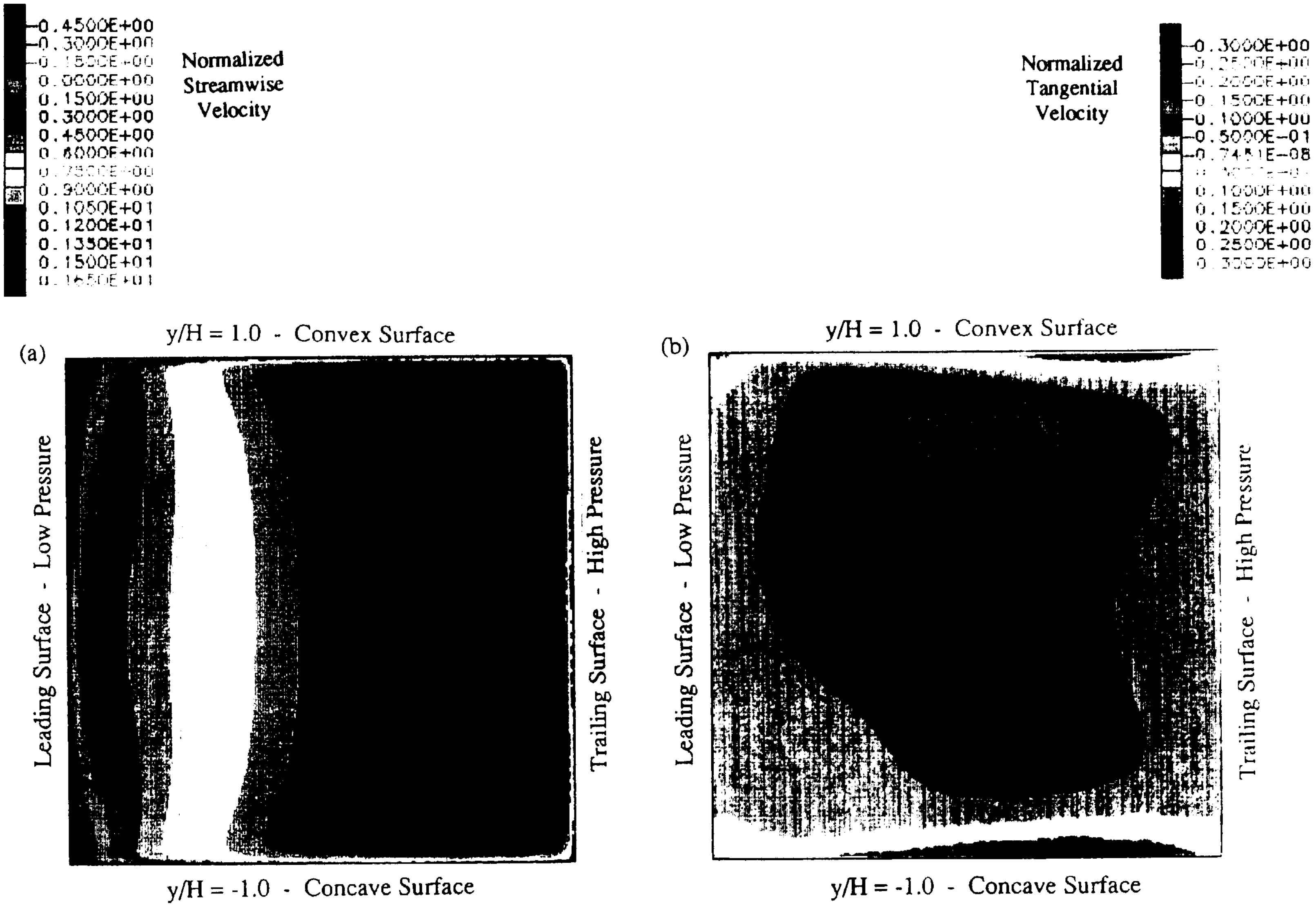

Figure 55 Streamwise and tangential velocity contours entering the first bend, x/D = 15.0, for compressible flow simulations using two-layer wall integration k-ε turbulence model

PRECEDING PAGE BLANK NOT FILMED

Leading Surface

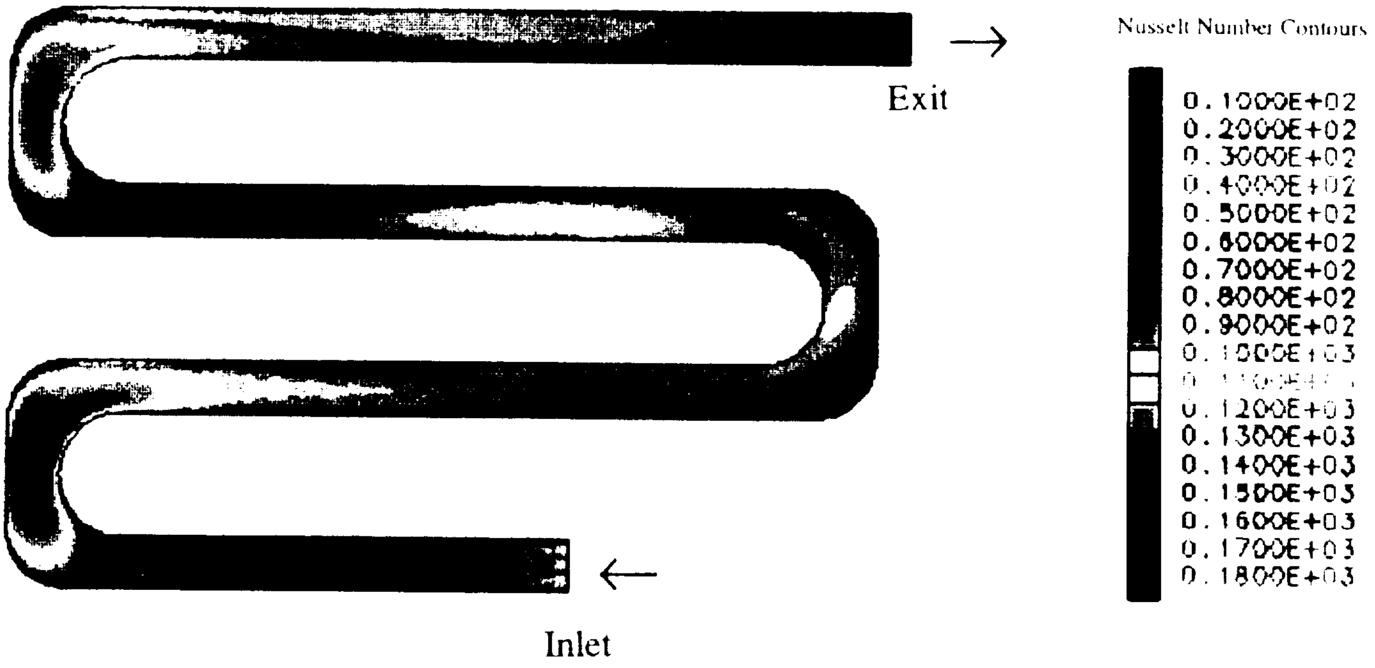

Trailing Surface

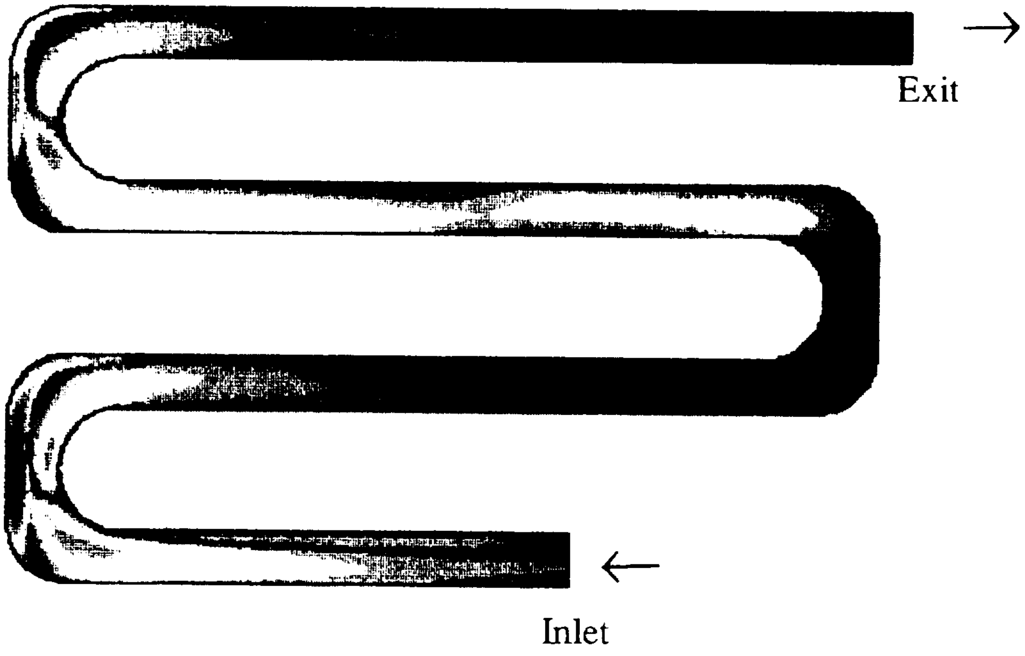

Figure 56 Compressible flow simulations show distinctly different Nusselt number contours for the turns with radially outward flow as compared with the turn with radially inward flow

174

compressible flow predictions increases the heat transfer on both the leading and trailing surfaces of this turn. Unlike the incompressible flow predictions in which the local heat transfer distribution on the trailing surface of the second turn was similar to the leading surface of the third turn; the centrifugal buoyancy force causes distinctly different heat transfer distributions in all of the turns.

Enlarged views of the Nusselt number contour plots in the turns for the wall integration simulations are shown in Figure 57. This simulation shows the largest predicted heat transfer gradients in the turns. However, the same general contour shape as predicted previously in the incompressible simulations is also predicted for the compressible flow predictions. On the leading surface, the region of high heat transfer is predicted at the 90° location and extends almost across the entire width of the passage. On the trailing surface, the predicted peak Nusselt number is approximately the same as on the leading surface. However, very large gradients in Nusselt number occur across the width of the passage.

For the two-layer wall integration simulation, Nusselt number contours on the leading and trailing surfaces were span-averaged and compared with the data of Wagner et al (1991) as shown in Figure 58. The Nusselt number was non-dimensionalized with the correlation value for fully developed turbulent flow in a stationary tube with constant wall temperature, $Nu_\infty = 0.021\ Pr^{0.5} Re^{0.8} = 58$. The high and low pressure surfaces as well as the turn are noted in the figure for reference. The data points of Wagner et al (1991) are represented by oval symbols; the length of the symbol corresponds to the length of the copper segment and the height of the symbol corresponds to the uncertainty of the measurement. The two-layer wall integration incompressible flow prediction is shown as a solid line and the compressible flow prediction is shown as a dashed line.

As expected, the effect of centrifugal buoyancy reduced the predicted heat transfer on the leading surface of the first leg by approximately 15% since the buoyancy force tends to reduce the streamwise velocity in the region. Comparison between the measurements and the compressible flow simulations show a dramatic improvement in the first turn of the leading surface as shown in Figure 58, In the second passage, buoyancy effects reduced heat transfer by 17% relative to the incompressible flow simulation. As stated previously, the Coriolis and centrifugal buoyancy forces act in the opposite direction in the second passage which reduces the heat transfer relative to the Coriolis force alone. Therefore, the agreement between the measurements of Wagner et al (1991) and the compressible flow simulations improve with the simulation overpredicting the data by approximately 30%.

Inclusion of centrifugal buoyancy also improves the comparison between the data of Wagner et al (1991) and the predictions on the trailing surface. The compressible flow simulation predicts an increase in heat transfer of approximately 70% relative to the stationary fully developed correlation. However, the Nusselt number is still underpredicted by 15% - 25% in the first passage and turn on trailing surface. Since the Coriolis and centrifugal buoyancy force act in the opposite direction in the second passages, the velocity profile is much more constant from the leading to trailing surface, as shown in Figure 54b.

176 INTENTIONALLY BLANK

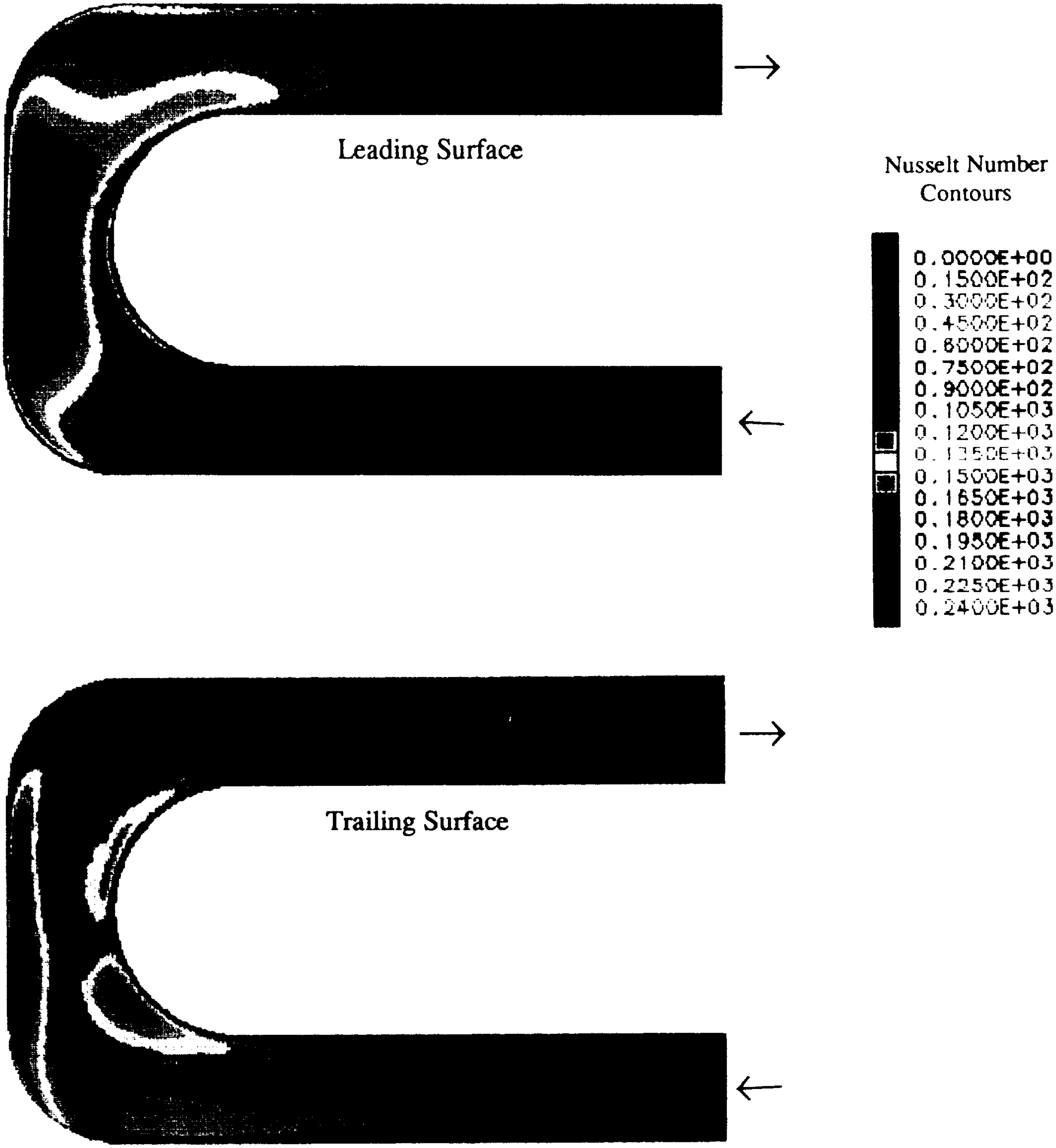

Figure 57 Enlargements of the Nusselt number contours in the first turn for compressible flow

PRECEDING PAGE BLANK NOT FILMED

PAGE 178 INTENTIONALLY BLANK

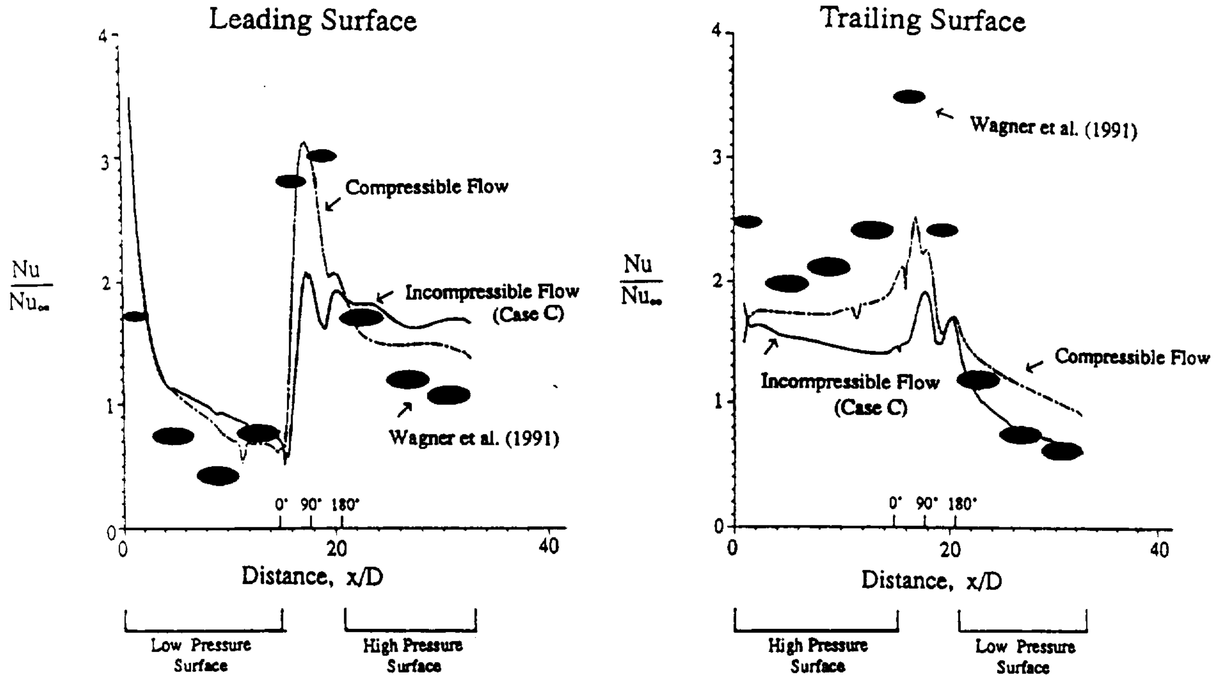

Figure 58 Comparison of the predicted span-average nusselt numbers with the measurements of Wagner et al (1991) improve with the addtion of centrifugal buoyancy force

PAGE 182 INTENTIONALLY BLANK

This phenomenon results in higher predicted heat transfer on the trailing side for the compressible flow simulation.

Overall, the heat transfer comparison between the data and the predictions improves throughout the duct. Since the centrifugal buoyancy force is a function of the temperature difference between the wall and the bulk fluid temperature, the effect of this force diminishes with distance due to the increased bulk temperature of the fluid. Therefore, the greatest difference between the incompressible and compressible flow predictions occur in the first part of the duct.

Some preliminary simulations in which the extra rates of strain (three-dimensionally of flow, rotation) are included in the turbulence model suggest further improvements in the heat transfer predictions can be obtained. In addition to those strains mentioned above, the effect of streamline curvature on the turbulence would be expected to be important in the flow field within a rotating serpentine passage.

In summary, due to the density variations of the fluid in the compressible flow simulations, large centrifugal buoyancy forces develop in the rotating serpentine passage. For radially outward flow, the Coriolis and buoyancy forces both tend to increase the velocity near the trailing edge and decrease the velocity near the leading edge. Including the buoyancy force in the simulations significantly improves the heat transfer prediction on the leading surface particularly in the first turn.

6. ASSESSMENT OF COOLING STRATEGIES

Velocity measurements and simulations show that rotation increases the velocity near the high pressure surface and decrease the velocity near the low pressure surfaces. Heat transfer simulations performed under the current effort as well as the measurements of Wagner et al (1991) show that rotation augments the heat transfer on the high pressure surface and suppresses it on the low pressure surface, which is consistent with the flow characteristics. The increase in heat transfer on the high pressure surface is more than the corresponding reduction on the low pressure surface so that the overall heat transfer increases in the presence of rotation.

Improvements in turbine blade durability, or reductions in cooling flow requirements are dependent upon the ability to accurately predict local "hot spots". Knowledge of the flow field and heat transfer characteristics gained under the present effort suggests several possible improvements in cooling strategies over the current state-of-the-art designs. These innovations fall into two basic categories; changing internal features which turbulate the flow and thus increase heat transfer, and directly changing the flow field.

Modern turbine blade cooling passages make use of trip strips to create secondary flow and augment heat transfer. The results of Johnson et al (1992) and Wagner et al (1991a) indicate secondary flow produced by staggered trips (of the order of 10% of the passage height) fitted on smooth walls have a large effect on heat transfer. Judicious placement of trip strips based on local heat transfer distributions may provide more uniform cooling than current designs. Numerical simulations show high heat transfer on the high pressure surface of the first passage and on both the high and low pressure surfaces of the first turn. High heat transfer associated with the turn continues for 2 to 4 hydraulic diameters downstream of the turn. At the same time, the simulations indicate relatively low heat transfer in the second turn. Measurements of Johnson et al (1992) with skewed trip strips in the straight passages also show relatively low heat transfer in the second turn. Typically, turbine blade passages are design with trip strips on the straight passages and smooth walls in the turns. Based on the current findings, a redistribution of trips is suggested. Removal of trip strips in the straight passages immediately downstream of the first turn (2 to 4 hydraulic diameters) as well as a less dense trip strip spacing on the high pressure surface of the first passage may be warranted. This would allow the addition of the trip strips in the second turn, where low heat transfer exists, with same overall pressure drop.

Turns induce strong secondary flows and large turbulence fluctuations which are beneficial to the augmentation of heat transfer. Furthermore, the consequent interaction of the secondary flow induced by the turn and by rotation produce swirl. Comparison of the heat transfer results and the velocity measurements indicates that swirl, strong secondary flow and large turbulence fluctuation augment heat transfer by up to 100%. The use of passages with rippled-wall rather than the passages with smooth wall can extend the effect of the turn along the entire passage instead of confining it to the end. The internal cooling passages of current turbine blades are formed with a splitter plate. Introducing a wavy rippled-wall pattern on the splitter plate should not complicate the manufacturing process significantly. Its implementation in current and future turbine-blade is viable. Wavy walls can have a rippled pattern of height greater than 10% of the passage height and generate large scale secondary flow without causing flow separation near the wall.

The presence of swirl in the vicinity of the turn can augment heat transfer in the region by up to 100%. Introducing swirl into the straight section of the passage is expected to enhance significantly the overall heat transfer. Swirl can be generated by tangential injection of the coolant at the inlet. However, space is limited in the inlet manifold of a turbine-blade cooling passage and fitting a tangential injection setup within the manifold may not be practical. Furthermore, the velocity measurements indicated entrance effects will extend beyond 6.4 D downstream of the inlet. Swirl generated at the inlet plenum is not expected to augment the heat transfer beyond the first half of the first passage. Introducing swirl at the inlet plenum does not appear to be a promising approach.

7. CONCLUSIONS

A rig has been fabricated for investigating the characteristics of the flow within a rotating turbine-blade coolant passage. High quality and detailed velocity measurements were obtained in a rotating serpentine passage at realistic Reynolds numbers (25,000 and 12,500) and Rotation numbers (0.12, 0.24, 0.36 and 0.48). Although the current effort is isothermal and incompressible, many of the heat transfer results obtained by Wagner et al (1991) can be explained by the flow fields measured here. Buoyancy effects are included in the computational study.

Baseline condition, Re = 25,000 and Ro = 0.24 (experimental investigation):

1. The velocity measurements show that, in the straight passage, there is a net tangential convection from the low pressure surface (leading surface in the radially outward flow passage and trailing surface in the radially inward flow passage) to high pressure surface (trailing surface in the radially outward flow passage and leading surface in the radially inward flow passage) due to Coriolis effects. The tangential convection increases steadily the streamwise velocities on the high pressure surface and induces a velocity deficit on the low pressure surface.

2. Coriolis induced secondary flow increases in streamwise velocity (convective heat transfer) on the high pressure (trailing) side at the end of the first passage (radially outward flow passage) by 20%, which leads to a 16% increase in heat transfer based on the $Nu\text{-}Re^{0.8}$ correlation. Wagner et al (1991) show increases in heat transfer of 100% on the high pressure side at the end of the first passage. Previously measured increases in heat transfer, Wagner et al (1991), are attributed to both the Coriolis and centrifugal buoyancy forces increasing the streamwise velocity near the high pressure surface. In addition, the Coriolis induced secondary flow causes convection of the cool fluid from the center of the passage to the trailing surface which may be a significant contributor to the measured heat transfer increase.

3. Coriolis effects reduce the streamwise velocity on the low pressure (leading) side, relative to the stationary case, in the first half of the first passage. The heat transfer on the low pressure side in the latter half of the first passage, Wagner et al (1991), is higher than that of the stationary case. Buoyancy forces reinforce the velocity deficits on the leading side. The increase in heat transfer on the low pressure side in the latter half of the first passage is associated with enhanced mixing between the near-wall fluid and the cross-flow generated by the development of strong secondary flow toward the end of the passage. The Coriolis induced secondary flows are strong enough to offset the reduction in heat transfer associated with reductions in streamwise velocity induced by Coriolis and buoyancy effects. This result confirms the importance of the Coriolis induced secondary flow in determining the heat transfer characteristics.

4. The interaction of the secondary flows induced by the turn and rotation produce swirl at the first and second turns. Swirl enables the interface between the hotter near-wall

fluid and the cooler cross-flow to be rapidly distorted and increased in area many times and this augments heat transfer. The high pressure drop associated with the turn results in secondary flows of the order of 95% U_b (cross-flow at speeds of up to 50% higher than that in the straight passage) and turbulence intensities of the order of 10% higher than those in the straight passage.

5. Augmentation of heat transfer in the vicinity of the first turn by up to 100%, Wagner et al (1991), is attributed to swirl, strong secondary flow and large turbulence fluctuations. The effect of the turn extends beyond 2D downstream of the turn but does not extend beyond 4D downstream of the turn.

6. The Coriolis induced secondary flow tends to increase heat transfer on the high pressure surfaces by increasing the streamwise velocity and also transporting the cooler fluid from the center of the passage toward the surface. Coriolis effects increase the streamwise velocities on the high pressure (leading) side at the end of the second passage (radially inward flow passage) by 20%. This increase in velocity leads to a 16% increase in heat transfer based on the $Nu\text{-}Re^{0.8}$ correlation. Wagner et al (1991) show increases in heat transfer of the order of 10 to 20% on the high pressure side of the second passage. Since the transport of the cool fluid toward the high pressure surface is expected to further increase the heat transfer, these results indicate that the centrifugal buoyancy and Coriolis induced secondary flows offset each other in the second passage.

7. The cross-flow exiting the second turn has steeper gradients and stronger near-wall flows than that exiting the first.

The effect of Reynolds number, Rotation number and buoyancy parameter:

8. The effect of Reynolds number in the range 12,500 and 25,000 extends beyond 25D downstream of the inlet but it is limited to within 33D downstream of the inlet.

9. The effect of Rotation number on the streamwise velocity is asymptotic and there are not significant differences between the streamwise velocity characteristics at the end of the first passage for Ro = 0.24, 0.36 and 0.48. The relative tangential velocities increase approximately linearly with Ro in the first passage. The variations in the streamwise and tangential velocity characteristics on the high pressure and low pressure surfaces along the second passage with Ro are higher than those along the first passage.

Baseline Condition, Re = 25,000 and Ro = 0.24 (computational investigation):

10. The flow field predictions, in which the two-layer wall integration turbulence model was implemented, agree well with data through the first turn. Although the two near wall shear-stress treatments (wall functions and two-layer wall integration) yield very similar results in the first passage, at the exit of the first turn, where large velocity gradients exist, the two-layer wall integration simulation provides an improvement over the wall function simulation.

11. Good agreement between the simulations and the measurements is dependent on a complete initialization of the inlet boundary conditions. For the simulation with the inlet secondary flow set to zero, the predicted secondary flow structure is different from the measurements even beyond the first turn. However, with a complete inlet flow field specified, the tangential velocity agrees well with the data.

12. Predicted heat transfer is enhanced in the turns and on the high pressure surfaces due to the Coriolis force. The measurements of Wagner et al (1991) show increases in heat transfer of 100% (relative to stationary fully developed flows) on the high pressure at the end of the first passage. However, the incompressible heat transfer predictions show increases of only 40% relative to stationary fully developed flow. This discrepancy between the measurements and the simulation indicates that the buoyancy induced flow which is present in the measurements may have a large impact on the heat transfer in these locations.

The Effect of Buoyancy

13. For radially outward flow, both the Coriolis and buoyancy induced secondary flow increase the velocity near the trailing surface and reduce the velocity near the leading surface. With the two layer wall integration simulation, this phenomenon yields reverse flow across the entire leading surface as flow enters the first turn.

14. Inclusion of the centrifugal buoyancy force in the heat transfer simulations improves the comparison between the data of Wagner et al (1991) and the wall integration prediction, particularly on the leading surface. Although the predicted heat transfer increases on the trailing, high pressure, surface in the first leg, the measured heat transfer is approximately 20% higher than the simulations. (However, the effect of buoyancy is greatest in the first part of the duct since the centrifugal buoyancy force is a function of the temperature difference between the wall and the bulk temperature of the fluid.)

ACKNOWLEDGMENTS

The authors are glad to acknowledge the financial support form NASA/Lewis research center under SBIR Contract No. NAS3-26251. They welcome this opportunity to thank Dr. B. Johnson of UTRC for providing the heat transfer data for comparison. Thanks are due to Dr. B. Johnson of UTRC, Drs. F. Yeh and R. Simoneau of NASA Lewis and Drs. S. Tanrikut and O. Sharma of Pratt & Whitney for their many discussions providing important insight and suggestions during this program and to Mr. G. Winch of SRA for maintenance of the experimental facility.

REFERENCES

1. Bo, T., Iacovides, H. and Launder, B.E. (1991): The Prediction of Convective Heat Transfer in Rotating Square Ducts, Eighth Symposium on Turbulent Shear Flows.

2. Dash, S.M., Beddini, R.A., Wolf, D.E. and Sinha, N. (1983): "Viscous/Inviscid Analysis of Curved Sub- or Supersonic Wall Jets," AIAA paper 83-1679.

3. Eckert, E.R.G., Diaguila, A.J. and Curren, A.N. (1964): Experiments on Mixed-, Free- and Forced-Convective Heat Transfer with Turbulent Flow Through a Short Tube, NACA Technical Note 2974.

4. Johnson, B.V. Wagner, J.H., Steuber, G.D., and Yeh, F.C. (1992): "Heat Transfer in Rotating Serpentine Passages with Trips Skewed to the Flow," NASA TM 105581.

5. Kays, W.M. and Crawford: "Convective Heat and Mass Transfer," McGraw-Hill, Inc., New York, 1980.

6. Launder, B.E. and Spaulding, D.B. (1974): "The Numerical Computation of Turbulent Flows," Computer Methods in Applied Mechanics and Engineering, **3**:269-289.

7. Metais, B. and Eckert, E.R.G. (1964): Forced, Mixed and Free Convection Regimes, J. Heat Transfer, **64**:93-95.

8. Prakash, C., and Zerkle, R. (1992): "Prediction of Turbulent Flow and Heat Transfer in a Radially Rotating Square Duct," 1992 Winter Annual Meeting.

9. Rhie, C.M. (1986): "A Pressure Based Navier-Stokes Solver Using the Multigrid Method," AIAA Paper 86-0207.

10. Thompson, B.E., Hogan, M.B. Tse, D.G.N. and Shamroth, S.J. (1990): "Flow in Turbine Blade Passages", Scientific Reseach Associates, Inc. Report R90-900078-F.

11. Wagner, J.H., Johnson, B.V. and Kopper, F.C. (1991): "Heat Transfer in Rotating Serpentine Passages with Smooth Walls," ASME Journal of Turbomachinery, **113**: 321-330.

12. Wagner, J.H., Johnson, B.V., Graziani, R.A. and Yeh, F.C. (1991a): "Heat Transfer in Rotating Serpentine Passages with Trips Normal to the Flow," ASME Paper 91-GT-256, June 1991. Also issued as NASA TM 103758, 1991.

13. Yang, W-J., Zhang, N. and Chiou, J. (1992): "Local Heat Transfer in a Rotating Serpentine Flow Passage," ASME J. Heat Transfer, **114**:354-361.

REPORT DOCUMENTATION PAGE

Form Approved
OMB No. 0704-0188

Public reporting burden for this collection of information is estimated to average 1 hour per response, including the time for reviewing instructions, searching existing data sources, gathering and maintaining the data needed, and completing and reviewing the collection of information. Send comments regarding this burden estimate or any other aspect of this collection of information, including suggestions for reducing this burden, to Washington Headquarters Services, Directorate for Information Operations and Reports, 1215 Jefferson Davis Highway, Suite 1204, Arlington, VA 22202-4302, and to the Office of Management and Budget, Paperwork Reduction Project (0704-0188), Washington, DC 20503.

1. AGENCY USE ONLY (*Leave blank*)

2. REPORT DATE
May 1994

3. REPORT TYPE AND DATES COVERED
Final Contractor Report

4. TITLE AND SUBTITLE
A Combined Experimental/Computational Study of Flow in
Turbine Blade Cooling Passage

5. FUNDING NUMBERS
WU–505–62–52

6. AUTHOR(S)
D.G.N. Tse, J.P. Kreskovsky, S.J. Shamroth, and D.B. McGrath

7. PERFORMING ORGANIZATION NAME(S) AND ADDRESS(ES)
Scientific Research Associates
50 Nye Road, P.O. Box 1058
Glastonbury, Connecticut 06033

8. PERFORMING ORGANIZATION REPORT NUMBER
E–8243

9. SPONSORING/MONITORING AGENCY NAME(S) AND ADDRESS(ES)
National Aeronautics and Space Administration
Lewis Research Center
Cleveland, Ohio 44135–3191

10. SPONSORING/MONITORING AGENCY REPORT NUMBER
NASA CR–4584

11. SUPPLEMENTARY NOTES
D.G.N. Tse, J.P. Kreskovsky, and S.J. Shamroth, Scientific Research Associates, Inc. Glastonbury, Connecticut 06033 (work funded by NAS3–26251) and D.B. McGrath, Pratt & Whitney, 400 Main Street, East Hartford, Connecticut 06018. Project Manager, Frederick C. Yeh, Internal Fluids Mechanics Division, organization code 2630, (216) 433–5872.

12a. DISTRIBUTION/AVAILABILITY STATEMENT
Unclassified - Unlimited
Subject Category 34

12b. DISTRIBUTION CODE

13. ABSTRACT ***(Maximum 200 words)***

Laser velocimetry was utilized to map the velocity field in a serpentine turbine blade cooling passage at Reynolds and Rotation numbers of up to 25,000 and 0.48. These results were used to assess the combined influence of passage curvature and Coriolis force on the secondary velocity field generated. A Navier-Stokes code (NASTAR) was validated against incompressible test data and then used to simulate the effect of bouyancy. The measurements show a net convection from the low pressure surface to high pressure surface. The interaction of the secondary flows induced by the turns and rotation produces swirl at the turns, which persisted beyond 2 hydraulic diameters downstream of the turns. The incompressible flow field predictions agree well with the measured velocities. With radially outward flow, the bouyancy force causes a futher increase in velocity on the high pressure surface and a reduction on the low pressure surface. The results were analyzed in relation to the heat transfer measurements of Wagner et al. (1991). Predicted heat transfer is enhanced on the high pressure surfaces and in turns. The incompressible flow simulation underpredicts heat transfer in these locations. Improvements observed in compressible flow simulation indicate that the bouyancy force may be important.

14. SUBJECT TERMS
Turbine cooling; Turbine blade

15. NUMBER OF PAGES
194

16. PRICE CODE
A09

17. SECURITY CLASSIFICATION OF REPORT	**18. SECURITY CLASSIFICATION OF THIS PAGE**	**19. SECURITY CLASSIFICATION OF ABSTRACT**	**20. LIMITATION OF ABSTRACT**
Unclassified	Unclassified	Unclassified	

National Aeronautics and
Space Administration
Code JTT
Washington, D.C. 20546-0001

Official Business
Penalty for Private Use $300

POSTMASTER: If Undeliverable — Do Not Return